ADVANCES IN INTRAVASCULAR IMAGING

EDITED BY: Christos Bourantas, Patrick W. Serruys and Farouc Jaffer
PUBLISHED IN: Frontiers in Cardiovascular Medicine

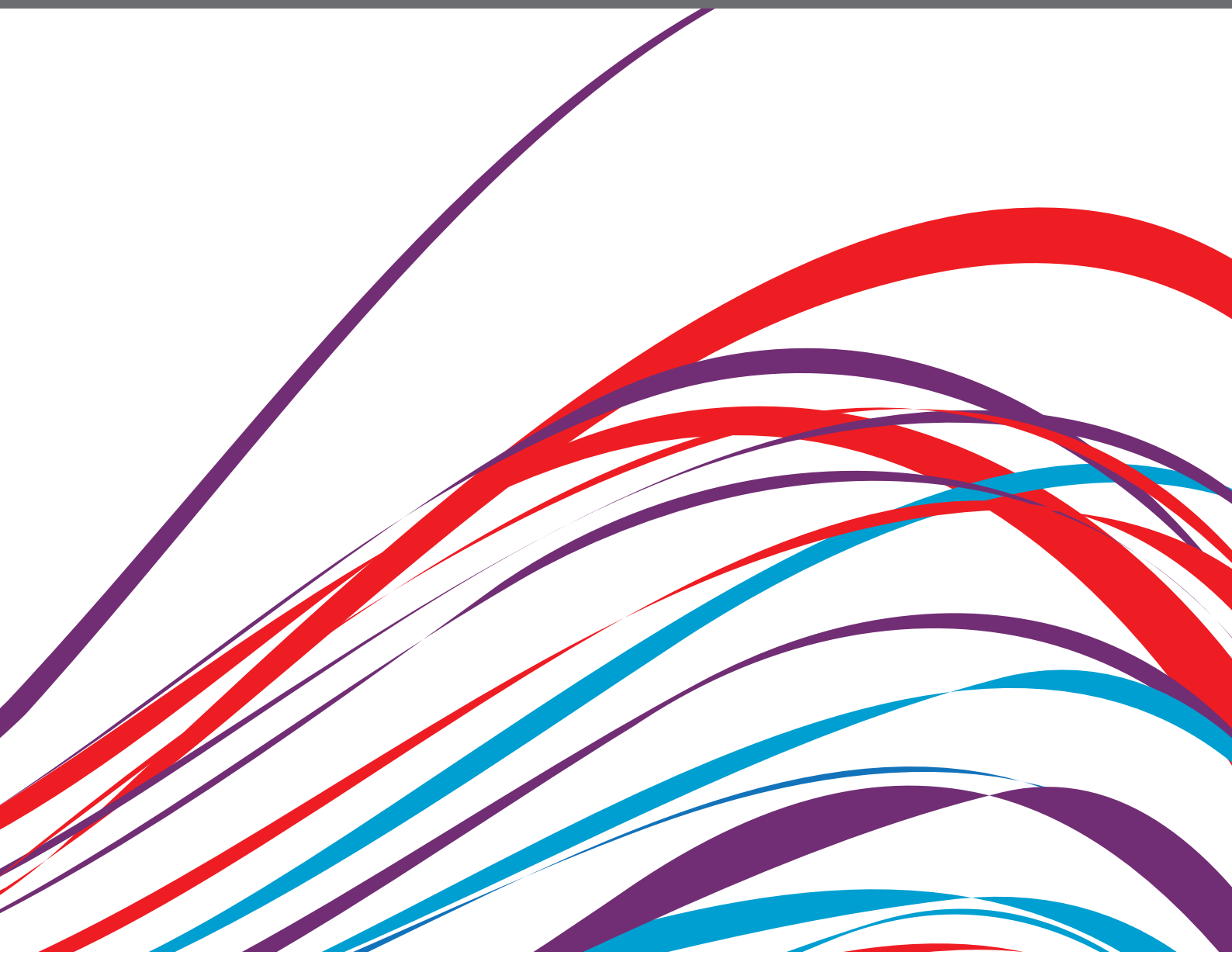

frontiers Research Topics

ISSN 1664-8714
ISBN 978-2-88971-582-4
DOI 10.3389/978-2-88971-582-4

About Frontiers

Frontiers is more than just an open-access publisher of scholarly articles: it is a pioneering approach to the world of academia, radically improving the way scholarly research is managed. The grand vision of Frontiers is a world where all people have an equal opportunity to seek, share and generate knowledge. Frontiers provides immediate and permanent online open access to all its publications, but this alone is not enough to realize our grand goals.

Frontiers Journal Series

The Frontiers Journal Series is a multi-tier and interdisciplinary set of open-access, online journals, promising a paradigm shift from the current review, selection and dissemination processes in academic publishing. All Frontiers journals are driven by researchers for researchers; therefore, they constitute a service to the scholarly community. At the same time, the Frontiers Journal Series operates on a revolutionary invention, the tiered publishing system, initially addressing specific communities of scholars, and gradually climbing up to broader public understanding, thus serving the interests of the lay society, too.

Dedication to Quality

Each Frontiers article is a landmark of the highest quality, thanks to genuinely collaborative interactions between authors and review editors, who include some of the world's best academicians. Research must be certified by peers before entering a stream of knowledge that may eventually reach the public - and shape society; therefore, Frontiers only applies the most rigorous and unbiased reviews.
Frontiers revolutionizes research publishing by freely delivering the most outstanding research, evaluated with no bias from both the academic and social point of view. By applying the most advanced information technologies, Frontiers is catapulting scholarly publishing into a new generation.

What are Frontiers Research Topics?

Frontiers Research Topics are very popular trademarks of the Frontiers Journals Series: they are collections of at least ten articles, all centered on a particular subject. With their unique mix of varied contributions from Original Research to Review Articles, Frontiers Research Topics unify the most influential researchers, the latest key findings and historical advances in a hot research area! Find out more on how to host your own Frontiers Research Topic or contribute to one as an author by contacting the Frontiers Editorial Office: frontiersin.org/about/contact

ADVANCES IN INTRAVASCULAR IMAGING

Topic Editors:
Christos Bourantas, University College London, United Kingdom
Patrick W. Serruys, Imperial College London, United Kingdom
Farouc Jaffer, Harvard Medical School, United States

Citation: Bourantas, C., Serruys, P. W., Jaffer, F., eds. (2021). Advances in Intravascular Imaging. Lausanne: Frontiers Media SA.
doi: 10.3389/978-2-88971-582-4

Table of Contents

frontiers in Cardiovascular Medicine

EDITORIAL
published: 16 September 2021
doi: 10.3389/fcvm.2021.764378

Editorial: Advances in Intravascular Imaging

Christos V. Bourantas[1,2,3]*, *Farouc A. Jaffer*[4], *Yoshinubo Onuma*[5] and *Patrick W. Serruys*[5,6]

[1] Department of Cardiology, Barts Heart Centre, Barts Health NHS, London, United Kingdom, [2] Institute of Cardiovascular Sciences, University College London, London, United Kingdom, [3] William Harvey Research Institute, Queen Mary University London, London, United Kingdom, [4] Cardiovascular Research Center and Cardiology Division, Harvard Medical School and Massachusetts General Hospital, Boston, MA, United States, [5] Department of Cardiology, National University of Ireland, Galway, Ireland, [6] Faculty of Medicine, National Heart & Lung Institute, Imperial College London, London, United Kingdom

Keywords: hybrid intravascular imaging, coronary artery disease, percutaneous coronary intervention, intravascular ultrasound, optical coherence tomography

Editorial on the Research Topic

Advances in Intravascular Imaging

Intravascular imaging was introduced 30 years ago to assess coronary artery morphology and facilitate percutaneous coronary intervention (PCI). Today, invasive imaging has an established role in clinical practice and research (1). Cumulative data over the recent years have underscored the value of intravascular ultrasound (IVUS) and optical coherence tomography (OCT) in optimizing PCI results, while prospective studies of coronary atherosclerosis have provided convincing evidence that both modalities are capable to detect lesions that are likely to progress and cause events. These reports however, also revealed limitations of these techniques in guiding PCI and in identifying vulnerable plaques (2). To overcome these drawbacks efforts have been made to design advanced intravascular imaging systems that can provide a more detailed and complete evaluation of plaque pathology and biology, either by combining two intravascular imaging probes or by enabling acquisition of additional information by a single imaging probe (3). This special issue of Frontiers in Cardiovascular Medicine provides an overview of the developments in the field and summarizes the evidence supporting the use of novel intravascular imaging catheters in clinical practice and research.

Near-infrared spectroscopy (NIRS)-IVUS imaging is the first hybrid intravascular imaging modality that had clinical applications. The catheter incorporates a NIRS and IVUS integrated probe that acquire simultaneous imaging data which are co-registered to generate hybrid NIRS-IVUS images. The review article of Kuku et al. published in this issue describes the evolution in catheter design and presents the evidence supporting the value of this modality in guiding PCI and detecting vulnerable plaques. Muller—the inventor of NIRS imaging—and Madder, also highlight, in their review, the potential of hybrid NIRS-based imaging in optimizing PCI results and identifying high-risk lesions and patients who would benefit from aggressive treatments targeting atherosclerosis, and introduce a combined NIRS-OCT system that is expected to have clinical applications in the near future (Muller and Madder). Another hybrid intravascular imaging modality that appears superior to standalone IVUS or OCT imaging in assessing plaque phenotype is the combined IVUS-OCT imaging, which has also reached clinical translation. Several prototypes have been presented over the last years and one of them the Novasight Hybrid^{TM} System (Conavi Medical Inc, Toronto, Canada) had recently first-in-man studies (4). Ono et al. in their review discuss the challenges of combined IVUS-OCT imaging, present the evidence supporting its use in PCI and summarize the findings of histology studies which indicate that hybrid IVUS-OCT imaging is superior to standalone IVUS and OCT in assessing plaque features associated with increased vulnerability (4).

OPEN ACCESS

Edited by:
Takashi Muramatsu, Fujita Health University Hospital, Japan

Reviewed by:
Grigorios Korosoglou, GRN Klinik Weinheim, Germany
Erhan Tenekecioglu, University of Health Sciences, Turkey

****Correspondence:***
Christos V. Bourantas
cbourantas@gmail.com

Specialty section:
This article was submitted to Cardiovascular Imaging, a section of the journal Frontiers in Cardiovascular Medicine

Received: *25 August 2021*
Accepted: *25 August 2021*
Published: *16 September 2021*

Citation:
Bourantas CV, Jaffer FA, Onuma Y and Serruys PW (2021) Editorial: Advances in Intravascular Imaging. Front. Cardiovasc. Med. 8:764378. doi: 10.3389/fcvm.2021.764378

The above developments in intravascular imaging may enable more precise evaluation of plaque composition but cannot detect vascular inflammation which is an important instigator of plaque evolution. Near-infrared fluorescence (NIRF) imaging was introduced to address this unmet need. This modality can be combined with IVUS or OCT and appears capable to identify the presence of macrophages, cathepsin protease activity, oxidized low-density lipoprotein and thrombus. NIR autofluorescence (NIRAF)-OCT intracoronary imaging has been performed in patients and may identify high-risk plaques with intraplaque hemorrhage or oxidized lipid, without the need for a contrast agent. The developments in the field are described in detail by the inventors of NIRF in a comprehensive review that also discusses the potential value of hybrid NIRF-IVUS and OCT-NIRF imaging in secondary prevention (Khraishah and Jaffer).

Another intravascular imaging modality that is capable to accurately detect the presence of macrophages in the superficial plaque and thus vascular biology is florescence lifetime imaging (FLIm). The study of Bec et al. published in this special issue of Frontiers in Cardiovascular Medicine compared the efficacy of FLIm and Raman spectroscopy in characterizing plaque composition using histology as reference standard. The authors showed that FLIm, in contrast to Raman spectroscopy, has a limited efficacy in detecting different tissue types. In this report the co-registered FLIm and Raman data allowed more precise evaluation of the efficacy of FLIm imaging in characterizing plaque composition and showed that increased lifetime values are associated with the presence of cholesterol and carotenes and not with collagen, as it was shown in previous studies.

In parallel to the design of novel hybrid imaging catheters for more detailed assessment of the atheroma, efforts have been made to optimize standalone intravascular imaging catheters. Toward this direction polarization sensitive (PS)-OCT imaging was introduced. This approach relies on the analysis of the polarization properties of the reflected OCT signal (Otsuka et al.). The inventors of this approach present a thorough review which describes the basic principles of PS-OCT and highlights its value in characterizing atheroma. Summarizing their research in the field the authors suggest that PS-OCT is capable to assess collagen and smooth muscle cell content in fibrous caps, and improve the efficacy of OCT in identifying necrotic cores, macrophage accumulations and cholesterol crystals—plaque features that are seen in high-risk lesions. Finally, PS-OCT offers a unique potential to automatically quantify tissue types allowing fast processing of large imaging data.

Despite the high resolution of OCT there are plaque micro-features that cannot be visualized by this imaging technique. To address this limitation micro-(μ)OCT has been developed that allows plaque imaging with a resolution of 1–2 μm. Nishimiya and Tearney in a comprehensive review present the technical developments in the field, and highlight the potential of this approach in assessing plaque vulnerability and PCI results. Another emerging imaging modality is optically generated ultrasound imaging (OpUS). This approach offers increase signal penetration (>20 mm) and is capable to acquire images with a resolution of >50 μm. Preliminary data has shown that it is able to characterize plaque composition. OpUS is still in its infancy and its full potential has not been evaluated yet; moreover further developments are needed before this modality has applications in interventional cardiology (Little et al.).

From the above it is apparent that the field of intravascular imaging is rapidly evolving and that soon the interventional cardiologists will have numerous options for assessing plaque morphology and guiding percutaneous revascularisation. Which modality is likely to dominate in the clinical arena is difficult to predict, as this will depend not only on its imaging capabilities but also on the time needed to interrogate a vessel, on how easy will be image interpretation and on how fast will be data post-processing. What is obvious however, is that the emerging imaging techniques are likely to fulfill our expectations allowing not only better treatment planning but also complete visualization of vessel pathology, biology and physiology—after coronary reconstruction and blood flow simulation with easy to use software (Kilic et al.)—and thus more precise identification of vulnerable lesions and high-risks patients that will benefit from emerging therapies targeting atherosclerosis (5).

In addition, the above advances in intravascular imaging is also likely to enable more precise evaluation of new developments in non-invasive imaging and in particular in computed tomography coronary angiography (CTCA) and positron emission tomography (PET)-CT/CTCA. In contrast to intravascular imaging that is associated with a risk of complications and do not allow complete assessment of the coronary artery tree, non-invasive imaging appears as the ideal approach for stratifying cardiovascular risk as it can be used in asymptomatic individuals, requires a lower dose of radiation and enables complete study of all the major coronary arteries (5). Yet CTCA and PET-CT/CTCA image analysis is time consuming, the positive predictive value of CTCA in detecting vulnerable plaques is low while the additive value of PET-CT/CTCA to stratify cardiovascular risk over CTCA has not been well-studied (6). Therefore, further research is needed, and developments are required to enhance image resolution expedite data analysis and identify new imaging-markers that will allow more precise identification of lesions at risk and enable the broad use of non-invasive imaging in the clinical arena to detect vulnerable patients that will benefit from emerging therapies targeting atherosclerosis.

AUTHOR CONTRIBUTIONS

CB drafted the manuscript while FJ, YO, and PS reviewed, edited, and approved the final draft. All authors contributed to the article and approved the submitted version.

REFERENCES

1. Bourantas CV, Tenekecioglu E, Radu M, Raber L, Serruys PW. State of the art: role of intravascular imaging in the evolution of percutaneous coronary intervention - a 30-year review. *EuroIntervention.* (2017) 13:644–53. doi: 10.4244/EIJ-D-17-00471
2. Ramasamy A, Serruys PW, Jones DA, Johnson TW, Torii R, Madden SP, et al. Reliable *in vivo* intravascular imaging plaque characterization: a challenge unmet. *Am Heart J.* (2019) 218:20–31. doi: 10.1016/j.ahj.2019.07.008
3. Bourantas CV, Garcia-Garcia HM, Naka KK, Sakellarios A, Athanasiou L, Fotiadis DI, et al. Hybrid intravascular imaging: current applications and prospective potential in the study of coronary atherosclerosis. *J Am Coll Cardiol.* (2013) 61:1369–78. doi: 10.1016/j.jacc.2012.10.057
4. Ono M, Kawashima H, Hara H, Gao C, Wang R, Kogame N, et al. Advances in IVUS/OCT and future clinical perspective of novel hybrid catheter system in coronary imaging. *Front Cardiovasc Med.* (2020) 7:119. doi: 10.3389/fcvm.2020.00119
5. Bourantas CV, Garcia-Garcia HM, Torii R, Zhang Y-J, Westwood M, Crake T, et al. Vulnerable plaque detection: an unrealistic quest or a feasible objective with a clinical value? *Heart.* (2016) 102:581–9. doi: 10.1136/heartjnl-2015-309060
6. Johnson TW, Raber L, di Mario C, Bourantas C, Jia H, Mattesini A, et al. Clinical use of intracoronary imaging. Part 2: acute coronary syndromes, ambiguous coronary angiography findings, and guiding interventional decision-making: an expert consensus document of the European Association of Percutaneous Cardiovascular Interventions. *Eur Heart J.* (2019) 40:2566–84. doi: 10.1093/eurheartj/ehz332

Conflict of Interest: The authors declare that the research was conducted in the absence of any commercial or financial relationships that could be construed as a potential conflict of interest.

frontiers in Cardiovascular Medicine

REVIEW
published: 31 March 2020
doi: 10.3389/fcvm.2020.00033

The Evolution of Data Fusion Methodologies Developed to Reconstruct Coronary Artery Geometry From Intravascular Imaging and Coronary Angiography Data: A Comprehensive Review

*Yakup Kilic[1], Hannah Safi[2], Retesh Bajaj[1,3], Patrick W. Serruys[4], Pieter Kitslaar[5], Anantharaman Ramasamy[1,3], Vincenzo Tufaro[3], Yoshinobu Onuma[6], Anthony Mathur[1,3], Ryo Torii[7], Andreas Baumbach[1,3] and Christos V. Bourantas[1,2,3]**

[1] Department of Cardiology, Barts Heart Centre, Barts Health NHS Trust, London, United Kingdom, [2] Institute of Cardiovascular Sciences, University College London, London, United Kingdom, [3] Centre for Cardiovascular Medicine and Device Innovation, Queen Mary University London, London, United Kingdom, [4] Faculty of Medicine, National Heart & Lung Institute, Imperial College London, London, United Kingdom, [5] Department of Radiology, Leiden University Medical Center, Leiden, Netherlands, [6] Erasmus University Medical Center, Rotterdam, Netherlands, [7] Department of Mechanical Engineering, University College London, London, United Kingdom

OPEN ACCESS

Edited by:
Sebastian Kelle,
Deutsches Herzzentrum
Berlin, Germany

Reviewed by:
Johan Reiber,
Leiden University, Netherlands
Antonios Karanasos,
Hippokration General Hospital, Greece

***Correspondence:**
Christos V. Bourantas
cbourantas@gmail.com

Specialty section:
This article was submitted to Cardiovascular Imaging, a section of the journal Frontiers in Cardiovascular Medicine

Received: 29 November 2019
Accepted: 21 February 2020
Published: 31 March 2020

Citation:
Kilic Y, Safi H, Bajaj R, Serruys PW, Kitslaar P, Ramasamy A, Tufaro V, Onuma Y, Mathur A, Torii R, Baumbach A and Bourantas CV (2020) The Evolution of Data Fusion Methodologies Developed to Reconstruct Coronary Artery Geometry From Intravascular Imaging and Coronary Angiography Data: A Comprehensive Review. Front. Cardiovasc. Med. 7:33. doi: 10.3389/fcvm.2020.00033

Understanding the mechanisms that regulate atherosclerotic plaque formation and evolution is a crucial step for developing treatment strategies that will prevent plaque progression and reduce cardiovascular events. Advances in signal processing and the miniaturization of medical devices have enabled the design of multimodality intravascular imaging catheters that allow complete and detailed assessment of plaque morphology and biology. However, a significant limitation of these novel imaging catheters is that they provide two-dimensional (2D) visualization of the lumen and vessel wall and thus they cannot portray vessel geometry and 3D lesion architecture. To address this limitation computer-based methodologies and user-friendly software have been developed. These are able to off-line process and fuse intravascular imaging data with X-ray or computed tomography coronary angiography (CTCA) to reconstruct coronary artery anatomy. The aim of this review article is to summarize the evolution in the field of coronary artery modeling; we thus present the first methodologies that were developed to model vessel geometry, highlight the modifications introduced in revised methods to overcome the limitations of the first approaches and discuss the challenges that need to be addressed, so these techniques can have broad application in clinical practice and research.

Keywords: hybrid intravascular imaging, data fusion methodologies, 3D reconstruction, coronary artery modeling, coronary angiography

INTRODUCTION

Invasive coronary angiography is the reference standard for assessing the extent and severity of coronary artery disease (CAD) which is a leading cause of death in the developed and developing world (1). This modality however provides only a two dimensional (2D) representation of lumen anatomy and thus it has limitations in quantifying luminal stenosis especially in the cases of

foreshortening and vessel overlapping (2). Moreover, coronary angiography cannot assess 3D vessel geometry and accurately quantify lesion length. To address these limitations computerized based methodologies have been developed that allow 3D reconstruction of the coronary artery anatomy from two or multiple angiographic views (2–4); These approaches enable assessment of vessel geometry and accurate estimation of lesion length and stenosis severity (2, 3). But on the other hand they do not allow visualization of plaque characteristics which determine plaque evolution and vulnerability (5–7).

Over the last few decades intravascular imaging catheters have been designed which can be advanced into the coronary arteries to obtain high-resolution cross-sectional images of the vessels. This enables comprehensive visualization of the lumen and plaque pathology. Intravascular ultrasound (IVUS) and optical coherence tomography (OCT) were the first invasive imaging techniques that were used to study plaque pathobiology and provided unique insights about the mechanisms that regulate plaque evolution. Validation studies using histology as the gold standard have demonstrated the advantages but also the limitations of IVUS and OCT in assessing plaque characteristics and led research toward the development of novel invasive imaging modalities that were able to overcome the drawbacks of the first techniques (8–11). Near infrared spectroscopy (NIRS), photoacoustic imaging (IVPA), near infrared fluorescence imaging (NIRF), and time resolved fluorescence spectroscopy (TRFS) imaging are some of these invasive imaging techniques that were introduced to provide additional information about vessel pathology and biology. These modalities have been combined with IVUS or OCT in hybrid intravascular catheters that are currently undergoing clinical or preclinical evaluation and are expected to provide unique mechanistic insights about atherosclerotic evolution (4, 11). A limitation of these hybrid techniques is that they are unable to portray the 3D vessel geometry. To overcome this drawback several data fusion methodologies have been developed that can retrospectively process intravascular imaging and coronary angiography to generate 3D realistic models of vessel architecture (**Table 1**). These models allow comprehensive visualization of the distribution of the plaque and can be processed with computational fluid dynamic (CFD) techniques to estimate plaque structural stress (PSS) and endothelial shear stress (ESS), which determine atherosclerotic evolution and predict future events (12, 13). The aim of this review article is to provide a comprehensive overview of the data fusion methodologies developed for vessel modeling; we describe the approaches introduced to fuse intravascular imaging and angiographic data to model vessel geometry, present the modifications that were made to optimize vessel reconstruction and facilitate their application in research, and discuss the challenges that should be overcome so that these approaches can be broadly used in the study of atherosclerosis (**Figure 1**).

FIRST ATTEMPTS FOR CORONARY ARTERY RECONSTRUCTION

Roelandt et al. were the first that attempted to reconstruct coronary artery anatomy from IVUS imaging data (14). They assumed that the catheter pull-back trajectory was a straight line and then stacked the IVUS frames perpendicularly onto the catheter trajectory to create a 3D model of the vessel wall that had a cylindrical shape. The final model enabled evaluation of the plaque volume and facilitated the development of methodologies that would allow segmentation of the lumen and outer vessel

TABLE 1 | The evolution of 3D reconstruction methodologies.

Methodology	Accurate extraction of lumen geometry	Accurate estimation of the orientation of the intravascular imaging frames	Extensive validation	Side branch reconstruction	Capable to fuse non-gated intravascular images	No need for prospective imaging protocol	Reliable reconstruction of stent architecture
Klein et al. (22)	✓	✗	✗	✗	✗	✗	✗
Lengyel et al. (23)	✓✓	✓	✗	✗	✗	✗	✗
Wahle et al. (27)	✓✓	✓✓✓	✓✓✓	✗	✗	✗	✗
Slager et al. (32)	✓✓	✓✓✓	✓✓✓	✗	✗	✗	✗
Bourantas et al. (29)	✓✓	✓✓✓	✓✓✓	✗	✗	✗	✗
Giannoglou et al. (28)	✓✓	✓✓✓	✓✓✓	✗	✗	✗	✗
Tu et al. (83)	✓✓	✗	✓	✗	✓✓	✗	✗
Van der Giessen et al. (58)	✓✓✓	✓✓✓	✓	✓✓✓	✓✓	✗	✓
Bourantas et al. (43)	✓✓	✓✓✓	✓✓✓	✗	✓✓	✓✓✓	✓
Li et al. (57)	✓✓	✓	✗	✓✓	✓✓	✓✓✓	✓
Li et al. (77)	✓✓	✓	✗	✓✓	✓✓	✓✓✓	✓✓✓

✓✓✓, *excellent ability of the modality to detect the specific feature;* ✓✓, *moderate ability of the modality to detect the specific feature;* ✓, *weak ability of the modality to detect the specific feature;* ✗, *the modality is unable to detect the specific feature.*

Advantages and limitations of the data fusion imaging techniques developed to reconstruct coronary artery anatomy.

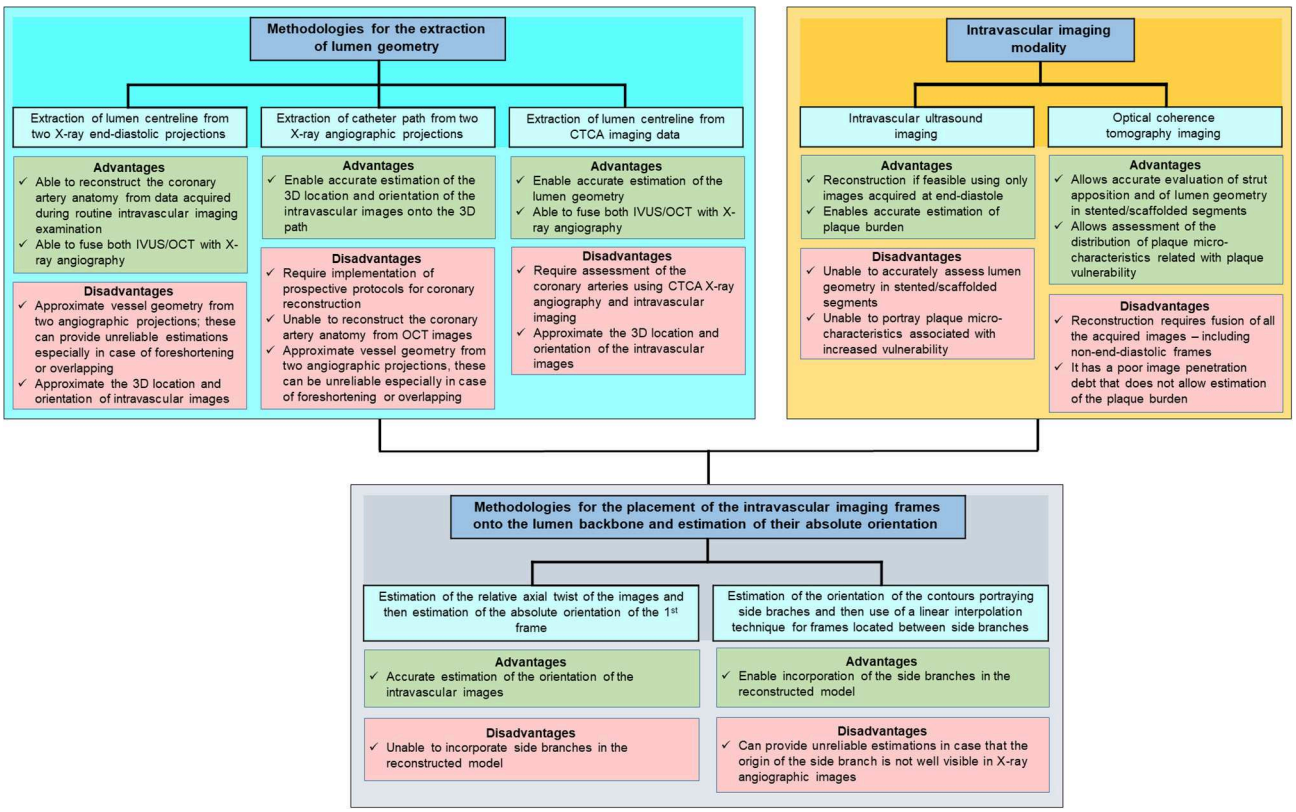

FIGURE 1 | Advantages and limitations of different intravascular imaging modalities and algorithms proposed in different reconstruction methodologies for the modelling of coronary artery geometry.

wall borders (15). A limitation of this approach is that the IVUS model included frames acquired during the entire cardiac cycle; however the vessel is moving during the cardiac cycle and as a consequence the relative lateral and longitudinal position of the IVUS probe with regards to the lumen changes (16). These changes result in the so called "saw tooth" artifact in the 3D model that is more prominent in normal vessels with increased diameter and preserved compliance. To address this pitfall electrocardiographic (ECG)-gated pull-back systems and methodologies for a retrospective gating of the ECG data were proposed; these approaches enabled selection of frames acquired at a specific period of the cardiac cycle (i.e., at the end-diastole) which were then used to reconstruct the vessel geometry (17, 18).

A similar approach was also introduced to reconstruct coronary artery anatomy from OCT data (19). The obtained models allowed evaluation of the distribution of the plaque, of stent apposition, accurate detection of stent fracture and visualization of the orifice of the side branches (20). Today commercially available software have been developed for this purpose and have been incorporated in the OCT systems enabling real time representation of vessel morphology, evaluation of the procedural results and optimal treatment planning.

Despite the undoubted role of these reconstruction methodologies in the clinical arena, they have significant limitations as they are unable to portray coronary artery geometry, evaluate the distribution of the plaque onto the vessel and accurately quantify plaque volume especially in the case of increased curvature where neglecting vessel curvature can lead to an underestimation of the plaque volume by 5% (21).

FUSION OF CORONARY ANGIOGRAPHY AND INTRAVASCULAR ULTRASOUND

In 1992 Klein et al. for the first time suggested fusion of IVUS and X-ray angiography for a more reliable assessment of vessel architecture (22). The proposed methodology included the segmentation of the IVUS images, the extraction of the luminal centerline from two angiographic projections and the placement of the detected contours onto the luminal centerline. A limitation of the proposed methodology is that it was unable to correctly orientate the IVUS borders onto the luminal centerline. Lengyel et al. (23) in 1995 overcame this limitation by using anatomical landmarks (i.e., side branches) that were visible in both IVUS and angiographic images to estimate the rotational orientation of the IVUS frames. This methodology was easy to use and appeared able to provide geometrically correct reconstruction; however it did not have applications in the clinical arena because it was not validated in detail (23).

A year later Shekhar et al. proposed an alternative approach for coronary reconstruction; the authors used an ECG-gated pull-back device for IVUS pull-back and acquired numerous biplane angiographic images during the pull-back so as to identify in X-ray images the position of the IVUS-catheter tip at each end-diastolic frame (24). They then extracted the IVUS catheter path from the biplane angiographic images and placed each frame onto the path in the corresponding position; each frame was then rotated at an angle so as its projections onto the angiographic images to best match with the luminal silhouette in these projections. *In vivo* validation of the developed methodology using X-ray angiography as the gold standard demonstrated that it provides accurate coronary modeling; however the time consuming protocol and increased radiation required for coronary reconstruction did not allow this method to have applications in the clinical arena (25).

Conversely the methodology of Laban et al. presented in 1995 required only two biplane angiographic projections for coronary artery reconstruction enabling its broad application in the study of atherosclerosis (26). The first biplane projection should portray a calibration object, the IVUS catheter and the lumen silhouette—obtained during diluted contrast agent injection—before the beginning of the IVUS pull-back while the second the calibration object the IVUS catheter and the lumen silhouette at the end of the pull-back. These projections were used to extract the IVUS catheter path where it was assumed that it corresponded to the IVUS trajectory during the pull-back. The end-diastolic frames acquired during IVUS imaging were identified and segmented and the detected contours were placed perpendicularly onto the catheter path. The Frenet-Serret formula was then used to estimate the relative axial twist of the IVUS frames. Their absolute orientation was estimated by comparing the projections of these frames and the projection of the reconstructed path onto the angiographic images with the lumen and path silhouette in these X-ray images. Similar approaches for coronary artery reconstruction were proposed by Wahle et al., Gianoglou et al. and Bourantas et al. who proposed a more robust methodology for the catheter path extraction from coronary angiography (27–29). The above approaches were extensively validated in phantom models, *in vivo* and *ex vivo* and were broadly used in the research arena to study plaque strain distribution and the implications of the local hemodynamic forces on plaque formation destabilization and rupture in native and stented segments (**Figures 2**, **3**) (27–29, 31–35).

However, a limitation of the above methodologies is the fact they require the implementation of a specific protocol in the catheterization laboratory that includes X-ray imaging of calibration objects and acquisition of biplane angiographic images that would allow visualization of the IVUS catheter and the lumen silhouette at the beginning and the end of the pull-back. To enhance the application of coronary modeling in research, Bourantas et al. proposed an updated reconstruction methodology that includes the extraction of the luminal centerline of the studied vessel from two angiographic projections—as suggested by Leyngyel et al. (23); the identification and segmentation of the end-diastolic IVUS images, the placement of the IVUS borders perpendicularly onto the vessel centerline, the estimation of their relative twist using the sequential triangulation algorithm and then the use of anatomical landmarks seen in both IVUS and X-ray imaging to define the orientation of the 1st IVUS frame (36). Validation of this approach using the conventional "catheter-path" reconstruction methodology (29) in 22 patients (27 vessels) demonstrated that this new approach allows reliable representation of vessel geometry, quantification of the luminal dimensions and atheroma burden and accurate estimation of the ESS distribution (36). This approach enabled for the first time coronary artery reconstruction using data acquired during conventional IVUS imaging and today it has been extensively used to process imaging data obtained in large intravascular imaging studies of coronary atherosclerosis such as the PROSPECT and IBIS 4 studies and examine the implications of the local hemodynamic forces on plaque progression and destabilization in native vessels and on neointima healing and composition in drug eluting and bare metal stents (37–39).

The "centerline" methodology presented by Bourantas et al. may have broadened the application of computational modeling in the study of atherosclerosis but it also has a major limitation as it does not incorporate side branches in the final model which appear to alter flow patterns and affect ESS estimations (40). To overcome this problem Samady et al. proposed inclusion of side branch geometry in the final model (41). Side branch reconstruction in this methodology is performed by taking into account its orifice in IVUS images and the side branch geometry extracted from the angiographic images. This approach has been used to examine the effect of the ESS and oscillatory ESS on plaque composition and morphology but is yet to be validated in detail (41, 42).

FUSION OF CORONARY ANGIOGRAPHY AND OPTICAL COHERENCE TOMOGRAPHY IMAGING

The fusion of IVUS and X-ray imaging may have provided unique opportunities for assessing vessel geometry, quantifying plaque burden and examining the effect of the local hemodynamic forces on plaque progression. However, it has failed to accurately assess the interplay between ESS and plaque micro-characteristics associated with increased vulnerability and the estimation of flow patterns following stent/scaffold implantation. To overcome these limitations and examine the implications of local hemodynamic forces on plaque destabilization and rupture, fusion of OCT and coronary angiography has been proposed. Bourantas et al. were the first that used OCT-based reconstruction to assess ESS distribution in a ruptured plaque (43). The culprit vessel was imaged using a M3 OCT system (LightLab Imaging Inc., Westford, MA, USA) that was pulled-back at a constant speed of 3 mm/s. From these images the end-diastolic frames were selected, using a view mixer that allowed simultaneous visualization of the ECG and OCT sequence, and these frames were then co-registered with the angiographic data using an established methodology that

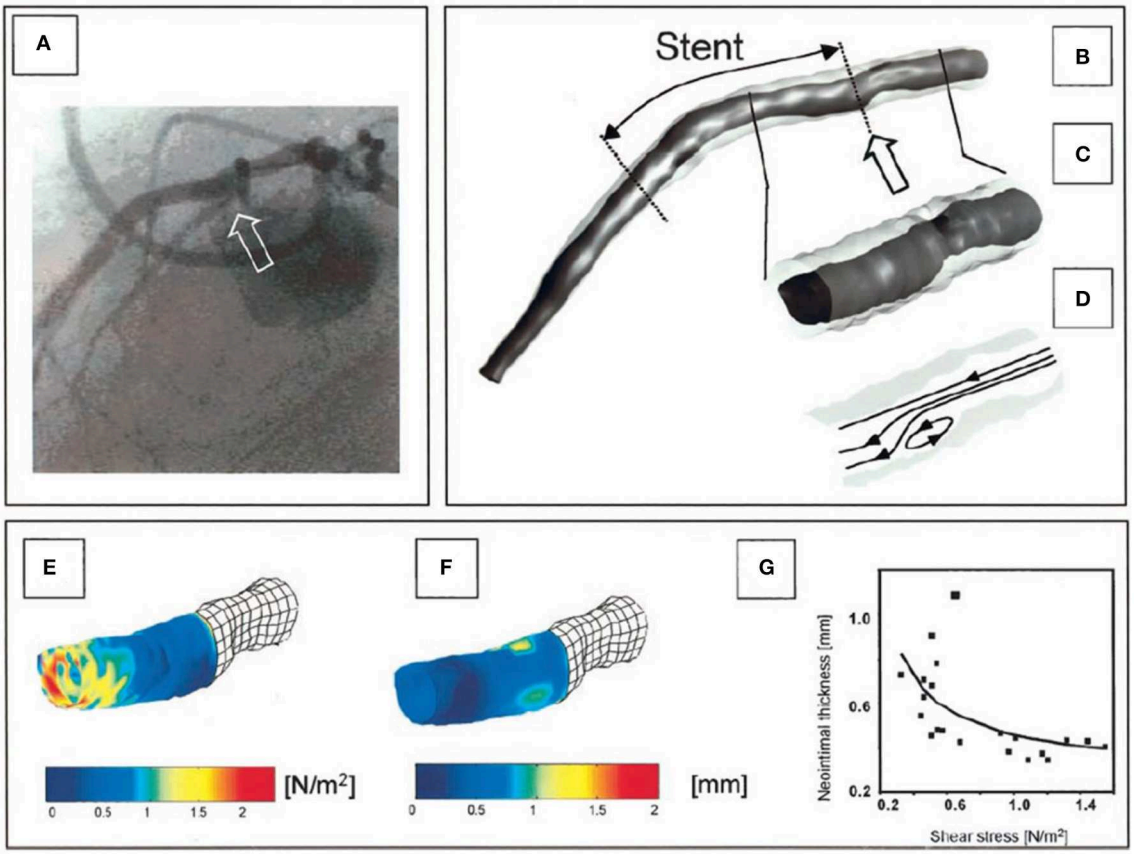

FIGURE 2 | One of the first applications of *in vivo* 3D-reconstruction modeling that examined the role of ESS on neointima formation. **(A)** shows an angiographic projection of the left anterior descending coronary artery treated with bare metal stents; the arrow indicates a step-up at the proximal segment of the stent. **(B)** shows the coronary artery model post stent implantation reconstructed from the fusion of X-ray angiography and IVUS; the outer vessel wall surface is shown in a semi-transparent fashion. The arrow indicates the step-up location noted in the angiographic images; **(C)** shows a magnified view of that segment while **(D)** portrays the blood flow streamlines estimated after blood flow simulation; a recirculation zone is noted at the step-up site. At that location low ESS are noted **(E)** that co-localize with increased neointima proliferation noted in the vessel model at 4 months follow-up **(F)**. A significant inverse association was reported between ESS and neointima thickness at follow-up **(G)**. The figure was obtained with permission from Thury et al. (30).

was proposed for the fusion of X-ray angiography and IVUS (29). Blood flow simulation was performed in the obtained model and the ESS was estimated. High ESS was noted in the region of the ruptured plaque; these findings are in line with the results reported in IVUS-based reconstructions and highlight the potential implications of flow patterns on plaque destabilization and rupture (44, 45).

The first methodology for geometrically correct reconstruction of the coronary artery anatomy from frequency domain (FD)-OCT and X-ray angiography was proposed by Athanasiou et al. (46) and validated by Papafaklis et al. (47). FD-OCT-based reconstruction poses a challenge, as in contrast to the IVUS-based modeling where only end-diastolic frames are used, in FD-OCT modeling all the frames have to be included. This is because the high pull-back speed (18–40 mm/s) in FD-OCT results in a very small number of end-diastolic images. Placement of non-end-diastolic frames onto the catheter path—as previous approaches suggested (27–29, 32)—would result in motion artifacts and a rugged luminal surface because of the relative lateral movement of the OCT catheter in the lumen during the cardiac cycle. In order to address this challenge Athanasiou et al. (46) proposed the use of the lumen centerline, extracted from two end-diastolic angiographic projections, for the placement of the OCT contours. Then the authors used the sequential triangulation algorithm and the origin of side branches to estimate the absolute orientation of the OCT frames. A similar approach for OCT-based reconstruction has been proposed by Toutouzas et al. (48). *In vivo* validation of the "centerline" methodology using IVUS-based reconstruction as the gold standard showed that OCT-based modeling is effective in assessing vessel geometry and estimating ESS distribution (47). Over the last years this methodology has been extensively used to examine the association between local hemodynamic forces and plaque micro-characteristics (49, 50), assess the implications of flow patterns on neointima and neo-atherosclerotic lesion formation and rupture (51, 52), and evaluate the effect of different stent/scaffold designs on the local hemodynamic environment (53–55).

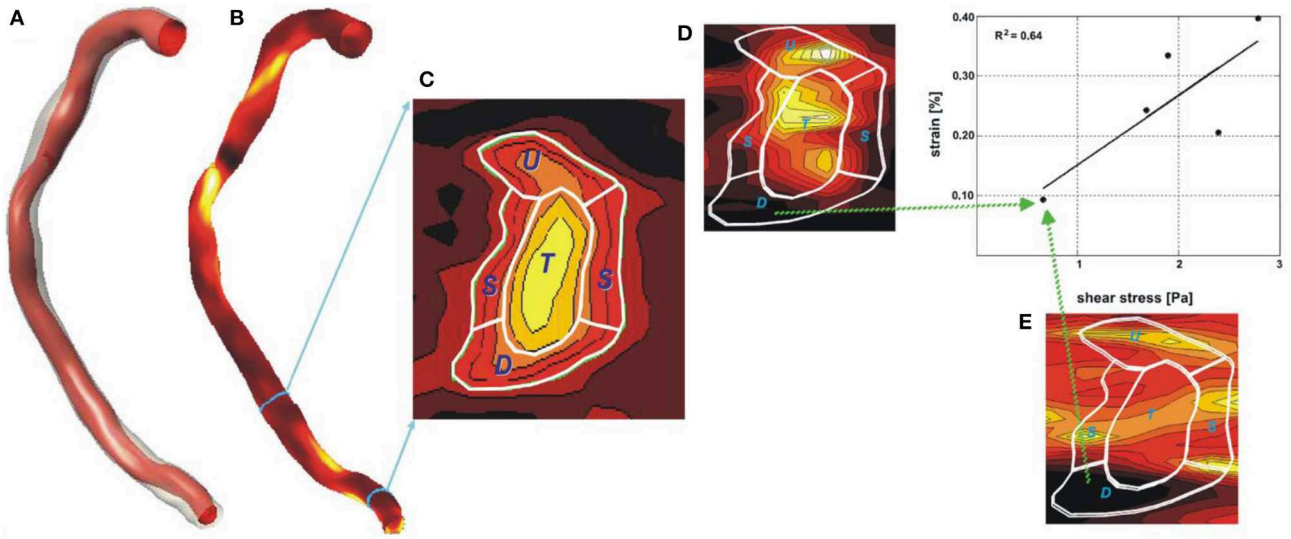

FIGURE 3 | Reconstruction of a right coronary artery from IVUS and angiographic data with the lumen surface portrayed in a red color and the outer vessel wall in a semi-transparent fashion **(A)**. In **(B)** the plaque distribution is displayed in a color-coded map (the red-brown color corresponds to low plaque thickness and yellow to increased plaque). **(C)** shows the distribution of the plaque in a stenotic segment in 2D. The symbols U, L, D, and T denote the upstream the lateral, the downstream shoulder and the throat of the plaque, respectively. **(D)** illustrates in 2D the plaque strain distribution and **(E)** the ESS distribution. It is obvious that there is a good correlation between vessel wall strain and ESS implying an interaction between these two variables. Image obtained with permission and modified from Gijsen et al. (31).

The above OCT-based reconstruction methodology may have significant applications in the research arena but it also has two significant limitations: (1) it is not able to correct the geometrical error caused by the longitudinal movement of the OCT catheter within the vessel during the cardiac cycle (16, 56) and (2) the obtained 3D models do not incorporate vessel's side branches. To address these drawbacks Li et al. proposed a modified approach for coronary artery reconstruction (57). This method suggested the use of 3D QCA to reconstruct the segment that was assessed by OCT and its side branches and then fuse the OCT images with the 3D QCA model. The orifices of the side branches were identified in the OCT images and this information was used to identify the longitudinal position of the OCT frames onto the 3D QCA model and estimate their absolute orientation. For the frames located between the side branches an interpolation technique was used to estimate their location and absolute orientation. A CFD analysis of the reconstructed models showed that the incorporation of the side branches had a significant effect on the ESS distribution with the average ESS being 4.64 Pa lower in models that included the side branches comparing to those that did not contain the side branches ($P < 0.0001$). Although this approach appears superior to others, previously reported in the literature, it does have limitations as it makes two assumptions; more specifically: (1) it implements an interpolation technique to place on the lumen centreline the OCT frames between those portraying side branches; this assumption cannot correct the error caused by the longitudinal motion of the OCT catheter that is increased at the beginning of the systole, and (2) it uses the origin of the side branches, which cannot be always accurately assessed in two angiographic projections, to estimate the rotational orientation of the OCT contours.

Moreover, this approach has not been thoroughly validated and therefore it is unclear what is the effect of the above limitations on vessel reconstruction and ESS computation.

FUSION OF COMPUTED TOMOGRAPHY CORONARY ANGIOGRAPHY AND INTRAVASCULAR IMAGING

The methodologies developed to reconstruct the coronary artery anatomy from X-ray angiography and intravascular imaging data rely on the extraction of the lumen centerline or the catheter path from two angiographic projections. The angle difference between the two projections as well as the presence of vessel foreshortening in these projections can affect the efficacy of these approaches in assessing vessel geometry. Moreover, as it was stated above, the origin of the side branches is likely to not be well visible in the projections used for coronary artery reconstruction and this can affect the accurate estimation of the absolute orientation of the intravascular images on the 3D model. These limitations can be overcome by the use of CTCA which provide 3D images of the coronary artery tree.

In 2010 van der Giessen et al. were the first to propose the fusion of CTCA and IVUS imaging to reconstruct the coronary arteries (58). This approach includes the following steps: (1) extraction of the lumen centerline from CTCA, (2) creation of CTCA cross sectional images that are perpendicular to the side branches, (3) identification of matched frames between end-diastolic IVUS and CTCA images, (4) placement of the IVUS frames showing side branches perpendicularly onto the lumen centerline in the corresponding locations in

CTCA, (5) estimation of their absolute orientation using these branches, and (6) placement of the end-diastolic IVUS frames located between the frames with identifiable landmarks onto the vessel centerline using linear interpolation and estimation of their rotational orientation using spherical interpolation (**Figure 2**). This approach has significant advantages as it allows: (1) full representation of the coronary artery anatomy and geometry including side branches, (2) accurate extraction of vessel architecture from the 3D CTCA imaging data, and (3) reliable orientation of the intravascular images.

This approach has been used to evaluate the role of ESS on vessel wall healing following bioresorbable scaffold implantation and investigate the role of multidirectional ESS on the development of advanced atherosclerotic plaques in pig models (59, 60). The accurate co-registration of intravascular imaging and CTCA also offers the potentiality for a direct comparison of these two techniques and thus detailed evaluation of the ability of non-invasive imaging in assessing the lumen and outer vessel wall dimensions and characterizing plaque morphology (58, 61–63). A major limitation of this approach is that coronary reconstruction requires CTCA, coronary angiography and intravascular imaging data. Moreover, similar to the other reconstruction approaches this methodology is laborious and time consuming as human interaction is needed in most of the reconstruction steps and it has not been validated yet.

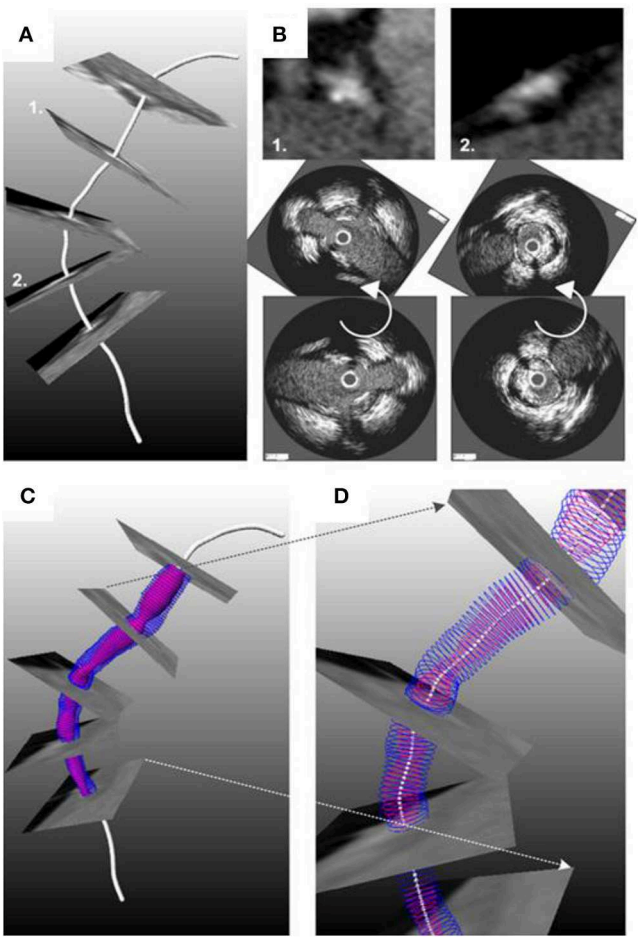

FIGURE 4 | Methodology developed for the reconstruction of the coronary artery anatomy from CTCA and intravascular imaging data. **(A)** The luminal centerline is extracted from the CTCA imaging data and then CTCA cross-sectional images are generated perpendicularly to the centerline. **(B)** The CTCA images are matched with the IVUS images using anatomical landmarks that are seen in both IVUS and CTCA; the IVUS images are placed onto the luminal centerline and then the landmarks are used to estimate their absolute orientation. An interpolation technique is used to estimate the location and orientation of the frames located between side branches. The final model is shown in **(C,D)**. The figure was obtained with permission from Gijsen et al. (78).

SOFTWARE DEVELOPED FOR CORONARY ARTERY MODELING

To enhance the research applicability of the 3D reconstruction methodologies mentioned above, user—friendly systems have been developed that operate in a user-friendly environment and expedite coronary reconstruction (**Figure 3**). The first software was developed by Wahle et al. and incorporated the algorithms of the methodology developed by Wahle et al. in 1999 (27). To visualize the final models the authors used the standardized Virtual Reality Modeling Language (VRML) and designed a module where the operator could assess the luminal and the media—adventitia surface and estimate the plaque burden distribution since the plaque thickness was color coded displayed (64). Moreover, this system allowed evaluation of vessel curvature that was also portrayed using a color coded map and incorporated a 3D graphical user interface that enabled virtual endoscopy of the reconstructed vessel. In addition, the software included a module for blood flow simulation and computation of the ESS. Despite these unique advantages this system had limited application in research as it required the implementation of prospective protocol for data acquisition and increased time for coronary artery reconstruction.

ANGIOCARE (**Figure 5**) was the 2nd system developed for the fusion of intravascular imaging and coronary angiography (**Figures 3A–D**) (65). This software incorporated the methodology for arterial reconstruction proposed by Bourantas et al. (29) and a module for the segmentation of the IVUS images (66). In addition, ANGIOCARE included a 3D photorealistic visualization platform that allowed comprehensive representation of the reconstructed model, visual inspection of vessel morphology and evaluation of the distribution of the plaque (depicted in a color—coded map). In addition, the developed module allowed the operator to interact with the model select a segment and obtain quantitative information (i.e., lesion length, plaque volume, minimum luminal area, the reference luminal area, etc.) that could be used for PCI planning. A limitation of ANGIOCARE is the fact that it did not allow blood flow simulation and estimation of the ESS distribution.

IVUSAngio tool is the only freely available software for the fusion of IVUS and angiographic imaging data (67). The software incorporated the methodology of Giannoglou et al. (67) and included modules designed for the segmentation of IVUS, the extraction of the catheter path and the fusion of the imaging data

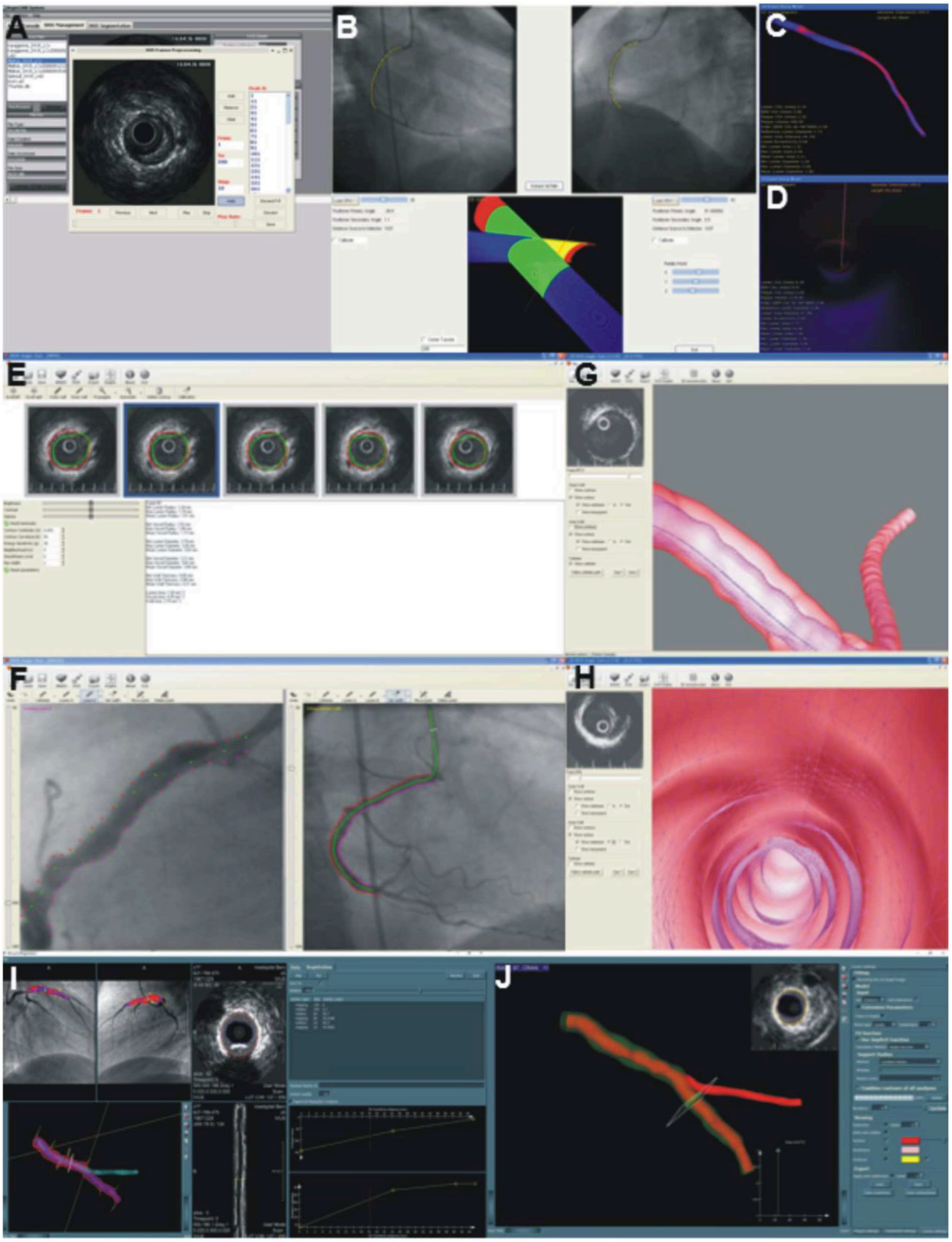

FIGURE 5 | Software developed to reconstruct the coronary artery anatomy in a user-friendly environment. **(A–D)** portray a snapshot of the ANGIOCARE software. **(A)** illustrates the module developed for the pre-processing and analysis of intravascular imaging data, while **(B)** the module designed for the extraction of the catheter

(Continued)

FIGURE 5 | path from two angiographic projections. Finally, **(C,D)** show the platform designed for the visualization of the 3D model. The operator can appreciate the lumen geometry **(C)**, assess plaque distribution portrayed in a color-coded map (blue indicates no plaque and red indicates increased plaque burden) and assess the lumen morphology from inside **(D)**. **(E–H)** portray snapshots of the IVUSAngio tool. **(E)** shows the module for IVUS analysis, **(F)** the tool designed for the catheter path extraction, **(G)** illustrates the 3D model with the media-adventitia shown in a semi-transparent fashion, enabling evaluation of the distribution of the plaque burden and **(H)** portrays an endoscopic view of the lumen morphology. Finally, **(I,J)** illustrate snapshots of the software designed by Leiden University for the reconstruction of coronary artery anatomy. The annotated intravascular imaging data and the 3D-QCA model are imported and fused. The operator can identify in the lumen centerline the location of frames portraying side branches and use these to estimate their rotational orientation **(I)**. The reconstructed lumen is then fused with the side branch model obtained by 3D-QCA to generate the final vessel geometry. **(J)** shows the reconstructed vessel; the outer vessel wall is shown in a semi-transparent fashion, which allows evaluation of the distribution of the plaque.

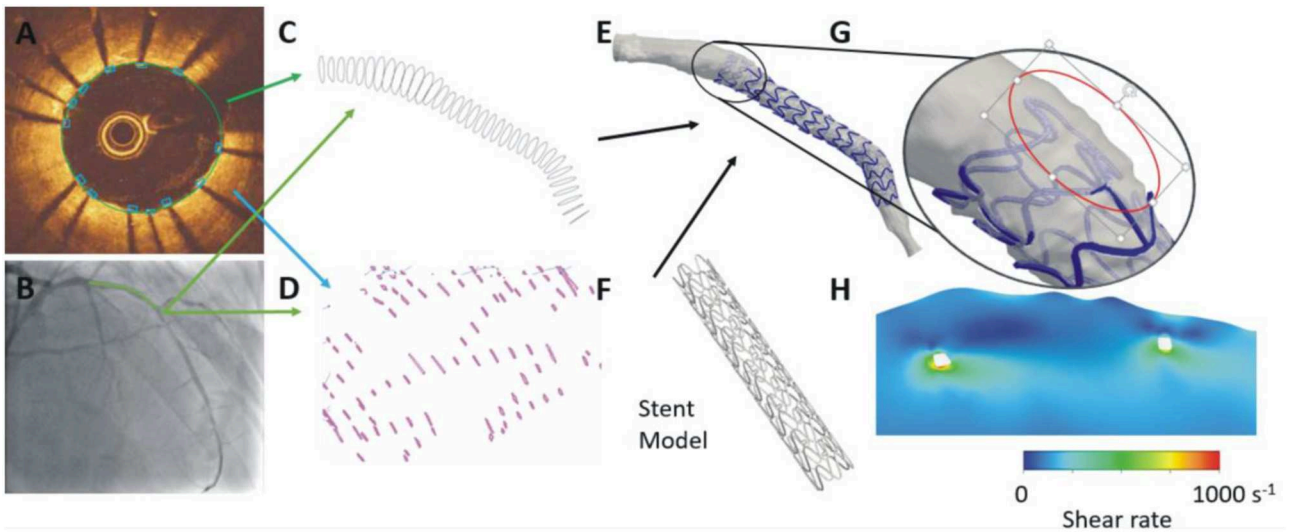

FIGURE 6 | Advanced methodology proposed for the reconstruction of stented segments. In each OCT frame the lumen border is detected and the location of the stent struts is annotated **(A)**. The OCT contours are placed perpendicularly onto the lumen centerline **(B)** extracted by two angiographic projections and the location of the side branches are used to estimate their absolute orientation **(C)**. A similar approach is used to estimate the location of the struts in 3D space **(D)**. A methodology that relies on the location of the stent struts in 3D space and on a priori knowledge of stent architecture is used to reconstruct the stent geometry that is fused with the lumen geometry to reconstruct the stented segment **(E,F)**. This approach enables accurate reconstruction of the protruded or malapposed struts **(G)** and evaluation of their implications on the local hemodynamic forces **(H)**.

and included a visualization platform where the operator could interact with the reconstructed vessel, review and examine model architecture and plaque distribution, identify the location of each frame onto the model and inspect the 3D model from inside using a fly through camera.

University of Leiden and Medis Medical Imaging Systems BV have recently developed a novel software for coronary reconstruction (**Figures 3E–H**). The software requires as an input the 3D QCA model—including vessel's side branches—of the segment assessed by IVUS/OCT that was reconstructed by the QAngio XA 3D software (Medis Medical Imaging Systems, Leiden, The Netherlands) and the IVUS/OCT borders segmented using the QCU-CMS software (Division of Image Processing, Department of Radiology, Leiden, The Netherlands, Leiden, The Netherlands). It has incorporated the algorithms of the methodology proposed by Li et al. (57) in a user-friendly environment and allows seamless reconstruction of vessel architecture and generation of 3D models that are stored in an .stl or .iges format. The latter software is currently used to process data collected in large scale prospective intravascular imaging studies of coronary atherosclerosis and assess the role of ESS distribution in predicting atherosclerotic disease progression and lesions with a vulnerable phenotype that will cause events.

DISCUSSION

Fusion of intravascular imaging data and X-ray angiography or CTCA imaging has enabled accurate reconstruction of coronary artery geometry and the generation of 3D models that can be processed with CFD techniques to evaluate vessel flow patterns and examine the effect of the hemodynamic forces on plaque evolution. These models have been enriched our understanding about the mechanisms that regulate atherosclerotic disease progression enabling more accurate prediction of lesions that are likely to progress and cause events (35, 37, 38).

The PREDICTION study which was the first prospective clinical study that used at scale fusion of intravascular imaging and X-ray angiography to assess the ESS distribution and highlighted the prognostic value of ESS in predicting plaque progression, thereby creating hope that an invasive assessment

of plaque morphology combined with CFD analysis could enable accurate detection of vulnerable plaques (35). The findings of this study led research toward the development of easy to use methodologies that will be able to generate accurate representation of vessel geometry by fusing IVUS or OCT data with X-ray imaging data acquired during a conventional coronary angiography. These approaches have been used to retrospectively analyze intravascular imaging data acquired in large scale imaging studies of coronary atherosclerosis. A CFD analysis of the data acquired in the PROSPECT study showed that lesions with a high-risk morphology that were exposed to low ESS were likely to progress and cause cardiovascular events. This study also showed that the patients who had lesions with an unfavorable plaque morphology and physiology were the most vulnerable and at a high-risk to suffer a cardiovascular event (37). Retrospective fusion of IVUS, OCT and coronary angiography has also been used to process the data acquired in the IBIS 4 study—a multicenter study that utilizes serial virtual histology(VH)-IVUS and OCT imaging to assess the implications of aggressive treatment with Rosuvastatin on plaque phenotype—and examine the predictive accuracy of ESS patterns and plaque characteristics assessed by multimodality imaging in detecting segments that were likely to exhibit disease progression at 13 months follow-up (38, 68). In this study low ESS and VH-IVUS-derived but not OCT-derived plaque characteristics were predictors of disease progression. The findings of this analysis casted doubts about the efficacy of multimodality imaging in detecting vulnerable plaques. A limitation of this study was the small number of the studied vessels and the absence of events that did not allow us to examine the potential of multimodality imaging combined with CFD-modeling in detecting plaques that will cause events. Future studies are expected to use hybrid intravascular imaging to thoroughly assess plaque morphology and pathology and fuse these data with X-ray angiography or CTCA to determine ESS distribution in order to accurately predict vulnerable plaques. Studies combining NIRS-IVUS and X-ray or CTCA imaging to examine the association of ESS and plaque composition and evaluate its role on plaque progression have been recently reported (60, 69); data acquired in the future by the combined IVUS-OCT imaging catheter or by the hybrid NIRS-OCT or the IVPA-IVUS catheter are anticipated to be merged with X-ray or CTCA images to assess more accurately the interplay between plaque phenotype and plaque physiology. Moreover, models obtained by NIRF-IVUS or NIRF-OCT imaging combined with X-ray or CTCA imaging data, are anticipated to allow assessment of the role of ESS distribution on vascular biology and plaque inflammation.

The developed user-friendly software that included established data fusion algorithms are expected to facilitate research in the field and allow more complex simulations and complete assessment of vessel physiology. Cumulative data have highlighted the role of PSS on plaque destabilization and its value in predicting vulnerable lesions (70–72). The studies however that examined the prognostic implications of PSS focused on the analysis of IVUS cross-sectional images and did not take into account 3D vessel geometry. Further advances in software design and incorporation of plaque composition in the 3D models-derived by hybrid intravascular imaging techniques or polarized OCT (73) are expected to enable accurate assessment of PSS and evaluation of the synergetic effect of ESS and PSS on vulnerable plaque formation, destabilization and rupture (74).

Recent reports have highlighted the need to refine the methodologies for the reconstruction of vessel architecture especially in stented segments (75–77). Advanced methodologies have been presented lately (**Figures 4**, **6**) that are able to separately reconstruct stent geometry and lumen surface and then fuse these models to generate a final lumen-stent object. These approaches are anticipated to provide more realistic representation of lumen architecture in stented segments and enable reliable evaluation of ESS distribution especially in the case of strut malapposition and at the orifice of the side branches where the protruded struts cause flow disturbances. These methods will be used in the future to conduct complex CFD analyses that will take into account the non-Newtonian behavior of the blood to precisely compute shear rate and stress distribution, quantify flow disturbances and identify areas that are exposed to an unfavorable hemodynamic milieu and are at risk of restenosis and stent/scaffold thrombosis (79–81). Moreover, these reconstruction approaches are expected to have value in the evaluation of the hemodynamic implications following implantation of different stent/scaffold designs and be extensively used to optimize stent configuration and develop revisions that will create a favorable hemodynamic environment following their implantation (54, 55, 82).

CONCLUSION

Fusion of intravascular imaging and angiographic or CTCA imaging data allows generation of 3D models that accurately portray the vessel geometry and enable evaluation of plaque composition. These approaches have been extensively used to examine the implications of flow patterns on atherosclerotic disease progression and stent/scaffold thrombosis. Further advances in intravascular imaging, catheter design and the development of methodologies that will allow estimation of the distribution of different plaque components on the 3D plaque, and accurate reconstruction of stent architecture are expected to provide a complete and detailed evaluation of luminal geometry and coronary artery pathology. They are also expected to permit more precise quantification of the local hemodynamic forces, better prediction of plaque evolution, and optimization of focal therapies developed for the treatment of culprit or vulnerable lesions.

AUTHOR CONTRIBUTIONS

All authors listed have made a substantial, direct and intellectual contribution to the work, and approved it for publication.

FUNDING

HS was funded by British Heart Foundation (PG/17/18/32883) while AR, RB, AB, and CB by Barts Biomedical Research Centre.

REFERENCES

1. Brown BG, Bolson E, Frimer M, Dodge HT. Quantitative coronary arteriography: estimation of dimensions, hemodynamic resistance, and atheroma mass of coronary artery lesions using the arteriogram and digital computation. *Circulation*. (1977) 55:329–37. doi: 10.1161/01.CIR.55.2.329
2. Yong AS, Ng AC, Brieger D, Lowe HC, Ng MK, Kritharides L. Three-dimensional and two-dimensional quantitative coronary angiography, and their prediction of reduced fractional flow reserve. *Eur Heart J*. (2011) 32:345–53. doi: 10.1093/eurheartj/ehq259
3. Bourantas CV, Tweddel AC, Papafaklis MI, Karvelis PS, Fotiadis DI, Katsouras CS, et al. Comparison of quantitative coronary angiography with intracoronary ultrasound. Can quantitative coronary angiography accurately estimate the severity of a luminal stenosis? *Angiology*. (2009) 60:169–79. doi: 10.1177/0003319708317338
4. Tu S, Xu L, Ligthart J, Xu B, Witberg K, Sun Z, et al. *In vivo* comparison of arterial lumen dimensions assessed by co-registered three-dimensional (3D) quantitative coronary angiography, intravascular ultrasound and optical coherence tomography. *Int J Cardiovasc Imaging*. (2012) 28:1315–27. doi: 10.1007/s10554-012-0016-6
5. Stone GW, Maehara A, Lansky AJ, de Bruyne B, Cristea E, Mintz GS, et al. A prospective natural-history study of coronary atherosclerosis. *N Engl J Med*. (2011) 364:226–35. doi: 10.1056/NEJMoa1002358
6. Waksman R, Di Mario C, Torguson R, Ali ZA, Singh V, Skinner WH, et al. Identification of patients and plaques vulnerable to future coronary events with near-infrared spectroscopy intravascular ultrasound imaging: a prospective, cohort study. *Lancet*. (2019) 394:1629–37. doi: 10.1016/S0140-6736(19)31794-5
7. Prati F, Romagnoli E, Gatto L, La Manna A, Burzotta F, Ozaki Y, et al. Relationship between coronary plaque morphology of the left anterior descending artery and 12 months clinical outcome: the CLIMA study. *Eur Heart J*. (2019) 41:383–91. doi: 10.1093/eurheartj/ehz520
8. Bourantas CV, Garcia-Garcia HM, Naka KK, Sakellarios A, Athanasiou L, Fotiadis DI, et al. Hybrid intravascular imaging: current applications and prospective potential in the study of coronary atherosclerosis. *J Am Coll Cardiol*. (2013) 61:1369–78. doi: 10.1016/j.jacc.2012.10.057
9. Bourantas CV, Jaffer FA, Gijsen FJ, van Soest G, Madden SP, Courtney BK, et al. Hybrid intravascular imaging: recent advances, technical considerations, and current applications in the study of plaque pathophysiology. *Eur Heart J*. (2017) 38:400–12. doi: 10.1093/eurheartj/ehw097
10. Ramasamy A, Serruys PW, Jones DA, Johnson TW, Torii R, Madden SP, et al. Reliable *in vivo* intravascular imaging plaque characterization: a challenge unmet. *Am Heart J*. (2019) 218:20–31. doi: 10.1016/j.ahj.2019.07.008
11. Bourantas CV, Garcia-Garcia HM, Diletti R, Muramatsu T, Serruys PW. Early detection and invasive passivation of future culprit lesions: a future potential or an unrealistic pursuit of chimeras? *Am Heart J*. (2013) 165:869–81.e4. doi: 10.1016/j.ahj.2013.02.015
12. Thondapu V, Bourantas CV, Foin N, Jang IK, Serruys PW, Barlis P. Biomechanical stress in coronary atherosclerosis: emerging insights from computational modelling. *Eur Heart J*. (2017) 38:81–92. doi: 10.1093/eurheartj/ehv689
13. Brown AJ, Teng Z, Evans PC, Gillard JH, Samady H, Bennett MR. Role of biomechanical forces in the natural history of coronary atherosclerosis. *Nat Rev Cardiol*. (2016) 13:210–20. doi: 10.1038/nrcardio.2015.203
14. Roelandt JR, di Mario C, Pandian NG, Wenguang L, Keane D, Slager CJ, et al. Three-dimensional reconstruction of intracoronary ultrasound images. Rationale, approaches, problems, and directions. *Circulation*. (1994) 90:1044–55. doi: 10.1161/01.CIR.90.2.1044
15. Dijkstra J, Koning G, Reiber JH. Quantitative measurements in IVUS images. *Int J Card Imaging*. (1999) 15:513–22. doi: 10.1023/A:1006334517720
16. Arbab-Zadeh A, DeMaria AN, Penny WF, Russo RJ, Kimura BJ, Bhargava V. Axial movement of the intravascular ultrasound probe during the cardiac cycle: implications for three-dimensional reconstruction and measurements of coronary dimensions. *Am Heart J*. (1999) 138(5 Pt 1):865–72. doi: 10.1016/S0002-8703(99)70011-6
17. De Winter SA, Hamers R, Degertekin M, Tanabe K, Lemos PA, Serruys PW, et al. Retrospective image-based gating of intracoronary ultrasound images for improved quantitative analysis: the intelligate method. *Catheter Cardiovasc Interv*. (2004) 61:84–94. doi: 10.1002/ccd.10693
18. von Birgelen C, Mintz GS, Nicosia A, Foley DP, van der Giessen WJ, Bruining N, et al. Electrocardiogram-gated intravascular ultrasound image acquisition after coronary stent deployment facilitates on-line three-dimensional reconstruction and automated lumen quantification. *J Am Coll Cardiol*. (1997) 30:436–43. doi: 10.1016/S0735-1097(97)00154-X
19. Tearney GJ, Waxman S, Shishkov M, Vakoc BJ, Suter MJ, Freilich MI, et al. Three-dimensional coronary artery microscopy by intracoronary optical frequency domain imaging. *JACC Cardiovasc Imaging*. (2008) 1:752–61. doi: 10.1016/j.jcmg.2008.06.007
20. Farooq V, Gogas BD, Okamura T, Heo JH, Magro M, Gomez-Lara J, et al. Three-dimensional optical frequency domain imaging in conventional percutaneous coronary intervention: the potential for clinical application. *Eur Heart J*. (2013) 34:875–85. doi: 10.1093/eurheartj/ehr409
21. Schuurbiers JC, von Birgelen C, Wentzel JJ, Bom N, Serruys PW, de Feyter PJ, et al. On the IVUS plaque volume error in coronary arteries when neglecting curvature. *Ultrasound Med Biol*. (2000) 26:1403–11. doi: 10.1016/S0301-5629(00)00295-7
22. Klein HM, Gunther RW, Verlande M, Schneider W, Vorwerk D, Kelch J, et al. 3D-surface reconstruction of intravascular ultrasound images using personal computer hardware and a motorized catheter control. *Cardiovasc Intervent Radiol*. (1992) 15:97–101. doi: 10.1007/BF02734099
23. Lengyel J, Greenberg DP, Richard P. Time-dependent three-dimensional intravascular ultrasound. In: Robert Cook, editor. *Proceedings of the SIGGRAPH 95 Conference on Comp Graphics USA*. Los Angeles, CA: ACM (1995).
24. Shekhar R, Cothren RM, Vince DG, Cornhill JF. Fusion of intravascular ultrasound and biplane angiography for three-dimensional reconstruction of coronary arteries. *In: Proc Comp in Cardiology 1996*. Indianapolis, IN: IEEE (1996).
25. Cothren RM, Shekhar R, Tuzcu EM, Nissen SE, Cornhill JF, Vince DG. Three-dimensional reconstruction of the coronary artery wall by image fusion of intravascular ultrasound and bi-plane angiography. *Int J Card Imaging*. (2000) 16:69–85. doi: 10.1023/A:1006304419505
26. Laban M, Oomen JA, Slager CJ, Wentzel JJ, Krams R, Schuurbiers JCH, et al. ANGUS: a new approach to three-dimensional reconstruction of coronary vessels by combined use of angiography and intravascular ultrasound. In: *Computes in Cardiology*. Vienna: IEEE (1995). p. 325–28.
27. Wahle A, Prause PM, DeJong SC, Sonka M. Geometrically correct 3-D reconstruction of intravascular ultrasound images by fusion with biplane angiography–methods and validation. *IEEE Trans Med Imaging*. (1999) 18:686–99. doi: 10.1109/42.796282
28. Giannoglou GD, Chatzizisis YS, Sianos G, Tsikaderis D, Matakos A, Koutkias V, et al. *In-vivo* validation of spatially correct three-dimensional reconstruction of human coronary arteries by integrating intravascular ultrasound and biplane angiography. *Coron Artery Dis*. (2006) 17:533–43. doi: 10.1097/00019501-200609000-00007
29. Bourantas CV, Kourtis IC, Plissiti ME, Fotiadis DI, Katsouras CS, Papafaklis MI, et al. A method for 3D reconstruction of coronary arteries using biplane angiography and intravascular ultrasound images. *Comput Med Imaging Graph*. (2005) 29:597–606. doi: 10.1016/j.compmedimag.2005.07.001
30. Thury A, Wentzel JJ, Vinke RV, Gijsen FJ, Schuurbiers JC, Krams R, et al. Images in cardiovascular medicine. Focal in-stent restenosis near step-up: roles of low and oscillating shear stress? *Circulation*. (2002) 105:e185–7. doi: 10.1161/01.CIR.0000018282.32332.13
31. Gijsen FJ, Wentzel JJ, Thury A, Mastik F, Schaar JA, Schuurbiers JC, et al. Strain distribution over plaques in human coronary arteries relates to shear stress. *Am J Physiol Heart Circ Physiol*. (2008) 295:H1608–14. doi: 10.1152/ajpheart.01081.2007
32. Slager CJ, Wentzel JJ, Schuurbiers JC, Oomen JA, Kloet J, Krams R, et al. True 3-dimensional reconstruction of coronary arteries in patients by fusion of angiography and IVUS (ANGUS) and its quantitative validation. *Circulation*. (2000) 102:511–6. doi: 10.1161/01.CIR.102.5.511
33. Papafaklis MI, Bourantas CV, Theodorakis PE, Katsouras CS, Naka KK, Fotiadis DI, et al. The effect of shear stress on neointimal response following sirolimus- and paclitaxel-eluting stent implantation compared

with bare-metal stents in humans. *JACC Cardiovasc Interv*. (2010) 3:1181–9. doi: 10.1016/j.jcin.2010.08.018
34. Wentzel JJ, Krams R, Schuurbiers JC, Oomen JA, Kloet J, van Der Giessen WJ, et al. Relationship between neointimal thickness and shear stress after Wallstent implantation in human coronary arteries. *Circulation*. (2001) 103:1740–5. doi: 10.1161/01.CIR.103.13.1740
35. Stone PH, Saito S, Takahashi S, Makita Y, Nakamura S, Kawasaki T, et al. Prediction of progression of coronary artery disease and clinical outcomes using vascular profiling of endothelial shear stress and arterial plaque characteristics: the PREDICTION Study. *Circulation*. (2012) 126:172–81. doi: 10.1161/CIRCULATIONAHA.112.096438
36. Bourantas CV, Papafaklis MI, Athanasiou L, Kalatzis FG, Naka KK, Siogkas PK, et al. A new methodology for accurate 3-dimensional coronary artery reconstruction using routine intravascular ultrasound and angiographic data: implications for widespread assessment of endothelial shear stress in humans. *EuroIntervention*. (2013) 9:582–93. doi: 10.4244/EIJV9I5A94
37. Stone PH, Maehara A, Coskun AU, Maynard CC, Zaromytidou M, Siasos G, et al. Role of low endothelial shear stress and plaque characteristics in the prediction of nonculprit major adverse cardiac events: The PROSPECT Study. *JACC Cardiovasc Imaging*. (2018) 11:462–71. doi: 10.1016/j.jcmg.2017.01.031
38. Bourantas CV, Raber L, Sakellarios A, Ueki Y, Zanchin T, Koskinas KC, et al. Utility of multimodality intravascular imaging and the local hemodynamic forces to predict atherosclerotic disease progression. *JACC Cardiovasc Imaging*. (2019) doi: 10.1016/j.jcmg.2019.02.026. [Epub ahead of print].
39. Bourantas CV, Raber L, Zaugg S, Sakellarios A, Taniwaki M, Heg D, et al. Impact of local endothelial shear stress on neointima and plaque following stent implantation in patients with ST-elevation myocardial infarction: a subgroup-analysis of the COMFORTABLE AMI-IBIS 4 trial. *Int J Cardiol*. (2015) 186:178–85. doi: 10.1016/j.ijcard.2015.03.160
40. Giannopoulos AA, Chatzizisis YS, Maurovich-Horvat P, Antoniadis AP, Hoffmann U, Steigner ML, et al. Quantifying the effect of side branches in endothelial shear stress estimates. *Atherosclerosis*. (2016) 251:213–8. doi: 10.1016/j.atherosclerosis.2016.06.038
41. Samady H, Eshtehardi P, McDaniel MC, Suo J, Dhawan SS, Maynard C, et al. Coronary artery wall shear stress is associated with progression and transformation of atherosclerotic plaque and arterial remodeling in patients with coronary artery disease. *Circulation*. (2011) 124:779–88. doi: 10.1161/CIRCULATIONAHA.111.021824
42. Timmins LH, Molony DS, Eshtehardi P, McDaniel MC, Oshinski JN, Giddens DP, et al. Oscillatory wall shear stress is a dominant flow characteristic affecting lesion progression patterns and plaque vulnerability in patients with coronary artery disease. *J R Soc Interface*. (2017) 14:20160972. doi: 10.1098/rsif.2016.0972
43. Bourantas CV, Papafaklis MI, Naka KK, Tsakanikas VD, Lysitsas DN, Alamgir FM, et al. Fusion of optical coherence tomography and coronary angiography - *in vivo* assessment of shear stress in plaque rupture. *Int J Cardiol*. (2012) 155:e24–6. doi: 10.1016/j.ijcard.2011.07.005
44. Slager CJ, Wentzel JJ, Gijsen FJ, Thury A, van der Wal AC, Schaar JA, et al. The role of shear stress in the destabilization of vulnerable plaques and related therapeutic implications. *Nat Clin Pract Cardiovasc Med*. (2005) 2:456–64. doi: 10.1038/ncpcardio0298
45. Fukumoto Y, Hiro T, Fujii T, Hashimoto G, Fujimura T, Yamada J, et al. Localized elevation of shear stress is related to coronary plaque rupture: a 3-dimensional intravascular ultrasound study with *in-vivo* color mapping of shear stress distribution. *J Am Coll Cardiol*. (2008) 51:645–50. doi: 10.1016/j.jacc.2007.10.030
46. Athanasiou LS, Bourantas CV, Siogkas PK, Sakellarios AI, Exarchos TP, Naka KK, Papafaklis MI, Michalis LK, Prati F, Fotiadis DI. 3D reconstruction of coronary arteries using frequency domain optical coherence tomography images and biplane angiography. *Conf Proc IEEE Eng Med Biol Soc*. (2012) 2012:2647–50. doi: 10.1109/EMBC.2012.6346508
47. Papafaklis MI, Bourantas CV, Yonetsu T, Vergallo R, Kotsia A, Nakatani S, et al. Anatomically correct three-dimensional coronary artery reconstruction using frequency domain optical coherence tomographic and angiographic data: head-to-head comparison with intravascular ultrasound for endothelial shear stress assessment in humans. *EuroIntervention*. (2015) 11:407–15. doi: 10.4244/EIJY14M06_11
48. Toutouzas K, Chatzizisis YS, Riga M, Giannopoulos A, Antoniadis AP, Tu S, et al. Accurate and reproducible reconstruction of coronary arteries and endothelial shear stress calculation using 3D OCT: comparative study to 3D IVUS and 3D QCA. *Atherosclerosis*. (2015) 240:510–9. doi: 10.1016/j.atherosclerosis.2015.04.011
49. Vergallo R, Papafaklis MI, Yonetsu T, Bourantas CV, Andreou I, Wang Z, et al. Endothelial shear stress and coronary plaque characteristics in humans: combined frequency-domain optical coherence tomography and computational fluid dynamics study. *Circ Cardiovasc Imaging*. (2014) 7:905–11. doi: 10.1161/CIRCIMAGING.114.001932
50. Yamamoto E, Siasos G, Zaromytidou M, Coskun AU, Xing L, Bryniarski K, et al. Low endothelial shear stress predicts evolution to high-risk coronary plaque phenotype in the future: A Serial Optical Coherence Tomography and Computational Fluid Dynamics Study. *Circ Cardiovasc Interv*. (2017) 10:e005455. doi: 10.1161/CIRCINTERVENTIONS.117.005455
51. Torii R, Stettler R, Raber L, Zhang YJ, Karanasos A, Dijkstra J, et al. Implications of the local hemodynamic forces on the formation and destabilization of neoatherosclerotic lesions. *Int J Cardiol*. (2018) 272:7–12. doi: 10.1016/j.ijcard.2018.06.065
52. Michail M, Torii R, Crake T, Ozkor M, Garcia-Garcia HM, Tenekecioglu E, et al. Local hemodynamics: an innocent bystander or a critical factor regulating neoatherosclerotic evolution? *JACC Cardiovasc Interv*. (2015) 8:e149–50. doi: 10.1016/j.jcin.2015.04.022
53. Torii R, Tenekecioglu E, Katagiri Y, Chichareon P, Sotomi Y, Dijkstra J, et al. The impact of plaque type on strut embedment/protrusion and shear stress distribution in bioresorbable scaffold. *Eur Heart J Cardiovasc Imaging*. (2019). doi: 10.1093/ehjci/jez155. [Epub ahead of print].
54. Tenekecioglu E, Torii R, Bourantas CV, Al-Lamee R, Serruys PW. Non-Newtonian pulsatile shear stress assessment: a method to differentiate bioresorbable scaffold platforms. *Eur Heart J*. (2017) 38:2570. doi: 10.1093/eurheartj/ehx358
55. Tenekecioglu E, Torii R, Bourantas C, Sotomi Y, Cavalcante R, Zeng Y, et al. Difference in haemodynamic microenvironment in vessels scaffolded with absorb BVS and Mirage BRMS: insights from a preclinical endothelial shear stress study. *EuroIntervention*. (2017) 13:1327–35. doi: 10.4244/EIJ-D-17-00283
56. van Ditzhuijzen NS, Karanasos A, Bruining N, van den Heuvel M, Sorop O, Ligthart J, et al. The impact of Fourier-Domain optical coherence tomography catheter induced motion artefacts on quantitative measurements of a PLLA-based bioresorbable scaffold. *Int J Cardiovasc Imaging*. (2014) 30:1013–26. doi: 10.1007/s10554-014-0447-3
57. Li Y, Gutierrez-Chico JL, Holm NR, Yang W, Hebsgaard L, Christiansen EH, et al. Impact of side branch modeling on computation of endothelial shear stress in coronary artery disease: coronary tree reconstruction by fusion of 3D angiography and OCT. *J Am Coll Cardiol*. (2015) 66:125–35. doi: 10.1016/j.jacc.2015.05.008
58. van der Giessen AG, Schaap M, Gijsen FJ, Groen HC, van Walsum T, Mollet NR, et al. 3D fusion of intravascular ultrasound and coronary computed tomography for *in-vivo* wall shear stress analysis: a feasibility study. *Int J Cardiovasc Imaging*. (2010) 26:781–96. doi: 10.1007/s10554-009-9546-y
59. Karanasos A, Schuurbiers JC, Garcia-Garcia HM, Simsek C, Onuma Y, Serruys PW, et al. Association of wall shear stress with long-term vascular healing response following bioresorbable vascular scaffold implantation. *Int J Cardiol*. (2015) 191:279–83. doi: 10.1016/j.ijcard.2015.04.231
60. Hoogendoorn A, Kok AM, Hartman EMJ, de Nisco G, Casadonte L, Chiastra C, et al. Multidirectional wall shear stress promotes advanced coronary plaque development - comparing five shear stress metrics. *Cardiovasc Res*. (2019). doi: 10.1093/cvr/cvz212. [Epub ahead of print].
61. Boogers MJ, Broersen A, van Velzen JE, de Graaf FR, El-Naggar HM, Kitslaar PH, et al. Automated quantification of coronary plaque with computed tomography: comparison with intravascular ultrasound using a dedicated registration algorithm for fusion-based quantification. *Eur Heart J*. (2012) 33:1007–16. doi: 10.1093/eurheartj/ehr465
62. Papadopoulou SL, Neefjes LA, Schaap M, Li HL, Capuano E, van der Giessen AG, et al. Detection and quantification of coronary atherosclerotic plaque by 64-slice multidetector CT: a systematic head-to-head comparison with intravascular ultrasound. *Atherosclerosis*. (2011) 219:163–70. doi: 10.1016/j.atherosclerosis.2011.07.005

63. Voros S, Rinehart S, Qian Z, Vazquez G, Anderson H, Murrieta L, et al. Prospective validation of standardized, 3-dimensional, quantitative coronary computed tomographic plaque measurements using radiofrequency backscatter intravascular ultrasound as reference standard in intermediate coronary arterial lesions: results from the ATLANTA (assessment of tissue characteristics, lesion morphology, and hemodynamics by angiography with fractional flow reserve, intravascular ultrasound and virtual histology, and noninvasive computed tomography in atherosclerotic plaques) I study. *JACC Cardiovasc Interv*. (2011) 4:198–208. doi: 10.1016/j.jcin.2010.10.008
64. Wahle A, Olszewski ME, Sonka M. Interactive virtual endoscopy in coronary arteries based on multimodality fusion. *IEEE Trans Med Imaging*. (2004) 23:1391–403. doi: 10.1109/TMI.2004.837109
65. Bourantas CV, Kalatzis FG, Papafaklis MI, Fotiadis DI, Tweddel AC, Kourtis IC, et al. ANGIOCARE: an automated system for fast three-dimensional coronary reconstruction by integrating angiographic and intracoronary ultrasound data. *Catheter Cardiovasc Interv*. (2008) 72:166–75. doi: 10.1002/ccd.21527
66. Bourantas CV, Plissiti ME, Fotiadis DI, Protopappas VC, Mpozios GV, Katsouras CS, et al. *In vivo* validation of a novel semi-automated method for border detection in intravascular ultrasound images. *Br J Radiol*. (2005) 78:122–9. doi: 10.1259/bjr/30866348
67. Doulaverakis C, Tsampoulatidis I, Antoniadis AP, Chatzizisis YS, Giannopoulos A, Kompatsiaris I, et al. IVUSAngio tool: a publicly available software for fast and accurate 3D reconstruction of coronary arteries. *Comput Biol Med*. (2013) 43:1793–803. doi: 10.1016/j.compbiomed.2013.08.013
68. Bourantas CV, Zanchin T, Sakellarios A, Karagiannis A, Ramasamy A, Yamaji K, et al. Implications of the local haemodynamic forces on the phenotype of coronary plaques. *Heart*. (2019) 105:1078–86. doi: 10.1136/heartjnl-2018-314086
69. Shishikura D, Sidharta SL, Honda S, Takata K, Kim SW, Andrews J, et al. The relationship between segmental wall shear stress and lipid core plaque derived from near-infrared spectroscopy. *Atherosclerosis*. (2018) 275:68–73. doi: 10.1016/j.atherosclerosis.2018.04.022
70. Costopoulos C, Maehara A, Huang Y, Brown AJ, Gillard JH, Teng Z, et al. Heterogeneity of plaque structural stress is increased in plaques leading to MACE: insights from the PROSPECT Study. *JACC Cardiovasc Imaging*. (2019). doi: 10.1016/j.jcmg.2019.05.024. [Epub ahead of print].
71. Costopoulos C, Huang Y, Brown AJ, Calvert PA, Hoole SP, West NEJ, et al. Plaque rupture in coronary atherosclerosis is associated with increased plaque structural stress. *JACC Cardiovasc Imaging*. (2017) 10:1472–83. doi: 10.1016/j.jcmg.2017.04.017
72. Brown AJ, Teng Z, Calvert PA, Rajani NK, Hennessy O, Nerlekar N, et al. Plaque structural stress estimations improve prediction of future major adverse cardiovascular events after intracoronary imaging. *Circ Cardiovasc Imaging*. (2016) 9:e004172. doi: 10.1161/CIRCIMAGING.115.004172
73. Villiger M, Otsuka K, Karanasos A, Doradla P, Ren J, Lippok N, et al. Coronary plaque microstructure and composition modify optical polarization: a new endogenous contrast mechanism for optical frequency domain imaging. *JACC Cardiovasc Imaging*. (2018) 11:1666–76. doi: 10.1016/j.jcmg.2017.09.023
74. Costopoulos C, Timmins LH, Huang Y, Hung OY, Molony DS, Brown AJ, et al. Impact of combined plaque structural stress andwall shear stress on coronary plaque progression, regression, and changes in composition. *Eur Heart J*. (2019) 40:1411–22. doi: 10.1093/eurheartj/ehz132
75. Migliori S, Chiastra C, Bologna M, Montin E, Dubini G, Aurigemma C, et al. A framework for computational fluid dynamic analyses of patient-specific stented coronary arteries from optical coherence tomography images. *Med Eng Phys*. (2017) 47:105–16. doi: 10.1016/j.medengphy.2017.06.027
76. O'Brien CC, Kolandaivelu K, Brown J, Lopes AC, Kunio M, Kolachalama VB, et al. Constraining OCT with knowledge of device design enables high accuracy hemodynamic assessment of endovascular implants. *PLoS ONE*. (2016) 11:e0149178. doi: 10.1371/journal.pone.0149178
77. Li Y, Li Z, Holck EN, Xu B, Karanasos A, Fei Z, et al. Local flow patterns after implantation of bioresorbable vascular scaffold in coronary bifurcations-novel findings by computational fluid dynamics. *Circ J*. (2018) 82:1575–1583. doi: 10.1253/circj.CJ-17-1332
78. Gijsen F, Katagiri Y, Barlis P, Bourantas C, Collet C, Coskun U, et al. Expert recommendations on the assessment of wall shear stress in human coronary arteries: existing methodologies, technical considerations, and clinical applications. *Eur Heart J*. (2019) 40:3421–33. doi: 10.1093/eurheartj/ehz551
79. Tenekecioglu E, Poon EK, Collet C, Thondapu V, Torii R, Bourantas CV, et al. The nidus for possible thrombus formation: insight from the microenvironment of bioresorbable vascular scaffold. *JACC Cardiovasc Interv*. (2016) 9:2167–8. doi: 10.1016/j.jcin.2016.08.019
80. Thondapu V, Tenekecioglu E, Poon EKW, Collet C, Torii R, Bourantas CV, et al. Endothelial shear stress 5 years after implantation of a coronary bioresorbable scaffold. *Eur Heart J*. (2018) 39:1602–9. doi: 10.1093/eurheartj/ehx810
81. Ng J, Bourantas CV, Torii R, Ang HY, Tenekecioglu E, Serruys PW, et al. Local hemodynamic forces after stenting: implications on restenosis and thrombosis. *Arterioscler Thromb Vasc Biol*. (2017) 37:2231–42. doi: 10.1161/ATVBAHA.117.309728
82. Tenekecioglu E, Sotomi Y, Torii R, Bourantas C, Miyazaki Y, Collet C, et al. Strut protrusion and shape impact on endothelial shear stress: insights from pre-clinical study comparing Mirage and Absorb bioresorbable scaffolds. *Int J Cardiovasc Imaging*. (2017) 33:1313–22. doi: 10.1007/s10554-017-1124-0
83. Tu S, Holm NR, Koning G, Huang Z, Reiber JH. Fusion of 3D QCA and IVUS/OCT. *Int J Cardiovasc Imaging*. (2011) 27:197–207. doi: 10.1007/s10554-011-9809-2

Conflict of Interest: The authors declare that the research was conducted in the absence of any commercial or financial relationships that could be construed as a potential conflict of interest.

The reviewer, AK, declared a past co-authorship with one of the authors, CB, to the handling editor.

frontiers in Cardiovascular Medicine

REVIEW
published: 04 June 2020
doi: 10.3389/fcvm.2020.00090

OCT-NIRS Imaging for Detection of Coronary Plaque Structure and Vulnerability

James Muller[1]* *and Ryan Madder*[2]

[1] *Brigham and Women's Hospital, Harvard Medical School, Boston, MA, United States,* [2] *Spectrum Health, Grand Rapids, MI, United States*

A combination optical coherence tomography and near-infrared spectroscopy (OCT-NIRS) coronary imaging system is being developed to improve the care of coronary patients. While stenting has improved, complications continue to occur at the stented site and new events are caused by unrecognized vulnerable plaques. An OCT-NIRS device has potential to improve secondary prevention by optimizing stenting and by identifying vulnerable patients and vulnerable plaques. OCT is already in widespread use world-wide to optimize coronary artery stenting. It provides automated lumen detection and can identify features of coronary plaques not accurately identified by angiography or intravascular ultrasound. The ILUMIEN IV study, to be completed in 2022, will determine if OCT-guided stenting will yield better clinical outcomes than angiographic guidance alone. While the superb spatial resolution of OCT enables the identification of many plaque structural features, the detection by OCT of lipids, an important component of vulnerable plaques, is limited by suboptimal specificity and interobserver agreement. In contrast, NIRS has been extensively validated for lipid-rich plaque detection against the gold-standard of histology and is the only FDA-approved method to identify coronary lipids. Studies in patients have demonstrated that NIRS detects lipid in culprit lesions causing coronary events. In 2019, the positive results of the prospective Lipid-Rich Plaque Study led to FDA approval of NIRS for detection of high-risk plaques and patients. The complementarity of OCT for plaque structure and NIRS for plaque composition led to the sequential performance of NIRS and OCT imaging in patients. NIRS identified lipid while OCT determined the thickness of the cap over the lipid pool. The positive results obtained with OCT and NIRS imaging led to development of a prototype combined OCT-NIRS catheter that can provide co-registered OCT and NIRS data in a single pullback. The data will provide structural and chemical information likely to improve stenting and deliver more accurate identification of vulnerable plaques and vulnerable patients. More precise diagnosis will then lead to OCT-NIRS guided treatment trials to improve secondary prevention. Success in secondary prevention will then facilitate development of improved primary prevention with invasive imaging and effective treatment of patients identified by non-invasive methods.

Keywords: OCT-NIRS imaging, intravascular coronary imaging, Near-IR Coronary Spectroscopy (NIRS), optical coherence tomography, vulnerable patients and vulnerable plaques, OCT for stenting

OPEN ACCESS

Edited by:
Christos Bourantas, Barts Health NHS Trust, United Kingdom

Reviewed by:
David Erlinge, Lund University, Sweden
Erhan Tenekecioglu, University of Health Sciences, Turkey

***Correspondence:**
James Muller
james.muller19@gmail.com

Specialty section:
This article was submitted to Cardiovascular Imaging, a section of the journal Frontiers in Cardiovascular Medicine

Received: *01 December 2019*
Accepted: *27 April 2020*
Published: *04 June 2020*

Citation:
Muller J and Madder R (2020) OCT-NIRS Imaging for Detection of Coronary Plaque Structure and Vulnerability. Front. Cardiovasc. Med. 7:90. doi: 10.3389/fcvm.2020.00090

Despite considerable progress, coronary artery disease continues to be the world's leading cause of death (1). A novel intracoronary (IC) imaging system that combines optical coherence tomography (OCT) with near-infrared spectroscopy (NIRS) is being developed to improve the secondary prevention of coronary events (2).

The need for a novel instrument is apparent from the continued occurrence of events post-coronary stenting, which is performed approximately 4 million times per year. Complications continue to occur at the stented site, and new events arise from dangerous non-stenotic vulnerable plaques not identified during the initial stenting procedure (**Figure 1**). In the PROSPECT Study the event rate 3.4 years post-enrollment was 12.9% due to new events caused by the stented site, and 11.6% due to events from non-stenotic vulnerable plaques not identified at the index stenting (3). Recent consensus documents have described the potential for invasive coronary imaging to optimize coronary interventions and improve the treatment of acute coronary syndromes (4, 5).

The combination OCT-NIRS instrument is being created as a means to improve outcomes post-stenting:

First, by reducing complications at the *stented site*;

Second, by identifying *vulnerable patients* as a means to guide intensity of pharmacologic therapy;

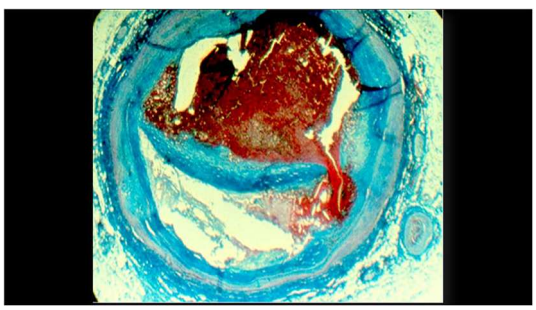

FIGURE 1 | A histologic cross-section of a previously vulnerable coronary plaque causing a fatal myocardial infarction. The cap covering the lipid core ruptured and led to an occlusive thrombus.

And, third, by identifying *vulnerable plaques* that might benefit from local therapy such as stenting.

While both OCT and NIRS have the potential to contribute to all 3 goals, the primary benefit of OCT is likely to be optimization of the stent result thereby decreasing events at the stented site, while the primary benefit of NIRS is likely to be the identification of vulnerable patients and vulnerable plaques.

The identification of vulnerable plaques, a long-sought goal identified in 1989 (6), and later refined (7), might lead to stenting of dangerous, non-stenotic lesions. This chapter will review the use of OCT and NIRS for the 3 goals of improved stenting, detection of vulnerable patients and detection of vulnerable plaques.

EXPERIENCE WITH OCT

OCT was introduced for medical diagnostics over 20 years ago as a means to use novel laser light sources and fiberoptic catheters to characterize tissue (8, 9). It has been successfully utilized in coronary patients to obtain higher resolution images of plaques and stented lesions than images obtained with intravascular ultrasound (IVUS) (10, 11). The improved resolution of OCT imaging has made it possible to identify many previously hidden features of plaques and stenting [(12), **Table 1**, **Figure 2**]. More recently, automated methods have been developed to measure lumen diameter (16).

OCT for Optimization of Coronary Stenting

Intracoronary structural imaging has shown considerable merit as a means to improve outcomes in patients undergoing percutaneous coronary intervention (PCI). A meta-analysis of 7 randomized trials of IVUS-guided stenting vs. angiographic-guided stenting showed markedly decreased major adverse cardiac events (MACE) rates with IVUS guidance [OR 0.66, 95% CI: 0.52–0.84, $P = 0.001$; (17)]. Although no adequately powered randomized controlled trials have similarly compared OCT-guided stenting vs. angiographic-guided stenting for clinical outcomes, several prior studies evaluating OCT-guided stenting are worth consideration (**Table 1**). An early observational comparison of OCT-guided PCI vs. angiographic-guided PCI

TABLE 1 | Summary of studies evaluating OCT-guided PCI.

Study	*N*	Design	Comparison	Primary endpoint	Major findings
Prati et al. (13) (CLI-OPCI)	670	Observational	OCT-guided PCI vs. angio-guided PCI	Death or MI at 1 year	OCT-guided PCI associated with lower rate of primary endpoint (adjusted OR 0.49 [95%CI 0.25–0.96], $p = 0.037$)
Meneveau et al. (14) (DOCTORS)	240	Prospective, Randomized	OCT-guided PCI vs. angio-guided PCI	Post-PCI FFR	OCT-guided PCI associated with higher post-PCI FFR (0.94 vs. 0.92, $p = 0.005$)
Ali (15) (ILUMIEN III)	450	Prospective, Randomized	OCT-guided PCI vs. angio-guided PCI vs. IVUS-guided PCI	Post-PCI MSA	OCT-guided PCI achieved non-inferior MSA (5.79 mm^2) compared to IVUS-guided PCI (5.89 mm^2; $p =$ 0.001 for non-inferiority), but not superior to MSA achieved with angio-guided PCI (5.49 mm^2; $p = 0.12$)

Angio, angiography; FFR, fractional flow reserve; IVUS, intravascular ultrasound; MI, myocardial infarction; MSA, minimum stent area; OCT, optical coherence tomography; OR, odds ratio; PCI, percutaneous coronary intervention.

TABLE 2 | Summary of OCT and NIRS studies for the detection of vulnerable patients.

References	*N*	Modality	Primary endpoint	Follow up	Major findings
Xing et al. (28)	1,474	OCT	MACE (cardiac death, acute MI, ischemia-driven revasc)	4 year	Non-culprit LRP in target vessel associated with increased risk of MACE RR 2.06 (95% CI 1.05–4.04)
Prati et al. (27)	1,003	OCT	Death and target segment MI	1 year	Simultaneous presence of 4 OCT features (MLA < 3.5 mm^2, fibrous cap thickness <75 μm, lipid arc >180°, macrophages) associated with primary endpoint: HR 7.54 (95% CI 3.1–18.6)
Oemrawsingh et al. (29)	203	NIRS	MACE (all-cause mortality, non-fatal ACS, stroke, unplanned coronary revasc)	1 year	LCBI in non-culprit coronary artery at or above median of 43 for study population associated with primary endpoint: HR 4.04 (95% CI 1.33–12.29)
Madder et al. (30)	121	NIRS	MACE (all-cause mortality, non-fatal ACS, cerebrovasc events)	≥1 year	$MaxLCBI_{4mm}$ ≥400 in non-stented segments of target artery associated with primary endpoint: HR 10.2 (95% CI 3.4–30.6)
Danek et al. (31)	239	NIRS	MACE (cardiac mortality, ACS, stroke, unplanned revasc)	5 years	Non-target vessel LCBI ≥77 associated with primary endpoint: HR 14.04 (95% CI 2.47–133.51)
Schuurman et al. (32)	275	NIRS	MACE (all-cause death, non-fatal ACS, unplanned revasc)	4 years	Each 100 unit increase $maxLCBI_{4mm}$ in non-culprit artery associated with primary endpoint: HR 1.19 (95% CI 1.07–1.32)
Karlsson et al. (33)	144	NIRS	MACE (all-cause mortality, ACS requiring revasc, cerebrovasc events)	≥1 year	$MaxLCBI_{4mm}$ ≥400 in non-culprit segments of culprit artery associated with primary endpoint: HR 3.67 (95% CI 1.46–9.23)
Waksman et al. (34)	1,563	NIRS	MACE (cardiac death, cardiac arrest, non-fatal MI, ACS, revasc, readmission for angina with more than 20% diameter stenosis progression)	2 years	Each 100 unit increase in non-culprit $maxLCBI_{4mm}$ associated with primary endpoint: HR 1.18 (95% CI 1.05–1.32)

ACS, acute coronary syndrome; cerebrovasc, cerebrovascular; HR, hazard ratio; MACE, major adverse cardiovascular events; MI, myocardial infarction; mo, months; NIRS, near-infrared spectroscopy; OCT, optical coherence tomography; revasc, revascularization; RR, risk ratio.

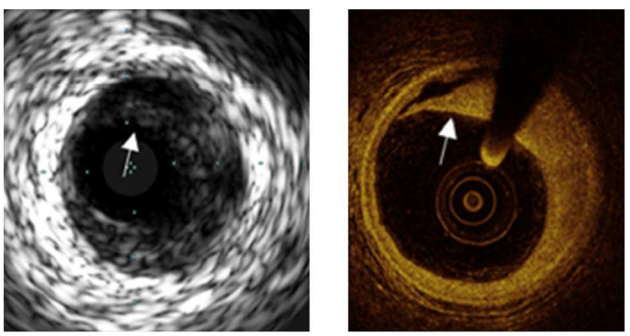

FIGURE 2 | A comparison of images obtained by IVUS and OCT from the same location. The superior resolution of OCT easily permits detection of a dissection (shown by arrows) less apparent by IVUS.

demonstrated improved clinical outcomes, including a reduction in mortality and myocardial infarction, in the OCT-guided cohort (13). These observational findings in favor of OCT have not yet been confirmed in a randomized controlled trial. In the prospective DOCTORS study, patients with non-ST-segment elevation acute coronary syndromes were randomized to undergo OCT-guided PCI or angiography-guided PCI (14). Post-PCI fractional flow reserve (FFR) was significantly higher among patients undergoing OCT-guided PCI. Furthermore, the frequency of an FFR value >0.90 post-PCI was substantially greater with OCT-guidance (82.5%) compared to angiographic guidance (64.2%; $p = 0.0001$).

The ILUMIEN III trial compared OCT-guided, IVUS-guided, and angiographic-guided PCI. The primary endpoint of this trial was minimum stent area (MSA) achieved after PCI, as larger MSA values after stenting have consistently been associated with improved clinical outcomes. OCT-guidance was superior to angiographic-guidance with respect to stent expansion and procedural success. The final minimum stent areas for the 3 approaches were (median [25 percent, 75 percent]) 5.79 [4.54, 7.34] mm^2 with OCT-guidance, 5.89 [4.67, 7.80] mm^2 with IVUS-guidance and 5.49 [4.39, 6.59] mm^2 with angiographic-guidance (15). Since ILUMIEN III was not powered to detect differences in clinical outcomes with the three guidance methods, ILUMIEN IV was launched to compare clinical outcomes in angiographic- vs. OCT-guided stenting in over 3,000 patients undergoing PCI (clinicaltrials.gov NCT03507777). Results of this pivotal trial are expected in 2022.

The use of OCT to guide PCI performance has been made easier by the recent development of software packages providing automated detection of several key anatomic features on the acquired OCT images (18). By automatically detecting lumen profiles, minimum lumen area, metallic stent struts, and stent strut malapposition, these novel software packages can assist operators in planning and optimizing PCI results.

OCT for Detection of Vulnerable Patients and Vulnerable Plaques

In the prospective PROSPECT Study, IVUS, the structural imaging predecessor of OCT, has been shown to be capable of detecting vulnerable plaques (3). For non-stented sites, IVUS

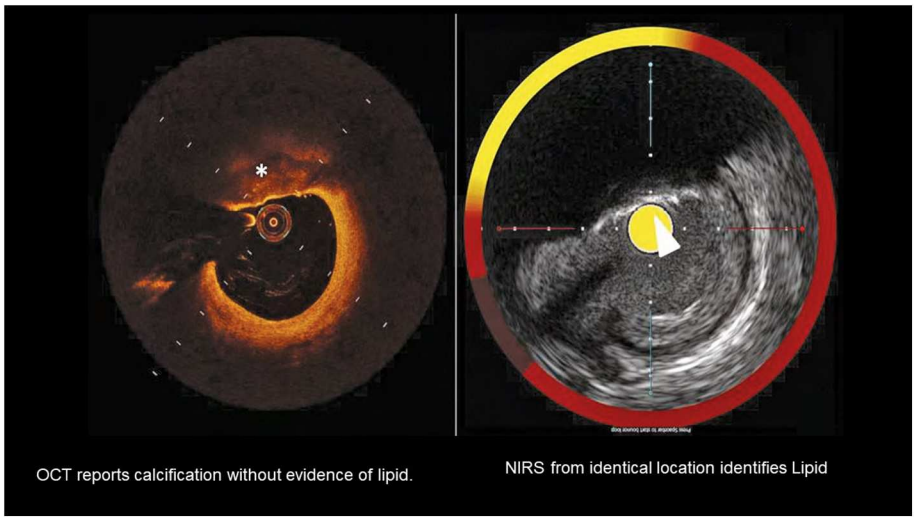

FIGURE 3 | A comparison of OCT detection of lipid with lipid detected by NIRS in the setting of superficial calcification. Calcification is marked by the * on the OCT image and by the arrow on the NIRS-IVUS image. The presence of calcium complicates detection of lipid by OCT.

was able to identify plaques likely to cause future events. Non-stenotic sites with a plaque burden ≥70%, minimal lumen area ≤4 mm^2 and signs of a thin-cap fibroatheroma (TCFA) had a 18.2% chance of causing a major adverse event during 3.4 years of follow-up. The ability of IVUS to identify vulnerable plaques was subsequently confirmed in the VIVA (19) and ATHEROREMO-IVUS studies (20). While the ability to identify plaques at risk was convincingly demonstrated in these studies, some have suggested the positive predictive value achieved by IVUS imaging alone may not be high enough to warrant attempts at local therapy. This is being actively investigated in two ongoing treatment trials of potentially vulnerable plaques, PROSPECT ABSORB (clinicaltrials.gov NCT02171065[1]) and PREVENT (21).

It is not yet known whether OCT is similarly capable of prospectively identifying lesions at risk of future site-specific events. Prati et al. have identified distinct OCT features of culprit lesions in a cross-sectional study (22). Whether non-culprit lesions having these OCT features of vulnerability actually represent vulnerable plaques at risk of causing future events remains unknown. The COMPLETE Study demonstrated that PCI of all stenotic lesions at the time of PCI for a culprit lesion causing a STEMI resulted in improved outcomes. An OCT substudy of 93 patients in the COMPLETE Study found OCT signs indicating that stenotic non-culprit lesions frequently shows signs of vulnerability and suggested that stenting of such lesions might be responsible for the positive results of COMPLETE (23).

A major limitation of OCT for detection of vulnerable plaques is the difficulty of identifying lipid deposits in the presence of calcification [(24); **Figure 3**]. However, OCT can accurately detect more features than IVUS (such as thrombus, vasa vasorum, cholesterol crystals, and cap thickness). Such improved plaque characterization might provide the increased positive predictive value that is needed (25). The prospective CLIMA study has performed baseline OCT imaging in 1,003 patients. The study developed a four component OCT grading system, which includes OCT-identified macrophages (26). The results of the CLIMA study, after 1 year of follow up, have been recently reported and demonstrated the presence of MLA <3.5 mm^2, fibrous cap thickness <75 μm, lipid arc >180°, and macrophages, as detected by OCT, were associated with an increased risk of the primary endpoint, a composite of death and target segment myocardial infarction (27). The simultaneous presence of all four of these OCT characteristics was an independent predictor of the primary endpoint with a HR of 7.54 (95% CI 3.1–18.6).

A vulnerable plaque *treatment* trial based on OCT-guidance has also been initiated. In the PREVENT Study Park et al. have enrolled over 1,000 patients with OCT, NIRS or IVUS signs of a non-stenotic vulnerable plaque (21). The suspected vulnerable plaques have been randomized to optimal medical therapy (OMT) alone, or OMT plus a stent or scaffold. Results are expected in 2022.

Whereas, the ability of OCT to prospectively detect vulnerable plaques has not yet been proven, OCT has been shown to be capable of identifying vulnerable patients, defined as those at an increased risk of future patient-level cardiovascular events (**Table 2**). In an observational study of 1,474 patients undergoing OCT imaging at baseline, the presence of non-culprit LRP detected by OCT in the target vessel was associated with a higher risk of patient-level major adverse cardiovascular events during 48 months of follow up (28). The results of the CLIMA study described above also support the ability of OCT to detect vulnerable patients (27).

[1]ClinicalTrials.gov NCT02171065, PROSPECT2-ABSORB Study.

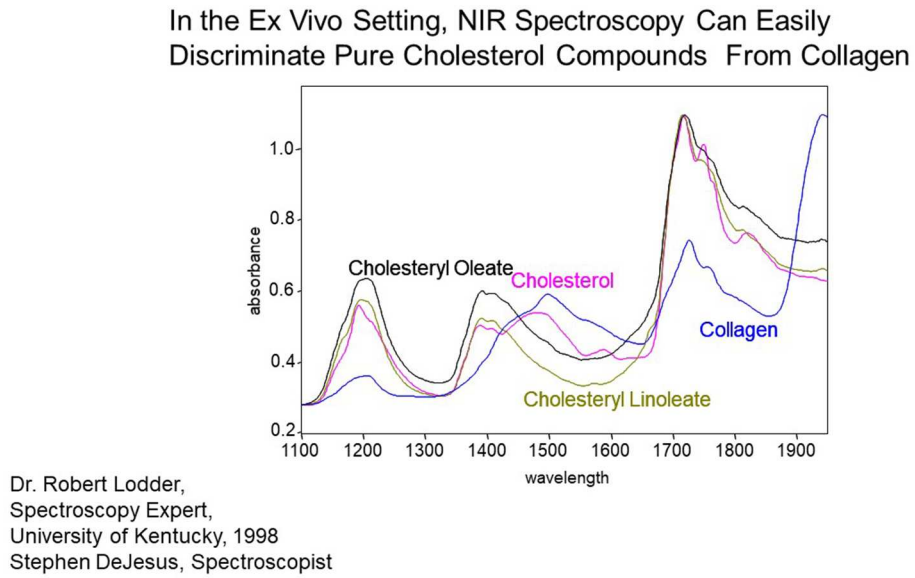

FIGURE 4 | Measurement of pure chemicals by spectroscopy in the absence of blood flow and motion. Substances of interest, such as collagen and cholesterol, are easily identified by their variable absorbance at different near-IR wavelengths.

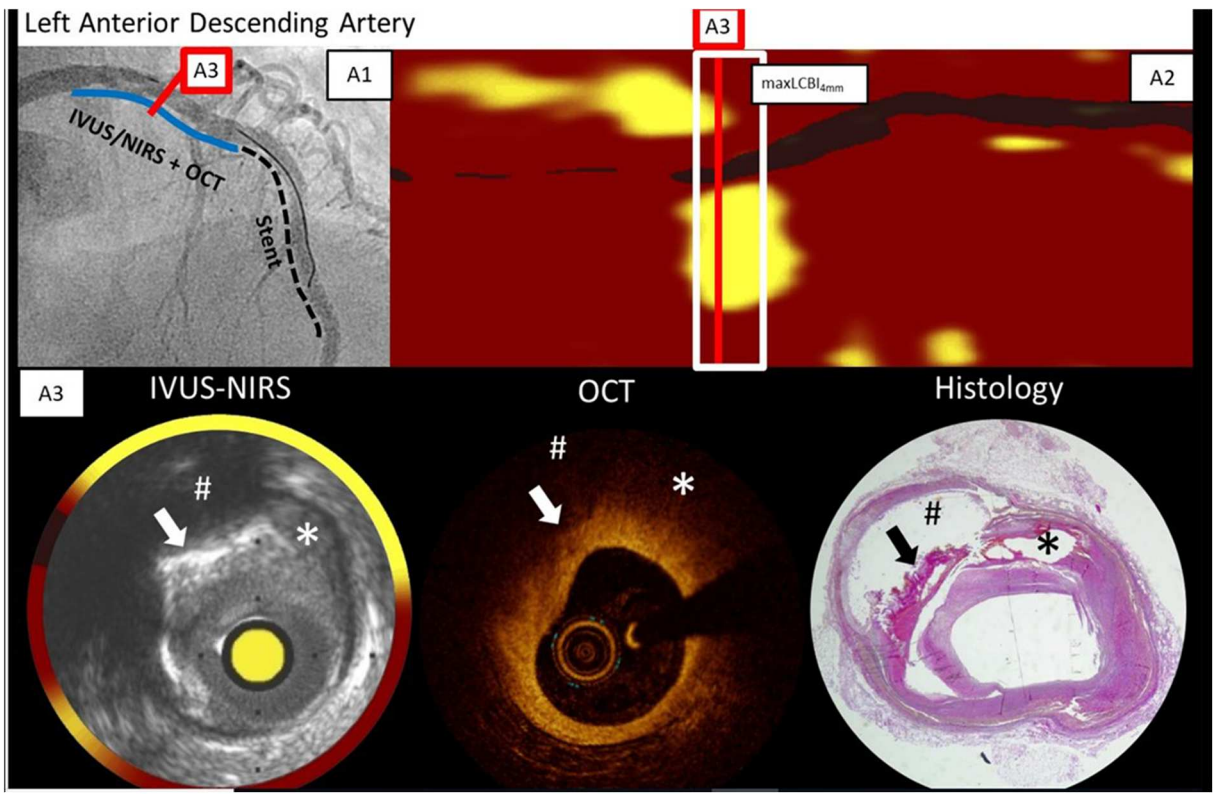

FIGURE 5 | Angiogram, NIRS, OCT, and histology findings in a patient who died of ventricular rupture 5 days after imaging. The blue line on the angiogram (A1) shows the IVUS-NIRS and OCT pullback location in LAD during stenting at a more distal location. The chemogram (A2) and cross-section IVUS-NIRS (A3) shows lipid from 10 p.m. to 3 p.m. OCT from the same cross-section shows a thick cap of 300 microns, and signs of calcification which complicate the detection of lipid by OCT. In each image, the arrow marks the location of superficial calcium, the hash-tag marks the location of a lipid core underlying the calcification, and the the asterisk marks the location of a lipid pool. Adapted from Zanchin et al. (49). The findings show the complementarity of NIRS and OCT data—NIRS identifies lipid without interference by calcium and OCT shows the thickness of the cap over the lipid. In this case in which the plaque was not causing obstruction, the lipid core would not be expected to be dangerous since a thick cap is present.

EXPERIENCE WITH NIRS

Intracoronary NIRS imaging was developed as a means to detect the lipid-core plaques suspected to be vulnerable to disruption and thrombosis (**Figure 4**). Initial studies demonstrated that NIRS could detect lipid core plaques in human coronary autopsy specimens as documented by histology (35). In 2019 the U.S. FDA cleared NIRS for the detection of patients and plaques at high-risk of causing a MACE on the basis of the Lipid-Rich Plaque Study results (34).

NIRS for Optimization of Coronary Stenting

It has been observed that dilation of a lipid-rich plaque is associated with no-reflow and periprocedural myocardial infarction, a serious complication of PCI. Using data from a large NIRS registry, Goldstein *et al* reported target lesions with a maxLCBI$_{4mm}$ $\geq$500 were associated with periprocedural myocardial infarction during PCI in 50% cases (36). This led to the concept that the use of a filter might be helpful in preventing peri-stenting myocardial infarction. The CANARY study confirmed the association between large LRP detected by NIRS and the risk of periprocedural myocardial infarction (37). However the CANARY Study was unable to demonstrate a beneficial effect of distal embolic protection (37). A recent report indicates that stenting of plaques with increased lipid by NIRS is associated with signs of microvascular injury (38).

The COLOR Registry demonstrated that stenting of lipid-rich plaque, as detected by NIRS carried no increased longer term risk, which supports study of the use of stenting for vulnerable plaques (39). It is possible that NIRS may identify optimal non-lipid-rich landing zones for the ends of stents and guide the selection of stent length to ensure adequate coverage of LRP. In this regard, a prior study has demonstrated LRP to frequently extend beyond the angiographic margins of the target lesion (40). Furthermore, LRP in the stent margins, as identified by OCT, has been associated with an increased risk of subsequent

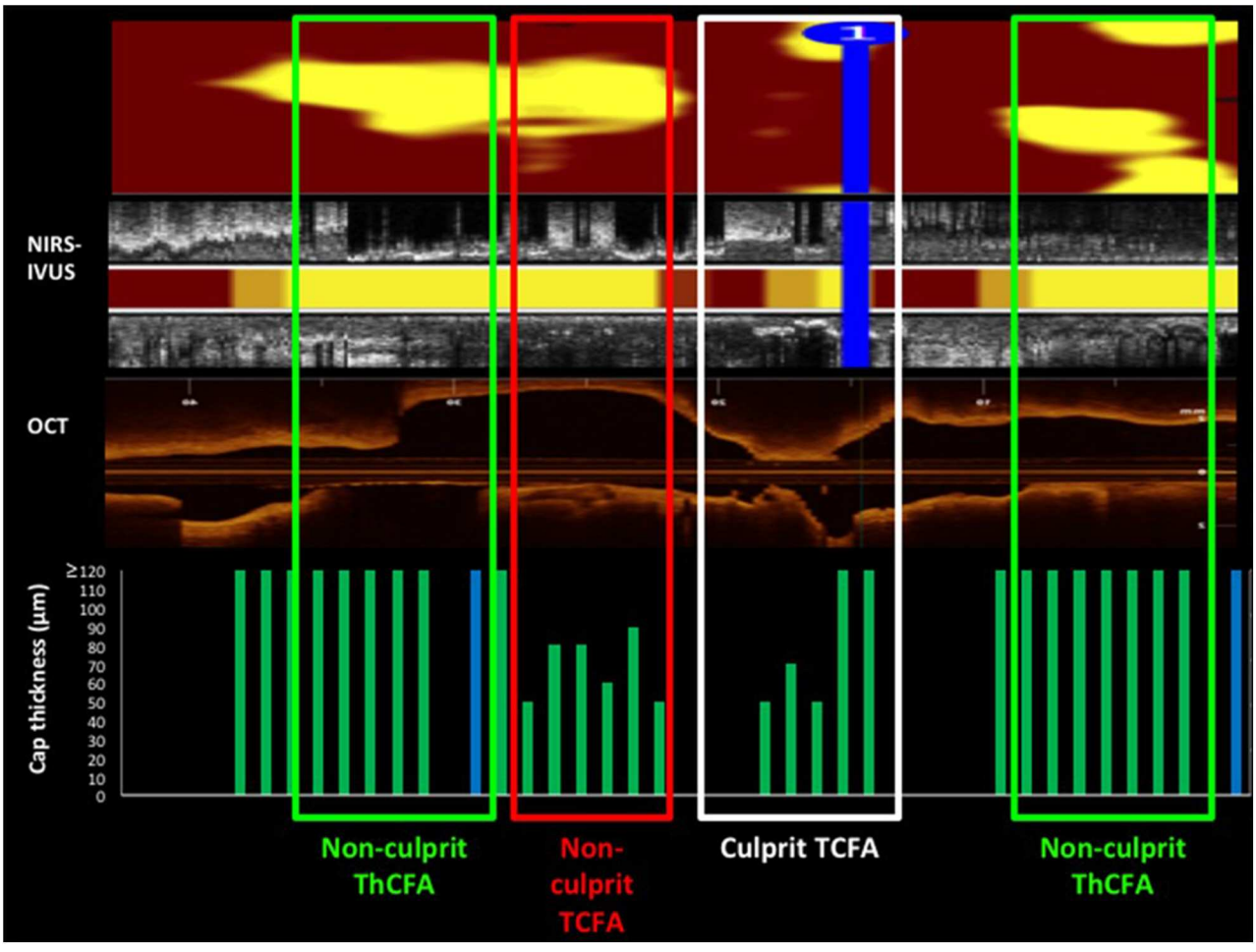

FIGURE 6 | A comparison of NIRS-IVUS and OCT imaging data in a patient with a coronary event. OCT was used to measure cap thickness in regions with lipid detected by NIRS and was able to differentiate lipid cores with thick and thin caps. The culprit lesion, identified by angiography plus IVUS and OCT imaging is indicated on the NIRS-IVUS and OCT pullbacks. The culprit lesion occurred at the relatively small lipid core plaque that had a thin cap as determined by OCT. The NIRS chemogram shows 2 large lipid core plaques (yellow spots) at non-culprit sites. Personal Communication from Dr. Ryan Madder.

restenosis, with larger lipid cores seemingly carrying greater risk (41). Whether LRP identified by NIRS in the stent margins after PCI similarly identifies a greater risk of restenosis has not been adequately investigated.

NIRS for Detection of Vulnerable Patients and Vulnerable Plaques

Multiple studies have demonstrated that the detection by NIRS of lipid in the walls of the coronary arteries identifies vulnerable patients at increased risk of a new event (33). There is also evidence that NIRS can detect vulnerable plaques, a more difficult goal than identifying vulnerable patients, but one that could lead to effective local therapy. The initial data suggesting that NIRS could identify vulnerable plaques were obtained from cross-sectional studies, in which NIRS evidence of a lipid core plaque was found at the site of culprit lesions causing ST-segment elevation myocardial infarction (STEMI) (42, 43). More recently Terada et al. demonstrated that the NIRS-IVUS instrument (Infraredx, Inc., a Nipro Company) can differentiate plaque rupture from erosion from calcified nodule as the cause of a coronary event (44).

The promising cross-sectional studies have now been supplemented with the required prospective data. As mentioned above, in April 2019, the US FDA approved NIRS for detection of both vulnerable patients and vulnerable plaques on the basis of the results of the Lipid-Rich Plaque Study (34). Thirty mm segments of artery were designated as "Ware Segments" and assessed for lipid core plaque by NIRS imaging at baseline. Lipid content was designated as the maximal lipid-core burden index in 4 mm lengths of pullback ($maxLCBI_{4mm}$). Patients were then followed for 2 years for evidence of new coronary events. For segments with a $maxLCBI_{4mm}$ more than 400, the unadjusted hazard ratio (HR) for non-Culprit-MACE was 4.22 (2.39–7.45; $p < 0{\cdot}0001$) and the adjusted HR was 3.39 (1.85–6.20; $p < 0{\cdot}0001$).

While an adjusted HR of 3.39 is significant, a higher hazard ratio would be helpful for identification of plaques that might benefit from local therapy.

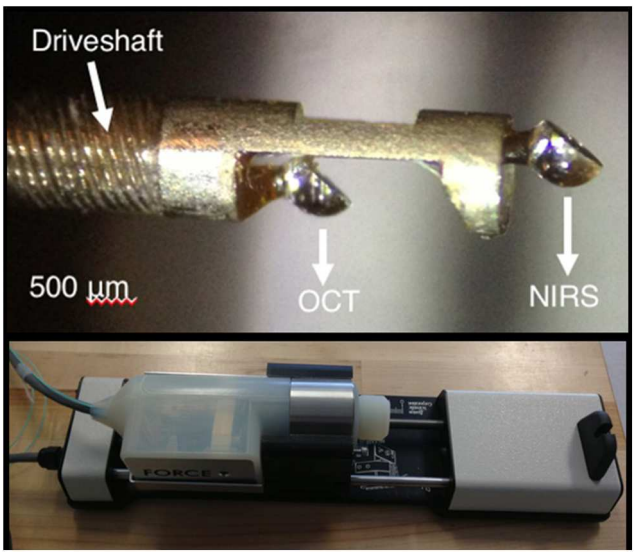

FIGURE 8 | A close-up of the tip of the prototype OCT-NIRS catheter created by the Tearney Lab. Light travels down a first optical fiber, and returns to provide the NIRS signal in a second optical fiber.

Comparison of Intra-coronary Imaging Technologies for Stent Optimization and Vulnerable Plaque Detection

	IVUS	Virtual Histology IVUS	OCT	NIRS	OCT NIRS
Resolution	+	+	++	NA	++
PCI (stent sizing, expansion)	++	+	++	NA	++
Necrotic core	±	+	+	++	++
Detection of thin cap	±	+	++	-	++
Thrombus	±	-	+	-	+
Stent tissue coverage	+	+	++	-	++

Adapted from Maehara A, Mintz GS, Weissman NJ. Advances in intravascular imaging.2009 Circulation: Cardiovascular Interventions.

7

FIGURE 7 | A comparison of the capabilities of multiple imaging modalities for the detection of various features of interest in a coronary artery. Adapted from Maehara et al. (51).

Results of a second study of NIRS-IVUS imaging to detect vulnerable plaque and vulnerable patients are expected in 2020. The PROSPECT 2-ABSORB (P2A) study, which is being led by Drs. David Erlinge and Gregg Stone, has completed enrollment of 900 patients in Sweden, Norway and Denmark (Clinicaltrials.gov NCT02171065). Among the endpoints to be evaluated will be the ability of additional information provided by IVUS to increase the hazard ratio for vulnerable plaques detected by NIRS. The ABSORB portion of P2A is a pilot study in 200 patients of the treatment of non-stenotic vulnerable plaques randomized to OMT or OMT plus a local therapy with a bioresorbable vascular scaffold (BVS). The results of this study will have to be interpreted in the context of the known scaffold thrombosis risk associated with BVS.

STUDIES WITH BOTH OCT AND NIRS MEASUREMENTS

The promising results cited above with both OCT and NIRS have led to interest in imaging with both OCT and NIRS in patients undergoing PCI. These studies were performed with separate OCT and NIRS catheters, which necessitated two pullbacks, and required efforts to establish co-registration of the OCT and NIRS images. Bourantas et al. have reviewed the overall status of hybrid instruments that can provide multiple types of information about a plaque in a single pullback (45).

For OCT plus NIRS imaging, the combination was successful in two separate reports in identifying thin caps over neoatheroma formed inside stents (46, 47). These results suggest combined OCT-NIRS imaging in pre-existing stents may overcome some of the limitations inherent to NIRS-IVUS imaging in identifying neoatherosclerosis (48).

Räber et al. performed NIRS and OCT imaging in a patient with a myocardial infarction who unfortunately died 5 days later of a ventricular rupture [(5); **Figure 5**]. This permitted comparison of OCT and NIRS data with histology (49). *In vivo* NIRS showed a large lipid-rich plaque validated by histology as expected from prior *ex vivo* autopsy validation studies. The *in vivo* OCT image indicated that the lipid core was covered by a thick cap—a finding also validated by histology. Hence the NIRS plus OCT suggested that a large lipid core was present, but that it was less likely to be vulnerable in the near-term due to the presence of thick cap.

Madder obtained OCT and NIRS data in a patient who experienced a coronary event [(50); **Figure 6**]. The NIRS chemogram showed 2 large and one small lipid core plaques. The OCT showed that the culprit event was caused not by the large lipid core plaques that had thick caps but by the smaller lipid core plaque that had a thin cap.

DEVELOPMENT OF A COMBINATION OCT-NIRS CATHETER

The complementarity of OCT and NIRS data led to interest in a combination OCT-NIRS catheter. The hybrid catheter would permit collection of automatically co-registered data in a single pullback. Features of a combination OCT-NIRS device are shown in **Figure 7**. OCT provides a broad range of features, while the sole contribution of the NIRS is the accurate and automated detection of lipid core plaque.

A prototype functional OCT-NIRS catheter has been developed in the Tearney Lab at the Massachusetts General Hospital, Boston MA [(2); **Figure 8**]. Studies performed in autopsy specimens demonstrated the detection of lipid by spectroscopy and structural features, including cap thickness, by OCT (**Figure 9**). As illustrated in **Figure 9**, a promising feature of the combined OCT-NIRS device is that OCT may facilitate determining the depth of lipid cores identified by NIRS. SpectraWAVE, Inc. is now building a commercial, combination OCT-NIRS catheter that will be available for clinical use in 2021.

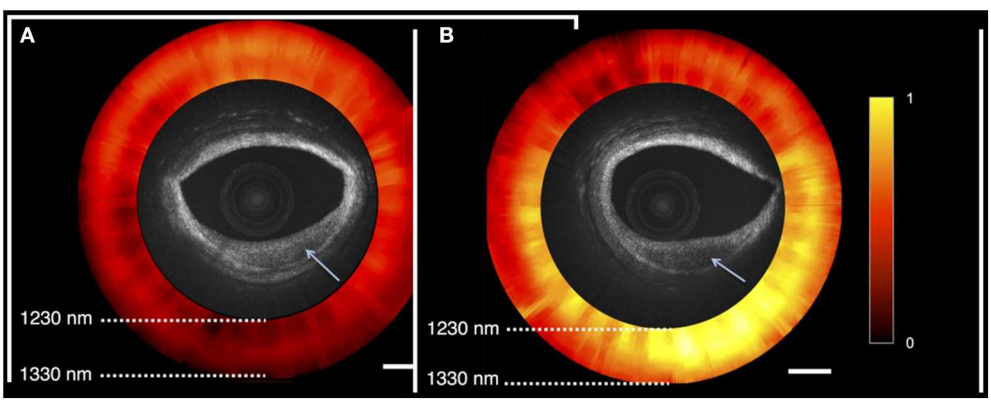

FIGURE 9 | OCT-NIRS images of cadaver coronary artery. Both OCT images show lesions with reduced backscattering (arrow). NIRS image (red and yellow) shows absorption spectra compatible with fibrotic tissue (red) in the left image **(A)**, and lipid-rich tissue (yellow) in the right image **(B)**. As shown on the right image, a promising feature of the combined OCT-NIRS device is that OCT may facilitate determining the depth of lipid cores identified by NIRS.

CONCLUSION

OCT already provides valuable information for PCI procedures, and NIRS has already been demonstrated to identify vulnerable patients based on the detection and quantification of coronary lipid. However, the effort to identify vulnerable plaques which has been in progress for 30 years and has yet to provide a validated, widely used method to identify and treat the focal lesions. This has led to criticism of the search for the vulnerable plaque, and the admonition that efforts should be shifted to identification of the vulnerable patient for this systemic disease (52). A counter-argument can be made in favor of identifying both the vulnerable patient, and the most dangerous plaques that are the focal manifestation of the disease.

It is expected that the OCT-NIRS catheter, with automated co-registration of data, will contribute to the triple goal of improving stenting and detecting and treating vulnerable patients and vulnerable plaques. An added benefit of improved secondary prevention will be an impetus for improved primary prevention made possible by precise invasive imaging and treatment of those deemed to be at higher risk by non-invasive imaging (53, 54).

AUTHOR CONTRIBUTIONS

All authors listed have made a substantial, direct and intellectual contribution to the work, and approved it for publication.

REFERENCES

1. World Health Organization (2019). Available online at: www.who.int/mediacentre/factsheets/fs310/en/ (accessed May 13, 2020).
2. Fard AM, Vacas-Jacques P, Hamidi E, Wang H, Carruth RW, Gardecki JA, et al. Optical coherence tomography – near infrared spectroscopy system and catheter for intravascular imaging. *Opt Express*. (2013) 21:30849–58. doi: 10.1364/OE.21.030849
3. Stone GW, Maehara A, Lansky AJ, de Bruyne B, Cristea E, Mintz GS, et al. A prospective natural-history study of coronary atherosclerosis. *N Engl J Med*. (2011) 364:226–35. doi: 10.1056/NEJMoa1002358
4. Johnson TW, Räber L, di Mario C, Bourantas C, Jia H, Mattesini A, et al. Clinical use of intracoronary imaging. Part 2: acute coronary syndromes, ambiguous coronary angiography findings, and guiding interventional decision-making: an expert consensus document of the European Association of Percutaneous Cardiovascular Interventions. *Eur Heart J*. (2019) 40:2566–84. doi: 10.1093/eurheartj/ehz332
5. Räber L, Mintz GS, Koskinas KC, Johnson TW, Holm NR, Onuma Y, et al. Clinical use of intracoronary imaging. Part 1: guidance and optimization of coronary interventions. An expert consensus document of the European Association of Percutaneous Cardiovascular Interventions. *Eur Heart J*. (2018) 39:3281–300. doi: 10.1093/eurheartj/ehy285
6. Muller J, Tofler G, Stone P. Circadian variation and triggers of onset of acute cardiovascular disease. *Circulation*. (1989) 79:733–43. doi: 10.1161/01.CIR.79.4.733
7. Stone G. In search of vulnerable plaque. *Circulation*. (2012) 5:428–30. doi: 10.1161/CIRCIMAGING.112.977629
8. Fujimoto JG, Brezinski ME, Tearney GJ, Boppart SA, Bouma B, Hee MR, et al. Optical biopsy and imaging using optical coherence tomography. *Nat Med*. (1995) 1:970–2. doi: 10.1038/nm0995-970
9. Tearney GJ, Jang IK, Kang DH, Aretz HT, Houser SL, Brady TJ, et al. Porcine coronary imaging *in vivo* by optical coherence tomography. *Acta Cardiol*. (2000) 55:233–7. doi: 10.2143/AC.55.4.2005745
10. Jang IK, Tearney G, Bouma B. Visualization of tissue prolapse between coronary stent struts by optical coherence tomography: comparison with intravascular ultrasound. *Circulation*. (2001) 104:2754. doi: 10.1161/hc4701.098069
11. Jang IK, Bouma BE, Kang DH, Park SJ, Park SW, Seung KB, et al. Visualization of coronary atherosclerotic plaques in patients using optical coherence tomography: comparison with intravascular ultrasound. *J Am Coll Cardiol*. (2002) 39:604–9. doi: 10.1016/S0735-1097(01)01799-5
12. Tearney G, Jang IK, Bouma B. Optical coherence tomography for imaging the vulnerable plaque. *J Biomed Opt*. (2006) 11:021002. doi: 10.1117/1.2192697
13. Prati F, Di Vito L, Biondi-Zoccai G, Occhipinti M, La Manna A, Tamburino C, et al. Angiography alone versus angiography plus optical coherence tomography to guide decision-making during percutaneous coronary intervention. *EuroIntervention*. (2012) 8:823–9. doi: 10.4244/EIJV8I7A125
14. Meneveau N, Souteyrand G, Motreff P, Caussin C, Amabile N, Ohlmann P, et al. Optical coherence tomography to optimize results of percutaneous coronary intervention in patients with non-ST-elevation acute coronary syndrome. *Circulation*. (2016) 134:906–17. doi: 10.1161/CIRCULATIONAHA.116.024393
15. Ali Z. Optical coherence tomography compared with intravascular ultrasound and with angiography to guide coronary stent implantation (ILUMIEN III: OPTIMIZE PCI): a randomised controlled trial. *Lancet*. (2016) 388:2618–28. doi: 10.1016/S0140-6736(16)31922-5
16. Cheimariotis GA, Chatzizisis YS, Koutkias VG, Toutouzas K, Giannopoulos A, Riga M, et al. ARCOCT: automatic detection of lumen border in intravascular OCT images. *Comput Methods Programs Biomed*. (2017) 151:21–32. doi: 10.1016/j.cmpb.2017.08.007
17. Steinvil A, Zhang YJ, Lee SY, Pang S, Waksman R, Chen SL. Intravascular ultrasound-guided drug-eluting stent implantation: an updated meta-analysis of randomized control trials and observational studies. *Int J Cardiol*. (2016) 216:133–9. doi: 10.1016/j.ijcard.2016.04.154
18. Tenekecioglu E, Albuquerque FN, Sotomi Y, Zeng Y, Suwannasom P, Tateishi H, et al. Intracoronary optical coherence tomography: clinical and research applications and intravascular imaging software overview. *Catheter Cardiovasc Interv*. (2017) 89:679–89. doi: 10.1002/ccd.26920
19. Calvert PA, Obaid DR, O'Sullivan M, Shapiro LM, McNab D, Densem CG, et al. Association between IVUS findings and adverse outcomes in patients with coronary artery disease: the VIVA study. *JACC Cardiovasc Imaging*. (2011) 4:894–901. doi: 10.1016/j.jcmg.2011.05.005
20. Cheng JM, Garcia-Garcia HM, de Boer SP, Kardys I, Heo JH, Akkerhuis KM, et al. *In vivo* detection of high-risk coronary plaques by radiofrequency intravascular ultrasound and cardiovascular outcome: results of the ATHEROREMO-IVUS study. *Eur Heart J*. (2014) 35:639–47. doi: 10.1093/eurheartj/eht484
21. Park SJ. Treatment of vulnerable patients and plaques: PREVENT rationale and update. In: *Presented at: TCT 2019*. San Francisco, CA (2019).
22. Prati F, Gatto L, Romagnoli E, Limbruno U, Fineschi M, Marco V, et al. *In vivo* vulnerability grading system of plaques causing acute coronary syndromes: an intravascular imaging study. *Int J Cardiol*. (2018) 269:350–5. doi: 10.1016/j.ijcard.2018.06.115
23. Pinilla-Echeverri N. Non-culprit lesion plaque morphology in patients with ST-segment elevation myocardial infarction: results from the COMPLETE trial optical coherence tomography OCT substudy. In: *Presented at: AHA 2019*. Philadelphia, PA (2019).
24. Di Vito L, Imola F, Gatto L, Romagnoli E, Limbruno U, Marco V, et al. Limitations of OCT in identifying and quantifying lipid components: an *in vivo* comparison study with IVUS-NIRS. *EuroIntervention*. (2017) 13:303–11. doi: 10.4244/EIJ-D-16-00317
25. Toutouzas K, Karansos A, Tousoulis D. Optical coherence tomography for the detection of the vulnerable plaque. *Eur Cardiol Rev*. (2016) 11:90–5. doi: 10.15420/ecr.2016:29:2

26. Romagnoli E, Gatto L, and Prati F. The CLIMA study: assessing the risk of myocardial infarction with a new anatomical score. *Eur Heart J Suppl.* (2019) 21(Suppl. B):B80–3. doi: 10.1093/eurheartj/suz032
27. Prati F, Romagnoli E, Gatto L, La Manna A, Burzotta F, Ozaki Y, et al. Relationship between coronary plaque morphology of the left anterior descending artery and 12 months clinical outcome: the CLIMA study. *Eur Heart J.* (2019) 41:383–91. doi: 10.1093/eurheartj/ehz520
28. Xing L, Higuma T, Wang Z, Aguirre AD, Mizuno K, Takano M, et al. Clinical significance of lipid-rich plaque detected by optical coherence tomography. *J Am Coll Cardiol.* (2017) 69:2502–13. doi: 10.1016/j.jacc.2017.03.556
29. Oemrawsingh RM, Cheng JM, Garcia-Garcia HM, van Geuns RJ, de Boer SPM, Simsek C, et al. Near-infrared spectroscopy predicts cardiovascular outcome in patients with coronary artery disease. *J Am Coll Cardiol.* (2014) 64:2510–8. doi: 10.1016/j.jacc.2014.07.998
30. Madder RD, Husaini M, Davis AT, VanOosterhout S, Khan M, Wohns D, et al. Large lipid-rich coronary plaques detected by near-infrared spectroscopy at non-stented sites in the target artery identify patients likely to experience future major adverse cardiovascular events. *Eur Heart J.* (2016) 17:393–9. doi: 10.1093/ehjci/jev340
31. Danek BA, Karatasakis A, Karacsonyi J, Alame A, Resendes E, Kalsaria P, et al. Long-term follow-up after near-infrared spectroscopy coronary imaging: insights from the lipid core plaque association with clinical events registry. *Cardiovasc Revasc Med.* (2017) 18:177–81. doi: 10.1016/j.carrev.2016.12.006
32. Schuurman AS, Vroegindewey M, Kardys I, Oemrawsingh RM, Cheng JM, de Boer S, et al. Near-infrared spectroscopy-derived lipid core burden index predicts adverse cardiovascular outcome in patients with coronary artery disease during long-term follow-up. *Eur Heart J.* (2018) 39:295–302. doi: 10.1093/eurheartj/ehx247
33. Karlsson S, Anesäter E, Fransson K, Andell P, Persson J, Erlinge D. Intracoronary near-infrared spectroscopy and the risk of future cardiovascular events. *Open Heart.* (2019) 6:e000917. doi: 10.1136/openhrt-2018-000917
34. Waksman R, Di Mario C, Torguson R, Ali ZA, Singh V, Skinner WH. Identification of patients and plaques vulnerable to future coronary events with near-infrared spectroscopy intravascular ultrasound imaging: a prospective, cohort study. *Lancet.* (2019) 394:1629–37. doi: 10.1016/S0140-6736(19)31794-5
35. Gardner CM, Tan H, Hull EL, Lisauskas JB, Sum ST, Meese TM, et al. Detection of lipid core coronary plaques in autopsy specimens with a novel catheter-based near-infrared spectroscopy system. *JACC Cardiovasc Imaging.* (2008) 1:638–48. doi: 10.1016/j.jcmg.2008.06.001
36. Goldstein J, Maini B, Dixon S, Brilakis E, Grines C, Rizik D, et al. Detection of lipid-core plaques by intracoronary near-infrared spectroscopy identifies high risk of periprocedural myocardial infarction. *Cardiovasc Intervent.* (2011) 4:429–37. doi: 10.1161/CIRCINTERVENTIONS.111.963264
37. Stone GW, Maehara A, Muller JE, Rizik DG, Shunk KA, Ben-Yehuda O, et al. Plaque characterization to inform the prediction and prevention of periprocedural myocardial infarction during percutaneous coronary intervention: the CANARY Trial (Coronary Assessment by Near-infrared of Atherosclerotic Rupture-prone Yellow). *JACC Cardiovasc Interv.* (2015) 8:927–36. doi: 10.1016/j.jcin.2015.01.032
38. Yang HM, Yoon MH, Lim HS, Seo KW, Choi BJ, Choi SY, et al. Lipid-core plaque assessed by near-infrared spectroscopy and procedure related microvascular injury. *Korean Circ J.* (2019) 49:1010–8. doi: 10.4070/kcj.2019.0072
39. Yamamoto MH, Maehara A, Stone GW, Kini AS, Brilakis ES, Rizik DG, et al. 2-year outcomes after stenting lipid-rich and nonrich coronary plaques. *J Am Coll Cardiol.* (2020) 75:1371–82. doi: 10.1016/j.jacc.2020.01.044
40. Hanson ID, Goldstein JA, Dixon SR, Stone GW. Comparison of coronary artery lesion length by NIRS-IVUS versus angiography alone. *Coronary Artery Dis.* (2015) 26:484–9. doi: 10.1097/MCA.0000000000000263
41. Ino Y, Kubo T, Matsuo Y, Yamaguchi T, Shiono Y, Shimamura K, et al. Optical coherence tomography predictors of edge restenosis after everolimus-eluting stent implantation. *Circ Cardiovasc Interv.* (2016) 9:e004231. doi: 10.1161/CIRCINTERVENTIONS.116.004231
42. Madder RD, Goldstein JA, Madden SP, Puri R, Wolski K, Hendricks M, et al. Detection by near-infrared spectroscopy of large lipid core plaques at culprit sites in patients with acute ST-segment elevation myocardial infarction. *JACC Cardiovasc Interv.* (2013) 6:838–46. doi: 10.1016/j.jcin.2013.04.012
43. Erlinge D. Near-infrared spectroscopy for intracoronary detection of lipid-rich plaques to understand atherosclerotic plaque biology in man and guide clinical therapy. *J Intern Med.* (2015) 278:110–25. doi: 10.1111/joim.12381
44. Terada K, Kubo T, Matsuo Y, Ino Y, Shimamura K, Shiono Y, et al. TCT-9 quantitative assessment of lipid composition by NIRS-IVUS is helpful for differentiating among plaque rupture, plaque erosion, and calcified nodule in the culprit lesion of ACS. *J Am Coll Cardiol.* (2019) 74:B9. doi: 10.1016/j.jacc.2019.08.032
45. Bourantas CV, Jaffer FA, Gijsen FJ, van Soest G, Madden S, Courtney BK, et al. Hybrid intravascular imaging: recent advances, technical considerations, and current applications in the study of plaque pathophysiology. *Eur Heart J.* (2017) 38:400–12. doi: 10.1093/eurheartj/ehw097
46. Roleder T, Galougahi KK, Chin CY, Bhatti NK, Brilakis E, Nazif TM, et al. Utility of near-infrared spectroscopy for detection of thin-cap neoatherosclerosis. *Eur Heart J Cardiovasc Imaging.* (2017) 18:663–9. doi: 10.1093/ehjci/jew198
47. Ino Y, Kubo T, Kameyama T, Shimamura K, Terada K, Matsuo Y, et al. Clinical utility of combined optical coherence tomography and near-infrared spectroscopy for assessing the mechanism of very late stent thrombosis. *JACC Cardiovasc Imaging.* (2018) 11:772–5. doi: 10.1016/j.jcmg.2017.11.015
48. Madder RD, Khan M, Husaini M, Chi M, Dionne S, VanOosterhout S, et al. Combined near-infrared spectroscopy and intravascular ultrasound imaging of pre-existing coronary artery stents. *Circ Cardiovasc Imaging.* (2016) 9:e003576. doi: 10.1161/CIRCIMAGING.115.003576
49. Zanchin C, Christe L, Räber L. Correlation between *in vivo* near-infrared spectroscopy and optical coherence tomography detected lipid-rich plaques with post-mortem histology. *EuroIntervention.* (2019). doi: 10.4244/EIJ-D-19-00775
50. Madder RD. *Personal Communication 2019, OCT and NIRS Features of a Culprit Coronary Lesion*. Grand Rapids (2019).
51. Maehara A, Mintz GS, Weissman NJ. Advances in intravascular imaging. *Cardiovasc Intervent.* (2009) 2:482–90. doi: 10.1161/CIRCINTERVENTIONS.109.868398
52. Arbab-Zadeh A, Fuster V. From detecting the vulnerable plaque to managing the vulnerable patient: JACC state-of-the-art review. *J Am Coll Cardiol.* (2019) 74:1582–93. doi: 10.1016/j.jacc.2019.07.062
53. Bom MJ, van der Heijden DJ, Kedhi E, van der Heyden J, Meuwissen M, Knaapen P, et al. Early detection and treatment of the vulnerable coronary plaque: can we prevent acute coronary syndromes? *Circ Cardiovasc Imaging.* (2017) 10:e005973. doi: 10.1161/CIRCIMAGING.116.005973
54. Braunwald E. Epilogue: what do clinicians expect from imagers? *J. Am. Coll. Cardiol.* (2006) 47(Suppl. 8):C101–3. doi: 10.1016/j.jacc.2005.10.072

Conflict of Interest: JM is CMO of SpectraWAVE, Inc, which is building an OCT-NIRS coronary catheter. RM has received research support and speaker honoraria from Infraredx and serves on the advisory board of Spectra WAVE, Inc.

frontiers in Cardiovascular Medicine

REVIEW
published: 30 June 2020
doi: 10.3389/fcvm.2020.00107

Near-Infrared Spectroscopy Intravascular Ultrasound Imaging: State of the Art

Kayode O. Kuku[1,2,3†], *Manavotam Singh*[2,3†], *Yuichi Ozaki*[2,3], *Kazuhiro Dan*[2,3], *Chava Chezar-Azerrad*[2,3], *Ron Waksman*[1,2,3] *and Hector M. Garcia-Garcia*[1,2,3*]

[1] MedStar Cardiovascular Research Network, MedStar Washington Hospital Center, MedStar Health Research Institute, Washington, DC, United States, [2] Section of Interventional Cardiology MedStar Washington Hospital Center, MedStar Heart and Vascular Institute, Washington, DC, United States, [3] Georgetown University Department of Medicine, Washington, DC, United States

Acute coronary syndromes (ACS) secondary to coronary vessel plaques represent a major cause of cardiovascular morbidity and mortality worldwide. Advancements in imaging technology over the last 3 decades have continuously enabled the study of coronary plaques via invasive imaging methods like intravascular ultrasound (IVUS) and optical coherence tomography (OCT). The introduction of near-infrared spectroscopy (NIRS) as a modality that could detect the lipid (cholesterol) content of atherosclerotic plaques in the early nineties, opened the potential of studying "vulnerable" or rupture-prone, lipid-rich coronary plaques in ACS patients. Most recently, the ability of NIRS-IVUS to identify patients at risk of future adverse events was shown in a prospective multicenter trial, the Lipid-Rich-plaque Study. Intracoronary NIRS-IVUS imaging offers a unique method of coronary lipid-plaque characterization and could become a valuable clinical diagnostic and treatment monitoring tool.

Keywords: near-infrared spectroscopy (NIRS), lipid-rich plaque, plaque-characterization, intravascular imaging, intravascular ultrasound (IVUS), coronary artery disease, coronary plaque

OPEN ACCESS

Edited by:
Christos Bourantas, Barts Health NHS Trust, United Kingdom

Reviewed by:
Herbert Loellgen, Johannes Gutenberg University Mainz, Germany
Nieves Gonzalo, San Carlos University Clinical Hospital, Spain

***Correspondence:**
Hector M. Garcia-Garcia
Hector.M.GarciaGarcia@medstar.net; Hect2701@gmail.com

[†] *These authors have contributed equally to this work*

Specialty section:
This article was submitted to Cardiovascular Imaging, a section of the journal Frontiers in Cardiovascular Medicine

Received: *15 January 2020*
Accepted: *21 May 2020*
Published: *30 June 2020*

Citation:
Kuku KO, Singh M, Ozaki Y, Dan K, Chezar-Azerrad C, Waksman R and Garcia-Garcia HM (2020) Near-Infrared Spectroscopy Intravascular Ultrasound Imaging: State of the Art. Front. Cardiovasc. Med. 7:107. doi: 10.3389/fcvm.2020.00107

INTRODUCTION

Coronary artery disease (CAD) has continued to be a major cause of morbidity and mortality worldwide, despite recent advances in medical and interventional therapies (1). The pathogenesis of acute coronary events involves the development of an early core with the accumulation of lipid-rich free cholesterol which then progresses to the formation of a fibroatheroma (2). Coronary angiography has been a crucial tool for detecting the gross presence of disease of coronary lesions, it however underestimates the magnitude of atherosclerosis in non-culprit arteries particularly in the early stages of disease process and provides no information regarding the composition of the plaque responsible for the lesion. Intracoronary imaging including intravascular ultrasound (IVUS) and near infrared spectroscopy (NIRS) have been studied to determine the plaque burden (PB) and plaque composition, respectively.

Intravascular Ultrasound provides 2-dimensional cross-sections of arterial vessels which enables the visualization and characterization of not just lumen and stent struts, but the vessel wall dimensions and the presence of plaques within it. In spite of the usefulness of IVUS in the study of plaques and vessel remodeling, it remains limited in the visualization and quantification of certain plaque characteristics mainly due to the inherent properties of sound waves (3). NIRS imaging offers the ability to penetrate blood and tissue to detect lipid core containing coronary plaques. The technology is based on the property of different organic molecules to scatter and absorb light at

different intensities and wavelengths (4, 5). The integration of NIRS and IVUS systems has provided a hybrid imaging modality which combines the penetration and high resolution of IVUS with the lipid core quantification and characterization of NIRS which has been demonstrated to correlate with the lipid detection (6, 7).

We will review the present and potential clinical and research utility of NIRS-IVUS imaging in the study of coronary lipid plaques in the context of CAD.

NEAR INFRARED SPECTROSCOPY TECHNIQUE

Near-infrared diffuse reflectance spectroscopy is a technique that relies on the property of substances to absorb and scatter NIR light (wavelengths from 800 to 2,500 nm) at different intensities as a function of wavelengths (8–10). NIRS as a technique has been used in various science fields, including chemistry and pharmaceuticals, for the determination of the chemical composition of substances.

Prior to the development of NIRS, various spectroscopy techniques (nuclear magnetic resonance spectroscopy, Raman spectroscopy, and fluorescence spectroscopy) had been studied for possible intravascular applications toward the study of atherosclerotic plaques. The Raman near-infrared spectroscopy (NIRS) which was widely used several disciplines was based on the inelastic scattering of photons following collision with molecules and while it was suggested to have the potential to identify vulnerable plaques, was limited by signal-to-noise problems (11–14). The NIRS technology was first used in 1993 by Cassis and Lodder in animal experiments in which they sought the characterization of low-density lipoprotein cholesterol accumulation in the aortas of hypercholesterolaemic rabbits. This was followed by the *in-vivo* use of diffuse reflectance NIRS in imaging the lipid content in human carotid plaques exposed during surgery (15, 16)

Validation of NIRS

In the early days of NIRS, 2 pivotal studies were carried out to validate its accuracy for the detection of lipid core plaques (LCPs) in human vessels. The first study by Gardner et al. made use of 84 human heart specimens- 33 hearts were used to develop NIRS algorithms and produce predefined endpoints while the remaining 51 hearts were used for prospective validation of algorithm, in a double-blinded study design, to evaluate the accuracy of NIRS in detecting LCPs. In order to have a quantitative target for constructing the algorithm and validating the findings, an LCP of interest was defined as a "fibroatheroma" (FA) with a lipid core $>60^{\circ}$ in circumferential extent, $>200\,\mu m$ thickness, and with a fibrous cap of mean thickness $<450\,\mu m$." The primary analysis which was done by comparing NIRS information presented on block chemogram readings vs. the classified histologic findings showed a "receiver operating characteristic (ROC) area under the curve (AUC) of 0.80 (95 % CI: 0.76–0.85)," confirming the ability of the NIRS system to accurately identify the LCPs (4).

Secondly, the Spectroscopic Assessment of Coronary Lipid (SPECTACL) study which was the first catheter-based technique to use NIRS in humans for percutaneous application was performed to validate the applicability of the autopsy-based LCP detection algorithm in patients. The study, in addition to showing that the NIRS imaging catheter had a similar safety profile to that of IVUS, demonstrated that the spectra obtained from imaging the epicardial vessels of living patients were similar to those from previously validated spectra from autopsy specimens, thereby supporting the use of NIRS for detection of LCPs in human patients (9).

Earlier, several *ex-vivo* studies had examined the ability of NIRS to identify histological features of lipid-rich atherosclerotic plaques in human blood vessels obtained at autopsy. These studies reported >90% sensitivity and specificity for the identification of characteristic features suggesting lipid-rich plaques including the rupture-prone thin-cap fibroatheromas (TCFAs) seen in ACS patients. More recent studies have corroborated these findings as well as pointing to the additive value of NIRS to IVUS-derived PB in detecting vulnerable plaques (17–21).

Intra- and Inter-catheter reproducibility of the NIRS catheter has also been validated in a number of independent studies (22, 23).

Principles of Near Infrared Spectroscopy-Intravascular Ultrasound (NIRS-IVUS) Catheter

A little over a decade ago, a single modality NIRS system was originally developed for the invasive detection of lipid core plaques (LipiScan™, Infraredx Inc., Bedford, MA, USA). In later years, a dual modality system which combined IVUS with NIRS was developed to provide in a single catheter information on both vessel structure and plaque composition in a single acquisition. The NIRS-IVUS systems have continued to evolve and now exist in the form of a dual frequency, dual modality system. (TVC Imaging System™ and Makoto Intravascular Imaging System™, Infraredx Inc.) **Table 1**.

The NIRS-IVUS system comprises a scanning NIR laser, a pullback and rotation unit, and a traditional IVUS-sized catheter. The 3.2F rapid exchange catheter has an entry profile of 2.4F and a shaft profile of 3.6F and is compatible with 6F guiding catheters. The NIRS-IVUS can be inserted over a 0.014-inch guide wire while its passage through the lesion is facilitated by the hydrophilic coating present on the flexible distal 50 cm end. The IVUS images are acquired during an automated pullback with

Abbreviations: ACS, Acute Coronary Syndrome; IVUS, Intravascular ultrasound; OCT, Optical Coherence Tomography; NIRS, Near infrared spectroscopy; PB: Plaque Burden CAD, Coronary Artery Disease; PCI, Percutaneous Coronary Intervention; LCP, lipid core plaques; LRP, Lipid rich plaque; FA, Fibroatheroma; ROC, Receiver Operating Characteristic; AUC, Area Under the Curve: TVC, True Vessel Characterization; LCBI, Lipid core burden index; NC-MACE, Non culprit major cardiovascular events; MACE, Major adverse cardiac events; FDA, Food and Drug Administration; TCFA, thin-capped fibroatheromas; PAD, Peripheral arterial disease; MACCE, Major Adverse cardiovascular and cerebrovascular events; FFR, Fractional Flow Reserve; RF-IVUS, Radiofrequency IVUS; BVS, Bioresorbable vascular scaffold.

TABLE 1 | Evolution of NIRS/NIRS-IVUS imaging-based systems.

Trade name	Model number	Year introduced (US)	Features/ design specifications	Advantages/ improvements/revisions	Additional comments
LipiScan	NIRS-MC5	2008	NIRS (8,000 NIRS spectra/100 mm)	First FDA cleared NIRS imaging System with two-dimensional map of LCP	
LipiScan IVUS	TVC-MC7	2010	NIRS (8,000 NIRS spectra/100 mm); 40 MHz, Grayscale IVUS	First FDA cleared dual imaging system which combined co-registered, grayscale, 40 MHz IVUS with proprietary NIR LCP detection technology to identify LCPs, degree of stenosis, reference vessel diameter, and plaque burden	
TVC Imaging System	TVC-MC8	2012	NIRS (32,000 NIRS spectra/100 mm); 40 MHz, Grayscale IVUS	First multimodality imaging to combine IVUS and NIRS. Improved IVUS Image quality and resolution with hydrophilic coating on catheter and added manual IVUS imaging features.	1. Lower frequency increases depth-of-field while the higher frequency improves clarity. 2. Improved resolution enhancing visualization of vessel details
Advanced TVC Imaging System	TVC-MC8x	2014	NIRS (32,000 NIRS spectra/100 mm); 35–65 MHz, Grayscale IVUS	High definition "HD" IVUS Image Quality with dual-modality frequency (up to 65 MHz) capabilities. Dual-layer hydrophilic coating. 40-micron axial resolution	
TVC Imaging System	TVC-MC9	2015	NIRS (32,000 NIRS spectra/100 mm); 35–65 MHz, Grayscale IVUS	Enhanced user interface and IVUS image with 20-micron axial resolution. Extended bandwidth rotational IVUS catheter.	
Makoto Imaging System	TVC-MC10	2019	NIRS (1,300 NIRS spectra/mm); 35–65 MHz IVUS	User Interface Enhancements. Multiple (0.5, 1.0, 2.0 mm/s) Pullback Speeds. 0.0, 2.0, 10.0mm/s Manual IVUS tip movement speed	

NIRS, Near-Infrared spectroscopy; FDA, Food Drug and Administration; TVC, True Vessel Catheterization; LCP, Lipid Core Plaque; IVUS, Intravascular Ultrasound; MHz, Megahertz (IVUS Transducer frequency).

simultaneous co-registered NIRS measurements. In the latest generation, the Makoto system, the catheter's imaging core pulls back at speeds of 0.5, 1.0, or 2.0 mm/s and rotates at 1800 rpm with a maximum imaging length of 15 cm, acquiring up to ∼130,000 NIRS per 100 mm (4, 9, 24) (**Figure 1**).

NIRS lipid core data are automatically displayed on a "chemogram" which displays the probability of the presence of a lipid rich plaque with the millimeters of pull-back on the x-axis and the circumferential position on the y-axis. Areas containing lipid core are displayed as yellow and those without any significant lipid core as red. A quantitative image metric is automatically reported as a numerical lipid-core burden index (LCBI), which represents the fraction of the chemogram yellow pixels whose probability of lipid exceeds 0.6, per 1,000. The LCBI provides a quantitative metric of the lipid core plaque present in a scanned vessel and can be computed over the entire length of a vessel scan, segments of scans, or defined width windows within segments (such as the 4 mm sliding window with the maximum LCBI, maxLCBI4mm) (9) (**Figure 2**).

APPLICATIONS OF NIRS-IVUS

Lipid Rich Plaque Characterization

Prior autopsy studies have shown that lesions with a thin fibrous cap(<65 mn of cap thickness) overlying a large necrotic core are most frequently prone to rupture (4, 25, 26). These "vulnerable" plaques have therefore become a target for identification by novel intracoronary imaging modalities. Several studies in ACS patients have since shown the presence of LCPs in the culprit arterial segments to be major precursors of the disease and the possible association of the lipid core burden with adverse cardiovascular outcomes in CAD patients overtime (27–34) (**Table 2**).

The PROSPECT (Providing Regional Observations to Study Predictors of Events in the Coronary Tree) Trial, a landmark study which included 697 acute coronary syndrome (ACS) patients was a natural history study that sought to provide *in vivo* evidence of the hypothesis that the histopathological characteristic of plaques and not the degree of stenosis on angiography was responsible for the development of ACS. The study investigated the non-culprit coronary lesions in patients with ACS who underwent three-vessel gray scale and VH-IVUS imaging after successful PCI of culprit lesion demonstrated that "independent predictors of non-culprit-related events were the presence of VH-IVUS thin-cap fibroatheroma (hazard ratio 3.35; 95% confidence intervals 1.77–6.36), a PB ≥70% (hazard ratio 5.03; 95% confidence intervals 2.51–10.11), and a minimum lumen area ≤4.0 mm^2 (hazard ratio 3.21; 95% confidence intervals 1.61–6.42)" (44).

Following the results from the PROSPECT Study, The **COLOR** registry prospectively observed a positive association between plaque morphology evaluated by NIRS and the degree of coronary artery stenosis. It demonstrated that increasing degree of stenosis seen by angiography was associated with more vulnerable plaque morphology as assessed by

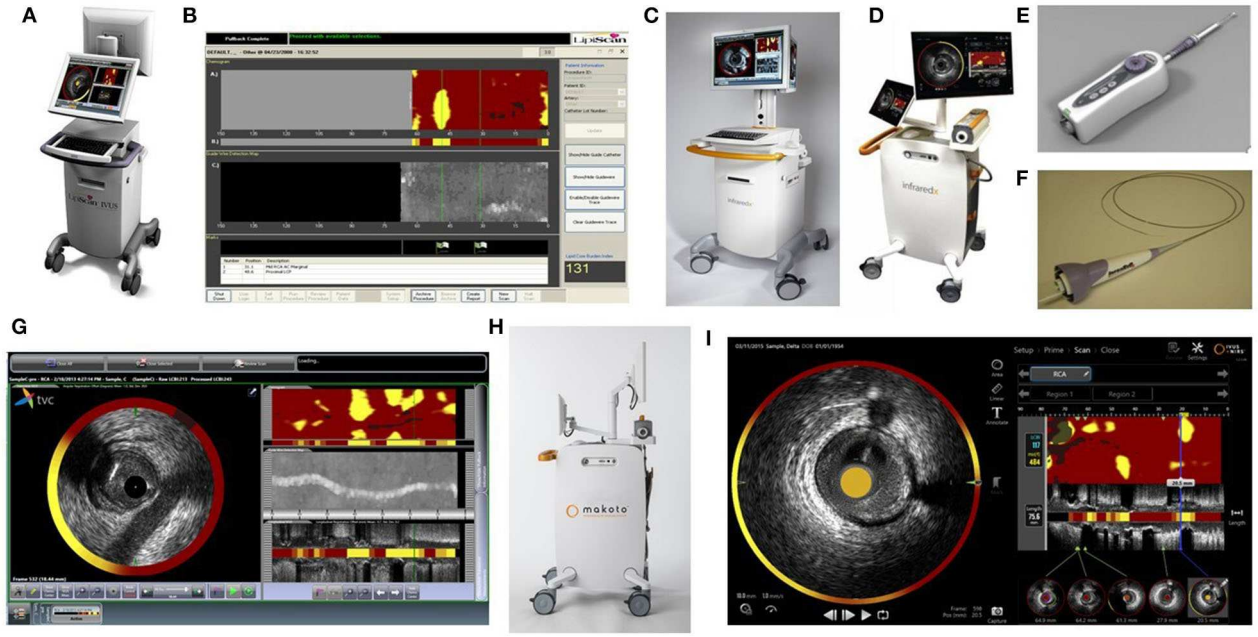

FIGURE 1 | NIRS Prototype figures **(A)** LipiScan-NIRS-MC5 **(B)** LipiScan-NIRS-MC5 Display **(C)** 2012 TVC Imaging System-MC8 **(D)** 2015 TVC Imaging System-MC9 **(E)** NIRS Pullback device **(F)** NIRS-IVUS catheter **(G)** 2012 TVC Display **(H)** Makoto Imaging System- MC10 **(I)** 2018 Makoto Display (All images in this Figure are licensed content by InfraRedX Inc. and shall not be reproduced).

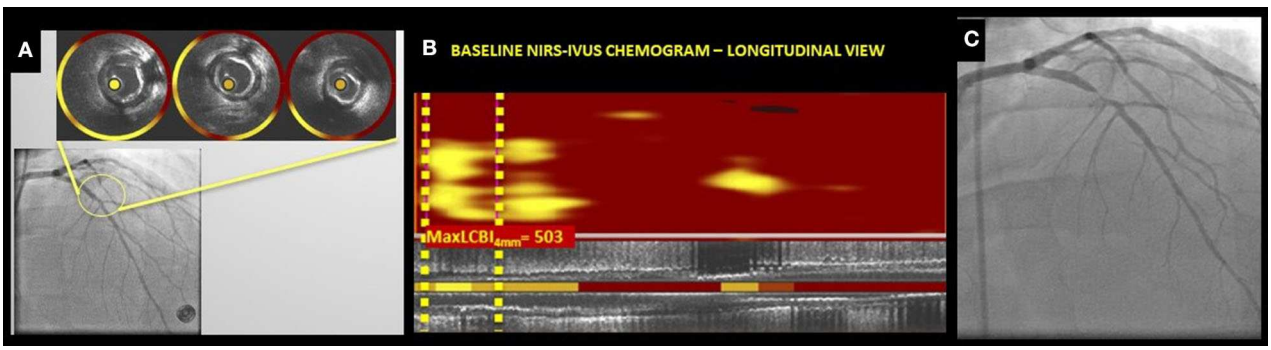

FIGURE 2 | (A–C) NIRS-IVUS chemograms in non-culprit lesions showing LCBI in non-stenotic angiographic segments; **(A)** Baseline Angiogram cine showing left anterior descending (LAD) segment with IVUS cross-sections and NIRS-IVUS rings indicating the presence of lipid plaque, **(B)** Baseline NIRS-IVUS chemogram (longitudinal view) showing the calculated maximum 4 mm LCBI (max4mmLCBI) in a 4 mm segment of the LAD segment shown in **(A)**. **(C)** Follow up angiogram of the same vessel segment showing a severely stenotic segment in the proximal LAD. (Courtesy of the MedStar Health Research Institute, MedStar Cardiovascular Research Network, Invasive Imaging Core Laboratory).

NIRS-IVUS system. Also, one of the first prospective human studies which evaluated high LCP by NIRS vs. cardiovascular events- The ATHEROREMO-NIRS (The European Collaborative Project on Inflammation and Vascular Wall Remodeling in Atherosclerosis—Near-Infrared Spectroscopy) trial, a sub-study of the ATHEROREMO-IVUS study of nearly 600 patients (to evaluate some of the limitations of VH IVUS identified after the PROSPECT and VIVA studies) produced promising results regarding the possibility of the technology. The relationship of LCBI value with the primary endpoint composite was found to be similar in both stable angina and ACS patients. In a more recent study, Matsumura et al. employed NIRS-IVUS in examining the features of coronary lesions with intraplaque hemorrhage (a key culprit in coronary lesion progression) in a histopathological validation study and demonstrated the presence of more FAs, greater IVUS PB and NIRS lipid core burden present in intraplaque hemorrhage segments compared to segments without intraplaque hemorrhage (35, 37, 45–47) **Table 2**.

In the most recent prospective multicenter natural history intracoronary imaging study—**The LRP (Lipid Rich Plaque)** identified patients and coronary segments at risk of future major

TABLE 2 | Overview of key studies evaluating the utility and efficacy of NIRS-IVUS imaging in CAD.

Study	Year	Study aim	Study design/	Sample size reported	Follow-Up duration	NIRS related endpoint	Key merits	Limitations	Main conclusion
The COLOR Trial (35)	2011	To determine whether intracoronary NIRS can identify plaques that are likely to cause periprocedural MI in patients undergoing elective PCI	Prospective observational	62		The rate of periprocedural MI in the groups with and without a large LCP in the treatment zone as assessed by NIRS and expressed as maxLCBI4 mm	1. Showed the relationship between the risk of periprocedural MI and NIRS-detected LCPs; 2. Included a comparison group of patients without large LCBI	1. Small sample size; 2. Selection bias due to the availability of post-PCI biomarkers	NIRS imaging provides a rapid and automated means of LCP identification can be used to identify large, stenotic, coronary LCPs, which in the study were found to be associated with a 50% risk of periprocedural MI when dilated during PCI
The YELLOW Trial (36)	2013	To evaluate the effect of short-term statin therapy on intracoronary plaque using FFR and NIRS-IVUS system in patients with multivessel CAD undergoing PCI and with at least 1 severely obstructive (FFR $\leq$ 0.8) non-culprit	Randomized Clinical Trial	87	7 weeks	Change in lipid-core burden index at the LCBI4 mm max segment	1. Evaluated the effect of therapeutics on NIRS-quantified lipid content; 2. NIRS imaging performed at baseline and follow-up; 3. Included correlation of physiology (FFR) against NIRS-derived LCBI; 4. Randomized study design	1. Small sample size; 2. Short follow-up duration; 3. IVUS and NIRS were performed using separate catheters 4. Differences in baseline LCBIs between the two study groups	Significant reduction in maxLCBI4mm in the intensive statin group vs the standard of care group
ATHEROREMO-NIRS Oemrawsingh et al. (37)	2014	To determine the long-term prognostic value of intracoronary NIRS as assessed in a non-culprit vessel in patients with CAD	Prospective observational	203	12 months	Composite of all-cause mortality, non-fatal ACS, stroke, and unplanned coronary revascularization exclusive of culprit lesion events	1. Clinical endpoints; 2. Results strongly suggested the prognostic value of NIRS imaging in non-stenotic, non-culprit segments	1. Small sample size; 2. A single non-culprit coronary artery was imaged per patient	"CAD patients with an LCBI equal to or above the median of 43.0, as assessed by NIRS in a non-culprit coronary artery, had a 4-fold risk of adverse cardiovascular events at 1-year follow-up These findings relate to the risk throughout the entire coronary tree and not necessarily at the imaged segment or a lesion-specific risk"

(Continued)

TABLE 2 | Continued

Study	Year	Study aim	Study design/	Sample size reported	Follow-Up duration	NIRS related endpoint	Key merits	Limitations	Main conclusion
The CANARY Trial (38)	2015	To determine whether pre-PCI plaque characterization using NIRS is capable of identifying lesions at risk of periprocedural myonecrosis	Prospective Randomized Pilot Trial	85		Incidence of periprocedural MI, defined as troponin or creatine kinase-myocardial band increase to 3 or more times the upper limit of normal within 72 h	1. Randomized design; 2. Correlation of NIRS measures vs. MI enzyme parameters; 3. Confirmed a relationship between NIRS-identified LRPs and periprocedural myonecrosis	1. Small study size; 2. Not all clinically relevant MIs.	Pre-interventional intravascular imaging with a combined NIRS-IVUS catheter is able to identify lesions at increased risk of periprocedural myonecrosis after stent implantation Furthermore, the use of a distal embolization protection filter did not prevent myonecrosis after PCI of lipid-rich plaques in this study
IBIS-3 (39, 40)	2016	To evaluate the effect of high intensity statin therapy on compositional coronary plaque changes using RF-IVUS and NIRS in non-culprit segments	Prospective observational	103	6 months-12 months	The effect of high intensity-rosuvastatin on LCP within non-stenotic NCLs	1. Evaluated the effect of lipid lowering therapeutics on NIRS-quantified LCBI in non-stenotic segments; 2. Included study of the stability of the plaque necrotic core; 3. NIRS imaging at baseline and follow-up	1. Lack of a randomized design (no comparison group); 2. Events incidence not sufficient to assess MACE	High dose rosuvastatin therapy resulted in non-significant change in Necrotic Core (NC) and a neutral effect was observed in LCBI
The YELLOW II Trial (41)	2017	Assess changes in plaque morphology using intravascular imaging, and evaluate cholesterol eflux capacity in stable multivessel CAD patients receiving high-dose statin therapy	Prospective observational	85	8–12 weeks	To examine lipid content changes in obstructive NCLs, measured by NIRS, and plaque morphology, assessed by OCT; and compare changes in lipid content and plaque morphology with changes in LDL, HDL, apo A-I, and macrophage functionality	1. Study design included genetic, clinical and plaque parameters 2. Multimodality imaging-Included OCT imaging in assessing plaque	1. Lack of a randomized design/ comparison group 2. Short follow-up duration	There was no significant change observed in plaque lipid content quantified using NIRS. But a significant increase in FCT of obstructive NCLs and enhancement of CEC in patients with stable coronary artery disease
LRP Study (42, 43)	2019	To establish the relationship between LRPs detected by NIRS-IVUS at the non-culprit sites and subsequent coronary events from new culprit lesions	Prospective cohort	1,271	24 months	Non-Index Culprit Lesion related Major Adverse Cardiac Events (NC-MACE) in patients and plaque in association with maxLCBI4 mm	1. Large multicenter study design with clinical endpoints; 2. Included plaque and patient level endpoints; 3. Largest intracoronary imaging study to identify patients and vessel segments at risk of future clinical events	1. Follow-up duration not extending beyond 2 years; 2. Only a few patients had all 3 major vessels scanned (average of 2.1 vessels scanned/patient)	Coronary segments at higher risk of subsequent NC-MACE were associated with higher analyzable $maxLCBI_{4mm} > 400$

adverse coronary events using NIRS-IVUS system. Patients with known or suspected CAD undergoing cardiac catherization with possible PCI were examined via NIRS-IVUS imaging in non-culprit arteries when possible. The study showed that 9% of the patients had subsequent non-culprit-major adverse cardiac events (NC-MACE) and out of these patients, higher event rate was associated with analyzable $maxLCBI_{4mm} > 400$ (HR 3.39; 95% confidence interval 1.85–6.20), pointing to the diagnostic value of the NIRS-IVUS (42, 43). Following these results, the FDA granted a label claim for NIRS detection and identification of patients at increased risk of major adverse cardiac events (MACE) **Table 2.**

Clinical Applications of Intracoronary Near-Infrared Spectroscopy

In general, the early evidence from NIRS-IVUS use points to multiple potential clinical applications of this imaging system. The identification and localization of vulnerable atherosclerotic plaques offers a clinical tool that could help assess precise lesion lengths including segments with a high lipid core burden toward optimal stenting (48). Secondly, NIRS-IVUS offers information on the necrotic core of atherosclerotic plaques and can predict the embolization of highly thrombogenic lipid depositions. The release of these elements into the blood stream which results in distal embolization is a known culprit in peri-procedural myonecrosis (35, 38, 49–51). Similarly, the utility of NIRS-IVUS in optimizing carotid artery stenting toward preventing periprocedural stroke is a subject of ongoing research (52, 53).

Furthermore, NIRS-IVUS has been employed in the study of plaque morphology and composition in the peripheral arteries-superficial femoral arteries in the setting of severe stenoses and symptomatic peripheral artery disease (PAD) (54, 55).

Several other studies (37, 43, 56, 57) which show the association of either max4mmLCBI or high LCBI (in the case of Danek et al. and Oemrawsingh et al.) in non-target/non-culprit vessel segment with increased incidence of MACCE and the risk of future coronary events subsequent to the presence of vulnerable plaques in non-culprit segments has given credence to retrospective autopsy studies regarding the assessment of plaque vulnerability. The ability of NIRS-IVUS to assess the possibility of future coronary events based on the LCBI values in non-culprit segments offers a unique diagnostic utility and a risk-stratification tool. The predictive role of NIRS-IVUS shown in these studies is being further studied in ongoing studies and raises the question of the need for treating non-culprit vulnerable plaques in vulnerable patients.

With the evolution of pharmacological therapies in addition to the performance of the present lipid-lowering therapies, NIRS-IVUS offers a tool for monitoring the effects of medications such as statins and PCSK9-inhibitors on the coronary vasculature lipid burden. Already, studies have investigated the effect of lipid-lowering medications on reducing necrotic-core containing plaques. The YELLOW (Reduction in Yellow Plaque by Aggressive Lipid-Lowering therapy) trial was a randomized clinical trial (rosuvastatin 40 mg daily vs. the standard-of-care lipid-lowering therapy) which recruited patients with multi-vessel CAD (including at least 1 severely obstructive [FFR≤0.8] non-culprit) undergoing revascularization by PCI. The non-target lesions in both groups were evaluated at baseline and following 7 weeks of therapy with fractional flow reserve (FFR), and NIRS-IVUS, comparison between baseline and follow up results for NTLs demonstrated that reduction in LCBI4mm max was significantly higher in intensive statin group as compared to standard group (36) In a follow up study -the YELLOW II, the effects of high-dose statin therapy on changes in plaque morphology (evaluated by OCT) and plaque lipid content by NIRS were assessed in obstructive non-culprit lesions (NCLs) in addition to a comprehensive assessment of cholesterol efflux capacity (CEC) and peripheral blood mononuclear cell (PBMC) transcriptomics. The mean baseline NIRS-derived maxLCBI4mm was over 400 (416.6 ± 172.9) and the study reported no significant change in plaque lipid content by NIRS albeit a significant change in fibrous cap thickness after about 12 weeks of statin therapy. (41). Almost similarly, the IBIS-3 (Integrated Biomarker and Imaging Study 3) trial demonstrated that "high dose rosuvastatin therapy had a neutral effect on LCP (assessed by NIRS LCBI) in non-stenotic NCLs in the coronary vessels after 6- and 12-month follow-up intervals despite a relatively lower mean baseline maxLCBI4mm (201.9 ± 1623.8), in the cohort of 103 patients"(39, 40). While differences in LCBI cut-offs of the various studies could be a possible reason for the discrepancy in findings, the mean baseline maxLCBI4mm in the YELLOW I and YELLOW II trials were similar, even though the baseline LCBI was significantly higher in patients randomly allocated to the intensive vs. standard therapy group in the YELLOW I and there was no comparative standard therapy group in the YELLOW II. There is also the question of short term LRP/LCBI regression occurring mostly in plaques with a large PB and large LRPs reported in a YELLOW trial sub-study evaluating the relationship between LRPs, plaque morphology and lesion progression or regression. These findings point to the need for further exploration of the effect of statins as well as novel lipid-lowering therapies on NIRS-derived LCPs and LCBI in conjunction with plaque morphology analysis via other intracoronary modalities (58).

FUTURE DIRECTIONS

The findings of Waksman et al. in the recent LRP study (43) strongly suggest the viability of NIRS-IVUS as a diagnostic and risk-stratifying modality and opens the door to further trials to evaluate therapeutic strategies against high lipid core burden and/or vulnerable plaques/patients in addition to studies which could explore the value of LCBI as a surrogate marker for the checking the effectiveness of new therapeutic interventions.

Notably, the effects of newer LDL-lowering medications are currently being studied in ongoing trials. The PACMAN AMI (Vascular Effects of Alirocumab in Acute MI-Patients) trial (ClinicalTrials.gov Identifier: NCT03067844) is examining the effects of PCSK9-inhibiting monoclonal antibody, alirocumab on coronary atherosclerosis in acute MI patients via NIRS, IVUS and OCT. Also, the FITTER (Functional Improvement of Coronary

Artery Narrowing by Cholesterol Reduction With a PCSK9 Antibody) Trial (ClinicalTrials.gov Identifier: NCT04141579), will be enrolling patients to investigate the impact of evolocumab plus statins on FFR of non-infarct related arteries (non-IRAs) in multivessel disease patients and correlating baseline NIRS-derived lipid core burden with changes in FFR in the non-IRAs.

In a study design which integrates a natural history study and a randomized trial, the PROSPECT II and PROSPECT ABSORB, ClinicalTrials.gov Identifier: NCT02171065), patients with high risk plaque were randomized to receive Absorb BVS alongside the standard of care, optimal medical therapy (OMT) or vs. OMT alone and changes in the plaque will be evaluated by IVUS and NIRS at follow up. Lastly, The Preventive Coronary Intervention on Stenosis With Functionally Insignificant Vulnerable Plaque (PREVENT) study, is presently recruiting patients to determine the effect of preventive PCI on functionally insignificant coronary lesions with vulnerable plaque characteristics using NIRS, IVUS, OCT and virtual histology-IVUS modalities (ClinicalTrials.gov Identifier: NCT02316886).

While the value of NIRS-IVUS and other intracoronary imaging techniques are being shown in various imaging trials, there are still limitations in assessing plaque characteristics which could explain some of the conflicting study results. Multimodality imaging may be critical in overcoming these limitations, thus emphasizing the need for co-registration of NIRS-IVUS with other imaging including angiography and as well as OCT or in the form of hybrid imaging catheters (59). Finally, the ability of NIRS-IVUS to predict the location of histologically-confirmed TCFA and the possibility of NIRS-guided cap thickness detection, and collagen content analysis which are already being explored in *ex-vivo* studies could represent a huge breakthrough in vulnerable plaque studies in the near future.

LIMITATIONS

One of the main limitations of NIRS-IVUS is the invasiveness of the technique which precludes its use in primary prevention in symptomatic patients with subclinical disease. Presently, NIRS imaging does not have the capability to detect the depth of the lipid core or vulnerable plaque features such as the thinness of the fibrous cap.

CONCLUSION

NIRS in conjunction with IVUS is certainly a diagnostically useful tool for the detection of vulnerable plaques and can help identify patients at risk of future coronary events. While there is a wide spectrum of clinical applications for this technology, its viability for demonstrating the effects of present and forthcoming lipid-lowering therapies could significantly influence clinical perspectives and practice in the years to come.

AUTHOR CONTRIBUTIONS

All authors made a substantial contributions to the conception or design of this review paper, including the drafting and revisions. All authors have granted their approval for all aspects the manuscript and its submission.

REFERENCES

1. Benjamin EJ, Muntner P, Alonso A, Bittencourt MS, Callaway CW, Carson AP, et al. Heart disease and stroke statistics-2019 update: a report from the American Heart Association. *Circulation*. (2019) 139:e56–528. doi: 10.1161/CIR.0000000000000659
2. Guyton JR, Klemp KF. Development of the lipid-rich core in human atherosclerosis. *Arterioscler Thromb Vasc Biol*. (1996) 16:4–11. doi: 10.1161/01.ATV.16.1.4
3. Garcia-Garcia HM, Costa MA, Serruys PW. Imaging of coronary atherosclerosis: intravascular ultrasound. *Eur Heart J*. (2010) 31:2456–69. doi: 10.1093/eurheartj/ehq280
4. Gardner CM, Tan H, Hull EL, Lisauskas JB, Sum ST, Meese TM, et al. Detection of lipid core coronary plaques in autopsy specimens with a novel catheter-based near-infrared spectroscopy system. *JACC Cardiovasc Imaging*. (2008) 1:638–48. doi: 10.1016/j.jcmg.2008.06.001
5. Friebel M, Helfmann J, Netz U, Meinke M. Influence of oxygen saturation on the optical scattering properties of human red blood cells in the spectral range 250 to 2,000 nm. *J Biomed Opt*. (2009) 14:034001. doi: 10.1117/1.3127200
6. Roleder T, Wojakowski W. Intravascular ultrasound, optical coherence tomography and near infrared spectroscopy. *Cor et Vasa*. (2015) 57:e439–45. doi: 10.1016/j.crvasa.2015.10.004
7. Yonetsu T, Suh W, Abtahian F, Kato K, Vergallo R, Kim SJ, et al. Comparison of near-infrared spectroscopy and optical coherence tomography for detection of lipid. *Catheter Cardiovasc Interv*. (2014) 84:710–7. doi: 10.1002/ccd.25084
8. Cao Q, Zhegalova NG, Wang ST, Akers WJ, Berezin MY. Multispectral imaging in the extended near-infrared window based on endogenous chromophores. *J Biomed Opt*. (2013) 18:101318. doi: 10.1117/1.JBO.18.10.101318
9. Waxman S, Dixon SR, L'Allier P, Moses JW, Petersen JL, Cutlip D, et al. *In vivo* validation of a catheter-based near-infrared spectroscopy system for detection of lipid core coronary plaques: initial results of the SPECTACL study. *JACC Cardiovasc Imaging*. (2009) 2:858–68. doi: 10.1016/j.jcmg.2009.05.001
10. Caplan JD, Waxman S, Nesto RW, Muller JE. Near-infrared spectroscopy for the detection of vulnerable coronary artery plaques. *J Am Coll Cardiol*. (2006) 47:C92–6. doi: 10.1016/j.jacc.2005.12.045
11. Schaeberle MD, Kalasinsky VF, Luke JL, Lewis EN, Levin IW, Treado PJ. Raman chemical imaging: histopathology of inclusions in human breast tissue. *Anal Chem*. (1996) 68:1829–33. doi: 10.1021/ac951245a
12. Zhang Y, Hong H, Cai W. Imaging with raman spectroscopy. *Curr Pharm Biotechnol*. (2010) 11:654–61. doi: 10.2174/138920110792246483
13. Butler HJ, Ashton L, Bird B, Cinque G, Curtis K, Dorney J, et al. Using raman spectroscopy to characterize biological materials. *Nat Protoc*. (2016) 11:664–87. doi: 10.1038/nprot.2016.036
14. Moreno PR, Muller JE. Identification of high-risk atherosclerotic plaques: a survey of spectroscopic methods. *Curr Opin Cardiol*. (2002) 17:638–47. doi: 10.1097/00001573-200211000-00010
15. Cassis LA, Lodder RA. Near-IR imaging of atheromas in living arterial tissue. *Anal Chem*. (1993) 65:1247–56. doi: 10.1021/ac00057a023
16. Dempsey RJ, Davis DG, Buice RG, Lodder RA. Biological and medical applications of near-infrared spectrometry. *Appl Spectr*. (1996) 50:18A–34A. doi: 10.1366/0003702963906537
17. Moreno PR, Lodder RA, Purushothaman KR, Charash WE, O'Connor WN, Muller JE. Detection of lipid pool, thin fibrous cap, and inflammatory cells in human aortic atherosclerotic plaques by near-infrared spectroscopy. *Circulation*. (2002) 105:923–7. doi: 10.1161/hc0802.104291

18. Muller JE, Abela GS, Nesto RW, Tofler GH. Triggers, acute risk factors and vulnerable plaques: the lexicon of a new frontier. *J Am Coll Cardiol*. (1994) 23:809–13. doi: 10.1016/0735-1097(94)90772-2
19. Jaross W, Neumeister V, Lattke P, Schuh D. Determination of cholesterol in atherosclerotic plaques using near infrared diffuse reflection spectroscopy. *Atherosclerosis*. (1999) 147:327–37. doi: 10.1016/S0021-9150(99)00203-8
20. Puri R, Madder RD, Madden SP, Sum ST, Wolski K, Muller JE, et al. Near-infrared spectroscopy enhances intravascular ultrasound assessment of vulnerable coronary plaque: a combined pathological and *in vivo* study. *Arterioscler Thromb Vasc Biol*. (2015) 35:2423–31. doi: 10.1161/ATVBAHA.115.306118
21. Inaba S, Mintz GS, Burke AP, Stone GW, Virmani R, Matsumura M, et al. Intravascular ultrasound and near-infrared spectroscopic characterization of thin-cap fibroatheroma. *Am J Cardiol*. (2017) 119:372–8. doi: 10.1016/j.amjcard.2016.10.031
22. Abdel-Karim ARR, Rangan BV, Banerjee S, Brilakis ES. Intercatheter reproducibility of near-infrared spectroscopy for the *in vivo* detection of coronary lipid core plaques. *Catheter Cardiovasc Interv*. (2011) 77:657–61. doi: 10.1002/ccd.22763
23. Garcia BA, Wood F, Cipher D, Banerjee S, Brilakis ES. Reproducibility of near-infrared spectroscopy for the detection of lipid core coronary plaques and observed changes after coronary stent implantation. *Catheter Cardiovasc Interv*. (2010) 76:359–65. doi: 10.1002/ccd.22500
24. Schultz CJ, Serruys PW, van der Ent M, Ligthart J, Mastik F, Garg S, et al. First-in-man clinical use of combined near-infrared spectroscopy and intravascular ultrasound: a potential key to predict distal embolization and no-reflow? *J Am Coll Cardiol*. (2010) 56:314. doi: 10.1016/j.jacc.2009.10.090
25. Meese TM, Lisauskas JB, Doucet C, Clark N, Gardner CM, Hull EL, et al. Spectroscopic identification of lipid-rich plaques causing intermediate stenosis: a study in coronary autopsy specimens. *Cardiovasc Revasc Med*. (2008) 9:108. doi: 10.1016/j.carrev.2008.02.026
26. Grainger SJ, Su JL, Greiner CA, Saybolt MD, Wilensky RL, Raichlen JS, et al. Ability of combined Near-Infrared Spectroscopy-Intravascular Ultrasound (NIRS-IVUS) imaging to detect lipid core plaques and estimate cap thickness in human autopsy coronary arteries. In: *Photons Plus Ultrasound: Imaging and Sensing*. San Francisco, CA: International Society for Optics and Photonics (2016). 97084V. doi: 10.1117/12.2209664
27. Narula J, Nakano M, Virmani R, Kolodgie FD, Petersen R, Newcomb R, et al. Histopathologic characteristics of atherosclerotic coronary disease and implications of the findings for the invasive and noninvasive detection of vulnerable plaques. *J Am Coll Cardiol*. (2013) 61:1041–51. doi: 10.1016/j.jacc.2012.10.054
28. Madder RD, Smith JL, Dixon SR, Goldstein JA. Composition of target lesions by near-infrared spectroscopy in patients with acute coronary syndrome versus stable angina. *Circ Cardiovasc Interv*. (2012) 5:55–61. doi: 10.1161/CIRCINTERVENTIONS.111.963934
29. Madder RD, Goldstein JA, Madden SP, Puri R, Wolski K, Hendricks M, et al. Detection by near-infrared spectroscopy of large lipid core plaques at culprit sites in patients with acute ST-segment elevation myocardial infarction. *JACC Cardiovasc Interv*. (2013) 6:838–46. doi: 10.1016/j.jcin.2013.04.012
30. Patel D, Hamamdzic D, Llano R, Patel D, Cheng L, Fenning RS, et al. Subsequent development of fibroatheromas with inflamed fibrous caps can be predicted by intracoronary near infrared spectroscopy. *Arterioscler Thromb Vasc Biol*. (2013) 33:347–53. doi: 10.1161/ATVBAHA.112.300710
31. Schuurman AS, Vroegindewey M, Kardys I, Oemrawsingh RM, Cheng JM, de Boer S, et al. Near-infrared spectroscopy-derived lipid core burden index predicts adverse cardiovascular outcome in patients with coronary artery disease during long-term follow-up. *Eur Heart J*. (2018) 39:295–302. doi: 10.1093/eurheartj/ehx247
32. Kolodgie FD, Burke AP, Farb A, Gold HK, Yuan J, Narula J, et al. The thin-cap fibroatheroma: a type of vulnerable plaque: the major precursor lesion to acute coronary syndromes. *Curr Opin Cardiol*. (2001) 16:285–92. doi: 10.1097/00001573-200109000-00006
33. Falk E, Shah PK, Fuster V. Coronary plaque disruption. *Circulation*. (1995) 92:657–71. doi: 10.1161/01.CIR.92.3.657
34. Karlsson S, Anesäter E, Fransson K, Andell P, Persson J, Erlinge D. Intracoronary near-infrared spectroscopy and the risk of future cardiovascular events. *Open Heart*. (2019) 6:e000917. doi: 10.1136/openhrt-2018-000917
35. Goldstein JA, Maini B, Dixon SR, Brilakis ES, Grines CL, Rizik DG, et al. Detection of lipid-core plaques by intracoronary near-infrared spectroscopy identifies high risk of periprocedural myocardial infarction. *Circ Cardiovasc Interv*. (2011) 4:429–37. doi: 10.1161/CIRCINTERVENTIONS.111.963264
36. Kini AS, Baber U, Kovacic JC, Limaye A, Ali ZA, Sweeny J, et al. Changes in plaque lipid content after short-term intensive versus standard statin therapy: the YELLOW trial (reduction in yellow plaque by aggressive lipid-lowering therapy). *J Am Coll Cardiol*. (2013) 62:21–9. doi: 10.1016/j.jacc.2013.03.058
37. Oemrawsingh RM, Cheng JM, García-García HM, van Geuns RJ, de Boer SPM, Simsek C, et al. Near-infrared spectroscopy predicts cardiovascular outcome in patients with coronary artery disease. *J Am Coll Cardiol*. (2014) 64:2510–8. doi: 10.1016/j.jacc.2014.07.998
38. Stone GW, Maehara A, Muller JE, Rizik DG, Shunk KA, Ben-Yehuda O, et al. Plaque characterization to inform the prediction and prevention of periprocedural myocardial infarction during percutaneous coronary intervention: the CANARY trial (coronary assessment by near-infrared of atherosclerotic rupture-prone yellow). *JACC Cardiovasc Interv*. (2015) 8:927–36. doi: 10.1016/j.jcin.2015.01.032
39. Simsek C, Garcia-Garcia HM, van Geuns RJ, Magro M, Girasis C, van Mieghem N, et al. The ability of high dose rosuvastatin to improve plaque composition in non-intervened coronary arteries: rationale and design of the integrated biomarker and imaging study-3 (IBIS-3). *EuroIntervention*. (2012) 8:235–41. doi: 10.4244/EIJV8I2A37
40. Oemrawsingh RM, Garcia-Garcia HM, van Geuns RJM, Lenzen MJ, Simsek C, de Boer SPM, et al. Integrated biomarker and imaging study 3 (IBIS-3) to assess the ability of rosuvastatin to decrease necrotic core in coronary arteries. *EuroIntervention*. (2016) 12:734–9. doi: 10.4244/EIJV12I6A118
41. Kini AS, Vengrenyuk Y, Shameer K, Maehara A, Purushothaman M, Yoshimura T, et al. Intracoronary imaging, cholesterol efflux, and transcriptomes after intensive statin treatment: the YELLOW II study. *J Am Coll Cardiol*. (2017) 69:628–40. doi: 10.1016/j.jacc.2016.10.029
42. Waksman R, Torguson R, Spad MA, Garcia-Garcia H, Ware J, Wang R, et al. The lipid-rich plaque study of vulnerable plaques and vulnerable patients: study design and rationale. *Am Heart J*. (2017) 192:98–104. doi: 10.1016/j.ahj.2017.02.010
43. Waksman R, Mario CD, Torguson R, Ali ZA, Singh V, Skinner WH, et al. Identification of patients and plaques vulnerable to future coronary events with near-infrared spectroscopy intravascular ultrasound imaging: a prospective, cohort study. *Lancet*. (2019) 394:1629–37. doi: 10.1016/S0140-6736(19)31794-5
44. Stone GW, Maehara A, Lansky AJ, de Bruyne B, Cristea E, Mintz GS, et al. A prospective natural-history study of coronary atherosclerosis. *N Engl J Med*. (2011) 364:226–35. doi: 10.1056/NEJMoa1002358
45. de Boer S, Baran Y, Garcia-Garcia HM, Eskin I, Lenzen MJ, Kleber ME, et al. The european collaborative project on inflammation and vascular wall remodeling in atherosclerosis - intravascular ultrasound (ATHEROREMO-IVUS) study. *EuroIntervention*. (2018) 14:194–203. doi: 10.4244/EIJ-D-17-00180
46. Calvert PA, Obaid DR, O'Sullivan M, Shapiro LM, McNab D, Densem CG, et al. Association between IVUS findings and adverse outcomes in patients with coronary artery disease: the VIVA (VH-IVUS in Vulnerable Atherosclerosis) Study. *JACC Cardiovasc Imaging*. (2011) 4:894–901. doi: 10.1016/j.jcmg.2011.05.005
47. Matsumura M, Mintz GS, Kang SJ, Sum ST, Madden SP, Burke AP, et al. Intravascular ultrasound and near-infrared spectroscopic features of coronary lesions with intraplaque haemorrhage. *Eur Heart J Cardiovasc Imaging*. (2017) 18:1222–8. doi: 10.1093/ehjci/jew217
48. Dixon SR, Grines CL, Munir A, Madder RD, Safian RD, Hanzel GS, et al. Analysis of target lesion length before coronary artery stenting using angiography and near-infrared spectroscopy versus angiography alone. *Am J Cardiol*. (2012) 109:60–6. doi: 10.1016/j.amjcard.2011.07.068

49. Goldstein JA, Grines C, Fischell T, Virmani R, Rizik D, Muller J, et al. Coronary embolization following balloon dilation of lipid-core plaques. *JACC Cardiovasc Imaging*. (2009) 2:1420–4. doi: 10.1016/j.jcmg.2009.10.003
50. Raghunathan D, Abdel-Karim ARR, Papayannis AC, daSilva M, Jeroudi OM, Rangan BV, et al. Relation between the presence and extent of coronary lipid core plaques detected by near-infrared spectroscopy with postpercutaneous coronary intervention myocardial infarction. *Am J Cardiol*. (2011) 107:1613–8. doi: 10.1016/j.amjcard.2011.01.044
51. Saeed B, Banerjee S, Brilakis ES. Slow flow after stenting of a coronary lesion with a large lipid core plaque detected by near-infrared spectroscopy. *EuroIntervention*. (2010) 6:545. doi: 10.4244/EIJ30V6I4A90
52. Štěchovský C, Hájek P, Horváth M, Špaček M, Veselka J. Near-infrared spectroscopy combined with intravascular ultrasound in carotid arteries. *Int J Cardiovasc Imaging*. (2016) 32:181–8. doi: 10.1007/s10554-015-0687-x
53. Horváth M, Hájek P, Štěchovský C, Honěk J, Veselka J. Intravascular near-infrared spectroscopy: a possible tool for optimizing the management of carotid artery disease. *Int J Angiol*. (2015) 24:198–204. doi: 10.1055/s-0035-1558644
54. Abbas AE, Zacharias SK, Goldstein JA, Hanson ID, Safian RD. Invasive characterization of atherosclerotic plaque in patients with peripheral arterial disease using near-infrared spectroscopy intravascular ultrasound. *Catheter Cardiovasc Interv*. (2017) 90:461–70. doi: 10.1002/ccd.27023
55. Zacharias SK, Safian RD, Madder RD, Hanson ID, Pica MC, Smith JL, et al. Invasive evaluation of plaque morphology of symptomatic superficial femoral artery stenoses using combined near-infrared spectroscopy and intravascular ultrasound. *Vasc Med*. (2016) 21:337–44. doi: 10.1177/1358863X16631420
56. Danek BA, Karatasakis A, Karacsonyi J, Alame A, Resendes E, Kalsaria P, et al. Long-term follow-up after near-infrared spectroscopy coronary imaging: insights from the lipid cORe plaque association with clinical events (ORACLE-NIRS) registry. *Cardiovasc Revasc Med*. (2017) 18:177–81. doi: 10.1016/j.carrev.2016.12.006
57. Madder RD, Husaini M, Davis AT, VanOosterhout S, Khan M, Wohns D, et al. Large lipid-rich coronary plaques detected by near-infrared spectroscopy at non-stented sites in the target artery identify patients likely to experience future major adverse cardiovascular events. *Eur Heart J Cardiovasc Imaging*. (2016) 17:393–9. doi: 10.1093/ehjci/jev340
58. Dohi T, Maehara A, Moreno PR, Baber U, Kovacic JC, Limaye AM, et al. The relationship among extent of lipid-rich plaque, lesion characteristics, and plaque progression/regression in patients with coronary artery disease: a serial near-infrared spectroscopy and intravascular ultrasound study. *Eur Heart J Cardiovasc Imaging*. (2015) 16:81–7. doi: 10.1093/ehjci/jeu169
59. Fard AM, Vacas-Jacques P, Hamidi E, Wang H, Carruth RW, Gardecki JA, et al. Optical coherence tomography–near infrared spectroscopy system and catheter for intravascular imaging. *Opt Express*. (2013) 21:30849–58. doi: 10.1364/OE.21.030849

Conflict of Interest: RW has served on advisory boards for Amgen, Boston Scientific, Cardioset, Cardiovascular Systems, Medtronic, Philips Volcano, and Pi-Cardia; has served as a consultant for Amgen, Biosensors, Biotronik, Boston Scientific, Cardioset, Cardiovascular Systems, Medtronic, Philips Volcano, and Pi-Cardia; and has received grant support from AstraZeneca, Biotronik, Boston Scientific, and Chiesi; and has participated at a speakers bureau for AstraZeneca and Chiesi; is an investor in MedAlliance.

The remaining authors declare that the research was conducted in the absence of any commercial or financial relationships that could be construed as a potential conflict of interest.

frontiers in Cardiovascular Medicine

ORIGINAL RESEARCH
published: 21 July 2020
doi: 10.3389/fcvm.2020.00122

Investigating Origins of FLIm Contrast in Atherosclerotic Lesions Using Combined FLIm-Raman Spectroscopy

Julien Bec[1,2,3]*, *Tanveer Ahmed Shaik*[3], *Christoph Krafft*[3], *Thomas W. Bocklitz*[2,3], *Alba Alfonso-Garcia*[1], *Kenneth B. Margulies*[4], *Jürgen Popp*[2,3] *and Laura Marcu*[1]

[1] *Department of Biomedical Engineering, University of California, Davis, Davis, CA, United States,* [2] *Institute of Physical Chemistry and Abbe Center of Photonics (IPC), Friedrich-Schiller-University, Jena, Germany,* [3] *Leibniz Institute of Photonic Technology, Jena, Germany,* [4] *Cardiovascular Institute, Perelman School of Medicine, University of Pennsylvania, Philadelphia, PA, United States*

OPEN ACCESS

Edited by:
Matteo Cameli,
University of Siena, Italy

Reviewed by:
Antonios Karanasos,
Hippokration General Hospital, Greece
Adrien Desjardins,
University College London,
United Kingdom

***Correspondence:**
Julien Bec
jbec@ucdavis.edu

Specialty section:
This article was submitted to Cardiovascular Imaging, a section of the journal Frontiers in Cardiovascular Medicine

Received: *07 December 2019*
Accepted: *12 June 2020*
Published: *21 July 2020*

Citation:
Bec J, Shaik TA, Krafft C, Bocklitz TW, Alfonso-Garcia A, Margulies KB, Popp J and Marcu L (2020) Investigating Origins of FLIm Contrast in Atherosclerotic Lesions Using Combined FLIm-Raman Spectroscopy. Front. Cardiovasc. Med. 7:122. doi: 10.3389/fcvm.2020.00122

Background: Fluorescence lifetime imaging (FLIm) is a spectroscopic imaging technique able to characterize the composition of luminal surface of arterial vessels. Studies of human coronary samples demonstrated that distinct atherosclerotic lesion types are characterized by FLIm features associate with distinct tissue molecular makeup. While conventional histology has provided indications about potential sources of molecular contrast, specific information about the origin of FLIm signals is lacking. Here we investigate whether Raman spectroscopy, a technique able to evaluate chemical content of biological samples, can provide additional insight into the origin of FLIm contrast.

Methods: Six human coronary artery samples were imaged using FLIm (355 nm excitation)-Raman spectroscopy (785 nm excitation) via a multimodal fiber optic probe. The spatial distribution of molecular contrast in FLIm images was analyzed in relationship with histological findings. Raman data was investigated using an endmember technique and compared with histological findings. A descriptive modeling approach based on multivariate regression was used to identify Raman bands related with changes in lifetime in four spectral channels (violet: 387/35 nm, blue: 443/29 nm, green: 546/38 nm, and red: 628/53 nm).

Results: Fluorescence lifetime variations in the violet, blue and green spectral bands were observed for distinct areas of each tissue sample associated with distinct pathologies. Analysis of Raman signals from areas associated with normal, pathological intimal thickening, and fibrocalcific regions demonstrated the presence of hydroxyapatite, collagenous proteins, carotene, cholesterol, and triglycerides. The FLIm and Raman descriptive modeling analysis indicated that lifetime increase in the violet spectral band was associated with increased presence of cholesterol and carotenes, a new finding consistent with LDL accumulation in atherosclerotic lesions, and not with collagen proteins, as expected from earlier studies.

Conclusions: The systematic, quantitative analysis of the multimodal FLIm-Raman dataset using a descriptive modeling approach led to the identification of LDL accumulation as the primary source of lifetime contrast in atherosclerotic lesions in the violet spectral range. Earlier FLIm validation studies relying on histopathological findings had associated this contrast to increased collagen content, also present in advanced lesions, thus demonstrating the benefits of alternative validation methods.

Keywords: imaging, spectroscopy, atherosclerosis, Raman spectroscopy, FLIm, time resolved fluorescence

INTRODUCTION

Atherosclerotic cardiovascular diseases is a major cause of mortality (1). Despite decades of studies, the mechanisms behind atherosclerotic plaque progression leading to acute coronary events are not fully understood. Conventional imaging techniques, such as intravascular ultrasound (IVUS) and intravascular optical coherence tomography (iv-OCT) have enabled *in vivo* assessment of atherosclerotic lesions morphology, but they lack sensitivity to associated compositional features. Thus, more recent efforts are focused on developing complementary label-free imaging techniques able to detect compositional changes associated with morphological changes and lesion progression (2). Among these are intravascular declinations of near-infrared spectroscopy (NIRS) (3), photoacoustic (PA) (4), polarization sensitive OCT (PS-OCT) (5), fluorescence spectroscopy (6), and Raman spectroscopy (RS) (7). NIRS, PS-OCT, and PA enable the identification of features from advanced lesions such as large lipid pools and cholesterol crystals, but the assessment of compositional changes associated with early lesion development, a key factor to further the understanding of lesion pathogenesis, is still elusive.

The autofluorescence signature of arterial vessels has shown potential for the identification of compositional changes associated with lesion development (8). Imaging catheters combining fluorescence lifetime imaging techniques with IVUS and OCT have been recently reported and found suitable for the interrogation of coronary arteries (6, 9). However, autofluorescence signal from biological tissues is complex as several fluorophores contribute to the emission (10). Fluorophores present peak emissions at specific wavelengths, and therefore may in some cases be identified using spectral characteristics. Unfortunately, the wide emission bands typical of biological fluorophores hinder identification of individual fluorophores based on spectral characteristics. This is especially true for the violet region where several common molecules present fluorescence emission peaks (collagen, elastin, lipids, lipoproteins, and proteoglycans). Time-resolved measurements enable further discrimination, but identification of specific fluorophores still presents challenges: comparison of the spectroscopic signature of tissue with measurements of pure compounds has been reported for intensity based approaches (11), but this approach is not suitable for fluorescence lifetime, as lifetime characteristics of molecular species are heavily influenced by their microenvironment (12), and therefore measurements of pure compounds in solution may differ significantly from their fluorescence decay properties when present within lesions.

Here, we investigate the sources of FLIm contrast using RS, well-known for its ability to provide highly specific information about the composition of biological samples. Earlier studies demonstrated that Raman is sensitive to the main constituents of atherosclerotic lesions (13, 14) and thus able to provide extensive compositional information. In this work, the dataset consists of co-registered FLIm and Raman data from *ex vivo* human coronary samples acquired with a combined FLIm and Raman imaging probe. An endmember identification technique is applied to the Raman data to identify the different lesion constituents. Histological evaluation at select locations is used to verify that these findings are consistent with previously reported results. A descriptive modeling approach based on linear regression models quantifies links between FLIm contrast and intensity variations of specific Raman spectral bands, improving on the more qualitative interpretation of multimodal imaging data reported in literature (15–17). This method is used to identify the molecular species associated with fluorescence lifetime variations, a critical step to support the adoption of FLIm as a quantitative tool for the characterization of atherosclerotic lesions biochemical makeup.

METHODS

FLIm-Raman Instrumentation

The bimodal FLIm-Raman scanning fiber optic probe used to image the arterial specimens was adapted from a previously reported probe configuration, with improved fiber arrangement and distal-end optics (18, 19). Briefly, the probe consists of one central fiber surrounded by nine peripheral fibers, all 300 μm-core UV low-OH fluorine doped fused silica. The central fiber, without distal end filter, is used for FLIm excitation and collection. One of the peripheral fibers is used for Raman excitation (785 nm) and is combined with a low-pass filter to suppress background fiber signal. Another unfiltered peripheral fiber is available for FLIm for separate excitation/collection paths (unused). The seven other fibers, combined with a high-pass filter that rejects the 785 nm excitation light, are collecting the Raman signals. The distal end optic consists of a 2 mm diameter 0.2 NA lithium doped GRIN lens, suitable for use in combination with 355 nm FLIm excitation. The working distance of the probe was determined experimentally at 1–1.5 mm for Raman and FLIm.

The Raman light source consists of a 785 nm multimode laser [0811A100-B model/Ocean optics (Innovative Photonic

solutions)]; the output power at the end of the probe was set at 93 mW. The collection fibers were connected to a Raman spectrometer (LS785, Princeton Instruments) with a reflective grating (830 grooves/mm, Princeton Instruments) and equipped with front illuminated CCD open electrode camera (PIXIS-256B Princeton Instruments). Detection was performed using a thermoelectrically cooled detector at −70°C, with 1 s exposure time and 10 accumulations per measurement point. The spectral range was 200–3,500 cm^{-1} with a spectral resolution of about 15 cm^{-1}.

FLIm was performed using a pulse sampling setup developed by our group (20). This instrument enables the collection of entire fluorescence decay measurements over four different wavelength channels from each excitation pulse. The excitation was generated using a Nd:YAG microchip Q-switched laser frequency tripled to 355 nm (Teem Photonics, France) with an externally controlled repetition rate of 4 kHz and a pulse energy of ∼1.23 μJ. The central wavelength and spectral widths of the instrument channels are determined by a series of dichroic mirrors and bandpass filters and are defined as follows: 387/35 nm (CH1), 443/29 nm (CH2), 546/38 nm (CH3), and 628/53 nm (CH4) and are comparable to spectral bands used for previous studies (6, 19, 21). A temporal multiplexing scheme using different lengths of delay fibers (1/13/25/37 m) is used so that the contributions from each channel are delayed in time (60 ns increment), thus enabling the use of a single photodetector (Microchannel plate photomultiplier tube, R3809U-50, Hamamatsu, JP), amplifier (AM-1607-3000, Miteq Inc., USA) and high-speed digitizer (12.5 GS/s, 3 GHz, PXIe-5185, National Instruments, TX). To improve signal to noise ratio, 64 waveforms were acquired and averaged for each sample location.

Data Acquisition

The bimodal fiber probe enables the simultaneous acquisition of FLIm and Raman data, but their respective acquisition speeds are very different (0.016 s/point for FLIm, 10 s/point for Raman). Therefore, the imaging sequence was implemented as follows. The combined FLIm–Raman probe was mounted on a 3D X-Y-Z translational stage (PROmech LP28, Parker, Charlotte, NC) used to scan the sample in a grid pattern with a step size of 250 μm × 250 μm. A raster scan of the whole sample was performed with FLIm (typical duration: 1–2 min). Based on reconstructed 2D FLIm images, 19 regions of interest (ROI) characterized by various by lifetime levels in CH1, CH2, and CH3 of the instrument were selected for interrogation using RS. Raman data acquisition was performed using the same 250 μm × 250 μm spatial sampling.

Sample Preparation, Imaging, Histology

Six human coronary artery samples were obtained from the University of Pennsylvania heart transplant in compliance with current legal requirements and guidelines and was under approval by the University of Pennsylvania Hospital Institutional Review Board as well as UC Davis Biological Use Authorization. Prospective informed consent for research use of heart tissue was obtained from all transplant recipients and next-of-kin in the case of organ donors. Coronary artery samples were harvested from hearts, chilled in isopentane, frozen in liquid nitrogen and stored at −80°C. Before imaging, each sample was thawed, and dissected longitudinally to expose the lumen. The samples were then sutured on a calcium fluoride slide to flatten the lumen surface and prevent tissue motion. Imaging was performed at room temperature and samples were kept hydrated using phosphate buffer saline solution. The entire surface of samples was imaged using FLIm, and 7,291 Raman spectra were collected from the 19 ROIs.

After imaging, the specimens still mounted on the holders were fixed in 10% buffered formalin. Histology processing was performed at the Texas Heart Institute (Houston, TX). Samples were first imaged using high resolution planar X-ray (Faxitron MX-20, Lincolnshire, IL). Samples were then decalcified, sliced in locations corresponding to FLIm-Raman scans, paraffin embedded, and sectioned (**Supplemental Figures 1**, **2**). Staining using hematoxylin and eosin (H&E) and Movat's pentachrome were performed to visualize plaque constituents. Immunohistochemical staining with CD68 was performed to visualize the presence of macrophage foam cells (mFC). Registration of imaging data with histology is performed based on sample outline and gross sectioning locations (**Supplemental Figures 1**, **2**).

Data Analysis

FLIm data were processed using a method previously reported by our group that enables fast and robust estimation of fluorescence decay parameters technique (22). Briefly, the fiber probe background was subtracted from the acquired waveform, and the contribution from each channel was separated and processed independently. A constrained least-square expansion technique using a set of Laguerre basis functions was used to obtain tissue fluorescence decays, from which average lifetimes were extracted for each point measurement and each channel of the instrument. En face FLIm images were reconstructed based on raster scanning parameters. CH4 (628 nm) signal was characterized by a low signal to noise ratio (mean SNR = 20.6 dB) due to weak fluorescence emission in that spectral range and was therefore not included in the analysis.

Histology registration with imaging data was performed based on gross sectioning location. In several sections, calcification visible in histological sections (L2/L4/L5/L9), as well as planar X-rays of the samples, enabled further confirmation of the histology sections location with respect to spectroscopic imaging data.

Raman signal recorded from the samples presented an autofluorescence background as well as etaloning artifacts from the CCD. Raman data were processed as follows. A wavenumber calibration was performed based on spectra from a reference sample (paracetamol) (23). A baseline correction to remove the autofluorescence contribution was performed using a sensitive non-linear iterative peak algorithm (SNIP) (24). Spectra were truncated to the 650–1,800 cm^{-1} wavenumber range and a vector normalization was applied. Etaloning artifacts were removed by reconstructing the spectra from the subset of first 10 artifact-free principal components. Finally,

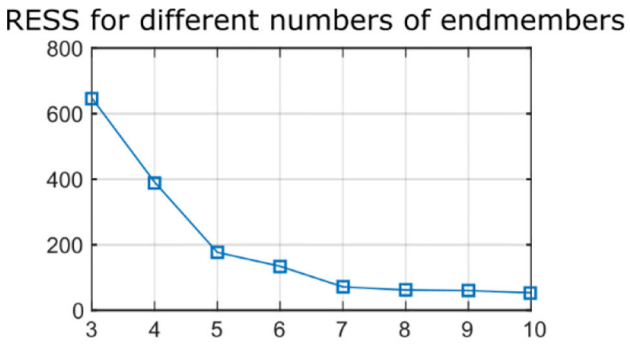

FIGURE 1 | Residual error sum of squares (RESS) for Raman data reconstructed with increasing number of endmembers ($n = 3$–10). Seven endmembers enable accurate reconstruction of the data.

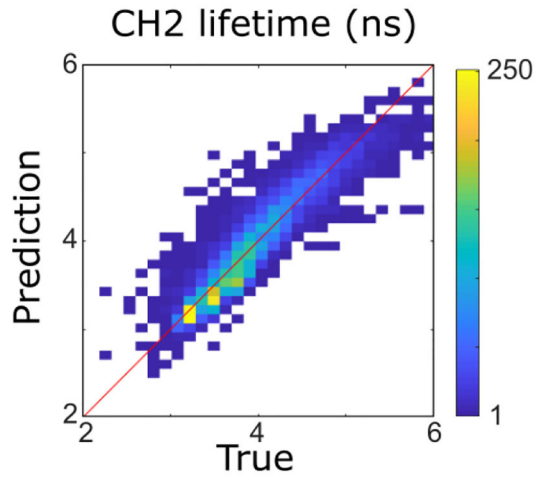

FIGURE 2 | Four hundred forty-three nanometers lifetime was accurately predicted ($R^2 = 0.89$) from 387 to 546 nm lifetimes using a multivariable linear model. It was therefore not considered for the rest of the analysis.

an endmember decomposition was performed with various numbers of endmembers ($n = 3$–10) using the unmixR package in R (25). The residual error sum of square (RESS) was computed, for an increasing number of endmembers, by reconstructing all acquired spectra as a linear combination of the endmembers and comparing the reconstructed spectra with the original data. Increasing the number of endmembers up to seven leads to a large reduction in the RESS, whereas additional endmembers beyond seven do not provide a noticeable reduction in RESS, therefore a number of 7 endmembers was retained for the rest of the study (**Figure 1**). In addition to the endmember determination based on a qualitative assessment of RESS improvement, it was observed that an 8-endmember decomposition led to two endmembers with very similar spectral shapes, and thus did not enable the identification of additional tissue components.

For each measurement point of the Raman ROIs, a high number of parameters were available (average lifetime for each FLIm spectral band, intensity for each Raman wavenumber). The relationship between variations of fluorescence lifetime values for each spectral channel and variations of Raman spectral features was investigated using linear regression analysis (26). It is expected that RS provides more information about the samples, and in order to investigate which species are likely to generate FLIm contrast, a regression model predicting Raman intensity based on FLIm information was computed.

As a first step, multicollinearity of FLIm lifetimes across the different wavebands was evaluated by computing the coefficient of multiple determination obtained by regressing the lifetime of each FLIm spectral band on the lifetimes of the other two channels. The highest value was obtained for CH2 ($R^2 = 0.89$), so this band was excluded from the analysis (**Figure 2**). The coefficient of multiple determination computed between the *LT1* (CH1 lifetime) and *LT3* (CH3 lifetime) was low ($R^2 = 0.16$) so collinearity between lifetime parameters derived from these two spectral bands was not an issue and interpretation of the regression vectors was meaningful (27).

The relationship between the FLIm and Raman datasets was investigated by applying a multivariate multiple linear regression model (26), using *LT1* and *LT3* as independent variables, and the Raman intensities for each wavenumber y as dependent variable, per Equation (1):

$$y_{ik} = b_{0k} + b_{1k}LT1 + b_{2k}LT3 + \varepsilon_{ik} \quad (1)$$

Where i is one of the 7,291 measurements, k is one of the 428 wavenumbers of the Raman spectra in the fingerprint region, and ε is an error term.

The regression model can be expressed in matrix form:

$$Y = X\beta + \varepsilon \quad (2)$$

Y is the 7,291 × 428 response matrix and consists of the Raman intensity for each measured location and wavenumber. X is the design matrix and consists of a column of ones and the *LT1* and *LT3* for each measured location. β is the 3 × 428 matrix of coefficients where the first row is the y-intercept and the 2nd and 3rd rows correspond to the expected changes in Raman spectra per unit of change in *LT1* and *LT3*, respectively. For simplification, the regression was performed on the centered FLIm variables. In that case, the y-intercept (offset) is the mean of the data. A cross validation scheme where each ROI was left out of the analysis was used. The matrix of coefficients $\hat{\beta}$ was estimated using an ordinary multivariate normal maximum likelihood estimation using Matlab (2019a, Mathworks, Natick, MA) excluding, in turn, data from a single ROI. The regression model was then used to predict Raman intensities from that ROI (**Figure 6**). Mean and standard deviations of the regression vectors computed for each cross validation were computed (**Figure 6**).

The Raman bands that correlate most with lifetime parameters were determined by computing the fitted Raman spectra:

$$\hat{Y} = X\hat{\beta} \tag{3}$$

Where $\hat{Y} = (\hat{y}_{i\,1}, \ldots \hat{y}_{ik}, \ldots, \hat{y}_{i\,428})$ correspond to the predicted Raman intensities for each point measurement.

The coefficient of multiple determination R_k^2, which corresponds to the ratios of regression sum of square divided by the total sum of squares, is computed for each wavenumber k according to Equation (4):

$$R_k{}^2 = \frac{\sum_{i=1}^{n} (\widehat{y_{ik}} - \overline{y_k})^2}{\sum_{i=1}^{n} (y_{ik} - \overline{y_k})^2} \tag{4}$$

Where n is the number of point measurements, and y_k is the average of the measured Raman intensities for the kth wavenumber.

The coefficient of multiple determination, represented as a function of wavenumber, allowed the identification of regions of the spectra that demonstrated the highest correlations with variations in fluorescence lifetime (**Figure 6**).

To better identify which Raman spectral band correlated the most each lifetime parameter, a single parameter prediction based on the model identified above was performed, using in turn only one measured lifetime parameter while fixing the other lifetime parameter. *LT1* prediction was assessed by replacing the observed *LT3* values in the design matrix by their average value and computing the corresponding fitted Raman spectra and coefficient of determinations using (Equations 3, 4). LT3 prediction was assessed by computing the coefficient of determination when replacing the *LT1* values in the design matrix by an average value (**Figure 6**).

Finally, the measurement points were partitioned in four subsets based on *LT1* and *LT3* values (above or below 4 ns), and the average Raman spectra of each subset were plotted to confirm the differences identified using the method described above (**Figure 7**).

RESULTS

FLIm

FLIm 2D maps of LT1 and LT3 illustrate the strong contrast observed from different regions of diseased vessel. Representative results from two samples are depicted in **Figure 3**, and more detailed presentation of histological findings is available in the **Supplemental Section**. Movat's pentachrome stained sections highlight that LT1 was only increasing in presence of intimal thickening. However, we observed that some locations characterized by a thickened intima do not present increased LT1 (e.g., the fibrocalcific lesions on the left side of ROI2 corresponding to sections L4 and L5). Many molecular species (e.g., some lipids, collagen, and elastin) present emission in the near-UV/blue regions (6, 10) and may cause the observed LT1 variations. The increase of LT3 was associated to the presence of mFCs as confirmed by CD68 stained sections. Another contributor of increased LT3 was perivascular adipose tissue. The penetration depth of FLIm excitation is limited, therefore perivascular adipocytes are not visible through the intima, but the adipocytes signature can be readily identified at the edges of the samples.

Raman Spectroscopy

Raman spectra obtained for individual locations were affected by noise despite the extended exposure time, limiting the ability to identify spectral features from single spectral measurements. Using the endmember technique reported here, it was possible to mitigate this limitation by expressing each measurement as a linear combination of the endmembers, and therefore extract robust compositional information at each location. Identification of species contributing to each endmember was performed based on known emission bands (16, 28, 29) of species expected in atherosclerotic lesions, combined with spatial information. Four endmembers relate to the actual lesion: collagen, calcification, triglycerides and cholesterol/carotene (**Figure 4**).

The advantage of the endmember identification technique is illustrated by the comparison of direct mapping of the 960 cm^{-1} hydroxyapatite peak intensity compared with mapping of the "calcification" endmember abundance (**Figure 5**) for a region that presents two small calcification areas. The endmember map demonstrated better quantification with negligible contribution of calcification over the rest of the field of view, whereas the band intensity image presented an elevated background. Mapping of the locations of triglycerides and Cholesterol/Carotene endmembers highlights the differences in their spatial distribution (**Figure 5**).

Combined FLIm-Raman

Figure 6 summarizes the findings from the multiple regression analysis. The regression coefficient vectors represented expected variations of Raman intensities from the average spectrum, for respective unitary increases of LT1 and LT3. Low values for a given wavenumber mean that the variance of the Raman data for this wavenumber was low, or that the FLIm values did not explain variations in Raman intensity. Conversely, high values of regression coefficients may only derive from high variance in the Raman data. The amount of Raman intensity variance explained by variations in fluorescence lifetime was represented by the coefficient of determination vector. Some of the Raman bands that stood out in the R^2 plot corresponded to higher values in the regression vectors as well, such as bands "b/c/d/e." Conversely, the 960 cm^{-1} band, linked with hydroxyapatite, presented high regression coefficient values but an R^2 close to zero, highlighting that observation of the regression coefficients was not sufficient to evaluate the strength of the relationships between datasets. On the contrary, band "a" had the highest R^2, and low regression coefficient values, explained by the low Raman intensity observed in this band.

The single parameter prediction highlighted that LT1 primarily explained Raman intensity changes, except for band "d" (carotene), equally split between LT1 and LT3. LT1 increase

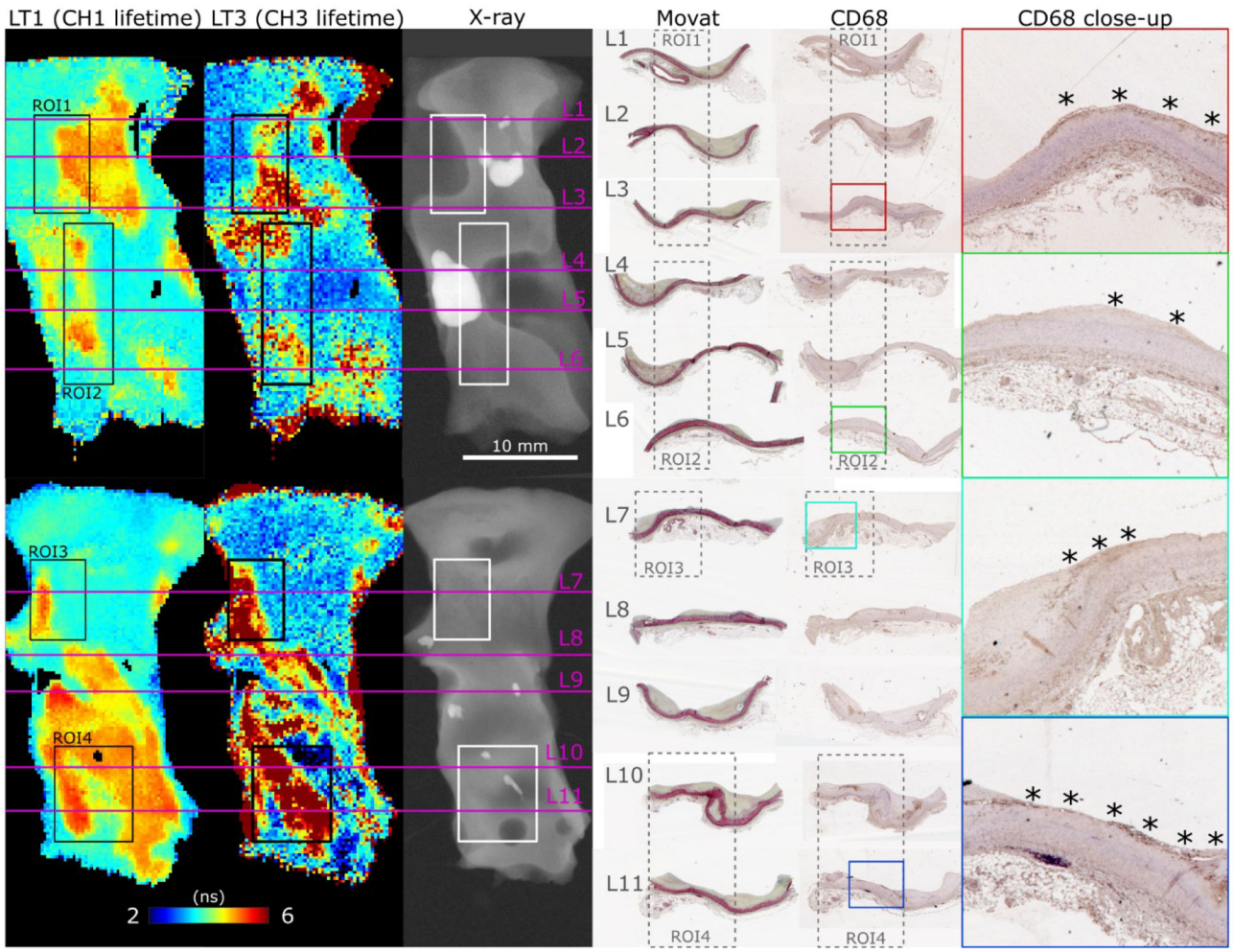

FIGURE 3 | En face FLIm maps of LT1 (387/35 nm lifetime) and LT3 (546/38 nm lifetime) for two samples illustrate the strong lifetime variations in both channels. ROI 1–4 correspond to locations where both FLIm and Raman data were acquired. Planar X-ray highlights calcification location. Histology sections (L1–L11) were positioned based on gross sectioning location and presence of calcification. Increase of LT1 was always observed in combination with intimal thickening, but some locations presented a thick intima without corresponding increase in lifetime (L4, L5, left side of ROI2). The source of LT1 was investigated in combination with Raman spectroscopy in the next section. LT3 corresponded to presence of superficial mFC, visible from the CD68 stained sections (marked with *).

was associated with increases in Raman bands associated with carotene and cholesterol, pointing to LDL accumulation as the origin of LT1 FLIm contrast. The single fluorescence channel prediction described here is not equivalent to a linear regression using LT1 or LT3 as unique independent variable that would be subject to omitted-variable bias: a simple regression is affected by the correlation between LT1 and LT3 caused by the colocalization of different species in atherosclerotic lesions.

Plots of measured vs. predicted Raman intensities (**Figure 6**, right panel) illustrate the predictive value of the regression model. Raman intensities in specific bands were impacted by variations in baseline subtraction between different measurements as well as the vector normalization scheme applied here, where increased emission in one band led to a relative reduction of the other bands. Because none of these effects were modeled by FLIm, the residual variance was expected to remain high even if the underlying relationships between Raman and FLIm signature were properly identified.

Identification of the Raman bands intensity variations highly correlated with fluorescence emission properties, using the regression method described above, were confirmed by subdividing the imaging dataset based on LT1 and LT3 values (threshold: 4 ns for both bands). The findings, presented in **Figure 7**, confirmed the validity of the approach. Average Raman spectra for each subset presented differences in correspondence to bands a-f identified from the regression analysis.

DISCUSSION

The current study demonstrated that the molecular specificity of RS allowed for the identification of molecular species and/or

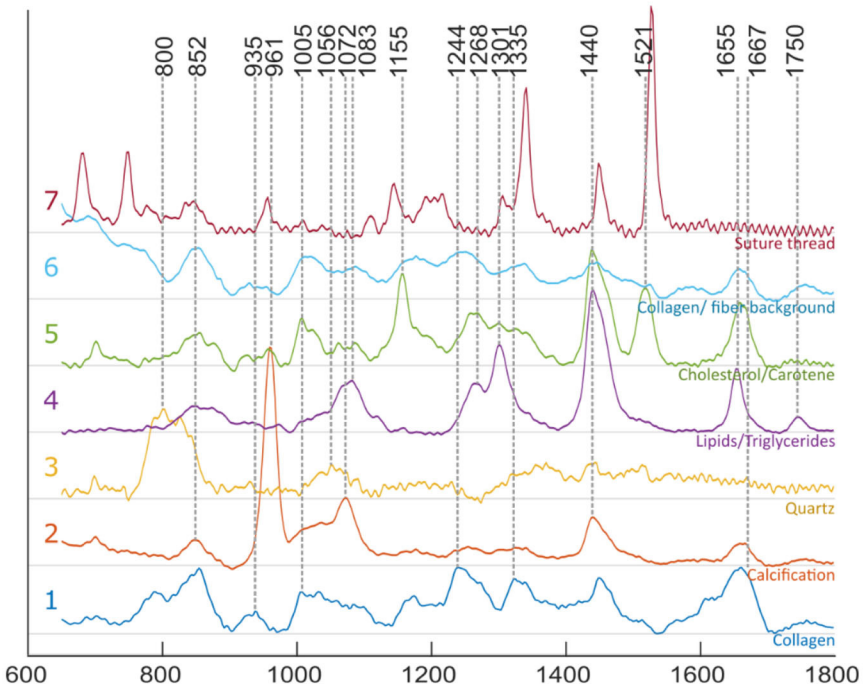

WN (cm-1)	Assignment	Endmember 1	2	3	4	5	6
800	Quartz			x			
852	Hydroxy-proline	x	x				x
935	C–C stretching	x					x
961	Hydroxy-apatite		x				
1005	Phenylalanine	x				x	x
1056	Quartz			x			
1072	PO_4^{3-}		x				
1083	Phospholipids O-P-O				x		
1155	carotene					x	
1244	Amide III	x					x
1268	Unsaturated fatty acid				x		
1271	Amide III	x					x
1301	CH_2 rotation (lipid)				x		
1335	CH_3CH_2 wagging	x					x
1440	CH_2 stretching		x		x	x	
1521	carotene					x	
1655	C=C (unsaturated lipids)				x	x	
1661	Amide I (collagen)	x	x				x
1667	Cholesterol					x	
1750	C = O				x		x

FIGURE 4 | Raman spectra of endmembers. Endmember decomposition was consistent with species expected from atherosclerotic lesions, and other elements present in the field of view [1, collagen; 2, calcification; 3, quartz (probe: fiber optic, distal lens); 4, lipid rich (unsaturated triglycerides); 5, cholesterol/ carotene rich; 6, collagen/ fiber background; and 7, suture thread].

composite of species resulting in changes in FLIm parameters in distinct spectral bands. More specifically, fluorescence lifetime increase in the violet spectral band was linked with increase in cholesterol and carotene Raman band intensities, indicative of LDL accumulation. These findings derive from a descriptive modeling approach (30) that was for the first time adapted to the analysis of FLIm-Raman imaging data.

While the autofluorescence spectra of biological compounds found in arterial vessels have distinct spectral peak emission, their emission is typically broad. Thus, each of the four spectral channels of the FLIm system is expected to capture varying amounts of signal from distinct sets of fluorophores. The first channel (violet spectral band) presented a significant lifetime increased for areas associated with atherosclerotic plaques. Earlier studies have associated the emission in this spectral band to that of structural proteins and mainly collagen in advanced lesions (31). However, measurements of pure compounds excited by 355 nm indicate that both structural proteins as well as lipids present violet autofluorescence emission (6), therefore other species such as lipids or proteoglycans could contribute to the lifetime increase observed in the violet channel. The histological analysis of coronary specimens has indicated the presence of collagen, proteoglycans as well as extracellular lipids, thus the direct identification of the molecular specie responsible for the observed LT1 increase was not possible. The FLIm results for the third emission channel (green spectral band) were found consistent with previous reports that linked lifetime increase in this band with mFCs accumulation (6, 32). The results for the second emission channel (blue spectral band) show that for these samples, the computed lifetime is to a large extent a linear combination of the violet and green bands, leading to its exclusion from the analysis.

Analysis of Raman using an endmember extraction, in combination with histology sections, yielded results consistent with previously reported work (13, 14). The regions presenting the most triglyceride contributions are areas where perivascular adipose tissue is exposed at the edge of the sample, but also regions of minimal intimal thickening. In that latter case, the total wall thickness of ∼200 μm and the large Raman cross section of lipids compared to proteins explain why the Raman signature is dominated by contributions from tissue located outside of the vessel. This association of triglycerides with perivascular adipose tissue was previously reported in the literature (13, 16). The second lipids contribution, related to cholesterol/carotene, was expressed in areas of increased intimal thickness, in agreement with earlier studies (16). Carotene presents a strong Raman cross section due to pre-resonance enhancement and is readily embedded in LDL, therefore its colocalization with cholesterol was expected. Cell studies on the tracking of LDL uptake into macrophages have taken advantage of this cholesterol/β-carotene colocalization (33). Applied in the context of biological human samples, the same cholesterol/β-carotene association highlighted LDL accumulation into the arterial wall.

The analysis of the regression model linking Raman and FLIm measurements identified a relationship between LT1 increase and accumulation of carotene and cholesterol associated with

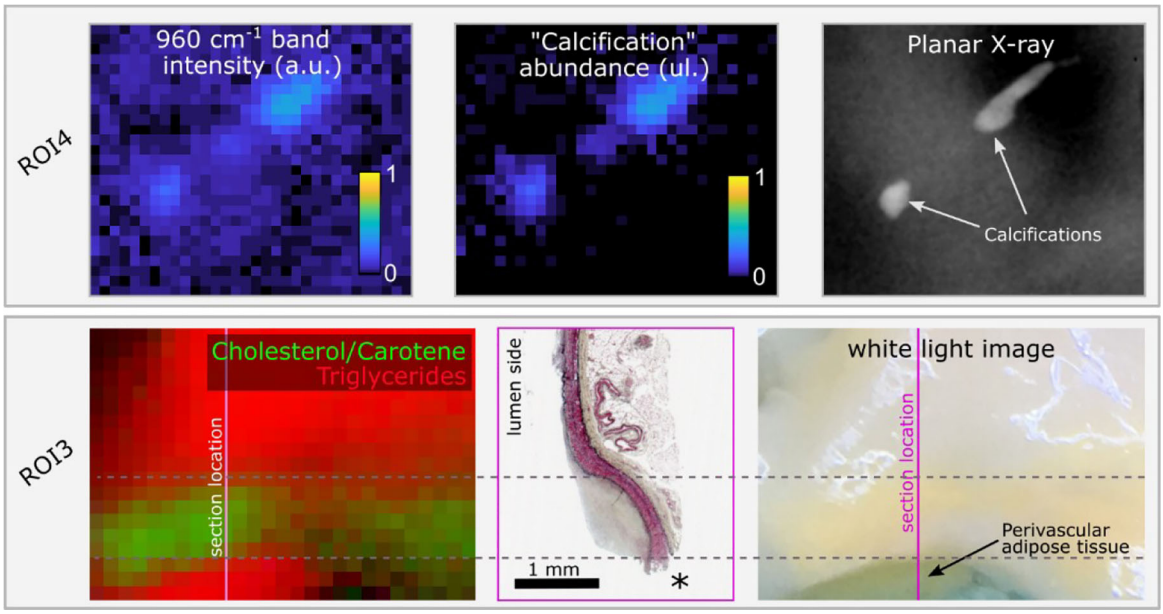

FIGURE 5 | Raman hydroxyapatite band intensity map (960 cm^{-1}) compared with "Calcification" endmember abundance map for ROI4 and ground truth location of calcifications obtained from planar X-ray. The two small calcifications are easily visible with both methods. The endmember image correctly shows no signature from calcifications over the rest of the sample, whereas the intensity image shows elevated background (upper panel). In ROI3, the color image represents the abundance of endmembers 4 ("triglycerides," red) and 5 ("cholesterol/carotene," green). Two distinct locations present an abundance of the "triglycerides" endmember. The lower spot corresponds to perivascular adipose tissue, rich in triglycerides, exposed at the edge of the sample, easily identified in the white light image, and lost during histology processing (location marked as *). The upper area corresponds to a diffuse intimal thickening region where perivascular adipose tissue contributes to the Raman signature due to the reduced wall thickness. In between, the region of predominant cholesterol/Carotene signature overlaps with the lesion location (lower panel).

LDL accumulation in developing lesions, as well as decreased contribution from perivascular adipose tissue triglycerides, due to increased intimal thickness. Perivascular adipose tissue is beyond the penetration depth of FLIm so the main contributing factor to variations in LT1 was attributed to LDL accumulation. On the other hand, collagen signature is readily identified in the Raman data but no correlation with variations of FLIm signature was observed. As a consequence, previous FLIm studies of atherosclerosis samples corroborated with histology that had associated lifetime contrast in that wavelength band with variations in collagen content may need revisiting (13, 34). These earlier findings may have stemmed from the ubiquitous presence of collagen in atherosclerotic lesions and the difficulties in properly characterizing lipids contribution in histology studies. This new finding highlights the superior ability of RS to perform direct, quantitative, lipid profiling. Variations of LT3 presented only weak relationships with Raman features. LT3 increase derives mostly from bright ceroids autofluorescence (34, 35), present in small amount and not known to present a high Raman cross section.

The method used to identify sources of FLIm contrast is constrained by the ability of RS to detect specific molecular species. For example, the contribution to the FLIm signature of species not identified in the Raman signal, such as proteoglycans, cannot be assessed with this approach. Proteoglycans are typically co-localized with LDL accumulation (36), thus the findings reported in this study cannot exclude that the contrast observed in LT1 is caused by proteoglycan accumulation. The performance of the regression model is also limited by the characteristics of the Raman data. Raman variance is explained by variations in tissue composition, but also variations in baseline correction, influence of vector normalization, and detection noise. Therefore, values of coefficients of multiple determination (R^2) observed for the regression model (<0.4) are expected, and adequate to support the findings of this descriptive study. Another confounding factor for this regression analysis is the difference in interrogated volume between FLIm and Raman. Here, 355 nm FLIm excitation is characterized by a low penetration depth in tissue, whereas 785 nm Raman excitation readily propagates in tissue up to 400–600 μm. Therefore, the contribution to the Raman signal of triglyceride in perivascular adipose tissue prevented the identification of possible triglycerides contribution within the FLIm penetration depth.

The availability of co-registered FLIm and Raman data enabled a model-based approach to the identification of relationships between FLIm and Raman variations. This approach, called descriptive modeling, is well-suited to the systematic and quantitative analysis of data consisting of a large number of variables, as is the case here. This modeling approach differs from previous comparative imaging studies reporting the combination of Raman imaging with other optical imaging

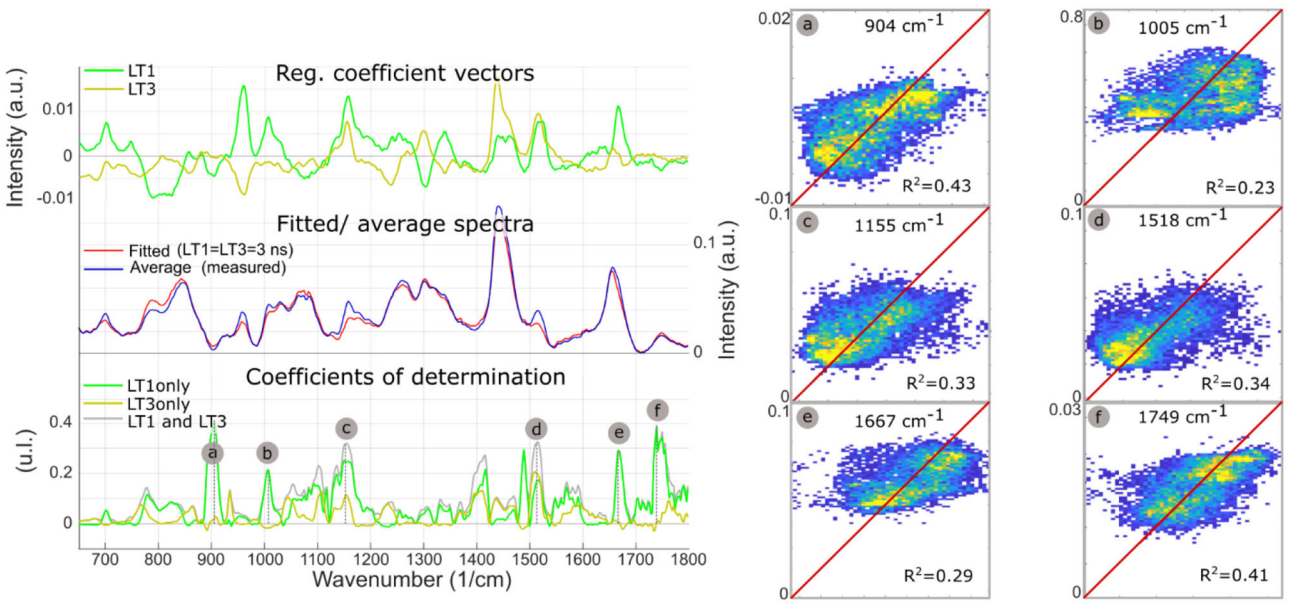

FIGURE 6 | LT1 and LT3 regression coefficient vectors are expected variations of Raman spectra for a respective unit increases of LT1 and LT3. The standard deviation of the regression vectors for each cross-validation subset is represented by the shaded area behind each curve. The offset vector of the regression is equal to the average Raman spectrum. Averaged measured Raman spectrum and modeled spectrum for diffuse intimal thickening regions (LT1 = 3 ns, LT3 = 3 ns), present few differences. Plot of coefficients of determination between measured Raman intensities and Raman intensities predicted from LT1 and LT3 (gray) demonstrates that the amount of variance that can be explained by lifetime variations varies for the different regions of the spectra: as expected, not all Raman bands can be predicted from FLIm values. Some locations show a correlation coefficient >0.3 (a, Protein/ Collagen; b, Phenylalanine/ Carotene; c/d, Carotene; e, Cholesterol; f, Ester bond). Prediction using lifetime from only one channel of the instrument (and replacing the other lifetime information by the average for the whole dataset) highlights which lifetime channel contributes most to the prediction (LT1: a/b/c/e/f). The predicted vs. measured intensities are represented for bands a/b/c/d/e/f (right panel).

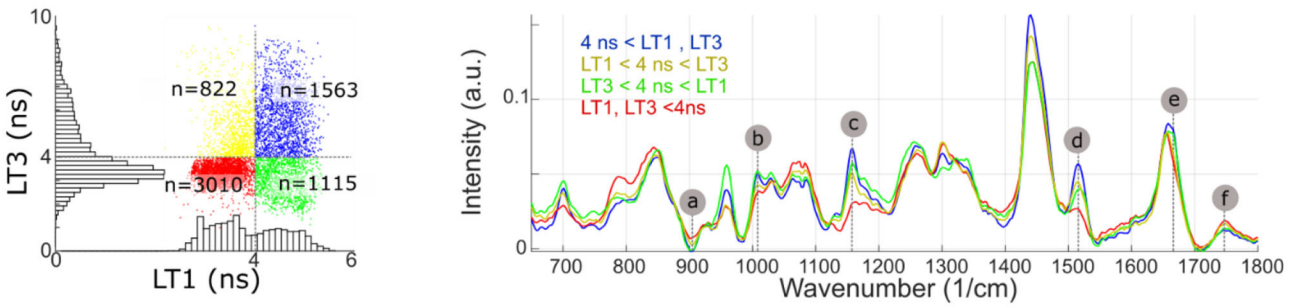

FIGURE 7 | Measurement points are partitioned based on LT1 and LT3 values (above or below 4 ns). The average Raman spectra of each subset present noticeable differences in bands identified from the regression analysis (a, Protein/ Collagen; b, Phenylalanine/ Carotene; c/d, Carotene; e, Cholesterol; f, Ester bond). Some of the regions where average spectra present noticeable differences (785, 960, and 1,440 cm^{-1}), conversely, only present very weak correlation with fluorescence lifetime.

modalities such as near-infrared spectroscopy, coherent anti-Stokes RS, or Fourier transform infrared spectroscopy (15–17) where the ability of each modality to identify specific components in the imaged sample was evaluated qualitatively or quantified on aggregated locations. A model-based approach, however, requires spatially co-registered datasets from both imaging modalities. Earlier comparative imaging studies using RS consisted of datasets acquired with dedicated (independent) instrumentation that differed in field of view, resolution, and/or spatial sampling, and thus were not suitable for a model-based approach. In contrast, the model-based approach described here enabled systematic and quantitative assessment of the presence of specific components. A limitation in the reported implementation is the mismatch of penetration depths of each modality, that could be addressed by matching the penetration depth of RS with the penetration depth of FLIm using a confocal probe design.

Predictive modeling approaches based on RS in combination with other analytical methods have been reported for a wide variety of applications, such as cell (37) or transcriptome (38) identification, or active pharmaceutical ingredient content quantification (39). Both predictive and descriptive modeling may rely on the same tools (e.g., multiple regression techniques),

but the purpose of predictive approaches is to use high dimensional Raman data to develop non-invasive prediction models of specific phenotypes or components. The emphasis was therefore on the performance of the classifier. However, the exact identification of the Raman spectral features that allowed differentiation, a key finding of this study, was not evaluated.

In this study, FLIm and Raman modalities were integrated in a single optical fiber imaging probe. This approach presents clear advantages for accurate registration of imaging datasets, but at the expense of the optical performance for each modality. While the compact fiber optic probe design is ideally suited to contact measurements on a variety of samples, when used to image irregularly shaped samples such design leads to variations in the probe to tissue distance across the field of view. For this dataset, a percentile ratio (90/10) of ∼3.3 was observed for the Raman intensity, meaning that signal collection was suboptimal in many locations. This could be addressed by performing an imaging scan where the imaging probe follows a 3D trajectory and maintains a consistent distance with tissue. Alternatively, an inverted setup, where imaging is performed through a transparent window and thus the sample to probe distance can be accurately maintained could be used (40). Ultimately, a setup able to perform FLIm-Raman imaging on thin ($<100\,\mu m$) tissue sections would also present the benefit of reducing the effect of differences in penetration depths between modalities and therefore represent an ideal tool for future FLIm/Raman comparative imaging, at the expense of additional sample preparation.

Validation of a new spectroscopic imaging technique by means of co-registration with an established reference modality (e.g., Raman spectroscopy characterized by high molecular specificity) requires reduced human intervention compared to histology-based validation. Sample preparation is minimal and data analysis requires little human input beyond the initial definition of the methods. Thus, expansion to a much higher sample number can be achieved more readily than with histopathology-based validation studies where human operations in sample processing, registration, and feature extraction is a bottleneck.

CONCLUSION

The ability of FLIm to provide label-free molecular contrast with a device suitable for the acquisition of data *in vivo* shows potential for improved characterization of atherosclerotic lesions, but identification of specific species based on FLIm contrast alone is a challenge due to the variety of endogenous fluorophores present in diseased arteries. On the other hand, several technical challenges limit the potential of Raman spectroscopy for *in vivo* interrogation of the vasculature, but its high specificity enables the identification of key components of atherosclerotic lesions. By combining both approaches, we identified in *ex vivo* human samples that the source of fluorescence lifetime increase in the violet spectral range observed in atherosclerotic lesions, previously thought to be linked with increased collagen content, is associated with LDL accumulation. This finding illustrates that histology-based validation of imaging techniques may be complemented by a multimodal imaging approach combined with a model-based data analysis, where a high specificity spectroscopic imaging method (Raman) is used to shed light on a high speed/lower specificity modality (FLIm). A broader range of imaging validation studies may benefit from such approach, due to the ability to detect molecular species not readily identified in formalin fixed/paraffin embedded histological sections, and the availability of data analysis methods suited to the efficient analysis of co-registered multimodal imaging data. This approach is also easily scalable to the analysis of large numbers of samples as limited user input is required beyond data acquisition, a clear benefit compared to histology-based validation that relies heavily on human operations for sample preparation and feature extraction.

DATA AVAILABILITY STATEMENT

The datasets generated for this study are available on request to the corresponding author.

ETHICS STATEMENT

The studies involving human participants were reviewed and approved by University of Pennsylvania Hospital Institutional Review Board UC Davis Biological Use Authorization. The patients/participants provided their written informed consent to participate in this study.

AUTHOR CONTRIBUTIONS

JB proposed the methodology, performed analysis, and wrote the manuscript. TS developed the Raman data acquisition code and supported data analysis. KM provided tissues for the analysis. JB and TS acquired the multimodal imaging data. TB performed Raman data pre-processing and provided guidance for comparative data analysis. CK assisted in determining chemical species based on Raman information. TB, AA-G, and CK provided input regarding data analysis methods and study findings. TS, TB, AA-G, CK, KM, JP, and LM provided inputs on the revision of the manuscripts. All authors contributed to the article and approved the submitted version.

FUNDING

This work was supported by NIH grants R01-HL67377 (to LM) and R01-HL105993 (to KM) and the German Program for Transatlantic Encounters funded by the European Recovery Program (ERP) of the German Federal Ministry for Economic Affairs and Energy.

SUPPLEMENTARY MATERIAL

The Supplementary Material for this article can be found online at: https://www.frontiersin.org/articles/10.3389/fcvm.2020.00122/full#supplementary-material

REFERENCES

1. CDC, NCHS. *Underlying Cause of Death 1999-2013 on CDC WONDER Online Database, Released 2015* (2015).
2. Mathur A, Michail M, Stettler R, Crake T, Bourantas CV, Serruys PW, et al. Intravascular multimodality imaging: feasibility and role in the evaluation of coronary plaque pathology. *Eur Heart J Cardiovasc Imaging.* (2017) 18:613–20. doi: 10.1093/ehjci/jew330
3. Madder RD, Husaini M, Davis AT, Van Oosterhout S, Harnek J, Götberg M, et al. Detection by near-infrared spectroscopy of large lipid cores at culprit sites in patients with non-st-segment elevation myocardial infarction and unstable angina. *Catheter Cardiovasc Intervent.* (2015) 86:1014–21. doi: 10.1002/ccd.25754
4. Wang P, Ma T, Slipchenko MN, Liang S, Hui J, Shung KK, et al. High-speed intravascular photoacoustic imaging of lipid-laden atherosclerotic plaque enabled by a 2-kHz barium nitrite Raman laser. *Sci Rep.* (2014) 4:6889. doi: 10.1038/srep06889
5. Villiger M, Otsuka K, Karanasos A, Doradla P, Ren J., Lippok N, et al. Coronary plaque microstructure and composition modify optical polarization: a new endogenous contrast mechanism for optical frequency domain imaging. *JACC Cardiovasc Imaging.* 11:1666–76. doi: 10.1016/j.jcmg.2017.09.023
6. Bec J, Phipps JE, Gorpas D, Ma D, Fatakdawala H, Margulies KB, et al. *In vivo* label-free structural and biochemical imaging of coronary arteries using an integrated ultrasound and multispectral fluorescence lifetime catheter system. *Sci Rep.* (2017) 7:8960. doi: 10.1038/s41598-017-08056-0
7. Matthaeus C, Dochow S, Bergner G, Lattermann A, Romeike BFM, Marple ET, et al. *In vivo* characterization of atherosclerotic plaque depositions by Raman-probe spectroscopy and *in vitro* coherent anti-stokes Raman scattering microscopic imaging on a rabbit model. *Anal Chem.* (2012) 84:7845–51. doi: 10.1021/ac301522d
8. Marcu L. Fluorescence lifetime in cardiovascular diagnostics. *J Biomed Opt.* (2010) 15:011106. doi: 10.1117/1.3327279
9. Lee MW, Song JW, Kang WJ, Nam HS, Kim TS, Kim S, et al. Comprehensive intravascular imaging of atherosclerotic plaque *in vivo* using optical coherence tomography and fluorescence lifetime imaging. *Sci Rep.* (2018) 8:14561. doi: 10.1038/s41598-018-32951-9
10. Croce AC, Bottiroli G. Autofluorescence spectroscopy and imaging: a tool for biomedical research and diagnosis. *Eur J Histochem.* (2014) 58:2461. doi: 10.4081/ejh.2014.2461
11. Scepanovic OR, Fitzmaurice M, Miller A, Kong CR, Volynskaya ZI, Dasari RR, et al. Multimodal spectroscopy detects features of vulnerable atherosclerotic plaque. *J Biomed Opt.* (2011) 16:011009. doi: 10.1117/1.3525287
12. Draxler S, Lippitsch ME. Lifetime-based sensing: influence of the microenvironment. *Anal Chem.* (1996) 68:753–7. doi: 10.1021/ac9507092
13. Buschman HP, Deinum G, Motz JT, Fitzmaurice M, Kramer JR, van der Laarse A, et al. Raman microspectroscopy of human coronary atherosclerosis: biochemical assessment of cellular and extracellular morphologic structures *in situ*. *Cardiovasc Pathol.* (2001) 10:69–82. doi: 10.1016/S1054-8807(01)00064-3
14. van de Poll SWE, Römer TJ, Puppels GJ, van der Laarse A. Raman spectroscopy of atherosclerosis. *J Cardiovasc Risk.* (2002) 9:255–61. doi: 10.1177/174182670200900505
15. Nallala J, Piot O, Diebold M-D, Gobinet C, Bouché O, Manfait M, et al. Infrared and Raman imaging for characterizing complex biological materials: a comparative morpho-spectroscopic study of colon tissue. *Appl Spectrosc.* (2014) 68:57–68. doi: 10.1366/13-07170
16. Lattermann A, Matthäus C, Bergner N, Beleites C, Romeike BF, Krafft C, et al. Characterization of atherosclerotic plaque depositions by Raman and FTIR imaging. *J Biophotonics.* (2013) 6:110–21. doi: 10.1002/jbio.201200146
17. Krafft C, Ramoji AA, Bielecki C, Vogler N, Meyer T, Akimov D, et al. A comparative Raman and CARS imaging study of colon tissue. *J Biophotonics.* (2009) 2:303–12. doi: 10.1002/jbio.200810063
18. Dochow S, Ma D, Latka I, Bocklitz T, Hartl B, Bec J, et al. Combined fiber probe for fluorescence lifetime and Raman spectroscopy. *Anal Bioanal Chem.* (2015) 407:8291–301. doi: 10.1007/s00216-015-8800-5
19. Dochow S, Fatakdawala H, Phipps JE, Ma D, Bocklitz T, Schmitt M, et al. Comparing Raman and fluorescence lifetime spectroscopy from human atherosclerotic lesions using a bimodal probe. *J Biophotonics.* (2016) 9:958–66. doi: 10.1002/jbio.201500341
20. Yankelevich DR, Ma D, Liu J, Sun Y, Sun Y, Bec J, et al. Design and evaluation of a device for fast multispectral time-resolved fluorescence spectroscopy and imaging. *Rev Sci Instrum.* (2014) 85:034303. doi: 10.1063/1.4869037
21. Fatakdawala H, Gorpas D, Bishop JW, Bec J, Ma D, Southard JA, et al. Fluorescence lifetime imaging combined with conventional intravascular ultrasound for enhanced assessment of atherosclerotic plaques: an *ex vivo* study in human coronary arteries. *J Cardiovasc Transl Res.* (2015) 8:253–63. doi: 10.1007/s12265-015-9627-3
22. Liu J, Sun Y, Qi J, Marcu L. A novel method for fast and robust estimation of fluorescence decay dynamics using constrained least-squares deconvolution with Laguerre expansion. *Phys Med Biol.* (2012) 57:843–65. doi: 10.1088/0031-9155/57/4/843
23. Dörfer T, Bocklitz T, Tarcea N, Schmitt M, Popp J. Checking and improving calibration of Raman spectra using chemometric approaches. *Zeitschrift für Physikalische Chemie.* (2011) 225:753–64. doi: 10.1524/zpch.2011.0077
24. Ryan CG, Clayton E, Griffin WL, Sie SH, Cousens DR. SNIP, a statistics-sensitive background treatment for the quantitative analysis of PIXE spectra in geoscience applications. *Nucl Instrum Methods Phys Res Sec B.* (1988) 34:396–402. doi: 10.1016/0168-583X(88)90063-8
25. McManus C, Fuller S, Beleites C, Hanson BA. *unmixR: Hyperspectral Unmixing in R.*
26. Rencher AC, Christensen WF. *Methods of Multivariate Analysis.* Hoboken, NJ: Wiley (2012).
27. Yoo W, Mayberry R, Bae S, Singh K, Peter He Q, Lillard JW Jr. A study of effects of multicollinearity in the multivariable analysis. *Int J Appl Sci Technol.* (2014) 4:9–19.
28. Krafft C, Neudert L, Simat T, Salzer R. Near infrared Raman spectra of human brain lipids. *Spectrochim Acta Part A.* (2005) 61:1529–35. doi: 10.1016/j.saa.2004.11.017
29. ur Rehman I, Movasaghi Z, Rehman S. *Vibrational Spectroscopy for Tissue Analysis.* (2013) Available online at: http://www.crcnetbase.com/isbn/9781439836088
30. Shmueli G. To explain or to predict? *Statist Sci.* (2010) 25:289–310. doi: 10.1214/10-STS330
31. Park J, Pande P, Shrestha S, Clubb F, Applegate BE, Jo JA. Biochemical characterization of atherosclerotic plaques by endogenous multispectral fluorescence lifetime imaging microscopy. *Atherosclerosis.* (2012) 220:394–401. doi: 10.1016/j.atherosclerosis.2011.10.034
32. Rico-Jimenez JJ, Serafino MJ, Shrestha S, Chen X, Kim W, Adame J, et al. Automated detection of superficial macrophages in atherosclerotic plaques using autofluorescence lifetime imaging. *Atherosclerosis.* (2019) 285:120-7. doi: 10.1016/j.atherosclerosis.2019.04.223
33. Stiebing C, Schmölz L, Wallert M, Matthäus C, Lorkowski S, Popp J. Raman imaging of macrophages incubated with triglyceride-enriched oxLDL visualizes translocation of lipids between endocytic vesicles and lipid droplets. *J Lipid Res.* (2017) 58:876–83. doi: 10.1194/jlr.M071688
34. Haka AS, Kramer JR, Dasari RR, Fitzmaurice M. Mechanism of ceroid formation in atherosclerotic plaque: *in situ* studies using a combination of Raman and fluorescence spectroscopy. *J Biomed Opt.* (2011) 16:011011. doi: 10.1117/1.3524304
35. Verbunt RJAM, Fitzmaurice MA, Kramer JR, Ratliff NB, Kittrell C, Taroni P, et al. Characterization of ultraviolet laser-induced autofluorescence of ceroid deposits and other structures in atherosclerotic plaques as a potential diagnostic for laser angiosurgery. *Am Heart J.* (1992) 123:208–16. doi: 10.1016/0002-8703(92)90767-P
36. Nakashima Y, Fujii H, Sumiyoshi S, Wight TN, Sueishi K. Early human atherosclerosis: accumulation of lipid and proteoglycans in intimal thickenings followed by macrophage infiltration. *Arterioscler Thromb Vasc Biol.* (2007) 27:1159–65. doi: 10.1161/ATVBAHA.106.134080
37. Ichimura T, Chiu L, Fujita K, Machiyama H, Yamaguchi T, Watanabe TM, et al. Non-label immune cell state prediction using Raman spectroscopy. *Sci Rep.* (2016) 6:37562. doi: 10.1038/srep37562

38. Kobayashi-Kirschvink KJ, Nakaoka H, Oda A, Kamei KF, Nosho K, Fukushima H, et al. Linear regression links transcriptomic data and cellular Raman spectra. *Cell Syst.* (2018) 7:104–17.e4. doi: 10.1016/j.cels.2018.05.015
39. Kim J, Noh J, Chung H, Woo YA, Kemper MS, Lee Y. Direct, non-destructive quantitative measurement of an active pharmaceutical ingredient in an intact capsule formulation using Raman spectroscopy. *Anal Chim Acta.* (2007) 598:280–5. doi: 10.1016/j.aca.2007.07.049
40. Shipp DW, Rakha EA, Koloydenko AA, Macmillan RD, Ellis IO, Notingher I. Intra-operative spectroscopic assessment of surgical margins during breast conserving surgery. *Breast Cancer Res.* (2018) 20:69. doi: 10.1186/s13058-018-1002-2

Conflict of Interest: The authors declare that the research was conducted in the absence of any commercial or financial relationships that could be construed as a potential conflict of interest.

frontiers in Cardiovascular Medicine

REVIEW
published: 28 August 2020
doi: 10.3389/fcvm.2020.00146

Intravascular Polarimetry: Clinical Translation and Future Applications of Catheter-Based Polarization Sensitive Optical Frequency Domain Imaging

Kenichiro Otsuka[1†], *Martin Villiger*[1†], *Seemantini K. Nadkarni*[1] *and Brett E. Bouma*[1,2,3*]

[1] Wellman Center for Photomedicine, Harvard Medical School, Massachusetts General Hospital, Boston, MA, United States,
[2] Institute for Medical Engineering and Science, Massachusetts Institute of Technology, Cambridge, MA, United States,
[3] Department of Cardiology, Erasmus University Medical Center, Rotterdam, Netherlands

OPEN ACCESS

Edited by:
Christos Bourantas,
Barts Health NHS Trust,
United Kingdom

Reviewed by:
Erhan Tenekecioglu,
University of Health Sciences, Turkey
Rob Krams,
Queen Mary University of London,
United Kingdom

***Correspondence:**
Brett E. Bouma
bouma@mgh.harvard.edu

[†]These authors have contributed equally to this work

Specialty section:
This article was submitted to Cardiovascular Imaging, a section of the journal Frontiers in Cardiovascular Medicine

Received: 04 January 2020
Accepted: 10 July 2020
Published: 28 August 2020

Citation:
Otsuka K, Villiger M, Nadkarni SK and Bouma BE (2020) Intravascular Polarimetry: Clinical Translation and Future Applications of Catheter-Based Polarization Sensitive Optical Frequency Domain Imaging. Front. Cardiovasc. Med. 7:146. doi: 10.3389/fcvm.2020.00146

Optical coherence tomography (OCT) and optical frequency domain imaging (OFDI) visualize the coronary artery wall and plaque morphology in great detail. The advent of these high-resolution intracoronary imaging modalities has propelled our understanding of coronary atherosclerosis and provided enhanced guidance for percutaneous coronary intervention. Yet, the lack of contrast between distinct tissue types and plaque compositions impedes further elucidation of the complex mechanisms that contribute to acute coronary syndrome (ACS) and hinders the prospective identification of plaques susceptible to rupture. Intravascular polarimetry with polarization-sensitive OFDI measures polarization properties of the coronary arterial wall using conventional intravascular imaging catheters. The quantitative polarization metrics display notable image contrast between several relevant coronary plaque microstructures that are difficult to identify with conventional OCT and OFDI. Tissues rich in collagen and smooth muscle cells exhibit birefringence, while lipid and macrophages cause depolarization. In this review, we describe the basic principles of intravascular polarimetry, discuss the interpretation of the polarization signatures, and outline promising avenues for future research and clinical implications.

Keywords: optical coherence tomography, polarimetry, atherosclerosis, collagen, smooth muscle cells, macrophage, neoatherosclerosis, drug-eluting stent

INTRODUCTION

Coronary artery disease is a chronic inflammatory disease that in its most fatal complication provokes acute coronary syndrome (ACS) and in the long term leads to heart failure, causing immense disease burden, and economic cost worldwide (1–3). Substantial research efforts have been devoted to prospectively identifying "vulnerable plaques" that are prone to rupture and causing ACS with the goal to improve clinical therapy (4, 5). The ability to identify thin-capped fibroatheromas (TCFAs), heralded as the archetypical vulnerable

plaque, has been a driving motivation for the development of intracoronary optical coherence tomography (OCT), and optical frequency domain imaging (OFDI)[1] (6). These intravascular imaging methods visualize the subsurface microstructure of the arterial wall and atherosclerotic lesions with high spatial resolution (10 μm axial; 20–40 μm lateral), using light in the near infrared wavelength range (6). Today, OCT facilitates guiding percutaneous coronary intervention (PCI) with better physiological outcomes than using coronary angiography alone (7, 8), and has been shown to assess functional stenosis severity more accurately than intravascular ultrasound (IVUS) (9).

However, the majority of TCFAs identified by OCT (10–12) or virtual-histology IVUS (13–15) do not cause any acute events, calling into question the established structural criteria of the "vulnerable plaque" (5, 16, 17). Plaque composition has been identified as an additional critical factor of a lesion's susceptibility to precipitate ACS (4, 14, 18–20). Also, it is now a well-accepted concept that plaque rupture and erosion frequently occur silently without causing clinical symptoms, emphasizing the crucial role of vascular healing in determining the fate of a lesion (1, 21). Therefore, the mechanisms that impair vascular healing are increasingly investigated to explain disease progression and the development of ACS (22–24). Following stent implantation, vascular healing and tissue response play a similar decisive role in defining the risk of stent failure and future complications (25–28). Thus, there is an urgent need for imaging methods that afford refined insight into a lesion's make-up, composition, and healing, in order to address pertinent questions regarding the pathophysiology of atherosclerosis and to ultimately improve the risk stratification and management of patients with coronary artery disease.

Near-infrared spectroscopy, near-infrared fluorescence, and photoacoustic imaging assess aspects of coronary plaque composition, but depend on integration with intracoronary OCT or IVUS for structural imaging (29, 30). This multimodality approach requires significant modifications of the imaging catheter. To benefit from existing hardware and simplify clinical translation, we have been extending the capabilities of intravascular OCT by advancing polarization sensitive (PS-) OCT (31–33). Intravascular polarimetry (IVP) with PS-OCT measures the depth-dependent polarization state of the light scattered by tissue and provides spatially resolved maps of tissue birefringence and depolarization (34–36). IVP employs existing imaging catheters and can be performed with only minor modifications of current clinical intracoronary OCT systems (34, 36). The microscopic structure and organization of the arterial wall influence the polarization of the infrared light used by OCT, providing a compelling contrast mechanism. Birefringence is elevated in tissue with fibrillar architecture, such as interstitial collagen or smooth muscle cells (SMC), which play a critical role in plaque stability and vascular healing. Microscopic PS-OCT has been used early on to leverage this contrast mechanism (37–39), and birefringence measured in human aortic plaques *ex vivo* positively correlated with thick collagen fibers and SMCs (39). Despite its demonstrated potential, polarimetry with catheter-based PS-OCT proved challenging because of the dynamic variation of the polarization states transmitted through the rotating catheter (40) and polarization distortions induced by system components (41). We developed a reconstruction method that mitigates the resulting artifacts (42) enabling, for the first time, measurement of depth-resolved birefringence through intravascular imaging catheters, first *ex vivo* (34) and then in patients (35, 43–45). Measurement of the polarization states of the light returning from the tissue also permits evaluation of depolarization (46–48). Depolarization complements birefringence and provides the polarimetric characterization of tissues rich in lipid, cholesterol crystals, and macrophages (34–36).

IVP provides quantitative metrics of tissue polarization properties measured through conventional intravascular imaging catheters. Birefringence and depolarization complement the conventional tomograms of tissue microstructure with additional insights into tissue organization and composition that are highly relevant for studying the progression of coronary atherosclerosis and stratifying the risk of individual lesions. Here, we review the basic principles, clinical translation, and future prospects of IVP, and discuss how it may help advance our understanding of coronary artery disease.

WORKING PRINCIPLE OF IVP WITH PS-OCT

Light is a transverse electromagnetic wave that oscillates in a plane orthogonal to the propagation direction of the beam. The oscillation pattern of the fields within this orthogonal plane defines the polarization state of the light, which may be altered by the optical components of the imaging system and catheter or by the vessel wall. Because the fiber-optic probe rotates inside the imaging catheter, the polarization state of the transmitted light varies dynamically. OCT measures the interference between back-reflected sample light and a reference beam, which has its own defined polarization state. Only light with identical polarization states can interfere. To ensure that the sample signal is detected independently of its specific polarization state, conventional OCT systems use two detection channels with orthogonal polarization states (**Figure 1**). Both the sample and the reference light are split between the two channels. The reference signal is adjusted to provide equal power in both channels and the sample light is split according to its specific polarization state. Conventional OCT tomograms combine the two polarization channels to reveal the reflection intensity as a function of depth independent of polarization effects and catheter rotation.

PS-OCT analyzes the ratio and phase difference between the signals in the two detection channels to recover the polarization state of the detected sample light as a function of the depth it traveled into the tissue (33). To obtain a complete characterization of the polarization effects of the sample

[1]* Throughout this manuscript we generalize OFDI – a specific second-generation implementation of optical coherence tomography – to OCT, the general imaging method that includes all implementations of OCT, whenever suitable.

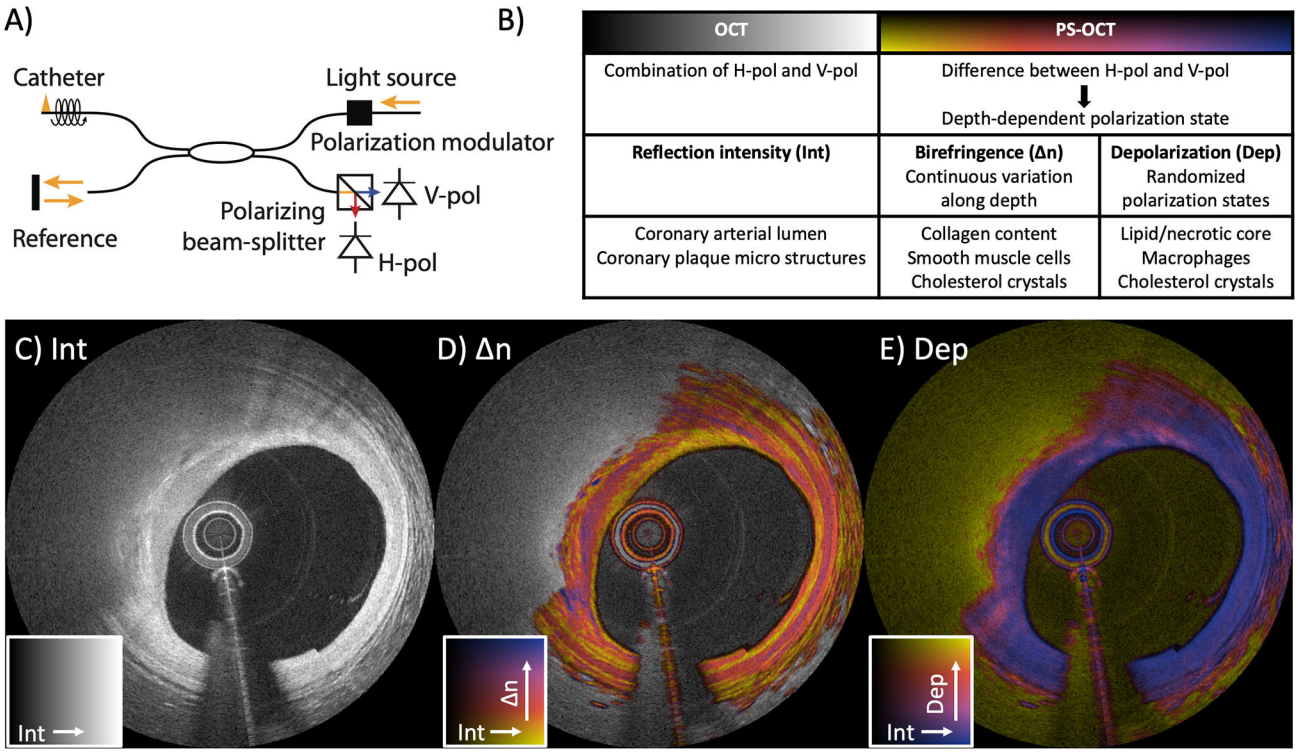

FIGURE 1 | Working principle of intravascular polarimetry (IVP) with polarization-sensitive optical coherence tomography (PS-OCT). IVP is compatible with current intravascular imaging catheters and enables measurements of tissue polarization properties, together with the conventional reflection intensity. **(A)** The only addition to conventional OCT for enabling PS measurements is a polarization modulator that alternates the polarization state of the light incident on the tissue between depth scans. **(B)** Analyzing the spatial variation of the detected states allows reconstruction of birefringence (Δn) and depolarization (Dep), in addition to the conventional reflection intensity image (Int). **(C–E)** IVP of a lipid-rich plaque imaged in the left anterior descending coronary artery of a 75-year-old male patient. **(C)** Intensity (Int) of the reflection signal visualizing subsurface plaque morphology in a conventional logarithmic gray scale. **(D)** Birefringence (Δn) in color hue, overlaid on the reflection signal in brightness, revealing a variety of birefringence features. Birefringence is displayed only in areas of low depolarization. **(E)** Depolarization (Dep) in color hue, overlaid on the reflection signal, showing areas of pronounced depolarization. Reproduced from Villiger et al. (34).

independent of the transmission through the optical fiber, fiber-based PS-OCT furthermore modulates the polarization state of the illumination between consecutive depth-scans (49), although recent work suggests that a single input state may suffice (50). Tissue with fibrillar architecture, such as interstitial collagen or layered arrays of arterial SMCs, exhibits birefringence (Δn), an optical property that results in a differential delay, or retardance, between light polarized parallel to the tissue fibrillar components and light having a perpendicular polarization. The general polarization state of the illumination is a superposition of the parallel and perpendicular components and results in a continuous change of the light's polarization state as it propagates through the birefringent tissue. The experienced retardance is strongest for fibrillar components aligned in a plane orthogonal to the probing beam's direction and vanishes for fibrous tissue that align with the beam's axis. By analyzing the rate of change of the polarization states along depth, we compute a quantitative measurement of the effective depth-resolved tissue birefringence Δn. This is achieved by using our robust reconstruction strategy (42) that mitigates artifacts (41) originating from the polarization effects of the imperfect system components.

The majority of developments in PS-OCT have been focused on employing birefringence as an additional tissue contrast mechanism. Yet, PS-OCT can also measure depolarization to complement birefringence for the polarimetric characterization of tissue (46, 47, 51). In contrast to birefringent tissue, which induces a continuous change of the polarization states along depth but maintains high correlation along the lateral directions, depolarization corresponds to a random change of the polarization states in adjacent resolution volumes along all spatial directions. Depolarization is caused by multiple scattering of light, or by randomly oriented structures with polarization-dependent scattering, as caused by lipid droplets that exceed the size of the wavelength used for OCT or small cholesterol crystals, respectively. Hence, in atherosclerotic tissues, depolarization is observed in plaque regions that are rich in lipid, cholesterol crystals, or macrophages. Depolarization evaluates this randomness in a small neighborhood around each pixel as the ratio of the depolarized signal intensity to the total signal intensity, corresponding to 1 minus the degree of polarization (34, 48). Depolarization ranges from 0 for completely polarized light without any randomness to 1 for completely random polarization

states. In addition to tissue-induced depolarization, regions where the OCT signal falls to the noise floor also appear depolarizing, requiring special consideration when interpreting the depolarization signal.

Displaying both the conventional and polarization channels available to IVP can be conveniently achieved using a color map that encodes the polarization metric as color hue and the conventional reflection signal as brightness. In all figures throughout this review, color maps display the range of 0-1.8 $\times$ 10^{-3} for birefringence, and 0-0.5 for depolarization (**Figure 1**). Given that the randomization of the polarization states frustrates a reliable measure of tissue birefringence, we display the conventional grayscale reflection tomogram in areas of increased depolarization in the birefringence maps.

CHARACTERIZATION OF PLAQUE MICROSTRUCTURES WITH IVP

Birefringence and depolarization are polarization metrics that enable quantitative analysis of intrinsic optical tissue properties related to the composition of coronary plaques. In order to identify the respective tissue components that cause observable polarization effects, we compared polarization properties measured with IVP in human cadaveric coronary arteries with matching histology (34). Birefringence maps reinforce several features that are already discernible in the OCT intensity image. As shown in **Figure 1**, the tunica media appears as a pinkish band with high birefringence, frequently bordered by fine yellow lines of low birefringence at the locations of the internal and external elastic laminae. Conventional OCT images, in comparison, show less pronounced contrast between the intima and the tunica media. Furthermore, fibrous tissue often exhibits heterogeneous birefringence maps across layers that appear homogeneous in the OCT intensity images. In **Figure 1D**, the fibrous cap features heterogeneous birefringence in the region of 9–12 o'clock. The depolarization map reveals low depolarization throughout the full thickness of the vessel wall in areas of adaptive intimal thickening, and abrupt strong depolarization in the lipid-rich area below the fibrous cap.

Figure 2 displays polarization features of several coronary plaque components along with matching histology, as well as measurements of polarization properties of individual tissue types [from (34)]. Quantitative analysis of segmented tissue types revealed the highest birefringence in the tunica media, followed by intimal regions containing fibrous tissue (**Figure 2F**). Consistent with a previous microscopic PS-OCT study (39), these observations suggest that collagen content

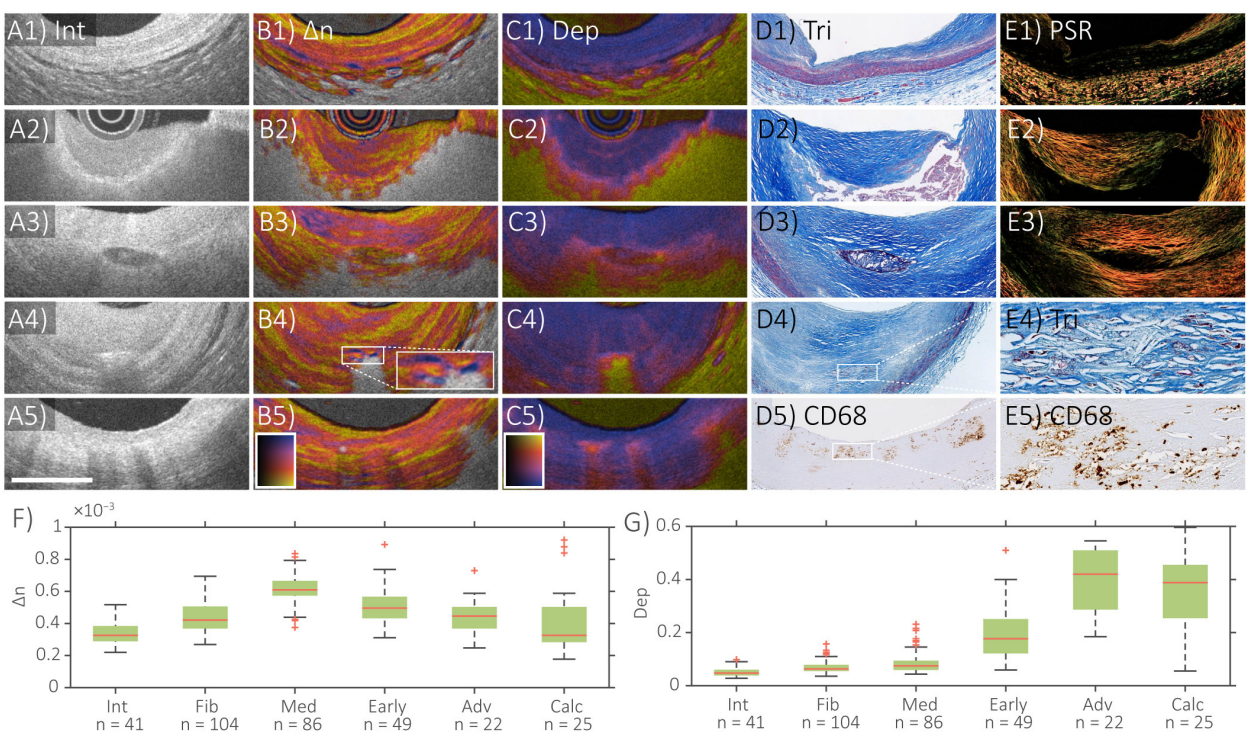

FIGURE 2 | Distinct polarization features of atherosclerotic human coronary arteries *ex vivo*. IVP of **(A1–E1)** normal artery, **(A2–E2)** fibroatheroma, **(A3–E3)** fibrocalcific plaque, **(A4–E4)** cholesterol crystals, and **(A5–E5)** macrophages, with matching histology. **(F)** Median and quartile birefringence (Δn) values in regions with depolarization <0.2 across tissue types. **(G)** Median and quartile depolarization (Dep) values across tissue types. Scale bar, 1 mm. Int, intensity; Δn, birefringence; Dep, depolarization; Tri, trichrome staining; PSR, Picrosirius red staining; In (F), Int, intima; Fib, fibrous tissue; Med, tunica media; Early, early lesions with dispersed lipid; Adv, advanced lesions with lipid pools or necrotic core; Calc, calcifications. Adapted from Villiger et al. (34) and Otsuka et al. (36).

and SMCs are the main source of the birefringence measured with IVP.

The highest depolarization was observed in segmented tissue corresponding to advanced lesions with a lipid/necrotic core (**Figure 2G**). Whereas conventional OCT lacks the ability to identify the presence of a necrotic core, and hence to differentiate between fibroatheroma and pathological intimal thickening (52, 53), depolarization offers additional insight that may enable diagnosis of fibroatheromas containing necrotic cores. In addition to the tissues and plaque components already discussed, **Figure 2** also shows examples of the IVP signatures of a calcification, cholesterol crystals (CCs), and macrophage accumulations. The OCT intensity image depicts calcifications as signal poor or heterogeneous regions with sharply delineated borders (54), while their birefringence is generally lower and the depolarization slightly higher than in fibrous tissue (A3–E3 in **Figure 2**). However, their polarization properties also depend on the presence of lipid in the surrounding tissue. Clinical studies have demonstrated that CCs identified by conventional OCT are related to coronary plaque vulnerability in patients (55–58). CCs appear as thin, linear regions of high intensity signal, usually found in the fibrous cap or even within the necrotic core (54). Confusion of CCs with microcalcifications, however, is possible, since they can cause similar reflection signals (59). Consistent with the known birefringence property and dimensions of CCs, plaque regions containing small disordered CCs depolarize and areas with larger or aligned CCs additionally cause a birefringence signature (34) (A4–E4 in **Figure 2**). IVP may, therefore, improve the objective identification of CCs. In conventional OCT images, macrophage infiltration in the fibrous cap causes confluent punctate regions or signal-rich, distinct, and bright spots that exceed the intensity of background speckle noise (54, 59). With IVP, subtle depolarization was additionally observed in superficial regions infiltrated by macrophages (A5–E5 in **Figure 2**), which may help to automatically detect and quantify the presence of macrophages.

IN VIVO REPEATABILITY OF IVP

We conducted the first-in-man pilot study of IVP at the Erasmus University Medical Center, the Netherlands, to investigate the robustness of IVP in a clinical setting. The quantitative metrics for tissue characterization provided by IVP are only meaningful if they can be evaluated repeatedly and robustly in the coronary arterial wall in patients. IVP employs commercialized OFDI catheters (FastView^{TM}, Terumo Corp., Tokyo, Japan) in combination with a custom console and the imaging procedure is identical to that using a conventional OFDI system (35, 43). To evaluate the reproducibility of the conventional backscatter intensity, the birefringence, and the depolarization signals, we compared each spatial location of 274 matching cross-sectional images among repeated pullbacks imaged in the coronary arteries of 30 patients (44). Bland-Altman analysis demonstrated best agreement for birefringence, followed by backscatter intensity, and depolarization. Pearson's correlation analysis confirmed highest correlation for birefringence ($r = 0.86$), preceding backscatter intensity ($r = 0.83$), and depolarization ($r = 0.78$). This finding confirmed that IVP provides reliable and repeatable measurement of tissue birefringence and depolarization through rotating catheters in a clinical setting and can serve for studying the polarization properties of coronary atherosclerosis in patients.

IVP OF CORONARY PLAQUES IN PATIENTS

Motivated by the robust results of IVP measurements in a clinical setting, we investigated the quantitative polarization features of different plaque types, classified using the conventional OCT morphological appearance, among the plaques found in 30 patients with ACS ($n = 12$) and stable angina pectoris (SAP, $n = 18$) (35). Coronary plaques with a greater lipid content featured reduced birefringence and pronounced depolarization. We also further investigated the polarization features of coronary calcification measured with IVP. Calcification of the coronary artery has been shown to serve as a robust surrogate marker of coronary risk and is related to disease burden of coronary atherosclerosis (60–63). The presence of spotty calcification in coronary atheromatous plaques has been shown to be associated with the high-risk plaque morphology responsible for ACS (60, 62), while dense calcification appeared as a marker of lesion stability (61). **Figure 3** shows IVP of two examples of intimal calcification together with the results from investigating all encountered calcifications within the analyzed cross-sections imaged in the 30 patients. In this sub-analysis, we observed that calcifications in fibrous regions featured lower birefringence compared to those in lipid-rich regions ($p < 0.001$). Although the possible clinical implication of the polarization features within calcifications measured with IVP remains unknown, we anticipate that IVP will provide further insight into the association of calcification and plaque stability.

Collagen is an extracellular matrix protein mainly synthesized by arterial SMC. Thick collagen fibers are known to impart mechanical integrity to fibrous caps (64). Collagen degradation by matrix-metalloproteinases plays a pivotal role in plaque destabilization (1). Because collagen is birefringent, evaluating birefringence can serve as unique metric for studying fibrous cap stability. In the first-in-human study of IVP, we further compared the polarization signatures measured locally in the fibrous caps of culprit lesions between patients with ACS and/or plaque rupture (PR) and patients with SAP (35). **Figure 4** shows a representative IVP image of both categories and the comparison of the polarization properties measured across all fibrous caps in patients with ACS/PR and SAP. The fibrous caps in ACS/PR patients featured significantly lower birefringence than those in SAP patients (35). Based on previous observations from a microscopic PS-OCT study on human aortic plaques *ex vivo* (39), our observation is consistent with a lack of thick collagen fibers or layered arrays of SMCs in ACS/PR fibrous caps. Further research is warranted to investigate how fibrous cap birefringence influences the biomechanical factors that are associated with plaque rupture and subsequent thrombosis

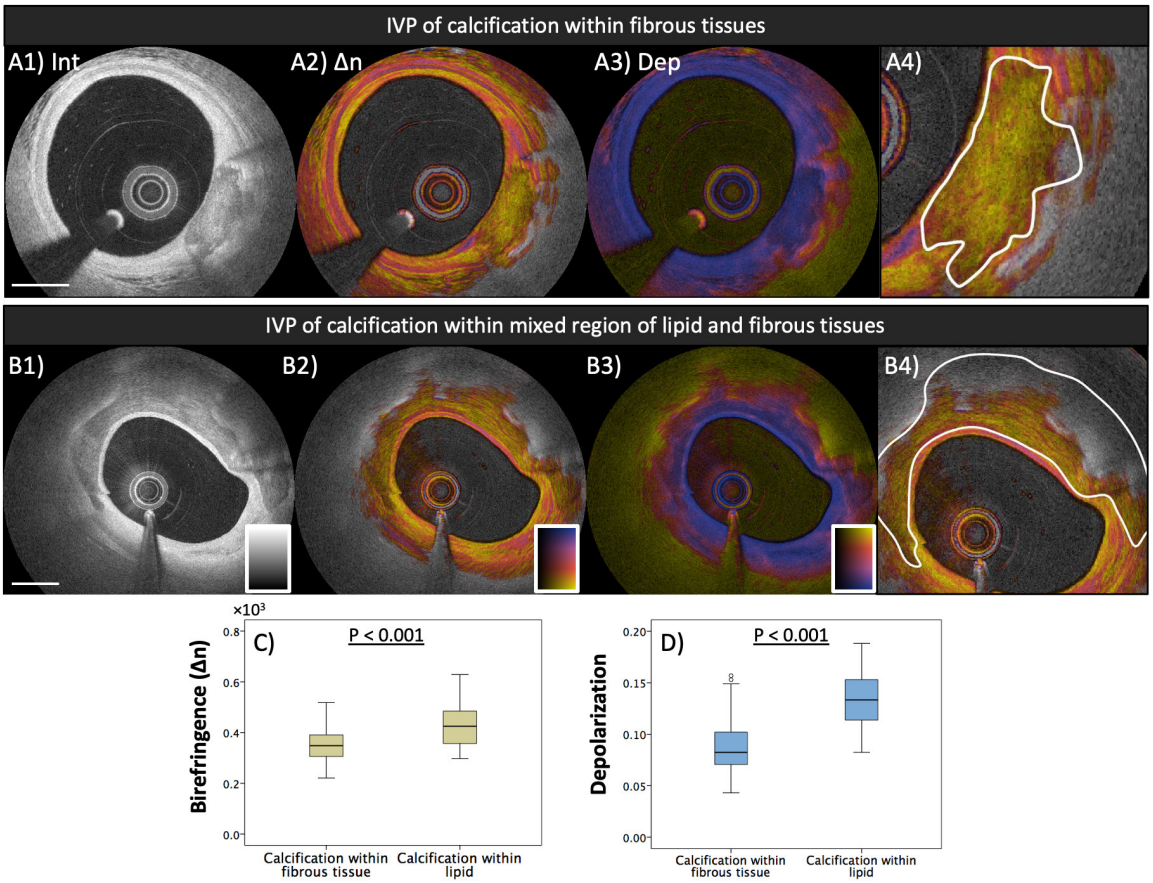

FIGURE 3 | Polarization properties of calcification. Median birefringence and depolarization were measured in calcified areas, manually segmented in the intensity images. Segmented areas were classified according to the presence or absence of lipid in the surrounding lesion (calcification within fibrous tissue or calcification within lipid). **(A1–A4)** IVP of calcification in fibrous tissue and segmentation of the calcified area. **(B1–B4)** Calcification in lipid-rich tissue. **(C)** Calcified areas in fibrous tissue exhibit lower birefringence than those in lipid-rich lesions ($p < 0.001$). **(D)** Higher depolarization was observed in calcified areas in lipid-rich tissue than in those located in fibrous tissue ($p < 0.001$). Adapted from Otsuka et al. (35).

(65, 66). Furthermore, inflammatory activity mainly caused by macrophages contributes to the thinning of the fibrous cap covering a necrotic core and to precipitating plaque rupture (21, 67, 68). In a focal analysis of the thinnest part of the fibrous caps, we found that depolarization correlated positively with normalized standard deviation, a metric based on the reflection intensity signal that has been shown to indicate macrophage accumulation (69–71). Depolarization may help to improve identification of local macrophage accumulation within the fibrous caps and also to automatically delimit the cap border. This may provide robust assessment of fibrous cap thickness without discordance between observers. Despite the promise of the observations with IVP, it should be noted that the influence of microcalcifications on the polarization features as well as their appearance in conventional OCT remain unknown (54, 59). We speculate that the presence of microcalcifications causes a reduction of birefringence in fibrous caps, similar to a lack of well-organized collagen or SMCs. Combination of Micro-OCT imaging (72, 73) with polarimetry may help elucidate the influence of microcalcifications on the polarimetric signatures of coronary plaques.

Although plaque erosion remains challenging to diagnose *in vivo* with OCT, its apparent prevalence in autopsy studies has motivated clinical research focused on studying its pathobiology and on improving therapeutic strategies for patients with ACS caused by this second most common mechanism of coronary thrombosis (68, 74). According to histopathological findings, eroded plaques feature negatively remodeled lesions with SMCs embedded in a proteoglycan-rich extracellular matrix consisting of collagen type III, hyaluronan, and versican (17). While the presence of fibrillar collagen type III may contribute to birefringence, in the IVP pilot study, we observed that fibrous caps of patients with plaque rupture and non-rupture ACS exhibited lower birefringence than those of patients with SAP. Further research is needed to better understand whether IVP may be able to provide additional insights into the mechanisms of ACS caused by plaque erosion.

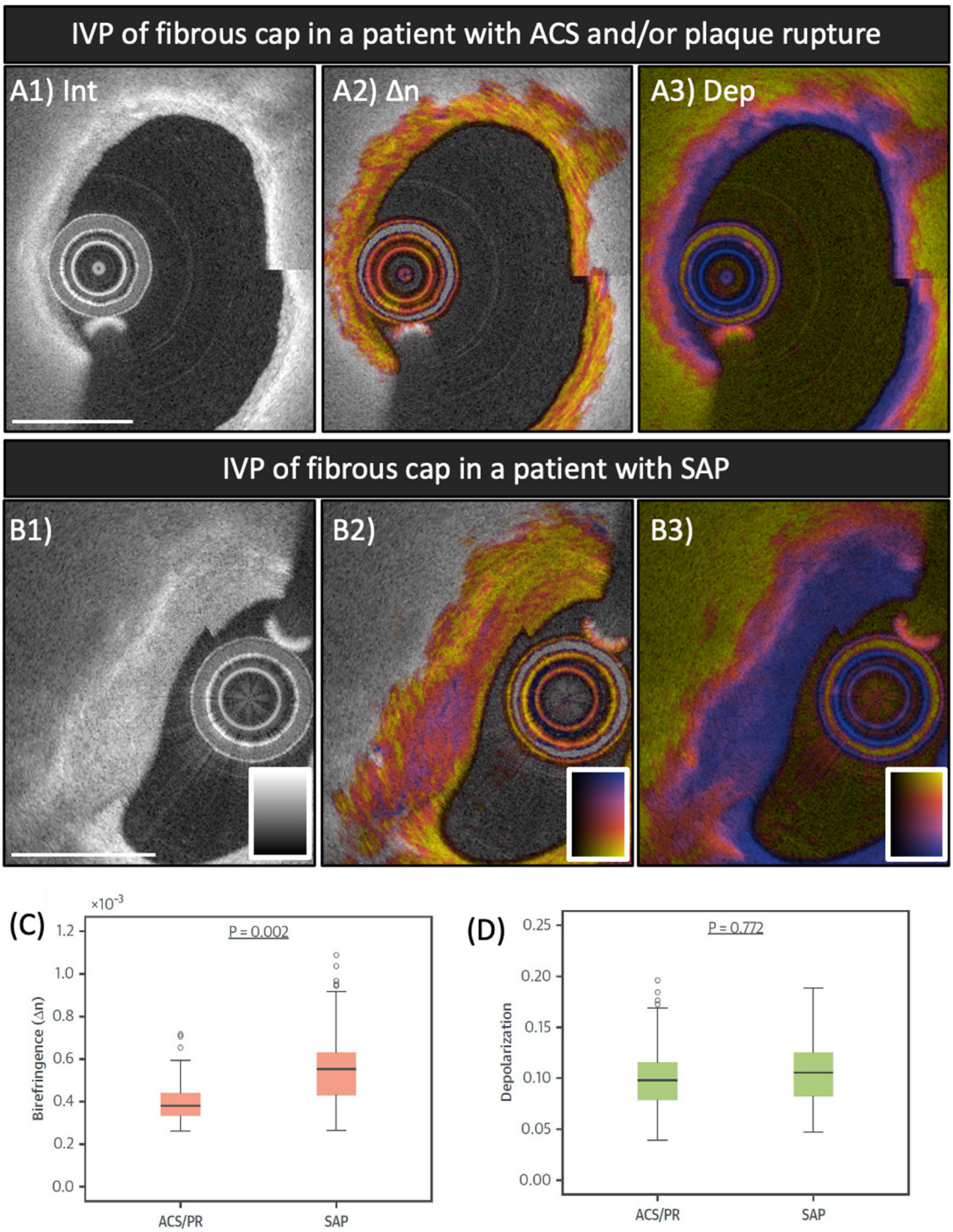

FIGURE 4 | Polarization features of fibrous caps of culprit lesions in ACS and SAP patients. **(A1–A3)** IVP of the culprit lesion in a patient with ACS. **(B1–B3)** IVP of the target lesion in a patient with SAP. **(C,D)** Comparison of mean birefringence and depolarization measured in the segmented fibrous caps between patients with ACS/PR and SAP. Fibrous caps in ACS/PR patients featured significantly lower birefringence compared to those in SAP patients. ACS, acute coronary syndrome; IVP, intravascular polarimetry; PR, plaque rupture; SAP, stable angina pectoris. Reproduced from Otsuka et al. (35, 36).

POLARIZATION SIGNATURES OF ACUTE AND ORGANIZING THROMBUS

Conventional OCT enables the discrimination between white and red acute thrombus based on the attenuation of the intensity signal (**Figures 5A1,B1**). White, platelet-rich thrombus causes little backscattering and appears homogeneous with low signal attenuation (**Figure 5A1**), while red thrombus, mainly composed of erythrocytes, is strongly backscattering with a high signal attenuation (**Figure 5B1**) (54). In the study population of the first-in-human pilot study of IVP, we observed that white thrombus displayed low birefringence and depolarization (**Figures 5A2,A3**) (35), but did not encounter any red thrombus. In the second pilot study of IVP at the Erasmus University Medical Center (POLARIS-I registry), we observed a few red thrombi in the culprit lesions of ACS patients. In the limited number of examples, red thrombus exhibited low birefringence. The apparent increase in depolarization along depth is likely an artifact caused by the rapid decline of the intensity signal along depth within red thrombus (**Figure 5B3**). In the same patient pool, we imaged a suspected culprit vessel of a 69-year-old female patient presenting with non-ST-segment elevation myocardial infarction several days after onset of intermittent chest pain (45). The OCT intensity image revealed honeycomb-like structures in the culprit lesion, which is a well-known OCT-specific feature of recanalization in organized thrombus or chronic total occlusion (26). IVP revealed high birefringence in the honeycomb-like structures (45), suggesting the presence of collagen and SMCs, which should be expected for organizing and healing thrombus.

Extensive research has focused on the mechanisms underlying rapid progression of coronary artery stenosis (22). This is important for the identification of patients at higher risk of coronary ischemic or thrombotic events. It is now widely accepted that only a minority of plaque ruptures and erosions progress to ACS with clinical manifestation. Subsequent thrombus formation and organization, in which the intimal microvasculature plays a pivotal role, are key to understanding the mechanisms of successful or failed vascular healing (24). In a recent *ex vivo* study investigating the accuracy of OCT for diagnosing healed ruptured plaques, Shimokado et al. proposed the presence of layered structures in the conventional OCT intensity signal as a predictor of histologically determined healed ruptures of coronary plaques (75). Furthermore, clinical studies have demonstrated that layered structure in superficial plaques identified by OCT are associated with plaque vulnerability or rapid progression of coronary artery stenosis (10, 76), although there remains some controversy and another study found similar features to indicate enhanced plaque stability (23). Despite the importance of assessing the healing process of coronary thrombus, the conventional OCT intensity image provides limited insight into the process of thrombus organization. The polarization signatures measured with IVP have the potential to characterize

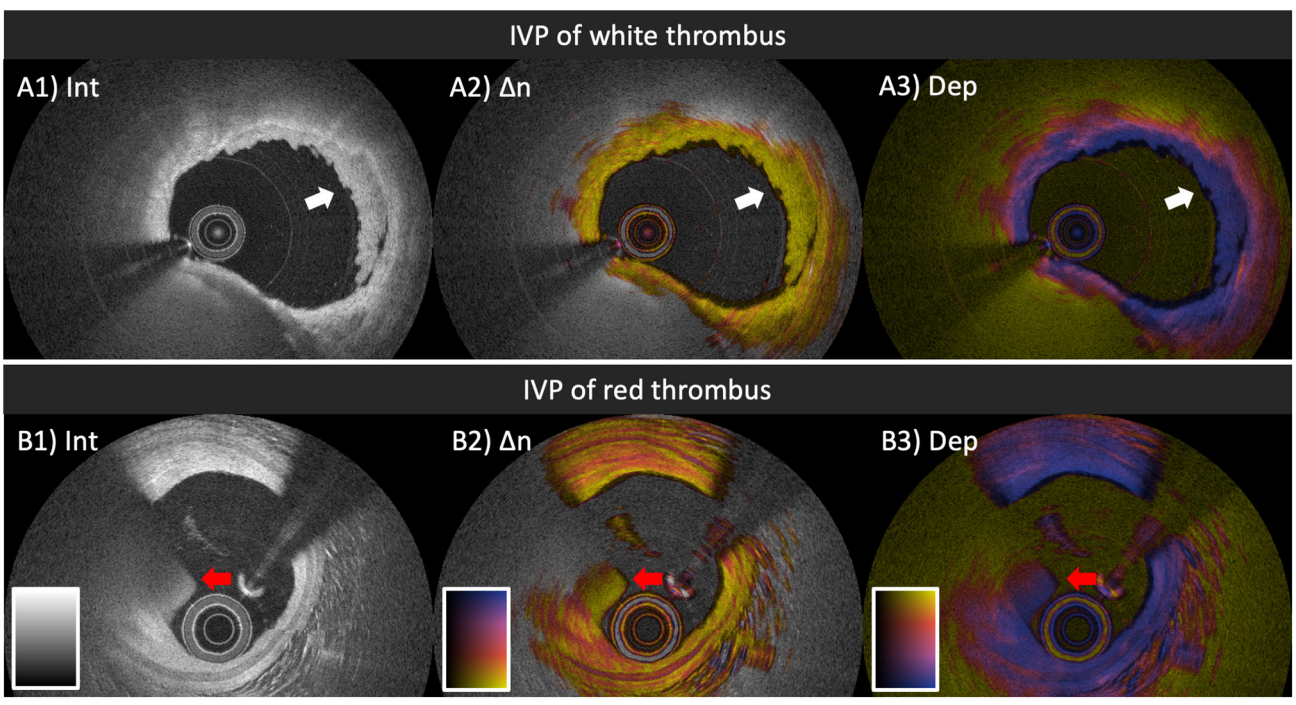

FIGURE 5 | IVP of thrombi in patients with ACS. **(A1–A3)** White thrombus (white arrow) attached to the luminal surface, exhibiting homogeneous backscattering and low attenuation **(A1)**, paired with low birefringence **(A2)** and low depolarization **(A3)**. **(B1–B3)** Red thrombus (red arrow) protruding into the lumen, featuring high backscattering, and attenuation **(B1)**, together with relatively low birefringence **(B2)** and gradually increasing depolarization **(B3)**. IVP, intravascular polarimetry.

the thrombus organization and healing process, since the deposition of collagen type III and later replacement with collagen type I should result in a change in birefringence (23, 77, 78). Assessment of coronary atherosclerosis with IVP *in vivo* may help investigate the mechanisms of impaired vascular healing that lead to ACS.

POLARIZATION SIGNATURES OF TISSUE RESPONSE AFTER STENT IMPLANTATION

The high-resolution of OCT provides detailed visualization of the tissue response to stent implantation, together with the assessment of stent apposition and expansion (79, 80). In

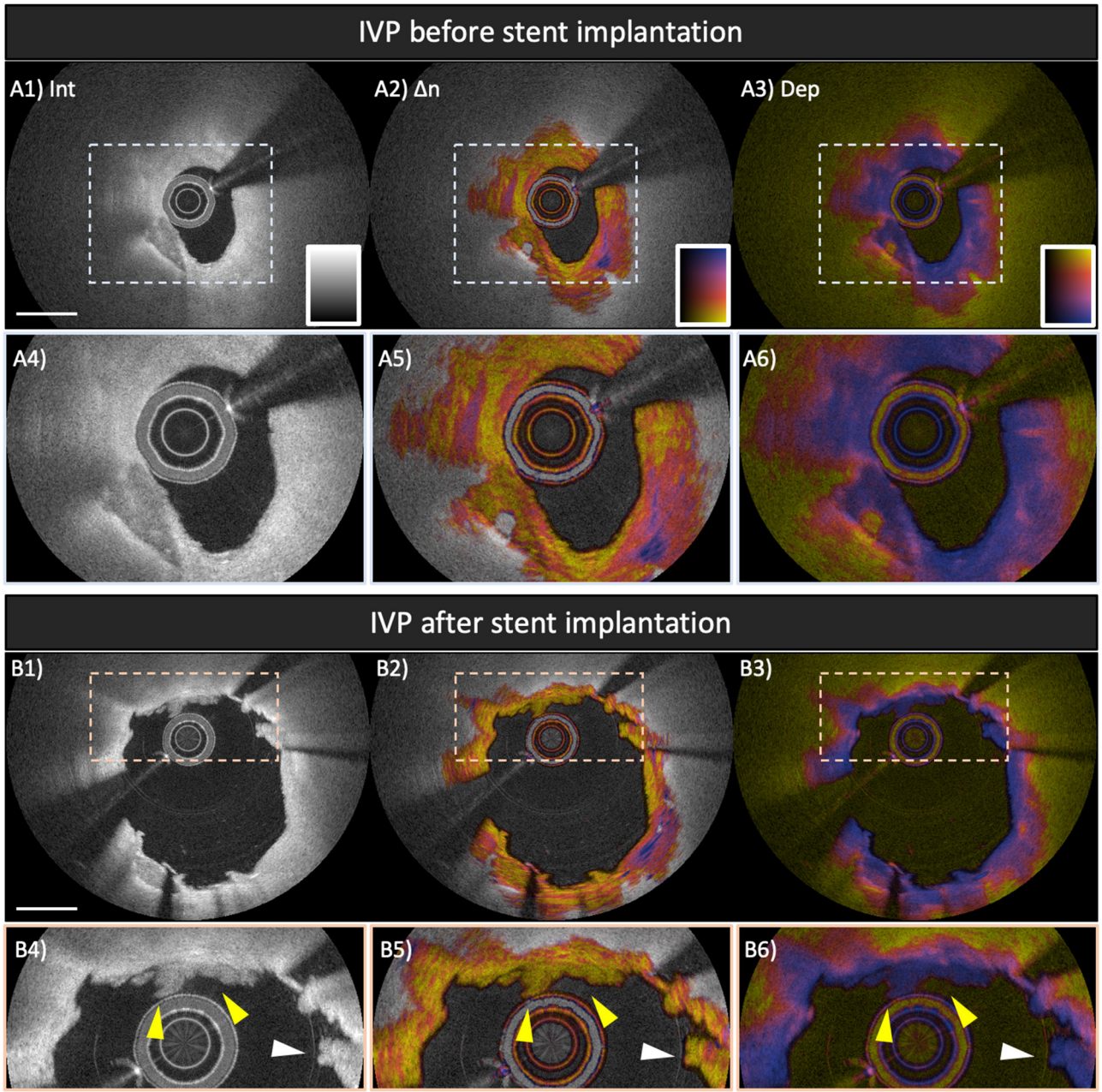

FIGURE 6 | Polarization features pre- and post-stent implantation in the culprit lesion of a patient with non-ST-elevation myocardial infarction. Broken lines in **(A1–A3)** and **(B1–B3)** indicate magnified views shown in **(A4–A6)** and **(B4–B6)**, respectively. **(A1,A4)** IVP of the culprit lesion showing a lipid-rich plaque with calcification at 7 o'clock **(A2, A5)** Birefringence image reveals highly birefringent tissues from 3 to 6 o'clock within the fibrous cap, suggesting well-organized fibrous tissues. **(B1–B6)** Post-stent IVP of the culprit lesion. **(B1,B4)** The reflection intensity images visualize tissue protrusion or prolapse (white arrowhead) and in-stent thrombus formation (yellow arrowheads). IVP clearly reveals in-stent thrombus showing low birefringence and low depolarization, which is the typical IVP appearance of white thrombus **(B2,B5)**. Scale bars indicate 1 mm. IVP, intravascular polarimetry.

addition to the plaque morphology before stent implantation, post-stent OCT features including stent-edge dissection, in-stent thrombus, and protrusion have been shown to be associated with peri-procedural myocardial injury/infarction (58, 81–83) and long-term device-oriented coronary events (84). **Figure 6** shows pre- and post-stent IVP images of the culprit lesion in a non-ST-segment elevation myocardial infarction patient. The intensity image visualizes tissue protrusion or prolapse (white arrowhead in **Figure 6B4**) and in-stent thrombus formation (yellow arrow heads in magnified view of **Figure 6B4**). The IVP image complements the intensity appearance of the in-stent thrombus with low birefringence and depolarization, which is, to the best of our knowledge, the typical IVP appearance of white thrombus. In comparison, the prolapsed tissue contains an area of increased birefringence. Given the additional tissue contrast provided by IVP, it may help to reduce the discordance in image interpretation between observers and may also offer additional insight into the vascular injury and the ensuing healing process of the coronary arterial wall related to stent implantation.

Long-term vascular tissue response to stent implantation is of importance for assessing the risk of stent failure, such as in-stent restenosis and stent thrombosis (25, 85, 86). In a swine study investigating vascular response to bioresorbable vascular scaffold implantation, polarization properties measured with PS-OCT reflected tissue organization and inflammation within the neointima (87). **Figure 7** shows several examples of IVP cross-sections in previously stented coronary arteries encountered in the patient cohorts of our pilot studies. Compared to native intima (**Figure 7A2**) it could be expected that the early neointima in drug-eluting stents exhibits lower birefringence (B2, C2, and D2 in **Figure 7**), owing to a drug-induced suppression of collagen content and SMCs (88). In contrast, the late neointima (7 years after stent implantation, **Figure 7H2**) shows relatively higher birefringence which is comparable to that of native plaques (**Figure 7E2**). A recent study conducted by Suna et al. demonstrated that aggrecan, a major extracellular matrix component of cartilaginous tissues that confers resistance to compression, plays a critical role in arterial remodeling after the

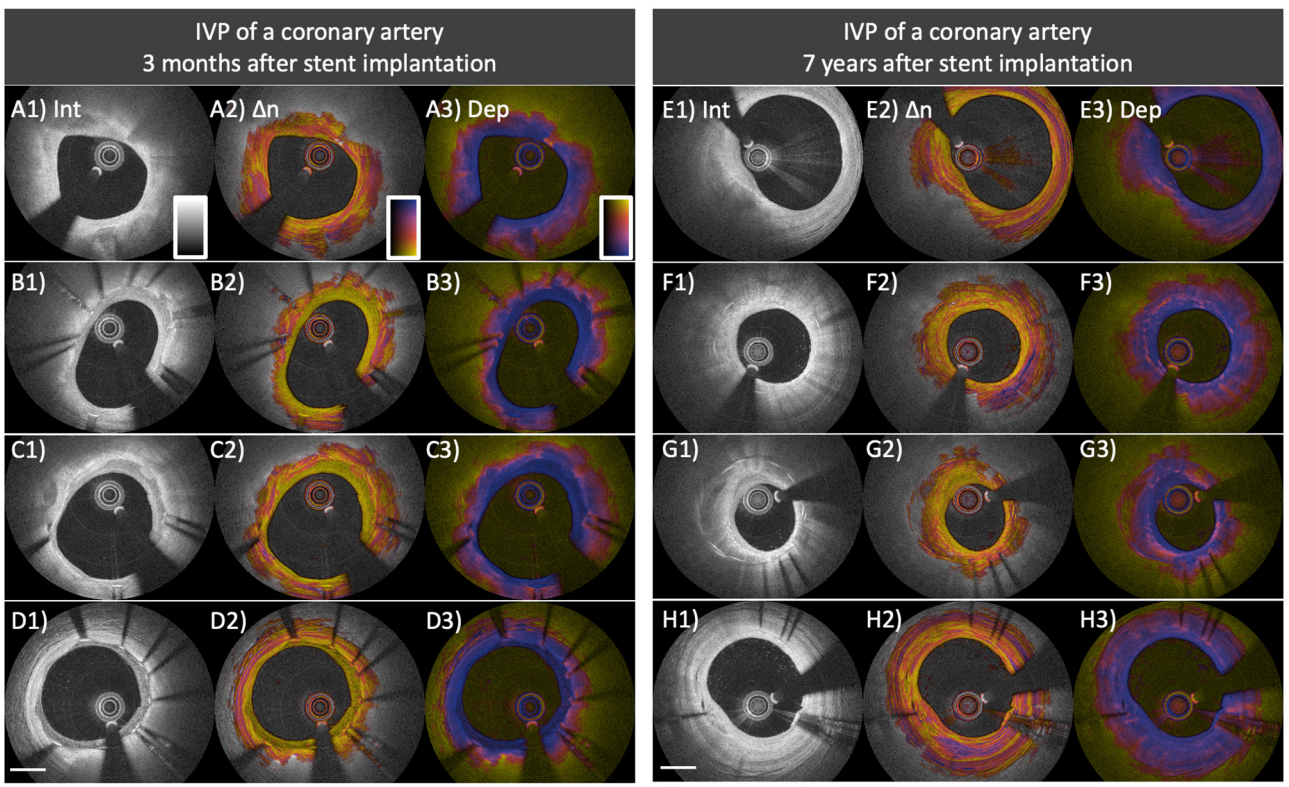

FIGURE 7 | Distinct polarization features of neointima and neoatherosclerosis. **(A–D)** IVP of a coronary artery 3 months after everolimus-eluting stent implantation. **(A1)** Native fibro-calcified plaque proximal of the stented segment. **(B1–D1)** The intensity images within the stented area show early neointima with high **(B1)** to low **(D1)** intensity signal. **(B2–D2)** Birefringence images reveal that early neointima exhibits low birefringence compared to that of the underlying native lesion. **(B3–D3)** Depolarization in early neointimal tissues remains low. **(E–H)** IVP of a coronary artery 7 years after paclitaxel-eluting stent implantation. **(F1)** Native fibro-calcified plaque proximal of the stented segment. **(F1,G1)** The intensity images show neoatherosclerosis featuring calcification, macrophage accumulation, and layered structure. **(F2,G2)** Birefringence images reveal lowly birefringent layered structures close to the surface of the arterial lumen. The layered structure in **(G2)** exhibits lower birefringence compared to the underlying neoatherosclerotic region. **(F3,G3)** Macrophage accumulations within neoatherosclerosis cause pronounced depolarization. **(H2)** The birefringence image of the late neointima without neoatherosclerosis reveals relatively high birefringence, comparable to that of underlying native plaque and the native plaque proximal of the stented segment **(E2)**.

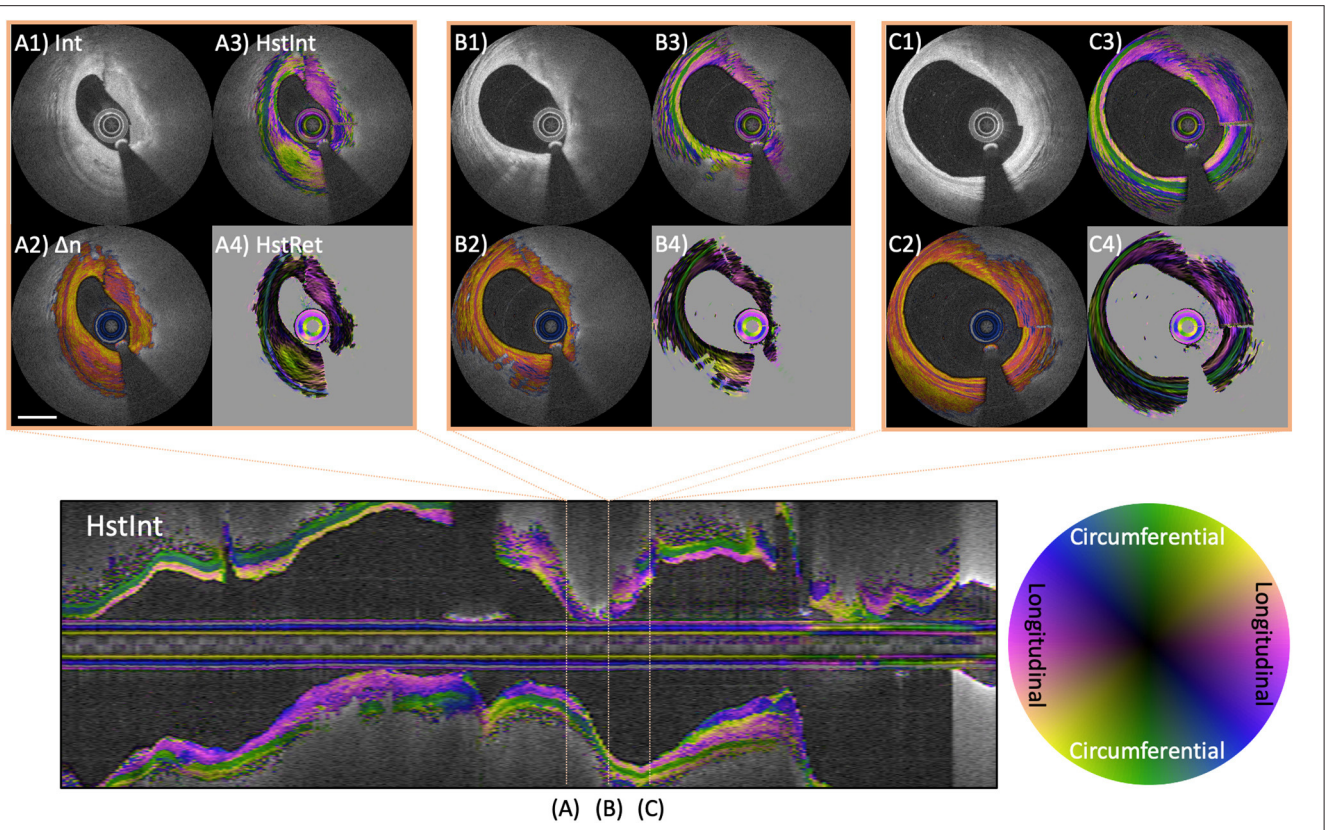

FIGURE 8 | Optic axis orientation in coronary atherosclerotic lesion. Longitudinal image displays the optic axis orientation overlaid on intensity of a coronary artery in a patient with stable angina pectoris. Color indicates axis orientation and brightness specifies intensity. **(A–C)** Three individual cross-sections, showing conventional intensity **(A1,B1,C1)**, birefringence **(A2,B2,C2)**, and depth-resolved optic axis overlaid on intensity **(A3,B3,C3)** or birefringence **(A4,B4,C4)**. The tunica media features green color, indicating circumferential orientation. **(A3,A4)** Heterogeneous optic axis orientation of the intimal fibrous tissue. The fibrous cap in **(B3,B4)** and fibrous areas in **(C3,C4)** feature longitudinal orientation of the optic axis. Scale bar indicates 1 mm.

implantation of drug-eluting stents (DES) (89). Furthermore, the same study showed that the extracellular matrix of the neointima within DES contained less collagen type I, III, and V than the neointima in bare metal stents (89). These findings offer a plausible explanation for the IVP appearance of early neointimal tissues in **Figure 7**, featuring very low birefringence. In addition, neoatherosclerosis (**Figures 7F2,G2**) features a layered pattern with relatively low birefringence. Histopathological studies have demonstrated that ECM deposition and migration of SMC contribute to the healing of thrombus and may result in rapid progression of luminal narrowing leading to ISR (25). Similar to native coronary atherosclerosis, assessing tissue composition with IVP may provide insight into the failure of vascular healing also after stent implantation.

While birefringence serves as a marker of the presence of collagen content and SMCs, depolarization corresponds to the presence of macrophage accumulation and the presence of a lipid/necrotic core (34, 36). Neoatherosclerosis is characterized by the presence of lipid-laden macrophages (85) and depolarization may offer a convenient quantitative metric for its identification (**Figures 7F2,G2**). We anticipate that IVP will advance our understanding of neoatherosclerosis and stent thrombosis, which in turn could improve the risk assessment and patient prognosis in a more personalized and precise manner.

FUTURE PERSPECTIVES

Additional histopathological studies will be needed to clarify in more detail the tissue and plaque morphology that underlies the observed polarization features and improve the interpretation of the quantitative polarization metrics. For instance, investigation of the mechanisms causing depolarization in lipid-rich and necrotic core material may offer a differentiating feature to enable accurate identification of fibroatheromas. Toward a similar goal, the combined use of IVUS and OCT has been shown to offer more accurate diagnosis of TCFAs than each modality alone (52, 90). A single catheter that integrates IVUS and OCT provides intrinsically co-registered cross-sectional images from both modalities (91–93). Combination of IVUS and IVP would be feasible using the same dual-modality catheters and offer the advantages of visualizing the entire lesion-depth with IVUS and more superficial fine structural details with OCT, together with

the improved tissue characterization of IVP. Another strategy toward increased compositional sensitivity could be to combine polarization analysis with detecting spectral absorption features that have been shown to help in the detection of lipid (94–96).

In a further development, we extended our reconstruction method to obtain not only the scalar amount of birefringence, but also its optic axis orientation as a function of depth in the vessel wall (97). The optic axis indicates the physical orientation of the fibrillar tissue structures giving rise to birefringence. More specifically, the optic axis orientation indicates the azimuthal direction of the fibrillar components, i.e., the orientation of their projection into a plane orthogonal to the beam axis. While the measured birefringence depends on the alignment of the fibrillar components with the beam direction, the full three-dimensional orientation of the fiber orientation cannot currently be recovered. Conveniently, in the arterial wall of coronary arteries the fibrillar tissue components can be assumed to be naturally oriented quite orthogonal to the OCT probing beam. As shown in **Figure 8**, the optic axis of fibrous tissues within the intima corresponding to adaptive intimal thickening aligns longitudinally along the vessel direction, while the tunica media features circumferential orientation. In advanced atherosclerotic lesions, the optic axis orientation frequently revealed distinct tissue layers that appear continuous in conventional OCT images and that also feature remarkably uniform scalar birefringence (**Figure 8**). Optic axis orientation may provide unique and mechanistic insight into the progression of coronary atherosclerosis and the tissue response to stent implantation. The vascular healing response is thought to lead to a distinct orientation of the organizing thrombus and the deposited collagen, producing noticeable features in the optic axis orientation. Improving the robustness of the reconstruction of optic axis orientation and histopathologic validation of this metric are still needed.

The *ex vivo* and clinical IVP studies thus far have established that IVP provides robust measurements of polarization properties of coronary atherosclerosis. The polarization signatures enable more detailed tissue characterization than conventional OCT. An important benefit is the quantitative nature of the polarization metrics, which will facilitate their standardization and assist OCT image interpretation. Despite our efforts of developing an intuitive display, the multiple signal channels of IVP are challenging to visualize and interpret. However, they offer the promising opportunity to leverage the powerful capability of state-of-the-art deep learning routines. Advanced machine learning techniques are poised to radically impact imaging-based methods. They can provide image segmentation and interpretation that is too time consuming to be performed manually in real-time but would furnish critical feedback to guide interventions. Artificial neural networks have already been adapted for robust lumen segmentation (98), for classification of intracoronary OCT images (99), and for improved stent strut detection (100). We anticipate that the additional contrast available to IVP paired with advanced deep learning routines will significantly improve the level of detail that can be automatically identified and extracted from IVP pullbacks and will enable robust automated segmentation and classification of coronary atherosclerotic lesions.

Lastly, it is worth pointing out that the spatial resolution of OCT by far exceeds the dimension of individual collagen fibrils and even fibers, or actin and myosin filaments. At best, OCT resolution may be sufficient to resolve collagen bundles. IVP provides insight into the organization and arrangement of tissue fibrils and filaments on a sub-resolution scale by detecting the resulting tissue birefringence. The thickness, density, and linearity of collagen fibrils in their hierarchical organization within the fibrous tissue of the intima all contribute to the observed birefringence. Furthermore, birefringence is non-specific and can also arise from the combined effect of different fibrillar tissue components. In a similar way, multiple mechanisms contribute to tissue depolarization. Current efforts are aimed at elucidating specific polarization effects in the attempt to disentangle the various contributions. Microscopic spatial resolution would help to identify specific tissue substrates but remains incompatible with imaging in a clinical setting.

CONCLUSIONS

IVP is an extension of conventional OCT that measures polarization properties of the coronary arterial wall through standard commercial imaging catheters and without altering the imaging procedure. Birefringence relates to the collagen and smooth muscle content, which is an important determinant of plaque stability and vascular healing. Depolarization highlights the presence of lipid and macrophages. The quantitative nature of the polarization metrics offers a pathway beyond the qualitative interpretation of conventional tomograms and toward automated identification of critical features, such as fibrous cap thickness. The improved insight into plaque composition afforded by IVP provides new opportunities to investigate disease progression and development of ACS. IVP may provide surrogate markers for improving risk stratification of patients with coronary artery disease.

AUTHOR CONTRIBUTIONS

All authors have participated in the drafting of the manuscript and have approved the final version of the manuscript.

FUNDING

This work was supported by the National Institutes of Health (grants P41EB-015903 and R01HL-119065) and by Terumo Corporation. BB was supported in part by the Professor Andries Querido visiting professorship of the Erasmus University Medical Center in Rotterdam.

ACKNOWLEDGMENTS

KO acknowledges partial support from the Japan Heart Foundation Bayer Yakuhin Research Grant Abroad, the Uehara Memorial Foundation Postdoctoral Fellowship, and the Japan Society for the Promotion of Science Overseas Research Fellowship.

REFERENCES

1. Libby P. Mechanisms of acute coronary syndromes and their implications for therapy. *N Engl J Med.* (2013) 368:2004–13. doi: 10.1056/NEJMra1216063
2. Benjamin EJ, Muntner P, Alonso A, Bittencourt MS, Callaway CW, Carson AP, et al. Heart disease and stroke statistics-2019 update: a report from the american heart association. *Circulation*. (2019) 139:e56–28. doi: 10.1161/CIR.0000000000000659
3. Fox KAA, Metra M, Morais J, Atar D. The myth of "stable" coronary artery disease. *Nat Rev Cardiol*. (2019) 17:9–21. doi: 10.1038/s41569-019-0233-y
4. Tarkin JM, Dweck MR, Evans NR, Takx RAP, Brown AJ, Tawakol A, et al. Imaging atherosclerosis. *Circ Res.* (2016) 118:750–69. doi: 10.1161/CIRCRESAHA.115.306247
5. Stone GW, Mintz GS, Virmani R. Vulnerable plaques, vulnerable patients, and intravascular imaging. *J Am Coll Cardiol.* (2018) 72:2022–6. doi: 10.1016/j.jacc.2018.09.010
6. Bouma BE, Villiger M, Otsuka K, Oh W-Y. Intravascular optical coherence tomography [Invited]. *Biomed Opt Express.* (2017) 8:2660–86. doi: 10.1364/BOE.8.002660
7. Ali ZA, Maehara A, Genereux P, Shlofmitz RA, Fabbiocchi F, Nazif TM, et al. Optical coherence tomography compared with intravascular ultrasound and with angiography to guide coronary stent implantation (ILUMIEN III: OPTIMIZE PCI): a randomised controlled trial. *Lancet*. (2016) 388:2618–28. doi: 10.1016/S0140-6736(16)31922-5
8. Meneveau N, Souteyrand G, Motreff P, Caussin C, Amabile N, Ohlmann P, et al. Optical coherence tomography to optimize results of percutaneous coronary intervention in patients with non-ST-elevation acute coronary syndrome: results of the multicenter, randomized doctors study. *Circulation.* (2016) 134:906–17. doi: 10.1161/CIRCULATIONAHA.116.024393
9. Ramasamy A, Chen Y, Zanchin T, Jones DA, Rathod K, Jin C, et al. Optical coherence tomography enables more accurate detection of functionally significant intermediate non-left main coronary artery stenoses than intravascular ultrasound: a meta-analysis of 6919 patients and 7537 lesions. *Int J Cardiol*. (2019) 301:226–34. doi: 10.1016/j.ijcard.2019.09.067
10. Yamamoto MH, Yamashita K, Matsumura M, Fujino A, Ishida M, Ebara S, et al. Serial 3-vessel optical coherence tomography and intravascular ultrasound analysis of changing morphologies associated with lesion progression in patients with stable angina pectoris. *Circ Cardiovasc Imaging.* (2017) 10:e006347. doi: 10.1161/CIRCIMAGING.117.006347
11. Räber L, Koskinas KC, Yamaji K, Taniwaki M, Roffi M, Holmvang L, et al. Changes in coronary plaque composition in patients with acute myocardial infarction treated with high-intensity statin therapy (IBIS-4): a serial optical coherence tomography study. *JACC Cardiovasc Imaging.* (2019) 12:1518–28. doi: 10.1016/j.jcmg.2018.08.024
12. Xing L, Higuma T, Wang Z, Aguirre AD, Mizuno K, Takano M, et al. Clinical significance of lipid-rich plaque detected by optical coherence tomography: a 4-year follow-up study. *J Am Coll Cardiol.* (2017) 69:2502–13. doi: 10.1016/S0735-1097(17)34364-4
13. Kubo T, Maehara A, Mintz GS, Doi H, Tsujita K, Choi SY, et al. The dynamic nature of coronary artery lesion morphology assessed by serial virtual histology intravascular ultrasound tissue characterization. *J Am Coll Cardiol.* (2010) 55:1590–7. doi: 10.1016/j.jacc.2009.07.078
14. Stone GW, Maehara A, Lansky AJ, de Bruyne B, Cristea E, Mintz GS, et al. A prospective natural-history study of coronary atherosclerosis. *N Engl J Med.* (2011) 364:226–35. doi: 10.1056/NEJMoa1002358
15. Cheng JM, Garcia-Garcia HM, de Boer SPM, Kardys I, Heo JH, Akkerhuis KM, et al. *In vivo* detection of high-risk coronary plaques by radiofrequency intravascular ultrasound and cardiovascular outcome: results of the ATHEROREMO-IVUS study. *Eur Heart J.* (2014) 35:639–47. doi: 10.1093/eurheartj/eht484
16. Arbab-Zadeh A, Fuster V. The myth of the "vulnerable plaque": transitioning from a focus on individual lesions to atherosclerotic disease burden for coronary artery disease risk assessment. *J Am Coll Cardiol.* (2015) 65:846–55. doi: 10.1016/j.jacc.2014.11.041
17. Libby P, Pasterkamp G. Requiem for the "vulnerable plaque." *Eur Heart J.* (2015) 36:2984–7. doi: 10.1093/eurheartj/ehv349
18. Noguchi T, Kawasaki T, Tanaka A, Yasuda S, Goto Y, Ishihara M, et al. High-intensity signals in coronary plaques on noncontrast T1-weighted magnetic resonance imaging as a novel determinant of coronary events. *J Am Coll Cardiol.* (2014) 63:989–99. doi: 10.1016/j.jacc.2013.11.034
19. Otsuka K, Fukuda S, Tanaka A, Nakanishi K, Taguchi H, Yoshiyama M, et al. Prognosis of vulnerable plaque on computed tomographic coronary angiography with normal myocardial perfusion image. *Eur Heart J Cardiovasc Imaging.* (2014) 15:332–40. doi: 10.1093/ehjci/jet232
20. Motoyama S, Ito H, Sarai M, Kondo T, Kawai H, Nagahara Y, et al. Plaque characterization by coronary computed tomography angiography and the likelihood of acute coronary events in mid-term follow-up. *J Am Coll Cardiol.* (2015) 66:337–46. doi: 10.1016/j.jacc.2015.05.069
21. Bentzon JF, Otsuka F, Virmani R, Falk E. Mechanisms of plaque formation and rupture. *Circ Res.* (2014) 114:1852–66. doi: 10.1161/CIRCRESAHA.114.302721
22. Ahmadi A, Leipsic J, Blankstein R, Taylor C, Hecht H, Stone GW, et al. Do plaques rapidly progress prior to myocardial infarction? The interplay between plaque vulnerability and progression. *Circ Res.* (2015) 117:99–104. doi: 10.1161/CIRCRESAHA.117.305637
23. Vergallo R, Porto I, D'Amario D, Annibali G, Galli M, Benenati S, et al. Coronary atherosclerotic phenotype and plaque healing in patients with recurrent acute coronary syndromes compared with patients with long-term clinical stability: an *in vivo* optical coherence tomography study. *JAMA Cardiol.* (2019) 4:321–9. doi: 10.1001/jamacardio.2019.0275
24. Brezinski M, Willard F, Rupnick M. Inadequate intimal angiogenesis as a source of coronary plaque instability. *Circulation.* (2019) 140:1857–9. doi: 10.1161/CIRCULATIONAHA.119.042192
25. Otsuka F, Byrne RA, Yahagi K, Mori H, Ladich E, Fowler DR, et al. Neoatherosclerosis : overview of histopathologic findings and implications for intravascular imaging assessment. *Eur Heart J.* (2015) 36:2147–59. doi: 10.1093/eurheartj/ehv205
26. Lutter C, Mori H, Yahagi K, Ladich E, Joner M, Ms RK, et al. Histopathological differential diagnosis of optical coherence tomographic image interpretation after stenting. *JACC Cardiovasc Intervent.* (2016) 9:2511–23. doi: 10.1016/j.jcin.2016.09.016
27. Joner M, Koppara T, Byrne RA, Castellanos MI, Lewerich J, Novotny J, et al. Neoatherosclerosis in patients with coronary stent thrombosis: findings from optical coherence tomography imaging (A report of the PRESTIGE consortium). *JACC Cardiovasc Intervent.* (2018) 11:1340–50. doi: 10.1016/j.jcin.2018.02.029
28. Torii R, Tenekecioglu E, Katagiri Y, Chichareon P, Sotomi Y, Dijkstra J, et al. The impact of plaque type on strut embedment/protrusion and shear stress distribution in bioresorbable scaffold. *Eur Heart J Cardiovasc Imaging*. (2019) 21:155. doi: 10.1093/ehjci/jez155
29. Suter MJ, Nadkarni SK, Weisz G, Tanaka A, Jaffer FA, Bouma BE, et al. Intravascular optical imaging technology for investigating the coronary artery. *JACC Cardiovasc Imaging.* (2011) 4:1022–39. doi: 10.1016/j.jcmg.2011.03.020
30. Bourantas CV, Jaffer FA, Gijsen FJ, Van Soest G, Madden SP, Courtney BK, et al. Hybrid intravascular imaging: recent advances, technical considerations, and current applications in the study of plaque pathophysiology. *Eur Heart J.* (2017) 38:400–12. doi: 10.1093/eurheartj/ehw097
31. Hee MR, Swanson EA, Fujimoto JG, HD. Polarization-sensitive low-coherence reflectometer for birefringence characterization and ranging. *J Opt Soc Am B.* (1992) 9:903. doi: 10.1364/JOSAB.9.000903
32. de Boer JF, Milner TE, van Gemert MJ, Nelson JS. Two-dimensional birefringence imaging in biological tissue by polarization-sensitive optical coherence tomography. *Opt Lett.* (1997) 22:934–6. doi: 10.1364/OL.22.000934
33. de Boer JF, Hitzenberger CK, Yasuno Y. Polarization sensitive optical coherence tomography - a review [Invited]. *Biomed Opt Express.* (2017) 8:1838–73. doi: 10.1364/BOE.8.001838
34. Villiger M, Otsuka K, Karanasos A, Doradla P, Ren J, Lippok N, et al. Coronary plaque microstructure and composition modify optical polarization. *JACC Cardiovasc Imaging.* (2018) 11:1666–76. doi: 10.1016/j.jcmg.2017.09.023
35. Otsuka K, Villiger M, Karanasos A, Van Znadvoort L, Doradla P, Ren J, et al. Intravascular polarimetry in patients with coronary artery disease. *JACC Cardiovasc Imaging.* (2019) 13:790–801. doi: 10.1016/j.jcmg.2019.06.015

36. Otsuka K, Villiger M, Nadkarni SK, Bouma BE. Intravascular polarimetry for tissue characterization of coronary atherosclerosis. *Circ Rep*. (2019) 1:550–7. doi: 10.1253/circrep.CR-19-0102
37. Giattina SD, Courtney BK, Herz PR, Harman M, Shortkroff S, Stamper DL, et al. Assessment of coronary plaque collagen with polarization sensitive optical coherence tomography (PS-OCT). *Int J Cardiol.* (2006) 107:400–9. doi: 10.1016/j.ijcard.2005.11.036
38. Kuo W-C, Chou N-K, Chou C, Lai C-M, Huang H-J, Wang S-S, et al. Polarization-sensitive optical coherence tomography for imaging human atherosclerosis. *Appl Opt.* (2007) 46:2520–7. doi: 10.1364/AO.46.002520
39. Nadkarni SK, Pierce MC, Park BH, de Boer JF, Whittaker P, Bouma BE, et al. Measurement of collagen and smooth muscle cell content in atherosclerotic plaques using polarization-sensitive optical coherence tomography. *J Am Coll Cardiol.* (2007) 49:1474–81. doi: 10.1016/j.jacc.2006.11.040
40. Pierce M, Shishkov M, Park B, Nassif N, Bouma B, Tearney G, et al. Effects of sample arm motion in endoscopic polarization-sensitive optical coherence tomography. *Opt Express.* (2005) 13:5739–49. doi: 10.1364/OPEX.13.005739
41. Villiger M, Zhang EZ, Nadkarni S, Oh W-Y, Bouma BE, Vakoc BJ. Artifacts in polarization-sensitive optical coherence tomography caused by polarization mode dispersion. *Opt Lett.* (2013) 38:923–5. doi: 10.1364/OL.38.000923
42. Villiger M, Zhang EZ, Nadkarni SK, Oh W-Y, Vakoc BJ, Bouma BE. Spectral binning for mitigation of polarization mode dispersion artifacts in catheter-based optical frequency domain imaging. *Opt Express.* (2013) 21:16353. doi: 10.1364/OE.21.016353
43. van der Sijde JN, Karanasos A, Villiger M, Bouma BE, Regar E. First-in-man assessment of plaque rupture by polarization-sensitive optical frequency domain imaging *in vivo*. *Eur Heart J.* (2016) 37:1932. doi: 10.1093/eurheartj/ehw179
44. Villiger M, Otsuka K, Karanasos A, Doradla P, Ren J, Lippok N, et al. Repeatability assessment of intravascular polarimetry in patients. *IEEE Trans Med Imaging.* (2018) 37:1618–25. doi: 10.1109/TMI.2018.2815979
45. van Zandvoort L, Otsuka K, Bouma B, Daemen J. Intracoronary polarimetry in honeycomb case. *EuroIntervention*. (2019) doi: 10.4244/eij-d-19-00431. [Epub ahead of print].
46. Adie SG, Hillman TR, Sampson DD. Detection of multiple scattering in optical coherence tomography using the spatial distribution of stokes vectors. *Opt Express.* (2007) 15:18033–49. doi: 10.1364/OE.15.018033
47. Gotzinger E, Pircher M, Geitzenauer W, Ahlers C, Baumann B, Michels S, et al. Retinal pigment epithelium segmentation by polarization sensitive optical coherence tomography. *Opt Express.* (2008) 16:16410–22. doi: 10.1364/OE.16.016410
48. Lippok N, Villiger M, Bouma BE. Degree of polarization (uniformity) and depolarization index: unambiguous depolarization contrast for optical coherence tomography. *Opt Lett.* (2015) 40:3954–7. doi: 10.1364/OL.40.003954
49. Saxer CE, de Boer JF, Park BH, Zhao Y, Chen Z, Nelson JS. High-speed fiber based polarization-sensitive optical coherence tomography of *in vivo* human skin. *Opt Lett.* (2000) 25:1355–7. doi: 10.1364/OL.25.001355
50. Xiong Q, Wang N, Liu X, Chen S, Braganza CS, Bouma BE, et al. Constrained polarization evolution simplifies depth-resolved retardation measurements with polarization-sensitive optical coherence tomography. *Biomed Opt Express.* (2019) 10:5207–22. doi: 10.1364/BOE.10.005207
51. Lippok N, Villiger M, Albanese A, Meijer EFJ, Chung K, Padera TP, et al. Depolarization signatures map gold nanorods within biological tissue. *Nat Photonics.* (2017) 11:583–8. doi: 10.1038/nphoton.2017.128
52. Nakano M, Yahagi K, Yamamoto H, Taniwaki M, Otsuka F, Ladich ER, et al. Additive value of integrated backscatter IVUS for detection of vulnerable plaque by optical frequency domain imaging: an *ex vivo* autopsy study of human coronary arteries. *JACC Cardiovasc Imaging.* (2016) 9:163–72. doi: 10.1016/j.jcmg.2015.07.011
53. Phipps JE, Hoyt T, Vela D, Wang T, Michalek JE, Buja LM, et al. Diagnosis of thin-capped fibroatheromas in intravascular optical coherence tomography images: effects of light scattering. *Circ Cardiovasc Intervent.* (2016) 9:3163. doi: 10.1161/CIRCINTERVENTIONS.115.003163
54. Tearney GJ, Regar E, Akasaka T, Adriaenssens T, Barlis P, Bezerra HG, et al. Consensus standards for acquisition, measurement, and reporting of intravascular optical coherence tomography studies: a report from the International working group for intravascular optical coherence tomography standardization and validation. *J Am Coll Cardiol.* (2012) 59:1058–72. doi: 10.1016/j.jacc.2011.09.079
55. Dai J, Tian J, Hou J, Xing L, Liu S, Ma L, et al. Association between cholesterol crystals and culprit lesion vulnerability in patients with acute coronary syndrome: an optical coherence tomography study. *Atherosclerosis.* (2016) 247:111–7. doi: 10.1016/j.atherosclerosis.2016.02.010
56. Nishimura S, Ehara S, Hasegawa T, Matsumoto K, Yoshikawa J, Shimada K. Cholesterol crystal as a new feature of coronary vulnerable plaques: an optical coherence tomography study. *J Cardiol.* (2017) 69:253–9. doi: 10.1016/j.jjcc.2016.04.003
57. Fujiyoshi K, Minami Y, Ishida K, Kato A, Katsura A, Muramatsu Y, et al. Incidence, factors, and clinical significance of cholesterol crystals in coronary plaque: an optical coherence tomography study. *Atherosclerosis.* (2019) 283:79–84. doi: 10.1016/j.atherosclerosis.2019.02.009
58. Otsuka K, Shimada K, Ishikawa H, Nakamura H, Katayama H, Takeda H, et al. Usefulness of pre- and post-stent optical frequency domain imaging findings in the prediction of periprocedural cardiac troponin elevation in patients with coronary artery disease. *Heart Vessels.* (2019) 35:451–62. doi: 10.1007/s00380-019-01512-z
59. Tearney GJ. OCT imaging of macrophages: a bright spot in the study of inflammation in human atherosclerosis. *JACC Cardiovasc Imaging.* (2015) 8:73–5. doi: 10.1016/j.jcmg.2014.09.019
60. Ehara S, Kobayashi Y, Yoshiyama M, Shimada K, Shimada Y, Fukuda D, et al. Spotty calcification typifies the culprit plaque in patients with acute myocardial infarction: an intravascular ultrasound study. *Circulation.* (2004) 110:3424–9. doi: 10.1161/01.CIR.0000148131.41425.E9
61. Criqui MH, Denenberg JO, Ix JH, McClelland RL, Wassel CL, Rifkin DE, et al. Calcium density of coronary artery plaque and risk of incident cardiovascular events. *JAMA.* (2014) 311:271–8. doi: 10.1001/jama.2013.282535
62. Nakahara T, Dweck MR, Narula N, Pisapia D, Narula J, Strauss HW. Coronary artery calcification: from mechanism to molecular imaging. *JACC Cardiovasc Imaging.* (2017) 10:582–93. doi: 10.1016/j.jcmg.2017.03.005
63. Lee SE, Chang HJ, Sung JM, Park HB, Heo R, Rizvi A, et al. Effects of statins on coronary atherosclerotic plaques: the PARADIGM study. *JACC Cardiovasc Imaging.* (2018) 11:1475–84. doi: 10.1016/j.jcmg.2018.04.015
64. Brown AJ, Teng Z, Evans PC, Gillard JH, Samady H, Bennett MR. Role of biomechanical forces in the natural history of coronary atherosclerosis. *Nat Rev Cardiol.* (2016) 13:210–20. doi: 10.1038/nrcardio.2015.203
65. Kwak BR, Bäck M, Bochaton-Piallat M-L, Caligiuri G, Daemen MJAP, Davies PF, et al. Biomechanical factors in atherosclerosis: mechanisms and clinical implications. *Eur Heart J.* (2014) 35:3013–20. doi: 10.1093/eurheartj/ehu353
66. Doradla P, Otsuka K, Nadkarni A, Villiger M, Karanasos A, van Zandvoort LJC, et al. Biomechanical stress profiling of coronary atherosclerosis: identifying a multifactorial metric to evaluate plaque rupture risk. *JACC Cardiovasc Imaging.* (2019) 13:804–16. doi: 10.1016/j.jcmg.2019.01.033
67. Narula J, Nakano M, Virmani R, Kolodgie FD, Petersen R, Newcomb R, et al. Histopathologic characteristics of atherosclerotic coronary disease and implications of the findings for the invasive and noninvasive detection of vulnerable plaques. *J Am Coll Cardiol.* (2013) 61:1041–51. doi: 10.1016/j.jacc.2012.10.054
68. Crea F, Liuzzo G. Pathogenesis of acute coronary syndromes. *J Am Coll Cardiol.* (2013) 61:1–11. doi: 10.1016/j.jacc.2012.07.064
69. Tearney GJ, Yabushita H, Houser SL, Aretz HT, Jang IK, Schlendorf KH, et al. Quantification of macrophage content in atherosclerotic plaques by optical coherence tomography. *Circulation.* (2003) 107:113–9. doi: 10.1161/01.CIR.0000044384.41037.43
70. Phipps JE, Vela D, Hoyt T, Halaney DL, Mancuso JJ, Buja LM, et al. Macrophages and intravascular OCT bright spots: a quantitative study. *JACC Cardiovasc Imaging.* (2015) 8:63–72. doi: 10.1016/j.jcmg.2014.07.027
71. Di Vito L, Agozzino M, Marco V, Ricciardi A, Concardi M, Romagnoli E, et al. Identification and quantification of macrophage presence in coronary atherosclerotic plaques by optical coherence tomography. *Eur Heart J Cardiovasc Imaging.* (2015) 16:807–13. doi: 10.1093/ehjci/jeu307
72. Liu L, Gardecki JA, Nadkarni SK, Toussaint JD, Yagi Y, Bouma BE, et al. Imaging the subcellular structure of human coronary atherosclerosis

using micro-optical coherence tomography. *Nat Med.* (2011) 17:1010–4. doi: 10.1038/nm.2409
73. Nishimiya K, Yin B, Piao Z, Ryu J, Osman H, Leung HM, et al. Micro-optical coherence tomography for endothelial cell visualization in the coronary arteries. *JACC Cardiovasc Imaging.* (2019) 12:1878–80. doi: 10.1016/j.jcmg.2019.01.021
74. Jia H, Abtahian F, Aguirre AD, Lee S, Chia S, Lowe H, et al. *In vivo* diagnosis of plaque erosion and calcified nodule in patients with acute coronary syndrome by intravascular optical coherence tomography. *J Am Coll Cardiol.* (2013) 62:1748–58. doi: 10.1016/j.jacc.2013.05.071
75. Shimokado A, Matsuo Y, Kubo T, Nishiguchi T, Taruya A, Teraguchi I, et al. *In vivo* optical coherence tomography imaging and histopathology of healed coronary plaques. *Atherosclerosis.* (2018) 275:35–42. doi: 10.1016/j.atherosclerosis.2018.05.025
76. Fracassi F, Crea F, Sugiyama T, Yamamoto E, Uemura S, Vergallo R, et al. Healed culprit plaques in patients with acute coronary syndromes. *J Am Coll Cardiol.* (2019) 73:2253–63. doi: 10.1016/j.jacc.2018.10.093
77. Burke AP, Kolodgie FD, Farb A, Weber DK, Malcom GT, Smialek J, et al. Healed plaque ruptures and sudden coronary death : evidence that subclinical rupture has a role in plaque progression. *Circulation.* (2001) 103:934–40. doi: 10.1161/01.CIR.103.7.934
78. Yahagi K, Kolodgie FD, Otsuka F, Finn A V., Davis HR, Joner M, et al. Pathophysiology of native coronary, vein graft, and in-stent atherosclerosis. *Nat Rev Cardiol.* (2016) 13:79–98. doi: 10.1038/nrcardio.2015.164
79. Räber L, Mintz GS, Koskinas KC, Johnson TW, Holm NR, Onuma Y, et al. Clinical use of intracoronary imaging. Part 1: guidance and optimization of coronary interventions. An expert consensus document of the European association of percutaneous cardiovascular interventions. *Eur Heart J.* (2018) 39:3281–300. doi: 10.1093/eurheartj/ehy285
80. Johnson TW, Räber L, di Mario C, Bourantas C, Jia H, Mattesini A, et al. Clinical use of intracoronary imaging. Part 2: acute coronary syndromes, ambiguous coronary angiography findings, and guiding interventional decision-making: an expert consensus document of the European association of percutaneous cardiovascular intervent. *Eur Heart J.* (2019) 40:2566–84. doi: 10.1093/eurheartj/ehz332
81. Porto I, Di Vito L, Burzotta F, Niccoli G, Trani C, Leone AM, et al. Predictors of periprocedural (type IVa) myocardial infarction, as assessed by frequency-domain optical coherence tomography. *Circ Cardiovasc Intervent.* (2012) 5:89–96, S1–6. doi: 10.1161/CIRCINTERVENTIONS.111.965624
82. Wijns W, Shite J, Jones MR, Lee SWL, Price MJ, Fabbiocchi F, et al. Optical coherence tomography imaging during percutaneous coronary intervention impacts physician decision-making: ILUMIEN I study. *Eur Heart J.* (2015) 36:3346–55. doi: 10.1093/eurheartj/ehv367
83. Matsumoto K, Ehara S, Hasegawa T, Otsuka K, Yoshikawa J, Shimada K. Prediction of the filter no-reflow phenomenon in patients with angina pectoris by using multimodality: magnetic resonance imaging, optical coherence tomography, and serum biomarkers. *J Cardiol.* (2018) 67:430–6. doi: 10.1016/j.jjcc.2015.06.015
84. Soeda T, Uemura S, Park S-J, Jang Y, Lee S, Cho J-M, et al. Incidence and clinical significance of poststent optical coherence tomography findings. *Circulation.* (2015) 132:1020–9. doi: 10.1161/CIRCULATIONAHA.114.014704
85. Nakazawa G, Otsuka F, Nakano M, Vorpahl M, Yazdani SK, Ladich E, et al. The pathology of neoatherosclerosis in human coronary implants bare-metal and drug-eluting stents. *J Am Coll Cardiol.* (2011) 57:1314–22. doi: 10.1016/j.jacc.2011.01.011
86. Nakano M, Otsuka F, Yahagi K, Sakakura K, Kutys R, Ladich ER, et al. Human autopsy study of drug-eluting stents restenosis: histomorphological predictors and neointimal characteristics. *Eur Heart J.* (2013) 34:3304–13. doi: 10.1093/eurheartj/eht241
87. van Ditzhuijzen NS, Kurata M, van den Heuvel M, Sorop O, van Duin RWB, Krabbendam-Peters I, et al. Neoatherosclerosis development following bioresorbable vascular scaffold implantation in diabetic and non-diabetic swine. *PLoS ONE.* (2017) 12:e0183419. doi: 10.1371/journal.pone.0183419
88. Otsuka K, Villiger M, van Zandvoort L, Neleman T, Karanasos A, Dijkstra J, et al. Polarimetric signatures of vascular tissue response to drug-eluting stent implantation in patients. *JACC Cardiovasc Imaging.* (2020) 75. doi: 10.1016/S0735-1097(20)31903-3
89. Suna G, Wojakowski W, Lynch M, Barallobre-Barreiro J, Yin X, Mayr U, et al. Extracellular matrix proteomics reveals interplay of aggrecan and aggrecanases in vascular remodeling of stented coronary arteries. *Circulation.* (2018) 137:166–83. doi: 10.1161/CIRCULATIONAHA.116.023381
90. Fujii K, Hao H, Shibuya M, Imanaka T, Fukunaga M, Miki K, et al. Accuracy of OCT, grayscale IVUS, and their combination for the diagnosis of coronary TCFA: an *ex vivo* validation study. *JACC Cardiovasc Imaging.* (2015) 8:451–60. doi: 10.1016/j.jcmg.2014.10.015
91. Li J, Li X, Mohar D, Raney A, Jing J, Zhang J, et al. Integrated IVUS-OCT for real-time imaging of coronary atherosclerosis. *JACC: Cardiovasc Imaging.* (2014) 7:101–3. doi: 10.1016/j.jcmg.2013.07.012
92. Li J, Ma T, Mohar D, Steward E, Yu M, Piao Z, et al. Ultrafast optical-ultrasonic system and miniaturized catheter for imaging and characterizing atherosclerotic plaques *in vivo. Sci Rep.* (2016) 5:18406. doi: 10.1038/srep18406
93. Sheth TN, Pinilla-Echeverri N, Mehta SR, Courtney BK. First-in-human images of coronary atherosclerosis and coronary stents using a novel hybrid intravascular ultrasound and optical coherence tomographic catheter. *JACC Cardiovasc Intervent.* (2018) 11:2427–30. doi: 10.1016/j.jcin.2018.09.022
94. Villiger M, Braaf B, Lippok N, Otsuka K, Nadkarni SK, Bouma BE. Optic axis mapping with catheter-based polarization-sensitive optical coherence tomography. *Optica.* (2018) 5:1329–37. doi: 10.1364/OPTICA.5.001329
95. Fleming CP, Eckert J, Halpern EF, Gardecki JA, Tearney GJ. Depth resolved detection of lipid using spectroscopic optical coherence tomography. *Biomed Opt Express.* (2013) 4:1269–84. doi: 10.1364/BOE.4.001269
96. Nam HS, Song JW, Jang S-J, Lee JJ, Oh W-Y, Kim JW, et al. Characterization of lipid-rich plaques using spectroscopic optical coherence tomography. *J Biomed Opt.* (2016) 21:075004. doi: 10.1117/1.JBO.21.7.075004
97. Tanaka M, Hirano M, Murashima K, Obi H, Yamaguchi R, Hasegawa T. 1.7-μm spectroscopic spectral-domain optical coherence tomography for imaging lipid distribution within blood vessel. *Opt Express.* (2015) 23:6645–55. doi: 10.1364/OE.23.006645
98. Yong YL, Tan LK, McLaughlin RA, Chee KH, Liew YM. Linear-regression convolutional neural network for fully automated coronary lumen segmentation in intravascular optical coherence tomography. *J Biomed Opt.* (2017) 22:1–9. doi: 10.1117/1.JBO.22.12.126005
99. Gessert N, Lutz M, Heyder M, Latus S, Leistner DM, Abdelwahed YS, et al. Automatic plaque detection in IVOCT pullbacks using convolutional neural networks. *IEEE Trans Med Imaging.* (2019) 38:426–34. doi: 10.1109/TMI.2018.2865659
100. Nam HS, Kim C-S, Lee JJ, Song JW, Kim JW, Yoo H. Automated detection of vessel lumen and stent struts in intravascular optical coherence tomography to evaluate stent apposition and neointimal coverage. *Med Phys.* (2016) 43:1662–75. doi: 10.1118/1.4943374

Conflict of Interest: Massachusetts General Hospital and the Erasmus University Medical Center have patent licensing arrangements with Terumo Corporation. BB and MV have the right to receive royalties as part of the licensing arrangements.

The remaining authors declare that the research was conducted in the absence of any commercial or financial relationships that could be construed as a potential conflict of interest.

frontiers in Cardiovascular Medicine

MINI REVIEW
published: 14 October 2020
doi: 10.3389/fcvm.2020.525530

Optically Generated Ultrasound for Intracoronary Imaging

Callum D. Little[1,2*†], *Richard J. Colchester*[2,3†], *Sacha Noimark*[2,3], *Gavin Manmathan*[1], *Malcolm C. Finlay*[2,3,4], *Adrien E. Desjardins*[2,3] *and Roby D. Rakhit*[1,2]

[1] Department of Cardiovascular Medicine, Royal Free NHS Foundation Trust, London, United Kingdom, [2] Wellcome-Engineering & Physical Sciences Research Council (EPSRC) Centre for Interventional and Surgical Sciences, London, United Kingdom, [3] Department of Medical Physics and Bioengineering, University College London, London, United Kingdom, [4] William Harvey Cardiovascular Research Institute, Queen Mary University of London and Barts Health Centre London, London, United Kingdom

Conventional intravascular ultrasound (IVUS) devices use piezoelectric transducers to electrically generate and receive US. With this paradigm, there are numerous challenges that restrict improvements in image quality. First, with miniaturization of the transducers to reduce device size, it can be challenging to achieve the sensitivities and bandwidths required for large tissue penetration depths and high spatial resolution. Second, complexities associated with manufacturing miniaturized electronic transducers can have significant cost implications. Third, with increasing interest in molecular characterization of tissue *in-vivo*, it has been challenging to incorporate optical elements for multimodality imaging with photoacoustics (PA) or near-infrared spectroscopy (NIRS) whilst maintaining the lateral dimensions suitable for intracoronary imaging. Optical Ultrasound (OpUS) is a new paradigm for intracoronary imaging. US is generated at the surface of a fiber optic transducer via the photoacoustic effect. Pulsed or modulated light is absorbed in an engineered coating on the fiber surface and converted to thermal energy. The subsequent temperature rise leads to a pressure rise within the coating, which results in a propagating ultrasound wave. US reflections from imaged structures are received with optical interferometry. With OpUS, high bandwidths (31.5 MHz) and pressures (21.5 MPa) have enabled imaging with axial resolutions better than 50 μm and at depths >20 mm. These values challenge those of conventional 40 MHz IVUS technology and show great potential for future clinical application. Recently developed nanocomposite coating materials, that are highly transmissive at light wavelengths used for PA and NIRS light, can facilitate multimodality imaging, thereby enabling molecular characterization.

Keywords: optical ultrasound, OPUS, optoacoustics, imaging, intravascular ultrasound, IVUS

OPEN ACCESS

Edited by:
Christos Bourantas, Barts Health NHS Trust, United Kingdom

Reviewed by:
Erhan Tenekecioglu, University of Health Sciences, Turkey
Julien Bec, University of California, Davis, United States

***Correspondence:**
Callum D. Little
c.little@ucl.ac.uk

† These authors have contributed equally to this work and share first authorship

Specialty section:
This article was submitted to Cardiovascular Imaging, a section of the journal Frontiers in Cardiovascular Medicine

Received: *09 January 2020*
Accepted: *04 September 2020*
Published: *14 October 2020*

Citation:
Little CD, Colchester RJ, Noimark S, Manmathan G, Finlay MC, Desjardins AE and Rakhit RD (2020) Optically Generated Ultrasound for Intracoronary Imaging. Front. Cardiovasc. Med. 7:525530. doi: 10.3389/fcvm.2020.525530

INTRODUCTION

Intravascular imaging has the ability to provide invaluable anatomical information to facilitate the treatment of coronary artery disease (1). Additionally, molecular compositional analysis of atherosclerotic plaque disease may help to identify targets for intervention (2). The two leading technologies in this field for microstructural imaging are Optical Coherence Tomography (OCT) and Intravascular Ultrasound (IVUS). OCT images are obtained using broadband near-infrared light (wavelengths typically in the vicinity of 1,310 nm), with reflections from tissue detected interferometrically. High axial (10 μm) and lateral (20 μm) resolutions allow for assessments of

both vascular endothelium and plaque structural components, albeit with limited tissue penetration (typically <2 mm) (3). IVUS is a modality analogous to OCT, in which ultrasonic reflections from tissue are detected. Typical commercial IVUS imaging catheters operate with transducer frequencies centered at around 40 MHz, providing an axial resolution of 100–150 μm, a lateral resolution of 200 μm and a tissue penetration of 4–8 mm (3). IVUS has established roles in sizing vessels, detecting calcium, and guiding optimal stent expansion. IVUS has seen exciting technological advancements in recent years, including the use of dual frequency probes to allow for high resolution imaging (4) and combinations with near-infrared spectroscopy (NIRS) (5) or photoacoustics (PA) (6) to provide hybrid imaging with molecular compositional analysis.

With contemporary IVUS devices, ultrasound (US) is generated and received electrically, using piezoelectric transducers. Whilst this electronic platform is well-established within the field of interventional cardiology, there are limitations that preclude its broader clinical use. First, with very small elements (e.g., diameter <150 μm), it can be challenging to achieve adequate sensitivity and bandwidth for high penetration depth and high resolution tissue imaging. Second, the complexities associated with fabricating and electrically connectorising broadband piezocomposite transducers can result in high manufacturing costs. Third, the broader applicability of electronic interventional devices in the coronary catheterization suite is challenged by sensitivities to electromagnetic interference and lack of MRI compatibility (7).

Optical ultrasound (OpUS) imaging probes, in which transmission and reception are both performed with light, are emerging as alternatives to their electrical counterparts. They offer several key advantages, including the potential to generate and detect the broadband US fields (tens of MHz) required for high resolution intravascular imaging (8) and immunity to EM interference. Moreover, optical fibers used for ultrasound transmission and reception can provide the required level of miniaturization for minimally invasive use and have costs that lend themselves to disposable devices. Furthermore, the use of optical fibers allows for the integration of complementary imaging and therapeutic modalities without compromising the device size or performance (9). In this review, we describe the application of OpUS to coronary imaging, including preclinical data acquired using this technology, and future translational applications.

Optical Ultrasound Generation and Reception

With optical ultrasound (OpUS) the generation of US occurs via the photoacoustic effect at the surface of a fiber optic transducer (8), wherein pulsed or modulated excitation light is absorbed in a coating and converted to thermal energy. The transient heat rise leads to a corresponding pressure rise which propagates as an ultrasound wave. The bandwidth of this wave depends on the temporal characteristics of the excitation light. In general, the bandwidth can be increased by decreasing the duration of excitation light pulses; however, in practice, these increases are limited by frequency-dependent ultrasound attenuation within the coating (10) and within blood and vascular tissue (11). To achieve efficient optical-US transduction, a material with a high optical absorption coefficient and a high thermal expansion coefficient is desirable. Studies to date have highlighted the efficacy of composite materials that comprise optical absorbers integrated within elastomers. With these considerations in mind, several nanocomposite materials have been explored, including carbonaceous materials (8), metallic nanoparticles (9), and organic pigments (9). Carbonaceous materials including carbon black (12), carbon nanofibers (13), candle soot (14), carbon nanotubes (15), and graphene (16) have high optical absorption across the visible and near-infrared wavelength ranges. Metallic nanoparticles such as gold, exhibit a relatively narrow optical absorbing window. Organic pigments such as crystal violet can display poor photostability with repeated usage causing photobleaching with loss of acoustic conversion efficiency (9). Noimark et al. showed for the first time that functionalized multiwalled carbon nanotube-polydimethylsiloxane (PDMS) composites can give rise to pressures of 21.5 MPa at the coating surface (the highest recorded pressure from a fiber optic transmitter, to our knowledge) and bandwidths of 39.8 MHz (15). These high pressures enable high imaging penetration depths, and the broad bandwidths give rise to high axial resolution. A small coating thickness can be important to minimize acoustic attenuation within nanocomposite materials (10). To this end, several methods have been explored for depositing nanocomposite materials onto the distal surface of the fiber optic transducer, including spin-coating (17), electrospinning (18), and dip-coating (15). With the latter method, a "bottom up" approach typically involves coating the substrate with an optical absorber and a subsequent polymer overcoat (for instance, PDMS). Control of the thickness of the nanocomposite region comprising the optical absorber and the polymer, and the total thickness of the polymer, is determined by both the viscosity of the material, which can be altered through the use of solvents, and the dipping speed of the optical fiber.

To allow for real-time pulse-echo US imaging, fiber-optic transmitters have been be paired with high-finesse Fabry-Pérot fiber-optic receivers [(19); **Figure 1A**]. These receivers, fabricated on the distal ends of optical fibers, comprise an epoxy dome with high-reflectivity coatings on both the planar and domed surfaces. When an ultrasound wave impinges on the dome, it causes nanometer-scale deformations in the dome surface. These deformations are measured using laser interferometry. Such devices are capable of measuring pressures lower than 100 Pascals, making them highly sensitive to ultrasound reflections and ideally suited to minimally invasive imaging. In contrast to piezoelectric receivers, whose sensitivities fall off with decreasing element size, fiber optic receivers can maintain their sensitivity even at scales of tens or hundreds of micrometers. Their small lateral dimensions (<250 μm outer diameter) enable integration into intracoronary imaging devices, and their large bandwidths yield high imaging performance [e.g., axial resolution better than 60 μm and cm-scale imaging depths without temporal averaging (20)]. Several other fiber optic reception technologies are promising for intracoronary imaging,

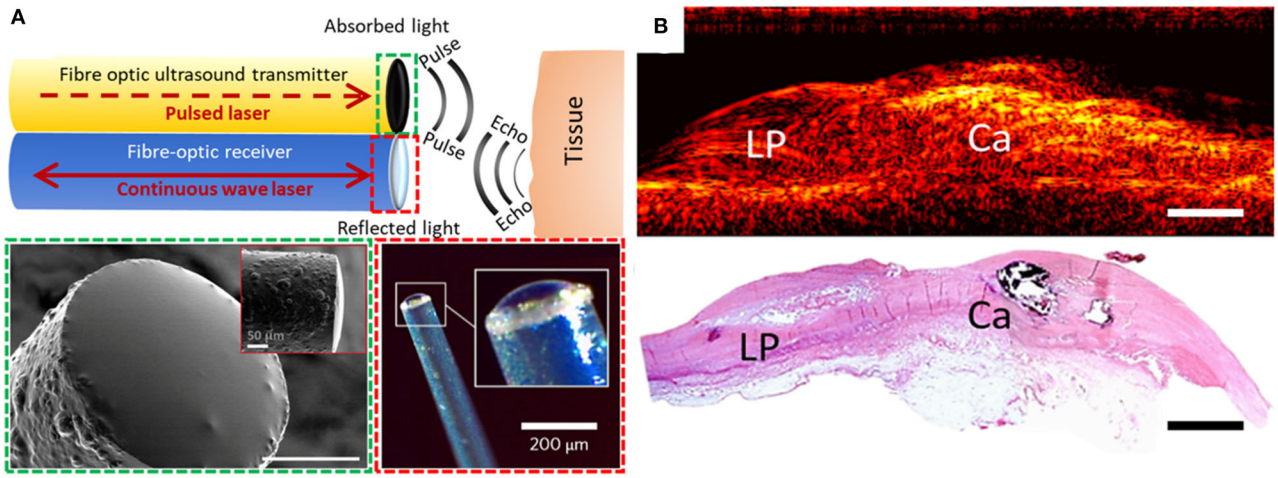

FIGURE 1 | (A) Generation and reception of OpUS. The schematic (top) includes both a transmitter and a receiver. Lower-left inset (dashed green box): scanning electron microscopy image of the transmitter fiber-tip coated with nanocomposite (scale bar: 50 µm) (15). Lower-right inset (dashed red box): optical microscopy of the fiber-optic receiver (19). **(B)** 2D longitudinal M-mode OpUS imaging of *ex-vivo* human coronary artery tissue with a lipid pool (LP), calcification (Ca), and corresponding histology (haematoxylin and eosin staining) (scale bars: 2 mm).

including fiber Bragg gratings (21–23) and microring resonators (24, 25).

With OpUS, high bandwidths and pressures have enabled imaging with resolutions better than 50 µm and tissue penetration depths >20 mm (20). These values challenge those of conventional 40 MHz IVUS technology and show great potential for future clinical application. As initial demonstrations of the viability of OpUS for *in-vivo* clinical imaging, forward-viewing configurations have been used. With these configurations, ultrasound was transmitted ahead of the optical fiber, in a direction colinear with the optical fiber axis. Axial and lateral resolutions of <60 and <90 µm, respectively, were achieved (26). A forward-viewing probe that was integrated within a transseptal puncture needle was used to obtain the first *in vivo* intracardiac images with OpUS (27). Recently, the first OpUS images of *ex-vivo* human coronary tissue samples (**Figure 1B**) were acquired and compared to histology. Numerous features of atherosclerotic plaque were identifiable, including a lipid pool, a calcified nodule, and the different layers of the vessel wall. Several other configurations relevant to intracoronary imaging have subsequently been developed, including side-viewing rotational imaging (20) and hybrid multimodality imaging (9).

OpUS Structural Imaging

Commercial intravascular imaging systems can employ rotational pullbacks of side-viewing probes in order to achieve cross-sectional imaging (with phased-array probes as alternatives). An analogous rotational implementation with OpUS can be realized with ultrasound transmitted perpendicular to the device axis. In a recent probe, perpendicular ultrasound transmission was made possible with an optically-absorbing nanocomposite coating extending perpendicular to the axis of the optical fiber that transmitted excitation light, in conjunction with a 45° mirror (**Figure 2A**). This optical fiber was connected to a rotary junction in order to allow for circumferential imaging, whilst the omnidirectional fiber-optic receiver remained stationary. The configuration of this imaging device had dimensions suitable for intracoronary imaging, with a maximum lateral dimension <1.25 mm at the distal tip. Image acquisition occurred with a frame rate of 5 frames per second. The imaging fidelity of the device was investigated with *ex-vivo* swine carotid tissue [(20); **Figure 2B**]. The broad bandwidths achieved (−6 dB bandwidth of 31.3 MHz), in conjunction with depth-dependent digital frequency filtering, allowed for both high axial resolutions at shallow depths and deep tissue visualization. Axial and lateral resolutions at a distance of 3 mm from the probe were superior to 50 µm and 15°. This device sets the stage for future devices with rotational lengths and encapsulation suitable for *in vivo* intracoronary imaging.

Multi-Modality US and Photoacoustic Imaging

Recently there has been intense interest in multi-modality intravascular imaging probes that provide complementary structural and molecular information. These probes include combinations such as US with photoacoustic (PA) imaging (6, 28) or with near-infrared spectroscopy (NIRS) (5, 29). A potential strong advantage of OpUS probes, as compared to their electronic counterparts, is that the optical fibers used to generate and receive ultrasound can also be used to transmit light for PA and NIRS. These efficiencies, which can be achieved through the use of nanocomposite fiber tip coatings that are absorbing at certain wavelengths and transmissive at others, could be valuable both for achieving high levels of miniaturization and cost reductions. In a study by Noimark and Colchester et al., gold nanoparticle composites and organic dye composites, applied to the distal ends

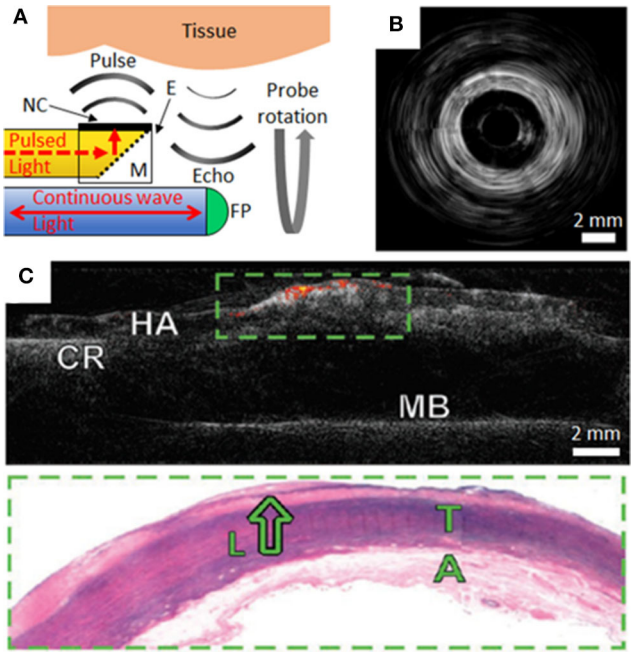

FIGURE 2 | (A) Schematic of side-viewing optical ultrasound imaging probe with pulsed excitation light transmitted along an optical fiber (yellow), reflected at a mirror (M) and absorbed at the nanocomposite (NC) coating surface of an epoxy-based (E) optical transducer housing. Ultrasound pulses reflect from tissue and the echoes are received through interferometric interrogation of the Fabry-Pérot (FP) cavity at the distal end of the receiving optical fiber (blue). The probe is rotated about its axis to achieve circumferential imaging. **(B)** Rotational optical ultrasound images obtained within an *ex-vivo* swine carotid artery (20). **(C)** Co-registered optical ultrasound (gray-scale) and photoacoustic images of human aortic tissue (HA) using a gold nanoparticle/PMDS composite transmitter. Areas of lipid are displayed as a color signal. The tissue was secured to a cork ring (CR) and metal base (MB) for imaging. Corresponding histology of the green boxed area highlights a lipid pool (L), tunica media (T) and adventitia (A) (9).

of optical fibers within an imaging probe, were used to generate ultrasound for OpUS (532 nm wavelength) and to transmit light for PA imaging (1,210 nm) from a single optical fiber (9). Co-registered ultrasound and photoacoustic images of an *ex-vivo* diseased human aorta were acquired. PA imaging provided molecular contrast for lipid rich coronary plaque, which was overlaid on the acquired ultrasound images (**Figure 2C**). Whilst the use of multi-modality OpUS for intracoronary imaging is at an early stage, there are strong indications that it could allow for measuring the plaque burden, which in turn could be valuable for guiding stent placement and for improving our understanding of the pathophysiology of coronary artery disease.

DISCUSSION

Direct comparison of OpUS to established intracoronary imaging devices is challenging at present due to a lack of *in-vivo* clinical data. Whilst detection of lipid and calcium by OpUS has been demonstrated (**Figure 1B**), further work is required to assess the efficacy of this technology for accurately sizing vessel diameter, luminal area, optimizing stent expansion, and detection of high risk atherosclerotic plaque morphological features including fibrous cap thickness, neovascularisation and macrophage infiltration. Nevertheless, OpUS potentially offers several prominent benefits over current generation electronically generated ultrasound. The axial resolution could be enhanced by the use of modulated excitation light that emphasizes higher ultrasound frequencies. Improvements to the lateral resolution could be achieved with curved transducers to achieve a focussed beam and with shorter excitation light pulses to increase the central frequency, and potentially with deep-learning beamforming for sub-sampled data (30). In order to improve image quality further refinements in image post-processing are possible, including complex filtering and reconstruction approaches, as well as adaptive frequency filtering to allow discrimination between acoustically dissimilar tissues (31–35). Significant increases in image acquisition rate are readily achievable. The rotational OpUS setup demonstrated to date (20) was limited to 5 frames per second by the data transfer rate and computation times, but further engineering developments with existing excitation lasers could potentially increase imaging rates to over 100 frames per second without compromising lateral resolution. To enable more rapid circumferential imaging for clinical translation, mechanical elements such as torque coils could be incorporated into the imaging probes, as used with OCT catheters. It is envisaged that lubricating fluid will be necessary to reduce frictional forces generated by the rotational components and to facilitate ultrasound coupling. Looking beyond the paradigm of rotating a single optical transducer, a phased array analogous to solid-state IVUS systems could be envisaged; however, it is likely to be challenging to achieve a high density of optical transducer elements within a coronary imaging device without compromising the device profile or deliverability. It is conceivable that spatial light modulators for controlling the propagation of laser light through multimode optical fibers (36) could be used in this context. A forward-looking volumetric probe analogous to electronic IVUS versions (37) could be envisaged; however, the spatial resolution would be highly dependent on the geometry and spatial configuration of the transducer elements.

Looking beyond aforementioned probes for vascular imaging that have been demonstrated at a pre-clinical level, there are uncharted frontiers in which OpUS probes could be extended to include new capabilities. They include enhanced diagnosis via pairing with OCT, photoacoustic imaging (38), and near-infrared fluorescence (NIRF) (39); additionally, they include therapeutic monitoring during atherectomy (40) and device tracking with the inclusion of fiber optic shape sensing (41). Speculatively, the inclusion of OCT could be enabled with a double-clad optical fiber, with ultrasound reception and OCT performed with light transmitted along the single-mode inner core and ultrasound transmission with the multi-mode outer core. Optically-generated ultrasound represents an exciting

development in the field of intravascular imaging. Whilst many steps along the translational path remain, there is strong potential to unite many modalities into a single fiber optic probe that could have broad applicability in cardiovascular medicine and beyond.

AUTHOR CONTRIBUTIONS

CL, RC, and AD co-wrote the paper. SN provided advice on descriptions of the nanocomposite materials. GM, MF, and RR provided advice on the clinical applications of OpUS. All authors contributed to the article and approved the submitted version.

FUNDING

CL, RC, AD, and RR gratefully acknowledge funding by the National Institute for Health Research UCL Biomedical Research Centre and the Wellcome/EPSRC Centre for Interventional and Surgical Sciences (WEISS) (203145Z/16/Z; NS/A000050/1). RC was funded by the Royal Academy of Engineering under the Research Fellowship scheme.

REFERENCES

1. Neumann FJ, Sousa-Uva M, Ahlsson A, Alfonso F, Banning AP, Benedetto U, et al. 2018 ESC/EACTS guidelines on myocardial revascularization. *Eur Heart J.* (2019) 40, 87–165. doi: 10.1093/ejurheartj/ehy394
2. Stone GW, Maehara A, Lansky AJ, de Bruyne B, Cristea E, Mintz GS, et al. a prospective natural-history study of coronary atherosclerosis. *N Engl J Med.* (2011) 364:226–35. doi: 10.1056/nejmoa1002358
3. Koganti S, Kotecha T, Rakhit RD. Choice of intracoronary imaging: when to use intravascular ultrasound or optical coherence tomography. *Interv Cardiol Rev.* (2016) 11:6–11. doi: 10.15420/icr.2016:6:1
4. Chin CY, Maehara A, Fall K, Mintz GS, Ali ZA. Imaging comparisons of coregistered native and stented coronary segments by high-definition 60-MHz intravascular ultrasound and optical coherence tomography. *JACC Cardiovasc Interv.* (2016) 9:1305–6. doi: 10.1016/j.jcin.2016.04.011
5. Waksman R, Di Mario C, Torguson R, Ali ZA, Singh V, Skinner WH, et al. Identification of patients and plaques vulnerable to future coronary events with near-infrared spectroscopy intravascular ultrasound imaging: a prospective, cohort study. *Lancet.* (2019) 294:1629–37. doi: 10.1016/S0140-6736(19)31794-5
6. Cao Y, Kole A, Hui J, Zhang Y, Mai J, Alloosh M, et al. Fast assessment of lipid content in arteries *in vivo* by intravascular photoacoustic tomography. *Sci Rep.* (2018) 8:2400. doi: 10.1038/s41598-018-20881-5
7. Raman VK, Lederman RJ. Interventional cardiovascular magnetic resonance imaging. *Trends Cardiovasc Med.* (2007) 17:196–202. doi: 10.1016/j.tcm.2007.05.003
8. Colchester RJ, Mosse CA, Bhachu DS, Bear JC, Carmalt CJ, Parkin IP, et al. Laser-generated ultrasound with optical fibres using functionalised carbon nanotube composite coatings. *Appl Phys Lett.* (2014) 104:173502. doi: 10.1063/1.4873678
9. Noimark S, Colchester RJ, Poduval RK, Maneas E, Alles EJ, Zhao T, et al. Polydimethylsiloxane composites for optical ultrasound generation and multimodality imaging. *Adv Funct Mater.* (2018) 28:1–16. doi: 10.1002/adfm.201704919
10. Alles EJ, Heo J, Noimark S, Colchester RJ, Parkin IP, Baac HW, et al. Acoustical characterisation of carbon nanotube-loaded polydimethylsiloxane used for optical ultrasound generation. In: *IEEE International Ultrasonics Symposium, IUS.* Washington, DC, (2017). p. 1–4. doi: 10.1109/ULTSYM.2017.8092343
11. Treeby BE, Zhang EZ, Thomas AS, Cox BT. Measurement of the ultrasound attenuation and dispersion in whole human blood and its components from 0-70 MHz. *Ultrasound Med Biol.* (2011) 37:289–300. doi: 10.1016/j.ultrasmedbio.2010.10.020
12. O'Donnell M, Hou Y, Kim JS, Ashkenazi S, Huang SW, Guo LJ. Optoacoustic generation of high frequency sound for 3-D ultrasonic imaging in medicine. *Eur Phys J Spec Top.* (2008) 153:53–8. doi: 10.1140/epjst/e2008-00392-9
13. Hsieh BY, Kim J, Zhu J, Li S, Zhang X, Jiang X. A laser ultrasound transducer using carbon nanofibers-polydimethylsiloxane composite thin film. *Appl Phys Lett.* (2015) 106:021902. doi: 10.1063/1.4905659
14. Aytac-Kipergil E, Alles EJ, Pauw HC, Karia J, Noimark S, Desjardins AE. Versatile and scalable fabrication method for laser-generated focused ultrasound transducers. *Opt Lett.* (2019) 44:6005–8. doi: 10.1364/ol.44.006005
15. Noimark S, Colchester RJ, Blackburn BJ, Zhang EZ, Alles EJ, Ourselin S, et al. Carbon-nanotube–PDMS composite coatings on optical fibers for all-optical ultrasound imaging. *Adv Funct Mater.* (2016) 26:8390–6. doi: 10.1002/adfm.201601337
16. Colchester RJ, Alles EJ, Desjardins AE. A directional fibre optic ultrasound transmitter based on a reduced graphene oxide and polydimethylsiloxane composite. *Appl Phys Lett.* (2019) 114:113505. doi: 10.1063/1.5089750
17. Biagi E, Cerbai S, Masotti L, Belsito L, Roncaglia A, Masetti G, et al. MOMS technology for fully fiber optic ultrasonic probes: a proposal for virtual biopsy. In: *Proceedings of IEEE Sensors.* Waikoloa, HI (2010). p. 1156–60. doi: 10.1109/ICSENS.2010.5690824
18. Poduval RK, Noimark S, Colchester RJ, Macdonald TJ, Parkin IP, Desjardins AE, et al. Optical fiber ultrasound transmitter with electrospun carbon nanotube-polymer composite. *Appl Phys Lett.* (2017) 110:223701. doi: 10.1063/1.4984838
19. Guggenheim JA, Li J, Allen TJ, Colchester RJ, Noimark S, Ogunlade O, et al. Ultrasensitive plano-concave optical microresonators for ultrasound sensing. *Nat Photonics.* (2017) 11:714–9. doi: 10.1038/s41566-017-0027-x
20. Colchester RJ, Little C, Dwyer G, Noimark S, Alles EJ, Zhang EZ, et al. All-optical rotational ultrasound imaging. *Sci Rep.* (2019) 9:5576. doi: 10.1038/s41598-019-41970-z
21. Rosenthal A, Razansky D, Ntziachristos V. High-sensitivity compact ultrasonic detector based on a pi-phase-shifted fiber Bragg grating. *Opt Lett.* (2011) 36:1833–5. doi: 10.1364/ol.36.001833
22. Wu Q, Okabe Y. High-sensitivity ultrasonic phase-shifted fiber Bragg grating balanced sensing system. *Opt Express.* (2012) 20:28353–62. doi: 10.1364/oe.20.028353
23. Tian J, Zhang Q, Han M. Distributed fiber-optic laser-ultrasound generation based on ghost-mode of tilted fiber Bragg gratings. *Opt Express.* (2013) 21:6109–14. doi: 10.1364/oe.21.006109
24. Dong B, Chen S, Zhang Z, Sun C, Zhang HF. Photoacoustic probe using a microring resonator ultrasonic sensor for endoscopic applications. *Opt Lett.* (2014) 39:4372–5. doi: 10.1364/ol.39.004372
25. Hsieh B-Y, Chen S-L, Ling T, Guo LJ, Li P-C. Integrated intravascular ultrasound and photoacoustic imaging scan head. *Opt Lett.* (2010) 35:2892–4. doi: 10.1364/ol.35.002892
26. Colchester RJ, Zhang EZ, Mosse CA, Beard PC, Papakonstantinou I, Desjardins AE. Broadband miniature optical ultrasound probe for high resolution vascular tissue imaging. *Biomed Opt Express.* (2015) 6:1502. doi: 10.1364/boe.6.001502
27. Finlay MC, Mosse CA, Colchester RJ, Noimark S, Zhang EZ, Ourselin S, et al. Through-needle all-optical ultrasound imaging *in vivo*: a preclinical swine study. *Light Sci Appl.* (2017) 6:e17103–7. doi: 10.1038/lsa.2017.103
28. Jansen K, Van Soest G, van der Steen AFW. Intravascular photoacoustic imaging: a new tool for vulnerable plaque identification. *Ultrasound Med Biol.* (2014) 40:1037–48. doi: 10.1016/j.ultrasmedbio.2014.01.008
29. Roleder T, Kovacic JC, Ali Z, Sharma R, Cristea E, Moreno P, et al. Combined NIRS and IVUS imaging detects vulnerable plaque using a single catheter system: a head-to-head comparison with OCT. *EuroIntervention.* (2014) 10:303–11. doi: 10.4244/EIJV10I3A53

30. Simson W, Paschali M, Navab N, Zahnd G. Deep learning beamforming for sub-sampled ultrasound data. In: *IEEE International Ultrasonics Symposium, IUS*. Kobe (2018). p. 1–4. doi: 10.1109/ULTSYM.2018.8579818
31. Park J, Kang JB, Chang JH, Yoo Y. Speckle reduction techniques in medical ultrasound imaging. *Biomed Eng Lett.* (2014) 432–40. doi: 10.1007/s13534-014-0122-6
32. Lediju Bell MA, Goswami R, Kisslo JA, Dahl JJ, Trahey GE. Short-Lag Spatial Coherence Imaging of Cardiac Ultrasound Data: Initial Clinical Results. *Ultrasound Med Biol.* (2013) 39:1861–74. doi: 10.1016/j.ultrasmedbio.2013.03.029
33. Rouyer J, Varray F, Pozo E, Basset O, Cachard C, Lavarello R. Evaluation of a frequency-domain ultrasonic imaging attenuation compensation technique. In: *Proceedings of the Annual International Conference of the IEEE Engineering in Medicine and Biology Society, EMBS*. Milan (2015). p. 1560–3. doi: 10.1109/EMBC.2015.7318670
34. Varray F, Cachard C, Kybic J, Novell A, Bouakaz A, Basset O. A multi-frequency approach to increase the native resolution of ultrasound images. In: *European Signal Processing Conference*. Bucharest (2012) p. 2733–7.
35. Allman D, Reiter A, Bell MAL. Photoacoustic source detection and reflection artifact removal enabled by deep learning. *IEEE Trans Med Imaging.* (2018) 37:1464–77. doi: 10.1109/TMI.2018.2829662
36. Cižmár T, Dholakia K. Shaping the light transmission through a multimode optical fibre: complex transformation analysis and applications in biophotonics. *Opt Express.* (2011) 19:18871–84. doi: 10.1364/oe.19.018871
37. Guldiken R, Zahorian J, Gurun G, Qureshi MS, Balantekin M, Tekes C, et al. Forward-looking IVUS imaging using a dual-annular ring CMUT array: Experimental results. In: *Proceedings - IEEE Ultrasonics Symposium*. New York, NY (2007). p. 1247–50. doi: 10.1109/ULTSYM.2007.313
38. van Soest G, Marcu L, Bouma BE, Regar E. Intravascular imaging for characterization of coronary atherosclerosis. *Curr Opin Biomed Eng.* (2017) 3:1–12. doi: 10.1016/j.cobme.2017.07.001
39. Yoo H, Kim JW, Shishkov M, Namati E, Morse T, Shubochkin R, et al. Intra-arterial catheter for simultaneous microstructural and molecular imaging *in vivo*. *Nat Med.* (2011) 171680–4. doi: 10.1038/nm.2555
40. Rawlins J, Din JN, Talwar S, O'Kane P. Coronary intervention with the excimer laser: review of the technology and outcome data. *Interv Cardiol Rev.* (2016) 11:27–32. doi: 10.15420/icr.2016:2:2
41. Shi C, Giannarou S, Lee SL, Yang GZ. Simultaneous catheter and environment modeling for Trans-catheter Aortic Valve Implantation. In: 2014 *IEEE International Conference on Intelligent Robots and Systems*. (2014) p. 2024–9. doi: 10.1109/IROS.2014.6942832

Conflict of Interest: AD, RC, and MF are shareholders of Echopoint Medical Ltd.

The remaining authors declare that the research was conducted in the absence of any commercial or financial relationships that could be construed as a potential conflict of interest.

frontiers in Cardiovascular Medicine

REVIEW
published: 23 November 2020
doi: 10.3389/fcvm.2020.587100

Intravascular Molecular Imaging: Near-Infrared Fluorescence as a New Frontier

Haitham Khraishah[1,2] *and Farouc A. Jaffer*[2,3]*

[1] Department of Medicine, Beth Israel Deaconess Medical Center and Harvard Medical School, Boston, MA, United States, [2] Division of Cardiology, Cardiovascular Research Center and Harvard Medical School, Massachusetts General Hospital, Boston, MA, United States, [3] Wellman Center for Photomedicine and Harvard Medical School, Massachusetts General Hospital, Boston, MA, United States

Despite exciting advances in structural intravascular imaging [intravascular ultrasound (IVUS) and optical coherence tomography (OCT)] that have enabled partial assessment of atheroma burden and high-risk features associated with acute coronary syndromes, structural-based imaging modalities alone do not comprehensively phenotype the complex pathobiology of atherosclerosis. Near-infrared fluorescence (NIRF) is an emerging molecular intravascular imaging modality that allows for *in vivo* visualization of pathobiological and cellular processes at atheroma plaque level, including inflammation, oxidative stress, and abnormal endothelial permeability. Established intravascular NIRF imaging targets include macrophages, cathepsin protease activity, oxidized low-density lipoprotein and abnormal endothelial permeability. Structural and molecular intravascular imaging provide complementary information about plaque microstructure and biology. For this reason, integrated hybrid catheters that combine NIRF-IVUS or NIRF-OCT have been developed to allow co-registration of morphological and molecular processes with a single pullback, as performed for standalone IVUS or OCT. NIRF imaging is approaching application in clinical practice. This will be accelerated by the use of FDA-approved indocyanine green (ICG), which illuminates lipid- and macrophage-rich zones of permeable atheroma. The ability to comprehensively phenotype coronary pathobiology in patients will enable a deeper understanding of plaque pathobiology, improve local and patient-based risk prediction, and usher in a new era of personalized therapy.

Keywords: intravascular imaging, atherosclerotic cardiovascular disease, optical coherence tomography, molecular imaging, near-infrared fluorescence (NIRF)

OPEN ACCESS

Edited by:
Xiaowei Wang,
Baker Heart and Diabetes Institute, Australia

Reviewed by:
Jinwei Tian,
Second Affiliated Hospital of Harbin Medical University, China
Amir Rosenthal,
Technion Israel Institute of Technology, Israel
Antonios Karanasos,
Hippokration General Hospital, Greece

***Correspondence:**
Farouc A. Jaffer
fjaffer@mgh.harvard.edu

Specialty section:
This article was submitted to Cardiovascular Imaging, a section of the journal Frontiers in Cardiovascular Medicine

Received: *24 July 2020*
Accepted: *30 October 2020*
Published: *23 November 2020*

Citation:
Khraishah H and Jaffer FA (2020) Intravascular Molecular Imaging: Near-Infrared Fluorescence as a New Frontier. Front. Cardiovasc. Med. 7:587100. doi: 10.3389/fcvm.2020.587100

INTRODUCTION

In 1989, Muller et al. (1) proposed the term "vulnerable plaque" to describe coronary artery plaques prone to rupture and cause acute myocardial infarction or sudden cardiac death. In 2003, a group of experts reached a consensus on a definition of vulnerable/high risk plaque being "a plaque that is at increased risk of thrombosis (or recurrent thrombosis) and rapid stenosis progression" (2). This definition extends beyond plaque rupture to include disruptions that may also occur from plaque erosions and penetrating calcified nodules. In general, the current paradigm of a high-risk plaque involves a thin cap fibroatheroma (TCFA), characterized by a large,

necrotic, lipid-rich core and an overlying thin fibrous cap of <65 μm thickness. Other high risk features include inflammation, microcalcifications, neovascularization, intraplaque hemorrhage and positive remodeling (3–5).

High-resolution intravascular imaging modalities, such as intravascular ultrasound (IVUS) and optical coherence tomography (OCT), assess *in vivo* atheroma burden and some high-risk features reflecting plaque vulnerability (6). Despite these advances, current anatomical intracoronary imaging modalities have their shortcomings in predicting future acute coronary syndrome (ACS) events, even when incorporating advanced IVUS-derived high risk plaque measures, such as high plaque burden >70%, minimal luminal area<4 mm^2, IVUS-virtual histology demarcated TCFA, and low endothelial shear stress (7–9). To address the limitations of anatomical intracoronary imaging, near-infrared fluorescence (NIRF) molecular imaging has emerged as a translational intravascular modality that allows visualization of plaque pathobiology by targeting certain molecular processes through specialized imaging agents [fluorophore-conjugates (10, 11) or protease-activatable constructs (12, 13) for example]. No single modality allows for the comprehensive evaluation of a plaque; to meet this need, hybrid catheters that allow co-registration of images acquired by different modalities have been developed. The aim of this review is to showcase the latest developments in molecular intravascular imaging, with a focus NIRF hybrid imaging modalities, and delve into current limitations and future prospects.

PLAQUE PATHOBIOLOGY

The underlying pathobiology of atherosclerosis provides a roadmap for molecular imaging targets and imaging agent synthesis (**Figure 1**). Atherosclerosis is a chronic inflammatory disease characterized by endothelial dysfunction, arterial wall thickening and persistent immune activation. An initial step in atherogenesis is vascular endothelial dysfunction, triggered by an increase in oxidative stress within a milieu of hyperlipidemia, hyperglycemia, smoking and hypertension (14). Small low-density lipoprotein (LDL) particles infiltrate through the impaired endothelial barrier and accumulate in the subendothelial matrix (15, 16). Oxidized LDL (oxLDL) is internalized by local macrophages giving rise to foam cells (17–19). Vascular smooth muscle cells (VSMCs) migrate from the tunica media to intima in response to inflammatory mediators, growth factors, and cytokines. There, they proliferate and secrete extracellular matrix including proteoglycans and collagen type 2, contributing to plaque stability through the formation of a fibrous cap (20, 21). Apoptosis and necrosis of activated macrophages and VSMCs results in the formation of a lipid-rich necrotic core that is encapsulated by collagen-rich fibrous tissue, a fibrous cap (18, 22). When a fibroatheroma exists under a thin fibrous cap (thinned by inflammatory proteases such as MMPs and cathepsins), these advanced lesions are denoted as TCFAs, the current paradigm of high-risk plaque.

Another high-risk plaque feature is microcalcification. Calcification is an active process that occurs during all stages of atherosclerosis. Macrocalcifications, which are detectable by CT scan due to high radiodensity [>400 Hounsfield unit (HU)], may be associated with more stable plaque phenotypes (23). In contrast, microcalcifications (<0.05 to 15 μm) are undetectable by conventional imaging modalities and may have a destabilizing effect on fibroatheromas (24). When microcalcifications, arise within the fibrous cap, local stress increases by 2-fold, putatively contributing to plaque vulnerability (25). Microcalcification-aggregation results in macrocalcifications (18). Another high-risk vulnerable plaque feature is spotty calcifications, small calcium deposits that can be detected via OCT, IVUS, and CT. For IVUS and OCT, spotty calcification is defined as a calcium length < 4 mm and a maximal calcium angle ranging from 22.5 to 90° (26). For CT, spotty calcifications are typically defined as average density >130 HU, diameter <3 mm in any direction, length of the calcium <1.5× the vessel diameter, and width of the calcification less than two-thirds of the vessel diameter (27).

Positive remodeling is thought to contribute to plaque instability by induction of neovascularization of vasa vasorum in the adventitia that eventually invade the intima and the fibroatheroma (28). These new microvessels have fragile walls leading to intraplaque hemorrhage (resulting in plaque expansion and pro-inflammatory milieu), and express adhesion molecules recruiting further macrophages into the plaque (**Figure 1**) (29).

DETECTING HIGH RISK PLAQUE: SIGNIFICANCE, CHALLENGES, AND INTRAVASCULAR IMAGING

The goal of detecting high-risk plaques is to identify rupture-prone plaques and intervene in a way (either medically or interventionally or both) to prevent future ACS. Very recently, the COMPLETE trial showed that in patients with STEMI and multivessel coronary artery disease (CAD), intervening on non-culprit lesions reduced a composite of CVD death and myocardial infarction (30), demonstrating the potential to identify a subgroup of high-risk, non-culprit lesions (admittedly a proportion of these lesions may have been flow-limiting and met common indications for revascularization, independently of the COMPLETE trial). However, in other clinical scenarios such as stable CAD, several challenges exist as to which non-culprit lesions to intervene upon. These challenges are due to imprecise knowledge of the natural history of plaque progression based on structural-based imaging trials and autopsy studies. Also, coronary artery plaques are of dynamic nature with lesion morphology oscillating from high risk to more stable and vice versa over time, as demonstrated by small longitudinal imaging studies (31–33). Additionally, current anatomical intravascular imaging modalities have limited ability to predict ACS arising from high risk plaques. In the PROSPECT trial, after incorporating all IVUS-derived predictive variables [high plaque burden >70%, minimal luminal area <4 square mm, or

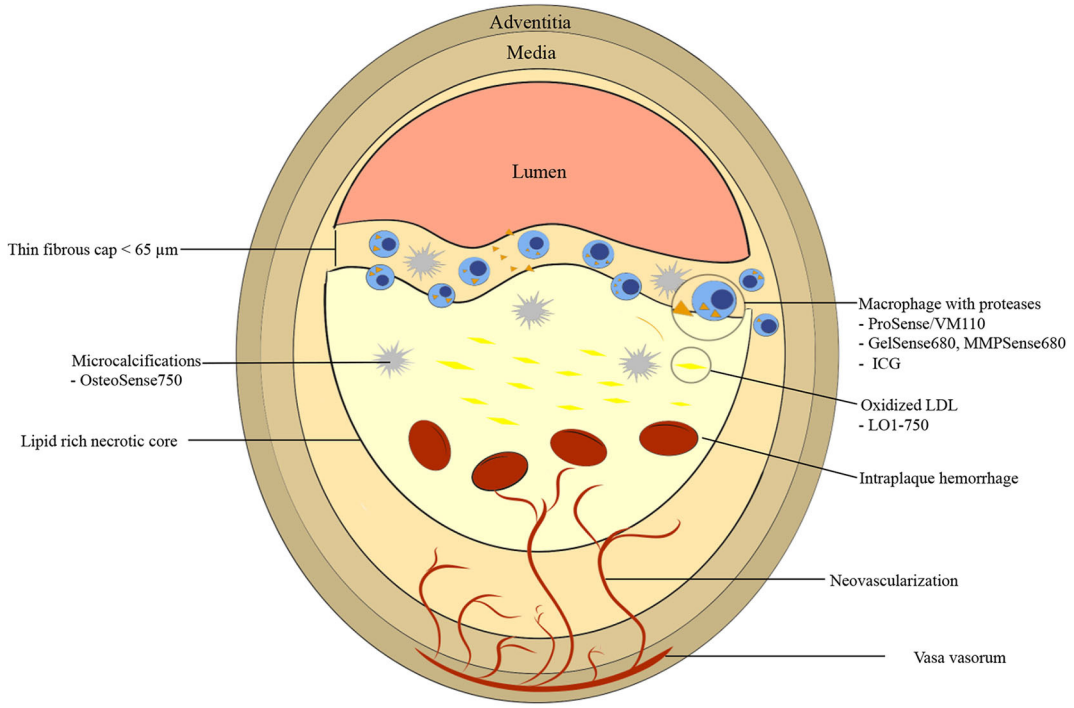

FIGURE 1 | Graphic representation of vulnerable plaque characteristics with emphasis on near-infrared fluorescence (NIRF) molecular imaging targets. High risk features include thin fibrous cap <65 µm, fibrous cap and necrotic core macrophages, large necrotic core, microcalcifications, neovascularization, and intraplaque hemorrhage. ICG, indocyanine green.

IVUS-virtual histology demarcated thin capped fibroatheroma (TCFA)], IVUS was limited in forecasting event-causing lesions with a relatively low positive predictive value (PPV) of 18.2% (meaning 4 out of 5 three-feature plaques did not produce in an event at 3 years) (9). Integrating endothelial shear stress parameters in the PREDICTION trial enhanced PPV to 41% (7), which is an improvement but still insufficient for routine clinical management. Therefore, new imaging approaches to more comprehensively phenotype atheroma are needed to improve lesion-specific risk prediction.

INTRAVASCULAR MOLECULAR IMAGING

To tackle the limitations of anatomical intravascular imaging modalities, intravascular molecular imaging has been developed to allow for *in vivo* visualization of molecular process that contribute to plaque vulnerability. The primary intravascular molecular imaging modality nearing clinical translation utilizes near infrared fluorescence (NIRF) detection of targeted NIR fluorophores, discussed in detail next.

NEAR-INFRARED FLUORESCENCE (NIRF)

Basics of Near-Infrared Fluorescence (NIRF) Molecular Imaging

Near-infrared fluorescence (NIRF) is an emerging translational, intravascular imaging modality that has the ability to capture a wide range of *in vivo* pathobiological processes (34). NIRF molecular imaging entails (1) injecting targeted or activatable NIRF molecular imaging agents, which consist of fluorescent conjugates (e.g., NIR fluorophores conjugated to an antibody, peptide, or small molecule) that concentrate in atheroma and bind to molecular targets, and (2) detecting the fluorophore emission signal from a NIRF catheter and console detection system (35). After injecting targeted fluorophores, excitation light from the near-infrared spectrum (650–900 nm) is directed at the arterial wall and used to stimulate fluorophores from ground state (S0) to an excited state (S1, S2). The excited fluorophores (S1, S2) emit energy in the form of photons (fluorescence emission) and then return to the ground state, and are then available for further excitation. Fluorescence emission occurs at a lower energy and a longer wavelength, and this emission light is detectable with a high sensitivity charge-coupled device (CCD) camera and appropriate emission filter that attenuates the initial shorter wavelength excitation light (34). Compared to visible light range fluorescence detection, characteristics of NIRF imaging that make it a highly sensitive imaging modality include: (A) less light absorption by hemoglobin, lipid, and water, allowing deeper penetration of light into tissue; and (B) reduced background tissue autofluorescence, allowing for high signal-to-background ratio (36, 37).

In 2008, Jaffer et al. (38) described the first intravascular, real-time NIRF catheter-based spectroscopic

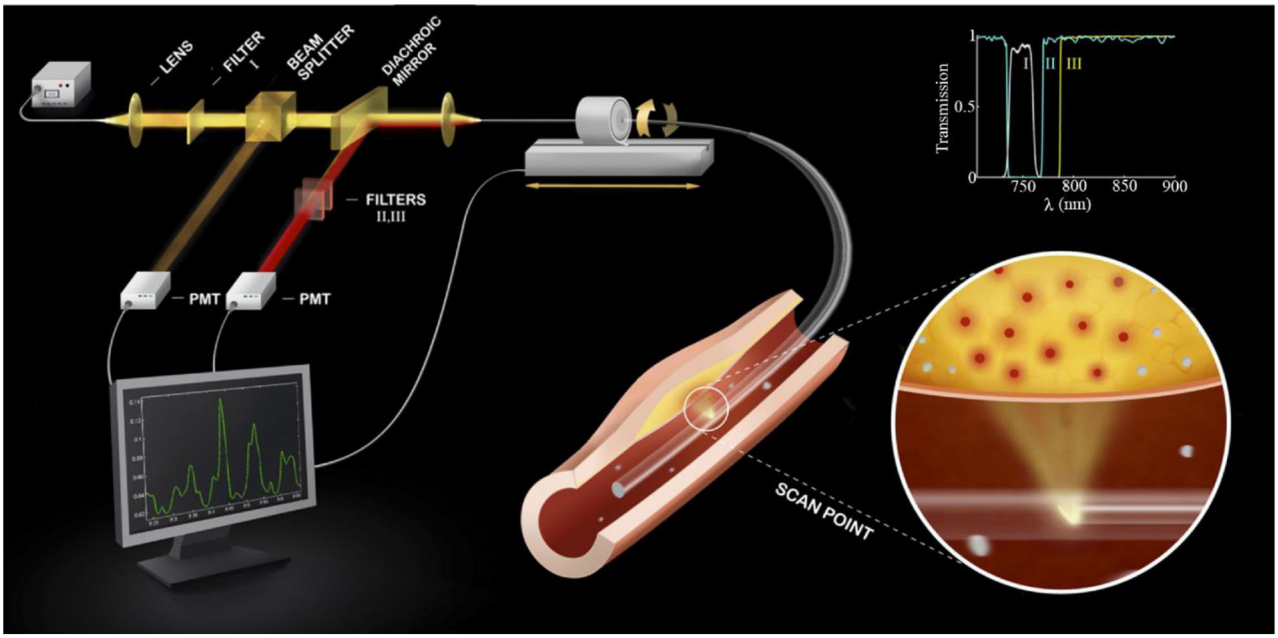

FIGURE 2 | Diagram of a first-generation standalone 2D NIRF Imaging System. The tip of the probe contains a right angle coated prism that focuses laser light into the artery wall, activating fluorophores to their excited state to allow fluorescence emission. Subsequently, fluorophores will emit longer wavelength (lower energy) fluorescent light back into the optical fiber. The fluorescent light is then directed to a dichroic beam splitter that selectively directs it into a photomultiplier tube. The beam passes additional filters to minimize the parasitic signals of laser photons and autofluorescence. The inset shows the spectra of the three filters (I, II, III) used in the system. 2D, 2-dimensional; NIRF, near-infrared fluorescence. Jaffer et al. (13), by permission of American College of Cardiology. License number: 4720261188070.

sensing probe (**Figure 2**). After intravenous injection of ProSense750/VM110, a cathepsin protease-activatable NIRF agent, it was possible to detect *in vivo* plaque inflammation in rabbit iliac arteries (1.5–2.5 mm in diameter) through blood (38). This system was able to detect NIRF signal in spectroscopic-type mode from a limited section of the circumferential arterial wall, given its non-rotational nature. As a result, in 2011 our group developed a two-dimensional rotational NIRF intravascular catheter with automated pullback, providing real-time, *in vivo* spatial mapping of arterial inflammation in atherosclerosis and in stented rabbit aortas (13). It is noteworthy that molecular and anatomical intravascular imaging provide complementary information about plaque structure and biology. This motivated the development of multimodal NIRF hybrid catheter systems that combines NIRF with either OCT or IVUS, for both molecular-structural co-registration, and improved quantification of NIR fluorescence signals.

NIRF Molecular Imaging Agents for Atheroma Targets

A number of NIRF molecular imaging fluorophores that target different molecular processes are now available. Those processes include protease activity, oxidized LDL, endothelial permeability, fibrin deposition, and microcalcifications. Neovascularization can be potentially detected using αv β3 integrin (39); however, to date it has not been studied for atheroma detection using intravascular NIRF catheters. At present, indocyanine green (ICG) is the only fluorophore approved by the US Food and Drug Administration (FDA) for use in human subjects, although a number of fluorophores are undergoing FDA approval in the oncology domain (40–43) and are expected to be translated to the field of atherosclerotic cardiovascular disease (CVD).

Inflammatory Protease Activity

Atheroma macrophage inflammatory activity can be detected using protease-activatable NIR fluorophores. Cathepsins and matrix metalloproteinases (MMP) are amongst the most widely studied proteases. Cysteine cathepsins are mainly found in lysosomes and have been in implicated in atheroma-blood vessel remodeling through elastolytic and collagenolytic activity (44–46). ProSense/VM110 is a cathepsin-activatable fluorophore that has been validated in animal models of atherosclerosis, and very recently has been evaluated in a patient (47). Once injected, baseline quenched ProSense/VM110 localizes to atheroma macrophages, where it is cleaved by cathepsins, yielding NIR fluorescent fragments (48). Two NIR versions of ProSense exist: ProSense 680, which is activated by Cathepsin B, L, and S with peak excitation of 680 nm and peak emission of 700 nm, and ProSense 750/VM110, activated by Cathepsins B, L, S, K, V, and D with peak excitation of 750 nm and peak emission of 780 nm (48). MMPs are another group of proteases that have been implicated in plaque destabilization (49). Similar to ProSense, gelatinases (GelSense680 and MMPSense680) are MMP-activatable fluorophores that exhibit a mosaic distribution of NIRF signal, differentiating hot spots, which correlate with

plaque instability (50, 51). Although label-free OCT detection of macrophages is possible (52, 53), NIRF offers a unique capability to visualize macrophage inflammatory activity *in vivo* is NIRF. A limitation is the need to inject ProSense/VM110 24 h prior to intended imaging; new inflammation sensors with faster pharmacokinetics are needed.

Oxidized Low-Density Lipoprotein

Oxidized LDL (oxLDL) particles are often found within atheroma lipid-rich necrotic core and have been explored as targets for NIRF imaging. Khamis et al. (11) designed a oxidized LDL NIRF targeted molecular imaging agent, termed LO1-750, that binds to oxLDL and fluoresces when illuminated with 750 nm light. LO1-750 has two components: LO1, which is an autoantibody that binds to oxidized LDL in mice, rabbits and humans (54), and AF750, which is a NIRF dye. By utilizing fluorescence molecular tomography (FMT) combined with micro-computed tomography (CT), the group showed LO1-750 accumulation within the aortic arch and its branches in atherosclerotic Ldlr $^{-/-}$ mice when compared to wild type (WT) (11). LO1-750 generated higher NIRF signal when compared to MMPSense signal. *Ex vivo* imaging of rabbit aortas using intravascular NIRF catheter, showed localization of LO1-750 in atheroma lesions. This agent represents a translatable platform for future use in human subjects to enable quantifying plaque oxidative stress. A limitation for LO1-750 long circulating half-life (21 h) and wide area of distribution to the liver, kidneys, and spleen, limiting the plaque target-to-background ratio (11).

Inflammation Determined by Impaired Endothelial Permeability

Plaques that demonstrate impaired endothelial permeability are prone to erosion and thrombosis. Utilizing iron oxide nanoparticles (CLIO), Stein-Merlob et al. (55) developed a NIRF fluorophore, called CLIO-CyAm7 that was used to investigate *in vivo* endothelial dysfunction-based inflammation in a rabbit model. The group demonstrated that within atheroma plaque, CLIO-CyAm7 deposited in macrophages and endothelial cells in areas of impaired endothelial barrier underlying areas of triggered plaque thrombosis (**Figure 3**) (55). This insight links surface inflammation and endothelial permeability to plaque rupture *in vivo*. A limitation of this approach is the use of a long circulating nanoparticle, which may limit point-of-care applications in the cath lab.

Fibrin Deposition

Subclinical plaque rupture may result in fibrin deposition at the plaque surface. In addition, unhealed stents are characterized by fibrin deposition and absent endothelium, and are at increased risk of stent thrombosis (56). In 2012, Hara et al. (10) developed FTP11-Cy7, a fibrin-targeted peptide (FTP11), conjugated to a NIRF dye (Cy7). FTP11-Cy7 binding to fibrin was validated *in vitro* using human plasma clots and *in vivo* by binding to murine thrombi using non-invasive NIRF imaging (10). Subsequently, using rabbit model and hybrid NIRF-OCT intravascular imaging, our group was able to demonstrate that drug eluting stents (DES) showed increased fibrin deposition and fibrin persistence when compared to bare metal stents (BMS), both at day 7 and day 28 (57). This finding also revealed the limitations of standalone OCT imaging, which cannot distinguish between healthy endothelial cell coverage vs. impaired healing demarcated by fibrin deposition. Indeed, a considerable percentage of stent struts appeared covered on OCT; however, a substantial portion of OCT covered struts were in fact covered by NIRF+ fibrin, rather than re-endothelialization, and therefore may indicate an increased risk of thrombosis. A possible limitation is NIRF imaging is not possible beneath the metallic stent struts.

Microcalcifications

Similar to the process of bone formation, plaque calcification is a tightly regulated process of mineralization through the differentiation of VSMCs into osteoblasts that express osteogenic regulating proteins such as alkaline phosphatase, osteopontin, osteocalcin, osteonectin and collagen types I and II (58). When microcalcifications arise within the fibrous cap, local stress increases by 2-fold, contributing to plaque vulnerability (25). A seminal NIRF imaging study in mice demonstrated the ability to detect osteogeneic activity, which precedes bulk calcification, in calcifying murine aortic valves (59). Vulnerable plaques are characterized by microcalcifications and osteogenic activity, both of which are associated with macrophage burden. OsteoSense750 (excitation 750 nm) is a NIRF agent that is derived from bisphosphonate and binds to sites of calcification *in vivo*, highlighting osteoblastic activity, and hence, potential target for vulnerability (58, 60–62). Microcalcifications can be detected by OCT; however, OCT has difficulty in visualizing cellular-level calcifications. Also NIRF has the ability to visualize osteoblastic activity (63). Only a limited studies are available on the use of OsteoSense in vascular biology and plaque vulnerability (59).

TABLE 1 | Individual and hybrid intravascular imaging in terms of detecting high risk plaque features.

	NIRF	OCT	IVUS	NIRF-OCT	NIRF-IVUS	NIRF-OCT-IVUS
Thin fibrous cap <65 μm	−	++	−	++	−	++
Lipid core	+++ (LO1-750)	+++	+	+++	+++	+++
Microcalcifications	+++ (OsteoSense)	+	+	+++	+++	+++
Macrophage infiltration	+++(ProSense, LUM015, MMPSense, and GelSense and ICG)	++	−	+++	+++	+++
Neovascularization	+Bevacizumab-IR800, Integrisense	+	−	++	+	++
Remodeling	−	−	++	−	++	++

IVUS, intravenous ultrasound; NIRF, near-infrared fluorescence; OCT, optical coherence tomography.

HYBRID INTRAVASCULAR NEAR-INFRARED FLUORESCENCE MOLECULAR IMAGING

Standalone NIRF imaging does not allow for distance correction and localization of the source of NIR light excitation and fluorescence emission. In addition, separate NIRF catheter-based imaging and then structural based imaging (e.g., IVUS, OCT) is impractical for clinical use. For these reasons, hybrid intravascular molecular-structural catheters have been developed to enable concurrent co-registration of molecular and anatomical images, and accurate distance-based correction/quantification of the NIRF signal (**Tables 1**, **2**) (64, 66).

Hybrid NIRF-OCT

OCT generates images with high spatial resolution (10–20 μm) but with relatively low depth of penetration (1–2 mm) (65). When combined with NIRF, the resulting hybrid catheter provides complementary data on plaque structure and biology (**Figure 4**). Two hybrid NIRF-OCT catheters have been developed; due to the OCT component, saline/contrast flushing is required during imaging acquisition. In 2011, Yoo et al. (66) developed a dual modality NIRF-OCT rotary catheter system with automated pullback and probe size of 2.4 Fr. The imaging probe comprised of a double-clad fiber with a single mode OCT core (1,320 nm) and inner cladding for NIR fluorescence collection (66). The system was validated using cadaveric human coronary artery with an implanted NIRF-fibrin labeled stent, and *in vivo* rabbit iliac arteries after balloon injury (66). Similarly, Lee et al. (68) designed a 2.6 Fr NIRF-OCT probe with frame acquisition rate of 100/s compared to 25.4/s in the Yoo et al. first-generation system. Using atherosclerosis rabbit models, ICG deposition was reliably identified in lipid- and macrophage-rich plaques *in vivo* (68). Later, the same group validated the use of NIRF-OCT system in drug eluting stent (DES)-stented swine coronary arteries, showing ICG localization within atheroma and behind implanted DES (69). Since NIRF-OCT is an all-optical fiber-based system, the engineering of the probe is more straightforward, compared to NIRF-IVUS or NIRF-IVUS-photoacoustic systems. Limitations of this system are low depth of penetration, and the need to flush during OCT image acquisition.

Hybrid NIRF-IVUS

IVUS was introduced to clinical practice in early 1990s (70), and ever since has been the most widely used intravascular imaging modality due to decent depth of penetration (5–8 mm) and moderate backscatter from blood between 20 and 50 MHz (does not require blood clearance), with a limitation of intermediate spatial resolution (100–250 μm) (65). Dixon and Hossack (71) designed the first NIRF-IVUS hybrid probe and validated its use in phantom coronary arteries. One limitation of this system was the relatively larger probe size of 4.2 Fr due to side-by-side probe arrangement, precluding its use in typical diameter coronary arteries. Subsequently, Abran et al. (64, 72) developed a similar NIRF-IVUS bimodal catheter, and assessed its validity using ICG in *ex vivo* rabbit atherosclerosis model. The first *in vivo*

TABLE 2 | Characteristics of NIRF hybrid intravascular molecular imaging.

		Probe diameter	Fiber characteristics	Depth of penetration	Axial resolution	Frame rate	Limitation
NIRF-OCT	Hara et al. (57)	2.4 Fr	• OCT: 1320 nm • NIRF: 750 nm	NIRF: 3 mm	OCT: 7 μm	25.4/s	Slower image acquisition speed
	Zaheer et al. (60)	2.6 Fr	• OCT: 1,290 nm • NIRF: 749–790 nm	OCT: 1–2 mm	OCT: 7 μm	100/s	–
NIRF-IVUS	Shi et al. (63)	4.2 Fr	• IVUS: 45 MHz • NIRF: 750 nm	• IVUS: 4 mm • NIRF: 2 mm	IVUS: N/A	30/s	Large probe size
	Abran et al. (64) (Coronary)	4.5 Fr	• IVUS: 40 MHz • NIRF: 750 nm	• IVUS: 4 mm • NIRF: 2 mm	IVUS: 150 μm	2.7/s	Large probe size
	Abran et al. (64) (Peripheral)	9.0 Fr	• IVUS: 15 MHz • NIRF: 750 nm	• IVUS: 4 mm • NIRF: 2 mm	IVUS: 270 μm	2.7/s	Large probe size
NIRF-IVUS-OCT	Maehara et al. (65)	3.9 Fr	• OCT: 1,310 nm • IVUS: 40 MHz • NIRF: 785 nm	• OCT: 3–5 mm • IVUS: 5–6 mm • NIRF: 3–5 mm	–	20/s	Large probe size

IVUS, intravenous ultrasound; NIRF, near-infrared fluorescence; OCT, optical coherence tomography.

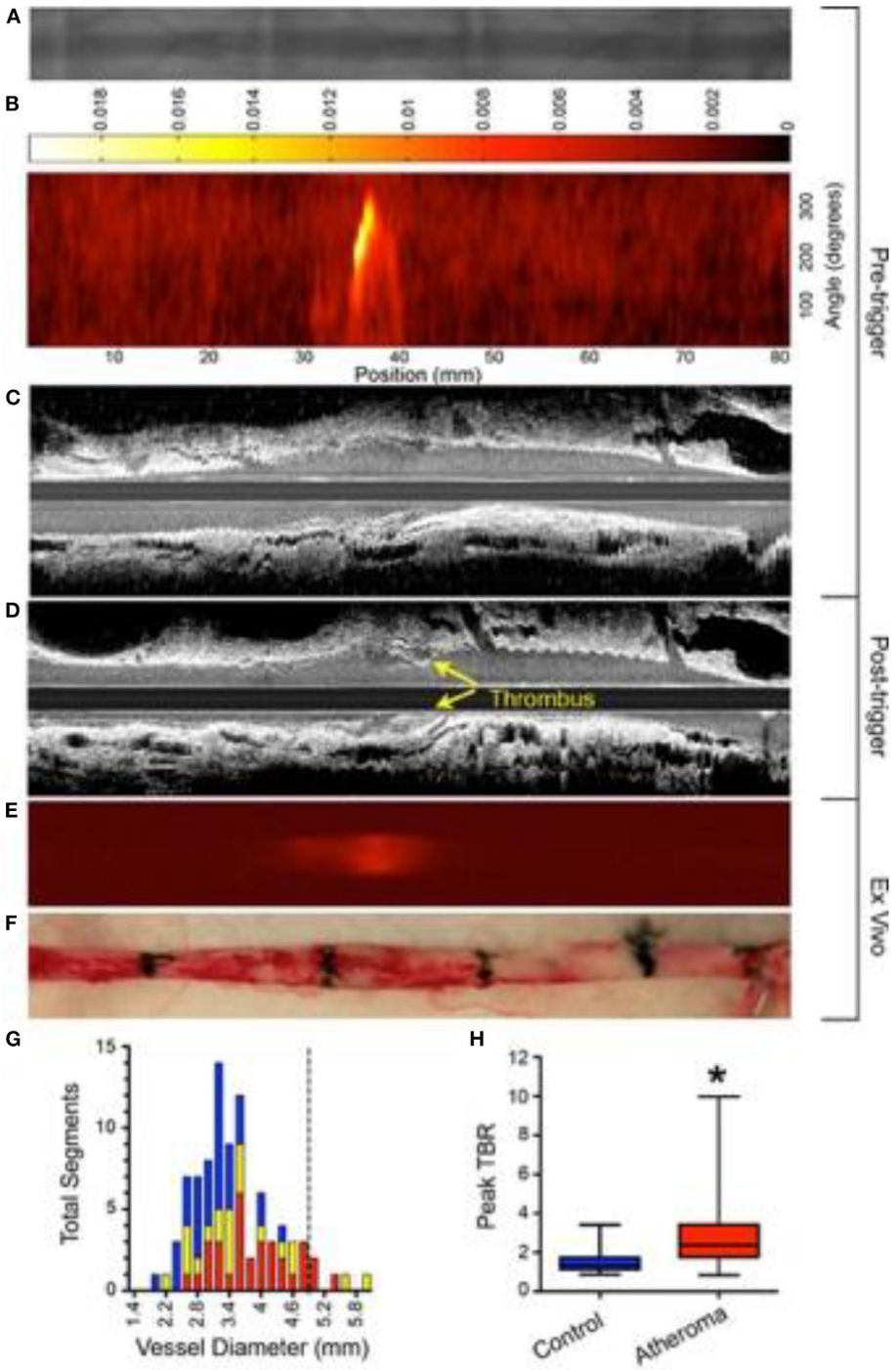

FIGURE 3 | Experimental *in vivo* and *ex vivo* near-infrared fluorescence (NIRF) imaging of inflammation and subsequent atherothrombosis. Rabbits underwent balloon injury at week 2, and were fed high cholesterol diet till week 8. Ten weeks after balloon injury, rabbits received CLIO-CyAm7 (a inflammation-sensitive nanoparticle-based fluorophore), and underwent pharmacologic-triggered plaque thrombosis 24 h later. **(A)** Pre-trigger x-ray angiography showing the aorta for image coregistration. **(B)** Pre-trigger *in vivo* NIRF imaging projected into a 2-dimensional (2D) matrix showing an area of increased signal between 30 and 40 mm. **(C,D)** Pre- and post-trigger intravascular ultrasound (IVUS) imaging demonstrating induced luminal thrombus (yellow arrows) corresponding to the region of increased NIRF signal intensity on pretrigger NIRF imaging in **(B)**. **(E,F)** *Ex vivo* fluorescence reflectance imaging of cross-linked iron oxide (CLIO)-CyAm7 verifying *in vivo* 2D NIRF imaging, and gross pathology of the resected aorta with 1.5 cm black tissue markings for histological analysis and coregistration. **(G)** Histogram of vessel diameter measured by cross-sectional IVUS imaging. Red indicates atheroma without attached thrombus, yellow indicates atheroma with attached thrombus, and blue indicates uninjured control aortic segments. The dashed line indicates the 5 mm cut-off for exclusion of NIRF imaging data because of distance attenuation of the NIRF signal in large vessels. **(H)** *In vivo* 2D NIRF imaging revealed significantly higher target/background ratio (TBR) in areas with atheroma, compared with uninjured segments of the aorta (peak TBR 2.86 ± 1.82 and 1.55 ± 0.65, $^*P = 0.001$). Stein-Merlob et al. (55), by permission of American Heart Asssociation (AHA). License number: 4720560395030.

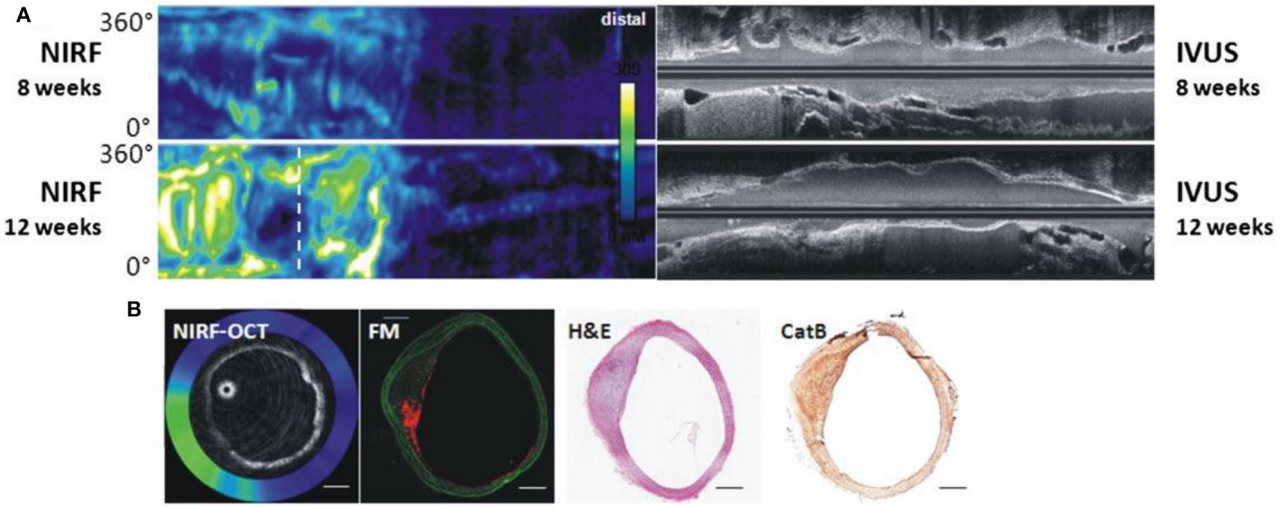

FIGURE 4 | Dual modality NIRF-OCT along separate IVUS images, obtained at weeks 8 and 12 following balloon injury in rabbit aorta. ProSenseVM110 is the fluorophore used to acquire NIRF imaging. **(A)** Longitudinal rabbit aorta sections. To the left, co-registered OCT-NIRF images and to the right corresponding IVUS images. **(B)** Cross sections of rabbit aortas corresponding to white dotted line in **(A)**. From left to right: cross-sectional co-registration of NIRF-OCT images (Green/white = high near-infrared fluorescence; blue/black = low near-infrared fluorescence), matched cross-sectional fluorescence microscopy (FM) (red = ProSense VM110; green = autofluorescence) and histopathological sections reveals increased ProSense VM110 NIRF signal within a moderate fibrofatty atheroma (H&E) associated with cathepsin B immunostain. Scale bars, 1 mm. Figure courtesy of Dr. Eric Osborn and Dr. Giovanni Ughi. Bourantas et al. (67), by permission of European Society of Cardiology. License Number: 4720391246688.

validation of a bimodal NIRF-IVUS system was demonstrated by Bozhko et al. (73) in angioplasty-induced vascular injury in swine peripheral arteries and experimental fibrin deposition on coronary artery stents, and of atheroma in a rabbit aorta, using ICG. Clinical translation of this hybrid catheter necessitates designing a smaller probe <3.0 Fr, appropriate for intracoronary use, and will likely require re-engineering of side-by-side designs to serial designs, similar to current clinical IVUS-NIR spectroscopy catheters.

Hybrid trimodal NIRF-OCT-IVUS Catheter

A tri-hybrid intravascular probe using IVUS, OCT and NIRF technologies was developed by Li et al. (74), offering the potential for multi-structural and molecular imaging in a single pullback. The system was validated using phantom and *ex vivo* experiments using pig and rabbit arteries (74). While this system offers the advantages of the three imaging modalities combined, the probe size at present (3.9 Fr) is currently too large for routine clinical type applications, but is an exciting advance nonetheless, and we await further validation *in vivo*.

NIRAF-OCT IMAGING

While NIRF intracoronary molecular imaging has not been performed in human subjects, a recent advance was the demonstration of clinical intracoronary OCT-NIR-autofluorescence (NIRAF, based at 633 nm), a new contrast-free autofluorescence-based method (75). In the first human study on 12 patients with CAD undergoing PCI, Ughi et al. (75) demonstrated that NIRAF signal correlated with vulnerable features like fibroatheroma, plaque rupture and in-stent restenosis in non-culprit lesions (75). Additionally, NIRAF signal was associated with components of components of intraplaque hemorrhage (e.g., bilirubin, protoporphyrin IX) (76). While NIRAF molecular imaging is very promising intravascular imaging modality, the complete set of molecules and biological processes underlying NIRAF remain to be elucidated. Compared to NIRAF, NIRF imaging through molecular-specific imaging agents allows targeting of specific patho-biological processes, like protease activity, oxidized LDL, endothelial permeability, fibrin deposition, and osteogenesis.

PHOTOACOUSTIC IMAGING

Intravascular photoacoustic (IVPA) is an emerging imaging modality that is a natural extension of IVUS, and has the potential to detect certain fluorophores and nanomaterials that could enable IVPA-based molecular imaging. IVPA is a novel structural and molecular imaging modality that uses multiple wavelengths to illuminate the tissue of interest and identifies the acoustic waves generated by the thermoelastic expansion of the environment surrounding absorbing molecules (77). In an *in vivo* experiment on rabbit aortas, Wang et al. (78) showed that IVPA/IVUS imaging can identify lipid deposits within vessel wall through the blood without the need of saline flushing or balloon occlusion. Excitingly, IVPA provided 3 dimensional images of the vessel wall. Recently, Iskandder-Risk et al. demonstrated IVPA *in vivo* imaging of swine coronary artery. The quality of images were adjudicated using OCT and histology (79).

TRANSLATIONAL OUTLOOK

To enable clinical intracoronary NIRF molecular imaging, the NIRF system will need to switch to 750–800 nm excitation, and clinical targeted/activatable NIRF imaging agents will need to be available. Currently, indocyanine green (ICG, ex/em 805/830 nm) is the only atherosclerosis-targeted NIR fluorophore approved by the US Food and Drug Administration (FDA) for human use, facilitating the use of NIRF catheter in human subjects once approved. The recognition that ICG, a blood flow imaging agent available for 50 years, could target atherosclerosis was somewhat unexpected. In 2011, Vinegoni et al. recognized that the amphiphilic properties of ICG might allow it to have an atheroma targeting profile. Using intravascular and *ex vivo* NIRF imaging, ICG was found to accumulate in atheroma macrophages and was detected *in vivo* rabbit atheroma (80), and in pig coronary plaques (69, 81). Subsequently in 2016, The BRIGHT-CEA trial (Indocyanine Green Fluorescence Uptake in Human Carotid Artery Plaque, a study of injection of ICG prior to patients undergoing carotid endarterectomy) was conducted (81). Five patients undergoing carotid endarterectomy were injected with ICG; plaques were resected 99 min afterwards. *Ex vivo* intravascular NIRF-OCT and fluorescence reflectance imaging showed that ICG NIRF signal localized to and accumulated in human atheroma for the first time in living patients (**Figure 5**). The authors concluded that

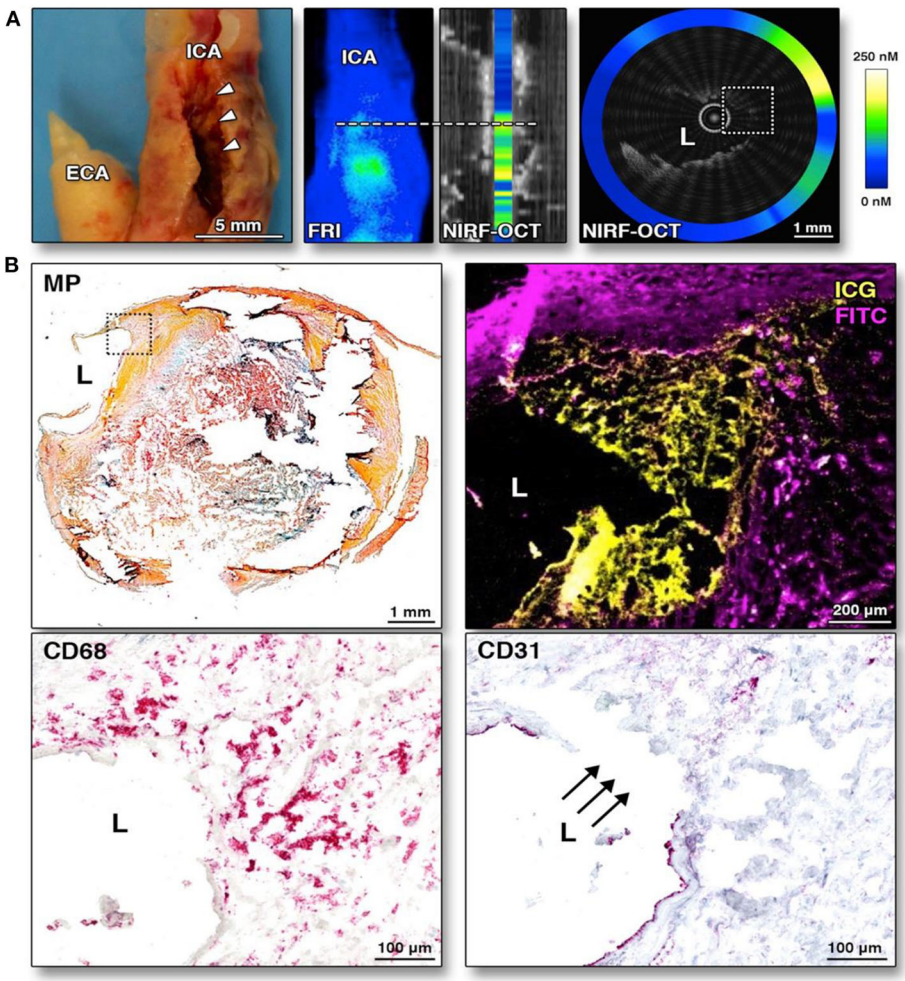

FIGURE 5 | *Ex-vivo* intravascular NIRF-OCT images of human carotid arteries following ICG injection and then endartectomy. ICG was injected into human subjects 99 min prior to endartectomy. ICG accumulates in atherosclerotic area especially endothelial discontinuation. **(A)** Corresponding gross internal carotid artery (ICA) specimen, along with corresponding fluorescence reflectance image (FRI), and NIRF-OCT cross sectional, coregistered images, illustrating similar ICG uptake pattern (light blue = low ICG signal; green-yellow = high ICG signal) at the stenotic region (white arrowheads) in the ICA. **(B)** Histological analysis of the same area of the NIRF-OCT cross-sectional image shown in **(A)**. Movat pentachrome (MP) shows a complex atherosclerotic plaque with a large necrotic core with lipid and cellular infiltration (dotted box). Higher magnification (10×) fluorescence microscopy of the boxed area illustrates ICG NIRF signal adjacent to the lumen, which is distinct from fluorescein isothiocyanate (FITC)-channel autofluorescence. CD68 staining of the same area validates that the ICG NIRF signal (yellow pseudocolor) spatially relates to CD68-defined plaque macrophages beneath the area of intimal disruption. The disruption is confirmed by CD31 staining in this same area. ECA, external carotid artery. Verjans et al. (81), by permission of American College of Cardiology (ACC). License number: 4720551416574.

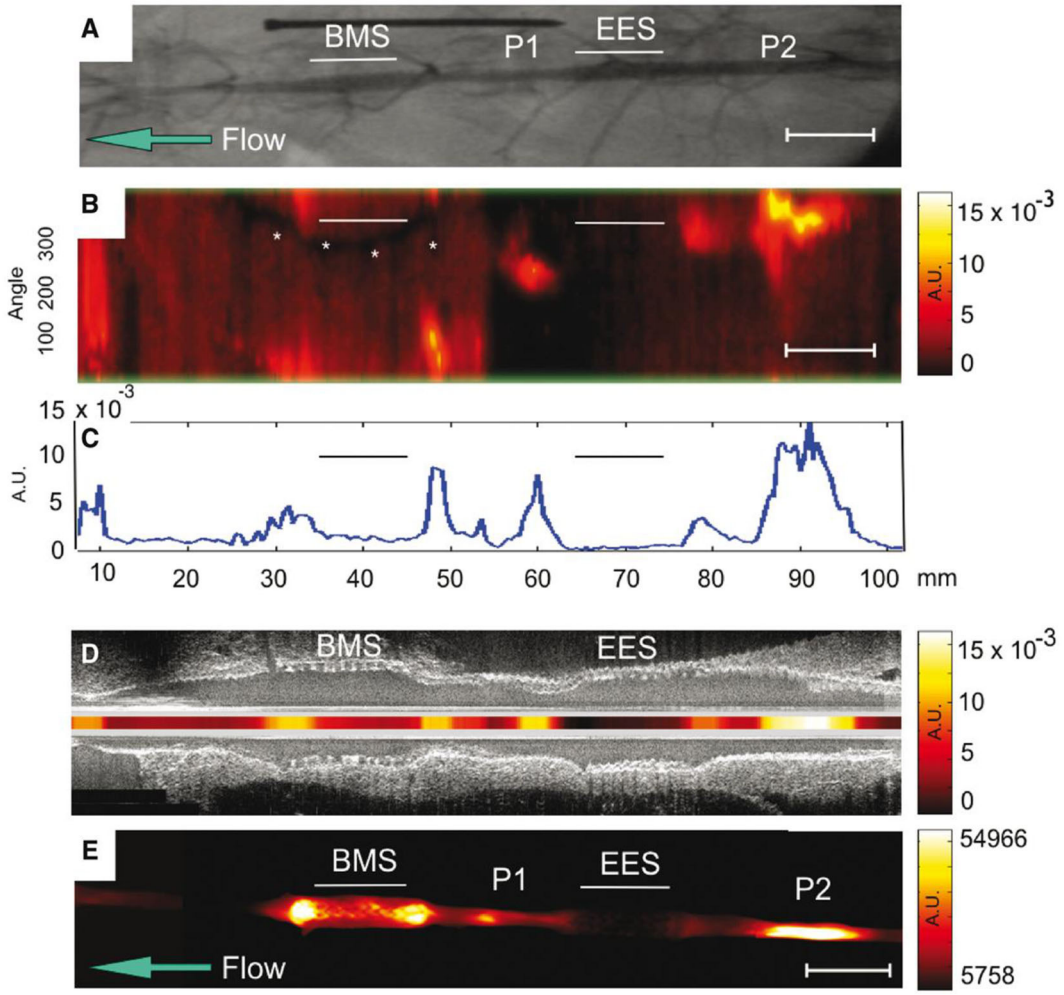

FIGURE 6 | NIRF molecular imaging of stent suppresion of plaque inflammation. *In vivo* and *ex vivo* imaging of rabbit aorta demonestrating inflammatory protease activity in bare metal stent (BMS)-, everolimus-eluting stent (EES)-treated, and unstented plaque zones. **(A)** Angiogram of the abdominal aorta, showing positions of BMS and EES. Areas of IVUS–visible plaque areas (P1 and P2 zones) are highlighted. **(B)** *In vivo* NIRF imaging, demonestrating increased signal intensity in areas corresponding to BMS. The y-axis represents the angular dimension (0–360°). The x-axis represents the longitudinal/axial dimension in millimeters. The asterisk denotes a guidewire artifact. **(C)** Averaged mean NIRF signal (unidimentional) along the longitudinal axis. NIRF signal is higher in unstented regions > BMS regions > EES regions **(D)** Co-reistered longitudinal IVUS and intravascular NIRF images. **(E)** *Ex vivo* FRI at 800 nm of the resected aorta, demonestrating higher signal in BMS region, compared to EES region. AU, arbitrary units; Scale bar, 10 mm. Calfon Press et al. (12), by permission of European Society of Cardiology. License number: 4720551036244.

ICG accumulated in plaques with impaired endothelial integrity, disrupted fibrous cap, and area of neovascularization (81). This study may pave the way for future human intracoronary NIRF-OCT using ICG to image pathobiological aspects of coronary atherosclerosis.

Another translatable aspect is the use of NIRF imaging to detect plaque inflammation modified by stent placement, and predict complications such as in-stent thrombosis and stenosis. Using an atheroma rabbit model, Calfon Press et al. (12) showed that everolimus-eluting DES could decrease *in vivo* plaque inflammation and macrophage accumulation. This finding provides evidence that DES may be a bio-stabilizer of high-risk, inflamed plaques (**Figure 6**), although neoatherosclerosis is still a potential limitation of such approach. In a recent study, Osborn et al. (82) have demonstrated that plaque inflammation is an independent predictor of plaque progression, using atheroma rabbit model and serial NIRF-OCT. These preclinical studies will provide an outline for clinical studies once a NIRF catheter is approved.

CONCLUSION AND FUTURE DIRECTIONS

Intravascular NIRF molecular imaging offers a new dimension for plaque assessment based on pathobiology, a key driver of coronary events, and is on the verge of clinical translation to human coronary arteries. We envision that intravascular

NIRF-OCT or NIRF-IVUS molecular-structural imaging will be used to comprehensively assess the coronary artery of patients already undergoing percutaneous coronary intervention. As PCI is now routinely being performed with intravascular imaging (IVUS or OCT), we anticipate that the only difference for NIRF-OCT or NIRF-IVUS will be the administration of a targeted molecular imaging agent at the start of PCI. Following PCI, completion NIRF-OCT or NIRF-IVUS will be performed, allowing assessment of non-culprit coronary artery segments proximal and distal to the target lesion that was stented. This will allow the generation of an integrated molecular-structural atheroma score reflecting the degree of pathobiology for the culprit artery. In addition another artery could be potentially imaged with the same goal. Ultimately, a NIRF-based pathobiology score will identify high-risk lesions, arteries, and patients, allowing the ability to more precisely target newer atheroma medical therapies (e.g., PCSK9 inhibitors, icosapent ethyl, ezetimibe, GLP1-receptor antagonists, SGLT2 inhibitors) to those at highest risk. Overall, integration of NIRF pathobiology assessment will enable personalized medical therapy for patients with CAD, instead of a one size fits all approach as currently practiced worldwide (e.g., statin and dual anti-platelet therapy, regardless of underlying pathobiological risk).

AUTHOR CONTRIBUTIONS

Both authors contributed to the writing of this review article.

FUNDING

This work was supported by NIH 1R01HL137913 (FAJ) and 1R01HL150538 (FAJ)

REFERENCES

1. Muller JE, Tofler GH, Stone PH. Circadian variation and triggers of onset of acute cardiovascular disease. *Circulation.* (1989) 79:733–43. doi: 10.1161/01.CIR.79.4.733
2. Schaar JA, Muller JE, Falk E, Virmani R, Fuster V, Serruys PW, et al. Terminology for high-risk and vulnerable coronary artery plaques. Report of a meeting on the vulnerable plaque, June 17 and 18, 2003, Santorini, Greece. *Eur Heart J.* (2004) 25:1077–82. doi: 10.1016/j.ehj.2004.01.002
3. Narula J, Nakano M, Virmani R, Kolodgie FD, Petersen R, Newcomb R, et al. Histopathologic characteristics of atherosclerotic coronary disease and implications of the findings for the invasive and noninvasive detection of vulnerable plaques. *J Am Coll Cardiol.* (2013) 61:1041–51. doi: 10.1016/j.jacc.2012.10.054
4. Burke AP, Farb A, Malcom GT, Liang YH, Smialek J, Virmani R. Coronary risk factors and plaque morphology in men with coronary disease who died suddenly. *N Engl J Med.* (1997) 336:1276–82. doi: 10.1056/NEJM199705013361802
5. van der Wal AC, Becker AE, van der Loos CM, Das PK. Site of intimal rupture or erosion of thrombosed coronary atherosclerotic plaques is characterized by an inflammatory process irrespective of the dominant plaque morphology. *Circulation.* (1994) 89:36–44. doi: 10.1161/01.CIR.89.1.36
6. Bode MF, Jaffer FA. IVUS and OCT: Current state-of-the-art in intravascular coronary imaging. *Curr Cardiovasc Imaging Rep.* (2019) 12:29. doi: 10.1007/s12410-019-9503-7
7. Stone PH, Saito S, Takahashi S, Makita Y, Nakamura S, Kawasaki T, et al. Prediction of progression of coronary artery disease and clinical outcomes using vascular profiling of endothelial shear stress and arterial plaque characteristics: the PREDICTION study. *Circulation.* (2012) 126:172–81. doi: 10.1161/CIRCULATIONAHA.112.096438
8. Xie Y, Mintz GS, Yang J, Doi H, Iñiguez A, Dangas GD, et al. Clinical outcome of nonculprit plaque ruptures in patients with acute coronary syndrome in the PROSPECT study. *JACC Cardiovasc Imaging.* (2014) 7:397–405. doi: 10.1016/j.jcmg.2013.10.010
9. Stone GW, Maehara A, Lansky AJ, de Bruyne B, Cristea E, Mintz GS, et al. A prospective natural-history study of coronary atherosclerosis. *N Engl J Med.* (2011) 364:226–35. doi: 10.1056/NEJMoa1002358
10. Hara T, Bhayana B, Thompson B, Kessinger CW, Khatri A, McCarthy JR, et al. Molecular imaging of fibrin deposition in deep vein thrombosis using fibrin-targeted near-infrared fluorescence. *JACC Cardiovasc Imaging.* (2012) 5:607–15. doi: 10.1016/j.jcmg.2012.01.017
11. Khamis RY, Woollard KJ, Hyde GD, Boyle JJ, Bicknell C, Chang S-H, et al. Near Infrared Fluorescence (NIRF) molecular imaging of oxidized LDL with an autoantibody in experimental atherosclerosis. *Sci Rep.* (2016) 6:21785. doi: 10.1038/srep21785
12. Calfon Press MA, Mallas G, Rosenthal A, Hara T, Mauskapf A, Nudelman RN, et al. Everolimus-eluting stents stabilize plaque inflammation *in vivo*: assessment by intravascular fluorescence molecular imaging. *Eur Heart J Cardiovasc Imaging.* (2017) 18:510–18. doi: 10.1093/ehjci/jew228
13. Jaffer FA, Calfon MA, Rosenthal A, Mallas G, Razansky RN, Mauskapf A, et al. Two-dimensional intravascular near-infrared fluorescence molecular imaging of inflammation in atherosclerosis and stent-induced vascular injury. *J Am Coll Cardiol.* (2011) 57:2516–26. doi: 10.1016/j.jacc.2011.02.036
14. Wu M-Y, Li C-J, Hou M-F, Chu P-Y. New insights into the role of inflammation in the pathogenesis of atherosclerosis. *Int J Mol Sci.* (2017) 18:2034. doi: 10.3390/ijms18102034
15. Khalil MF, Wagner WD, Goldberg IJ. Molecular interactions leading to lipoprotein retention and the initiation of atherosclerosis. *Arterioscler Thromb Vasc Biol.* (2004) 24:2211–8. doi: 10.1161/01.ATV.0000147163.54024.70
16. Williams KJ. Arterial wall chondroitin sulfate proteoglycans: diverse molecules with distinct roles in lipoprotein retention and atherogenesis. *Curr Opin Lipidol.* (2001) 12:477–87. doi: 10.1097/00041433-200110000-00002
17. Bentzon JF, Otsuka F, Virmani R, Falk E. Mechanisms of plaque formation and rupture. *Circ Res.* (2014) 114:1852–66. doi: 10.1161/CIRCRESAHA.114.302721
18. Bom MJ, van der Heijden DJ, Kedhi E, van der Heyden J, Meuwissen M, Knaapen P, et al. Early detection and treatment of the vulnerable coronary plaque: can we prevent acute coronary syndromes? *Circ Cardiovasc Imaging.* (2017) 10:e005973. doi: 10.1161/CIRCIMAGING.116.005973
19. Zhou M-S, Chadipiralla K, Mendez AJ, Jaimes EA, Silverstein RL, Webster K, et al. Nicotine potentiates proatherogenic effects of oxLDL by stimulating and upregulating macrophage CD36 signaling. *Am J Physiol Heart Circ Physiol.* (2013) 305:H563–74. doi: 10.1152/ajpheart.00042.2013
20. Falk E. Pathogenesis of atherosclerosis. *J Am Coll Cardiol.* (2006) 47:C7–12. doi: 10.1016/j.jacc.2005.09.068
21. Bennett MR, Sinha S, Owens GK. Vascular smooth muscle cells in atherosclerosis. *Circ Res.* (2016) 118:692–702. doi: 10.1161/CIRCRESAHA.115.306361
22. Yahagi K, Kolodgie FD, Otsuka F, Finn AV, Davis HR, Joner M, et al. Pathophysiology of native coronary, vein graft, and in-stent atherosclerosis. *Nat Rev Cardiol.* (2016) 13:79–98. doi: 10.1038/nrcardio.2015.164
23. New SEP, Aikawa E. Role of extracellular vesicles in *de novo* mineralization: an additional novel mechanism of cardiovascular calcification. *Arterioscler Thromb Vasc Biol.* (2013) 33:1753–8. doi: 10.1161/ATVBAHA.112.300128
24. Nakahara T, Dweck MR, Narula N, Pisapia D, Narula J, Strauss HW. Coronary artery calcification: from mechanism to molecular imaging. *JACC Cardiovasc Imaging.* (2017) 10:582–93. doi: 10.1016/j.jcmg.2017.03.005
25. Vengrenyuk Y, Carlier S, Xanthos S, Cardoso L, Ganatos P, Virmani R, et al. A hypothesis for vulnerable plaque rupture due to stress-induced debonding around cellular microcalcifications in thin fibrous caps. *Proc Natl Acad Sci USA.* (2006) 103:14678–83. doi: 10.1073/pnas.0606310103

26. Milzi A, Burgmaier M, Burgmaier K, Hellmich M, Marx N, Reith S. Type 2 diabetes mellitus is associated with a lower fibrous cap thickness but has no impact on calcification morphology: an intracoronary optical coherence tomography study. *Cardiovasc Diabetol.* (2017) 16:152. doi: 10.1186/s12933-017-0635-2
27. Lee JM, Choi KH, Koo B-K, Park J, Kim J, Hwang D, et al. Prognostic implications of plaque characteristics and stenosis severity in patients with coronary artery disease. *J Am Coll Cardiol.* (2019) 73:2413–24. doi: 10.1016/j.jacc.2019.02.060
28. Narula J, Strauss HW. The popcorn plaques. *Nat Med.* (2007) 13:532–4. doi: 10.1038/nm0507-532
29. Libby P, Ridker PM, Hansson GK, Leducq Transatlantic Network on Atherothrombosis. Inflammation in atherosclerosis: from pathophysiology to practice. *J Am Coll Cardiol.* (2009) 54:2129–38. doi: 10.1016/j.jacc.2009.09.009
30. Mehta SR, Wood DA, Storey RF, Mehran R, Bainey KR, Nguyen H, et al. Complete revascularization with multivessel PCI for myocardial infarction. *N Engl J Med.* (2019) 381:1411–21. doi: 10.1056/NEJMoa1907775
31. Kubo T, Maehara A, Mintz GS, Doi H, Tsujita K, Choi S-Y, et al. The dynamic nature of coronary artery lesion morphology assessed by serial virtual histology intravascular ultrasound tissue characterization. *J Am Coll Cardiol.* (2010) 55:1590–7. doi: 10.1016/j.jacc.2009.07.078
32. Zhao Z, Witzenbichler B, Mintz GS, Jaster M, Choi S-Y, Wu X, et al. Dynamic nature of nonculprit coronary artery lesion morphology in STEMI: a serial IVUS analysis from the HORIZONS-AMI trial. *JACC Cardiovasc Imaging.* (2013) 6:86–95. doi: 10.1016/j.jcmg.2012.08.010
33. Papadopoulou S-L, Neefjes LA, Garcia-Garcia HM, Flu W-J, Rossi A, Dharampal AS, et al. Natural history of coronary atherosclerosis by multislice computed tomography. *JACC Cardiovasc Imaging.* (2012) 5:S28–37. doi: 10.1016/j.jcmg.2012.01.009
34. Calfon MA, Rosenthal A, Mallas G, Mauskapf A, Nudelman RN, Ntziachristos V, et al. *In vivo* near infrared fluorescence (NIRF) intravascular molecular imaging of inflammatory plaque, a multimodal approach to imaging of atherosclerosis. *J Vis Exp.* (2011) 54:2257. doi: 10.3791/2257
35. Chowdhury MM, Tawakol A, Jaffer FA. Molecular imaging of atherosclerosis: a clinical focus. *Curr Cardiovasc Imaging Rep.* (2017) 10:2. doi: 10.1007/s12410-017-9397-1
36. Hong G, Antaris AL, Dai H. Near-infrared fluorophores for biomedical imaging. *Nat Biomed Eng.* (2017) 1:0010. doi: 10.1038/s41551-016-0010
37. Sevick-Muraca EM, Rasmussen JC. Molecular imaging with optics: primer and case for near-infrared fluorescence techniques in personalized medicine. *J Biomed Opt.* (2008) 13:041303. doi: 10.1117/1.2953185
38. Jaffer FA, Vinegoni C, John MC, Aikawa E, Gold HK, Finn AV, et al. Real-time catheter molecular sensing of inflammation in proteolytically active atherosclerosis. *Circulation.* (2008) 118:1802–9. doi: 10.1161/CIRCULATIONAHA.108.785881
39. Lin S-A, Patel M, Suresch D, Connolly B, Bao B, Groves K, et al. Quantitative longitudinal imaging of vascular inflammation and treatment by ezetimibe in apoE mice by FMT using new optical imaging biomarkers of cathepsin activity and α(v)β(3) integrin. *Int J Mol Imaging.* (2012) 2012:189254. doi: 10.1155/2012/189254
40. van Dam GM, Themelis G, Crane LMA, Harlaar NJ, Pleijhuis RG, Kelder W, et al. Intraoperative tumor-specific fluorescence imaging in ovarian cancer by folate receptor-α targeting: first in-human results. *Nat Med.* (2011) 17:1315–19. doi: 10.1038/nm.2472
41. Whitley MJ, Cardona DM, Lazarides AL, Spasojevic I, Ferrer JM, Cahill J, et al. A mouse-human phase 1 co-clinical trial of a protease-activated fluorescent probe for imaging cancer. *Sci Transl Med.* (2016) 8:320ra4. doi: 10.1126/scitranslmed.aad0293
42. Harlaar NJ, Koller M, de Jongh SJ, van Leeuwen BL, Hemmer PH, Kruijff S, et al. Molecular fluorescence-guided surgery of peritoneal carcinomatosis of colorectal origin: a single-centre feasibility study. *Lancet Gastroenterol Hepatol.* (2016) 1:283–90. doi: 10.1016/S2468-1253(16)30082-6
43. Nagengast WB, Hartmans E, Garcia-Allende PB, Peters FTM, Linssen MD, Koch M, et al. Near-infrared fluorescence molecular endoscopy detects dysplastic oesophageal lesions using topical and systemic tracer of vascular endothelial growth factor A. *Gut.* (2019) 68:7–10. doi: 10.1136/gutjnl-2017-314953
44. Turk V, Stoka V, Vasiljeva O, Renko M, Sun T, Turk B, et al. Cysteine cathepsins: from structure, function and regulation to new frontiers. *Biochim Biophys Acta.* (2012) 1824:68–88. doi: 10.1016/j.bbapap.2011.10.002
45. Sukhova GK, Shi GP, Simon DI, Chapman HA, Libby P. Expression of the elastolytic cathepsins S and K in human atheroma and regulation of their production in smooth muscle cells. *J Clin Invest.* (1998) 102:576–83. doi: 10.1172/JCI181
46. Jaffer FA, Kim D-E, Quinti L, Tung C-H, Aikawa E, Pande AN, et al. Optical visualization of cathepsin K activity in atherosclerosis with a novel, protease-activatable fluorescence sensor. *Circulation.* (2007) 115:2292–8. doi: 10.1161/CIRCULATIONAHA.106.660340
47. *VM110 in Detection of Microscopic Tumors: A Phase I Study*. Full Text View. ClinicalTrials.gov. Available online at: https://clinicaltrials.gov/ct2/show/NCT03286062 (accessed December 1, 2019).
48. Jaffer FA, Weissleder R. Seeing within: molecular imaging of the cardiovascular system. *Circ Res.* (2004) 94:433–45. doi: 10.1161/01.RES.0000119321.18573.5A
49. Newby AC. Metalloproteinase production from macrophages - a perfect storm leading to atherosclerotic plaque rupture and myocardial infarction. *Exp Physiol.* (2016) 101:1327–37. doi: 10.1113/EP085567
50. Wallis de Vries BM, Hillebrands J-L, van Dam GM, Tio RA, de Jong JS, Slart RHJA, et al. Images in cardiovascular medicine. Multispectral near-infrared fluorescence molecular imaging of matrix metalloproteinases in a human carotid plaque using a matrix-degrading metalloproteinase-sensitive activatable fluorescent probe. *Circulation.* (2009) 119:e534–6. doi: 10.1161/CIRCULATIONAHA.108.821389
51. Deguchi J, Aikawa M, Tung C-H, Aikawa E, Kim D-E, Ntziachristos V, et al. Inflammation in atherosclerosis: visualizing matrix metalloproteinase action in macrophages *in vivo*. *Circulation.* (2006) 114:55–62. doi: 10.1161/CIRCULATIONAHA.106.619056
52. Tearney GJ. OCT imaging of macrophages. *JACC.* (2015) 8:73–5. doi: 10.1016/j.jcmg.2014.09.019
53. Tearney GJ, Yabushita H, Houser SL, Aretz HT, Jang I-K, Schlendorf KH, et al. Quantification of macrophage content in atherosclerotic plaques by optical coherence tomography. *Circulation.* (2003) 107:113–19. doi: 10.1161/01.CIR.0000044384.41037.43
54. Chang S-H, Johns M, Boyle JJ, McConnell E, Kirkham PA, Bicknell C, et al. Model IgG monoclonal autoantibody-anti-idiotype pair for dissecting the humoral immune response to oxidized low density lipoprotein. *Hybridoma.* (2012) 31:87–98. doi: 10.1089/hyb.2011.0058
55. Stein-Merlob AF, Hara T, McCarthy JR, Mauskapf A, Hamilton JA, Ntziachristos V, et al. Atheroma susceptible to thrombosis exhibit impaired endothelial permeability *in vivo* as assessed by nanoparticle-based fluorescence molecular imaging. *Circ Cardiovasc Imaging.* (2017) 10:e005813. doi: 10.1161/CIRCIMAGING.116.005813
56. FinnAV JM, NakazawaG KF, NewellJ JMC. Pathological correlates of late drugeluting stent thrombosis: strut coverage as a marker of endothelialization. *Circulation.* (2007) 115:2435–41. doi: 10.1161/CIRCULATIONAHA.107.693739
57. Hara T, Ughi GJ, McCarthy JR, Erdem SS, Mauskapf A, Lyon SC, et al. Intravascular fibrin molecular imaging improves the detection of unhealed stents assessed by optical coherence tomography *in vivo*. *Eur Heart J.* (2017) 38:447–55. doi: 10.1093/eurheartj/ehv677
58. Aikawa E, Nahrendorf M, Figueiredo J-L, Swirski FK, Shtatland T, Kohler RH, et al. Osteogenesis associates with inflammation in early-stage atherosclerosis evaluated by molecular imaging *in vivo*. *Circulation.* (2007) 116:2841–50. doi: 10.1161/CIRCULATIONAHA.107.732867
59. Aikawa E, Nahrendorf M, Sosnovik D, Lok VM, Jaffer FA, Aikawa M, et al. Multimodality molecular imaging identifies proteolytic and osteogenic activities in early aortic valve disease. *Circulation.* (2007) 115:377–86. doi: 10.1161/CIRCULATIONAHA.106.654913
60. Zaheer A, Lenkinski RE, Mahmood A, Jones AG, Cantley LC, Frangioni JV. *In vivo* near-infrared fluorescence imaging of osteoblastic activity. *Nat Biotechnol.* (2001) 19:1148–54. doi: 10.1038/nbt1201-1148
61. Derwall M, Malhotra R, Lai CS, Beppu Y, Aikawa E, Seehra JS, et al. Inhibition of bone morphogenetic protein signaling reduces vascular calcification and atherosclerosis. *Arterioscler Thromb Vasc Biol.* (2012) 32:613–22. doi: 10.1161/ATVBAHA.111.242594

62. Figueiredo J-L, Aikawa M, Zheng C, Aaron J, Lax L, Libby P, et al. Selective cathepsin S inhibition attenuates atherosclerosis in apolipoprotein E-deficient mice with chronic renal disease. *Am J Pathol.* (2015) 185:1156–66. doi: 10.1016/j.ajpath.2014.11.026
63. Shi X, Gao J, Lv Q, Cai H, Wang F, Ye R, et al. Calcification in atherosclerotic plaque vulnerability: friend or foe? *Front Physiol.* (2020) 11:56. doi: 10.3389/fphys.2020.00056
64. Abran M, Stähli BE, Merlet N, Mihalache-Avram T, Mecteau M, Rhéaume E, et al. Validating a bimodal intravascular ultrasound (IVUS) and near-infrared fluorescence (NIRF) catheter for atherosclerotic plaque detection in rabbits. *Biomed Opt Express.* (2015) 6:3989–99. doi: 10.1364/BOE.6.003989
65. Maehara A, Matsumura M, Ali ZA, Mintz GS, Stone GW. IVUS-guided versus OCT-guided coronary stent implantation: a critical appraisal. *JACC Cardiovasc Imaging.* (2017) 10:1487–503. doi: 10.1016/j.jcmg.2017.09.008
66. Yoo H, Kim JW, Shishkov M, Namati E, Morse T, Shubochkin R, et al. Intra-arterial catheter for simultaneous microstructural and molecular imaging *in vivo*. *Nat Med.* (2011) 17:1680–4. doi: 10.1038/nm.2555
67. Bourantas CV, Jaffer FA, Gijsen FJ, van Soest G, Madden SP, Courtney BK, et al. Hybrid intravascular imaging: recent advances, technical considerations, and current applications in the study of plaque pathophysiology. *Eur Heart J.* (2017) 38:400–12. doi: 10.1093/eurheartj/ehw097
68. Lee S, Lee MW, Cho HS, Song JW, Nam HS, Oh DJ, et al. Fully integrated high-speed intravascular optical coherence tomography/near-infrared fluorescence structural/molecular imaging *in vivo* using a clinically available near-infrared fluorescence-emitting indocyanine green to detect inflamed lipid-rich atheromata in coronary-sized vessels. *Circ Cardiovasc Interv.* (2014) 7:560–9. doi: 10.1161/CIRCINTERVENTIONS.114.001498
69. Kim S, Lee MW, Kim TS, Song JW, Nam HS, Cho HS, et al. Intracoronary dual-modal optical coherence tomography-near-infrared fluorescence structural-molecular imaging with a clinical dose of indocyanine green for the assessment of high-risk plaques and stent-associated inflammation in a beating coronary artery. *Eur Heart J.* (2016) 37:2833–44. doi: 10.1093/eurheartj/ehv726
70. Potkin BN, Bartorelli AL, Gessert JM, Neville RF, Almagor Y, Roberts WC, et al. Coronary artery imaging with intravascular high-frequency ultrasound. *Circulation.* (1990) 81:1575–85. doi: 10.1161/01.CIR.81.5.1575
71. Dixon AJ, Hossack JA. Intravascular near-infrared fluorescence catheter with ultrasound guidance and blood attenuation correction. *J Biomed Opt.* (2013) 18:56009. doi: 10.1117/1.JBO.18.5.056009
72. Abran M, Cloutier G, Cardinal M-HR, Chayer B, Tardif J-C, Lesage F. Development of a photoacoustic, ultrasound and fluorescence imaging catheter for the study of atherosclerotic plaque. *IEEE Trans Biomed Circuits Syst.* (2014) 8:696–703. doi: 10.1109/TBCAS.2014.2360560
73. Bozhko D, Osborn EA, Rosenthal A, Verjans JW, Hara T, Kellnberger S, et al. Quantitative intravascular biological fluorescence-ultrasound imaging of coronary and peripheral arteries *in vivo*. *Eur Heart J Cardiovasc Imaging.* (2017) 18:1253–61. doi: 10.1093/ehjci/jew222
74. Li Y, Jing J, Qu Y, Miao Y, Zhang B, Ma T, et al. Fully integrated optical coherence tomography, ultrasound, and indocyanine green-based fluorescence tri-modality system for intravascular imaging. *Biomed Opt Express.* (2017) 8:1036–44. doi: 10.1364/BOE.8.001036
75. Ughi GJ, Wang H, Gerbaud E, Gardecki JA, Fard AM, Hamidi E, et al. Clinical characterization of coronary atherosclerosis with dual-modality OCT and near-infrared autofluorescence imaging. *JACC Cardiovasc Imaging.* (2016) 9:1304–14. doi: 10.1016/j.jcmg.2015.11.020
76. Htun NM, Chen YC, Lim B, Schiller T, Maghzal GJ, Huang AL, et al. Near-infrared autofluorescence induced by intraplaque hemorrhage and heme degradation as marker for high-risk atherosclerotic plaques. *Nat Commun.* (2017) 8:75. doi: 10.1038/s41467-017-00138-x
77. Burton NC, Patel M, Morscher S, Driessen WHP, Claussen J, Beziere N, et al. Multispectral opto-acoustic tomography (MSOT) of the brain and glioblastoma characterization. *Neuroimage.* (2013) 65:522–8. doi: 10.1016/j.neuroimage.2012.09.053
78. Wang B, Karpiouk A, Yeager D, Amirian J, Litovsky S, Smalling R, et al. *In vivo* intravascular ultrasound-guided photoacoustic imaging of lipid in plaques using an animal model of atherosclerosis. *Ultrasound Med Biol.* (2012) 38:2098–103. doi: 10.1016/j.ultrasmedbio.2012.08.006
79. Iskander S. *In vivo* intravascular photoacoustic imaging of plaque lipid in coronary atherosclerosis. *Eurointervention.* (2019) 15:452–6. doi: 10.4244/EIJ-D-19-00318
80. Vinegoni C, Botnaru I, Aikawa E, Calfon MA, Iwamoto Y, Folco EJ, et al. Indocyanine green enables near-infrared fluorescence imaging of lipid-rich, inflamed atherosclerotic plaques. *Sci Transl Med.* (2011) 3:84ra45. doi: 10.1126/scitranslmed.3001577
81. Verjans JW, Osborn EA, Ughi GJ, Calfon Press MA, Hamidi E, Antoniadis AP, et al. Targeted near-infrared fluorescence imaging of atherosclerosis: clinical and intracoronary evaluation of indocyanine green. *JACC Cardiovasc Imaging.* (2016) 9:1087–95. doi: 10.1016/j.jcmg.2016.01.034
82. Osborn EA, Ughi GJ, Verjans JW, Gerbaud E, Takx RA, Tawakol A, et al. Abstract 656: *in vivo* plaque inflammation and endothelial permeability independently predict atherosclerosis progression: a serial multimodality imaging study arteriosclerosis, thrombosis, and vascular biology. *Arterioscler Thromb Vasc Biol.* (2016) 36:A656.

Conflict of Interest: FAJ has received sponsored research grants from Canon and Siemens; he is a consultant for Boston Scientific, Abbott Vascular, Siemens, Acrostak, and Biotronik. Massachusetts General Hospital has a patent licensing arrangement with Canon, and FAJ has the right to receive royalties.

The remaining author declares that the research was conducted in the absence of any commercial or financial relationships that could be construed as a potential conflict of interest.

frontiers in Cardiovascular Medicine

REVIEW
published: 26 March 2021
doi: 10.3389/fcvm.2021.613400

Micro Optical Coherence Tomography for Coronary Imaging

Kensuke Nishimiya[1,2] *and Guillermo Tearney*[1,3,4]*

[1] Wellman Center for Photomedicine, Massachusetts General Hospital, Boston, MA, United States, [2] Department of Cardiovascular Medicine, Tohoku University Graduate School of Medicine, Sendai, Japan, [3] Department of Pathology, Massachusetts General Hospital, Boston, MA, United States, [4] Harvard-Massachusetts Institute of Technology (MIT) Division of Health Sciences and Technology Division, Cambridge, MA, United States

Intravascular optical coherence tomography (IVOCT) that produces images with 10 μm resolution has emerged as a significant technology for evaluating coronary architectural morphology. Yet, many features that are relevant to coronary plaque pathogenesis can only be seen at the cellular level. This issue has motivated the development of a next-generation form of OCT imaging that offers higher resolution. One such technology that we review here is termed micro-OCT (μOCT) that enables the assessment of the cellular and subcellular morphology of human coronary atherosclerotic plaques. This chapter reviews recent advances and ongoing works regarding μOCT in the field of cardiology. This new technology has the potential to provide researchers and clinicians with a tool to better understand the natural history of coronary atherosclerosis, increase plaque progression prediction capabilities, and better assess the vessel healing process after revascularization therapy.

Keywords: optical coherence tomography, micro-OCT, endothelial cells, inflammatory cells, macrophage—cell, cholesterol crystals, necrotic core, plaque erosion

OPEN ACCESS

Edited by:
Patrick W. Serruys, Imperial College London, United Kingdom

Reviewed by:
Antonios Karanasos, Hippokration General Hospital, Greece
Özge Özden Tok, Memorial Hospital, United States

***Correspondence:**
Guillermo Tearney
gtearney@partners.org

Specialty section:
This article was submitted to Cardiovascular Imaging, a section of the journal Frontiers in Cardiovascular Medicine

Received: *02 October 2020*
Accepted: *23 February 2021*
Published: *26 March 2021*

Citation:
Nishimiya K and Tearney G (2021) Micro Optical Coherence Tomography for Coronary Imaging. Front. Cardiovasc. Med. 8:613400. doi: 10.3389/fcvm.2021.613400

μOCT: BEYOND STANDARD OCT

In the early 1990's, intravascular optical coherence tomography (IVOCT) (1) commenced with the understanding that OCT (2) could be clinically applied beyond ophthalmology. Conventional IVOCT employs broadband near-infrared light centered at a wavelength of 1,300 nm (3), providing it with a spatial resolution of about 10 μm that is an order of magnitude higher than that of intravascular ultrasound (IVUS) (4). The roughly 10-μm-resolution of IVOCT provides detailed information on treated and untreated coronary plaque morphology by resolving varying arterial microscopic architectural structures (5–10). Similarly to the circumferential view of IVUS, depth information provided by IVOCT makes it possible to display coronary artery lumen cross-sections (9, 10), luminal narrowing (11), and intimal thickening (12). Its higher resolution enables other features to be clearly identified, including fibrous cap thickness (4–6, 13), lipid (4, 13), cholesterol crystals (4), thrombus (4), dissections (4), macrophage accumulations (4, 7), calcium (4–6), and intimal neo-vasculature (4). Hence, IVOCT has improved diagnostic accuracy for human coronary plaques (5, 7), and its feasibility for guiding coronary intervention has been consistently demonstrated (14–19). Over the past two decades, interventional cardiologists and engineers have worked together to make tremendous progress to develop and validate IVOCT as a useful instrument for visualizing the detailed morphology of coronary plaque and stents.

Despite the potential importance of physiological assessment of myocardial ischemia due to significant organic coronary stenosis (20), recent studies have highlighted that the initial interventional strategy with percutaneous coronary intervention or coronary artery bypass does not necessarily result in better clinical outcomes in stable (chronic) coronary artery disease (CAD) patients when compared to optimal medical therapy (21). These results have raised questions regarding what coronary morphological features bestow high risk of a future clinical event, regardless of the severity of the luminal narrowing. To address these questions, OCT with even higher resolution could illuminate the roles of coronary microstructures heretofore unseen, such as individual coronary endothelial cells (22, 23), inflammatory cells, cholesterol crystals (24), vascular smooth muscle cells (25), fibroblasts, (micro-)calcifications (26), and components of thrombi such as platelets and fibrin, all thought to play roles in natural history of coronary atherosclerosis and the clinical manifestations of high risk lesions (27).

In 2011, a new mode of OCT termed micro-OCT (μOCT) was demonstrated with a resolution of 1–2 μm (28). The initial μOCT technology was implemented using a bench-top microscope system and has shown broad utility for a variety of *in vitro* and *ex vivo* studies and applications (28–32). Recently, to implement μOCT clinically, a single fiber optic μOCT probe and intracoronary catheter have been created (33, 34)—the technology is now poised to be used in coronaries *in vivo* (35). In this article, we review the developments in μOCT technology and describe its potential clinical implications for intracoronary imaging.

μOCT FOR CORONARY ENDOTHELIAL CELL VISUALIZATION

Endothelial cells act as gatekeepers for the passage of low-density lipoprotein (LDL) and leukocytes into the intima, and thus endothelial disruption/dysfunction is considered to be an important catalyst of coronary atherogenesis (36, 37). Previous ultrastructural studies have demonstrated that endothelial cells cover the intima in a "cobblestone" pattern, also known as "endothelial pavementing" on *en-face* SEM (22). It has been recognized that coronary plaque erosion characterized by lesions with loss of endothelial cells beneath thrombus is the second most prevalent histopathological cause of acute coronary syndrome (ACS) (27, 38, 39).

μOCT has been shown to visualize swine and human coronary endothelial cells *ex vivo* (40). The capability of μOCT to visualize endothelial cells was validated with the current gold standard scanning electron microscopy (SEM) (22). The histological validation study included a visual comparison of swine coronary endothelial pavementing seen by μOCT, volume-rendered in three-dimension (3D-μOCT), with that seen by *en-face* SEM (**Figure 1**) (40). 3D-μOCT images clearly showed the uneven endothelial surface corresponding to coronary endothelial pavementing seen on corresponding SEM. After endothelial stripping (41), the surface roughness disappeared from the 3D-μOCT image, indicating the absence of endothelial cells. Quantitative analysis was performed by calculating surface roughness on a μOCT data-set and the corresponding SEM (40), demonstrating a high degree of correlation between μOCT and the SEM gold standard ($R^2 = 0.99$, $P < 0.01$).

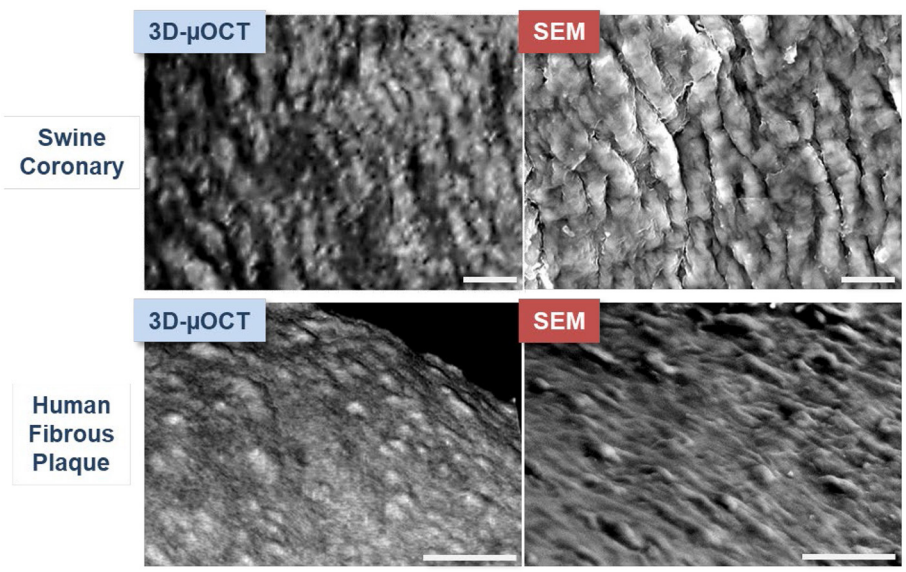

FIGURE 1 | μOCT images of endothelial pavementing and corresponding SEM in swine and human coronary arteries *ex vivo*. Upper panels: Swine coronary endothelial pavementing visualized by three-dimensionally (3D) volume-rendered μOCT is similar to that seen by scanning electron microscopy (SEM). Lower panels: Findings were consistent in human coronary fibrous plaque. Scale bars, 25 μm. Figure and capture reprinted with permission from Nishimiya et al. (40).

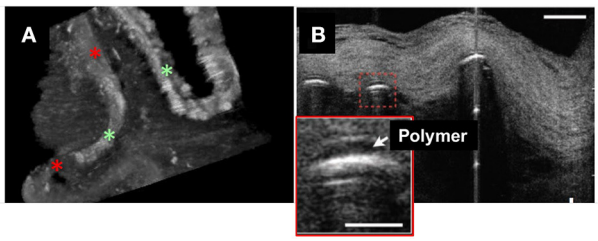

FIGURE 2 | 3D-μOCT of stent and endothelial coverage morphology in the human cadaver coronary artery *ex vivo*. **(A)** 3D-μOCT image of a drug-eluting stent (DES) implanted in a human coronary artery, showing tissue coverage with low intensity signal (red asterisks) and the surface of polymer coating as highly reflective regions (green asterisks). Scale bars, 100 μm. Unpublished data, obtained at the Massachusetts General Hospital. **(B)** DES struts showing polymers (red dashed box and inset) overlying the stent strut reflections. Scale bars, 30 μm. Figure and capture reprinted with permission from Liu et al. (28).

μOCT has also been used to visualize endothelial cells in human cadaver coronaries *ex vivo*. Endothelial pavementing was confirmed in early coronary lesions with intimal thickening and fibrous plaque (4) while lesions with superficial nodular calcification and necrotic core (4) lacked endothelial cells. Indeed, the results of surface roughness measurements indicated that endothelial cell distributions diminished over fibroatheromatous and fibrocalcific coronary plaques as compared with intimal-thickening and fibrous lesions (40). 3D-μOCT images of drug-eluting stents (DES) implanted in coronary segments also showed variable presence or absence of the endothelial cell coverage, which standard OCT was unable to identify (**Figure 2A**).

Studies have suggested that fluid shear stress induces spindle-shaped endothelial morphology that is aligned in the direction of flow while those exposed to low endothelial shear stress (ESS) are nonuniformly oriented (42). Furthermore, low and turbulent induce increased vascular permeability (36, 42) that may increase the probability of LDL and leukocyte influx. Because, it can be performed on fresh tissue and over large areas in three-dimensions, μOCT assessment of endothelial morphology's could increase our understanding of coronary regions altered by shear stress, such as bifurcations and segments at myocardial bridges (43).

Since ruptured coronary plaques account for the majority of ACS (44), an improved understanding of the role of endothelial cells in the progression of atherosclerosis and early identification of plaques at high risk are anticipated to have considerable clinical impact. A number of seminal studies have suggested that certain OCT features of thin cap fibroatheromas (TCFA), such as the thickness of fibrous caps, are critical (13, 45). However, OCT cut off values for high risk cap thicknesses are still undetermined (23). Evidence suggests that in TCFA lesions, apoptotic macrophages are not efficiently cleared by efferocytosis and are therefore prone to secondary necrosis, contributing to expansion of the necrotic core and further thinning of the fibrous cap (46). It is thus conceivable that endothelial cell wall border alignment can vary at the weakest point of these caps of TCFA. In this manner, 3D-μOCT visualization and calculation of endothelial surface roughness may augment precision definition of plaque vulnerability in humans.

Since the endothelial monolayer is below the resolution of OCT, the current OCT diagnostic criteria for a coronary erosion is defined as the presence of an intact fibrous cap at the culprit site with overlying thrombus (47). This criterion is a retrospective definition, as thrombus is required to demarcate this entity. In addition, clinically insignificant plaque erosion may occur without increased thrombogenicity resulting in healed plaque (48). Thus, there is a need for a prospective definition of a site that is at high risk of erosion and subsequent thrombus formation. Owing to its capacity to directly visualize the endothelium, μOCT may bridge these gaps in our diagnostic capabilities. Data has shown that μOCT is capable of imaging white thrombus containing fibrin (the type that is common in erosion), small platelets and multiple entrapped cells (28). Whether μOCT can clearly visualize the endothelium beneath thrombus remains an open question.

Compared to conventional OCT, which is incapable of distinctly visualizing endothelial cells, μOCT could make it possible to definitively assess endothelial coverage of stent struts and this information could be potentially used to shorten antiplatelet therapy treatment durations. In the emerging era of biodegradable-polymer DES (49) and bioresorbable scaffolds (50), μOCT should be capable of evaluating standalone stent polymers or polymer-coating overlying metal stents (**Figure 2B**). The use of μOCT technology to assess DES strut endothelial coverage may help resolve current questions and controversies regarding novel stent healing responses, potentially leading to a means for determining optimal antiplatelet therapy durations.

μOCT FOR THE VISUALIZATION OF INFLAMMATORY CELLS

Inflammatory cells, such as leukocytes, monocytes, and macrophages play key roles in developing coronary atherosclerotic lesions (51). Because of its exquisite resolution, μOCT is capable of typing leukocytes based on cellular and intracellular morphology (28, 52). Additionally, μOCT has been shown to be quite capable of imaging pseudopods that inform on the activity of these cells (**Figure 3A**) (28). For example, compared to smaller cells with scant cytoplasm, consistent with lymphocytes, some of large cells seen on the surface had bean-shaped nucleus inside, presumably corresponding to monocytes (**Figure 3B**) (28). Macrophages are also seen clearly by μOCT as highly scattering, flocculent, round or ellipsoidal cells (28, 52), and are frequently observed over and within necrotic core lesions (**Figure 3C**) (28, 52). Some of these features have been recently demonstrated in the nasal airways *in vivo*, as μOCT was shown to be able to clearly visualize granulocytes in the mucus and epithelium of patients with cystic fibrosis (32).

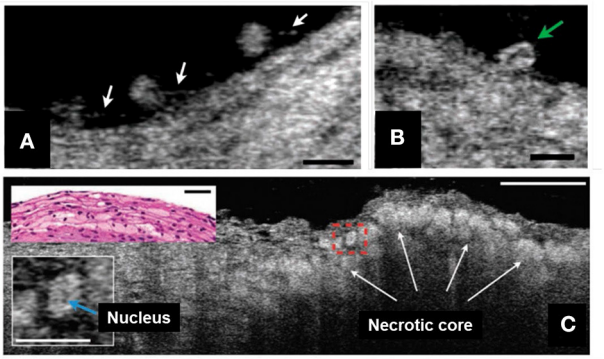

FIGURE 3 | μOCT for inflammatory cell morphology in human cadaver coronaries *ex vivo*. **(A)** Multiple leukocytes tethered to the endothelial surface by linear structures, suggestive of pseudopodia (white arrows). **(B)** A cell with an indented, bean-shaped nucleus (green arrow) suggestive of a monocyte. **(C)** Necrotic core fibroatheroma with highly scattering lipid-laden macrophages or foam cells (white arrows) infiltrating the fibrous-cap that were similarly seen in the corresponding histology (top left inset). An intracellular region of low signal, a suggestive of the nucleus, was shown within the cytoplasm of a foam cell (bottom left inset, denoted by blue arrow). Scale bars, 30 μm. Figure and capture reprinted with permission from Liu et al. (28).

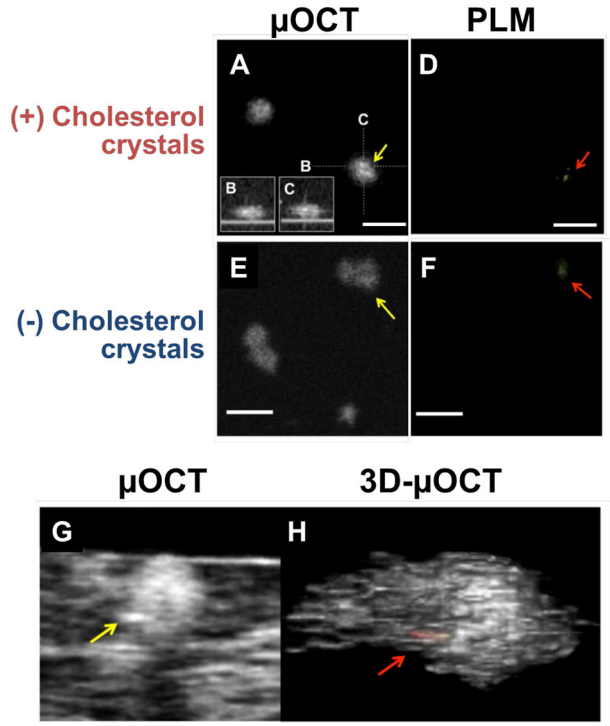

FIGURE 4 | μOCT for macrophages containing cholesterol crystals *in vitro* and *ex vivo*. **(A)** *En-face* and **(B,C)** cross-sections of the macrophage demonstrated highly scattering constituents inside its cytoplasm (yellow arrow). **(D)** Corresponding polarization microscopy (PLM) confirming the cholesterol crystal inclusions (red arrow). **(E)** Cholesterol crystals that was determined by PLM **(F)** was not definitive on the μOCT image (yellow arrow). **(G,H)** Representative μOCT images of the macrophage cell in human coronary artery *ex vivo* contained highly scattering cholesterol inclusions within their cytoplasm [yellow arrow in panel **(G)**; red in panel **(H)**]. Scale bars, 50 μm. Figure and capture reprinted with permission from Kashiwagi et al. (52).

Inflammatory cells play a pivotal role in all phases of coronary atherosclerosis. The compromised endothelial barrier permits them to invade into the tunica intima and initiate arterial wall thickening. Macrophages contribute to plaque vulnerability by producing proteolytic enzymes that digest extracellular matrix and destroy the integrity of the fibrous cap (46) and through their accumulation and death that form biomechanically unstable lipid deposits. For these and many other reasons, it is important to explore macrophage behavior in atherosclerotic lesions *in vivo*. Owing to its 3D imaging capabilities, μOCT makes it possible to observe such morphologic phenomena that are rarely seen in 2D cross sections. Due to the cellular resolution capabilities of μOCT, this technology could potentially also identify plaques with neutrophil extracellular trap (NETs) accumulations that induce endothelial cell apoptosis and resultant plaque erosion (53).

μOCT FOR THE VISUALIZATION OF INTIMAL CRYSTALS

In *in vitro* cell culture experiments, macrophages containing cholesterol crystals demonstrated higher cytoplasmic scattering in μOCT images when compared to those without cholesterol crystals (**Figure 4**) (52). Of note, there was a discrepancy that cholesterol crystals were detected by the gold-standard polarization microscopy but were not seen on the μOCT image (**Figures 4A,B**). Using polarization microscopy, the accuracy of cholesterol crystal inclusions in macrophages relied on the size of cholesterol crystals (the size $\geq$100 mm^2, 52% vs. <100 mm^2, 36%, $P < 0.05$). 3D-μOCT clearly visualized a macrophage cell with the high scattering cholesterol crystal within its cytoplasm (**Figure 4C**).

Cholesterol crystal protrusion toward the lumen has recently been proposed as a possible cause of thrombosis and resultant ACS (54). 3D-μOCT has shown clear delineation of multilayered cholesterol crystal sheets in human cadaver coronary arteries (**Figure 5A**) (28) and their protrusions that were similar to what seen by SEM (**Figure 5B**).

Several recent studies have highlighted that anti-inflammatory pharmacotherapeutic strategies (e.g., an interleukin-1β neutralizing human monoclonal antibody, colchicine) (55, 56) may have a high potential to eliminate residual risk of CAD. Intimal crystals have been identified as a possible therapeutic target for cardiovascular disease, due to the potential of these crystals to exacerbate inflammation through inflammasome-mediated cytokine production/activation (57, 58). Identification of localized vascular inflammation as intimal crystals surrounded by inflammatory changes using μOCT would be helpful for assessing the effects of these novel therapeutic agents in patients *in vivo*.

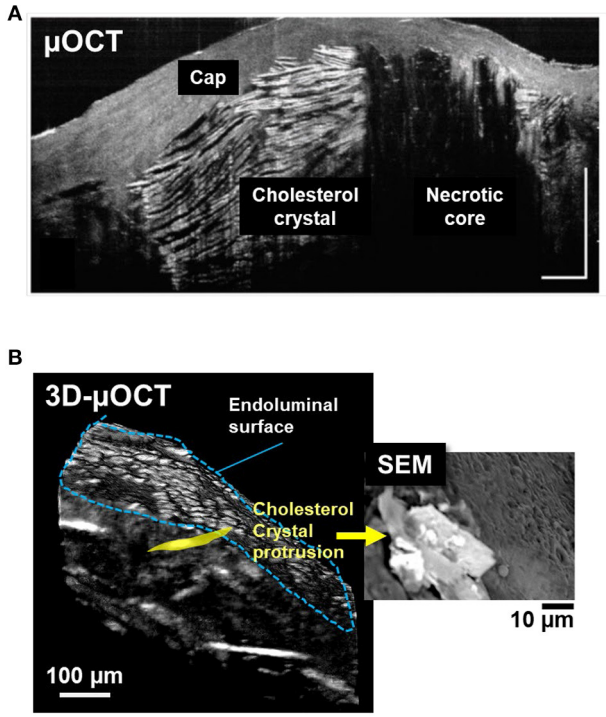

FIGURE 5 | 3D-μOCT for visualizing cholesterol crystals and their protrusion in the human cadaver coronary artery *ex vivo*. **(A)** Fibroatheroma with large necrotic core (NC) showing multilayered cholesterol crystals (CC), characterized by reflections from their top and bottom surfaces. Scale bars, 30 μm. Figure and capture reprinted with permission from Liu et al. (28). **(B)** 3D-μOCT for a fibroatheromatous human coronary plaque with manually segmenting a protruding cholesterol crystal (yellow area). **(B)** Corresponding SEM image showing cholesterol crystals protruding from the arterial wall. Unpublished data, obtained at the Massachusetts General Hospital.

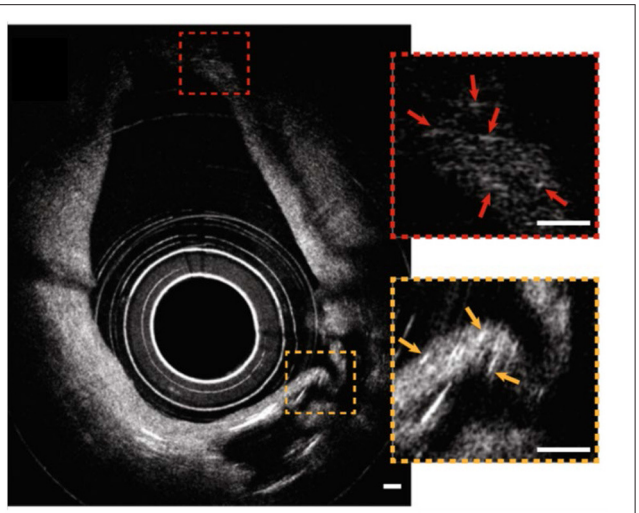

FIGURE 6 | Catheter-based intravascular μOCT for cholesterol crystals in the human cadaver coronary *ex vivo*. Circumferential image showing that μOCT was capable of resolving small cholesterol crystals at distances close to the sheath (a couple hundred microns, orange inset) and far from the sheath (~1 mm, red inset) simultaneously. Scale bars, 100 μm. Figure and capture reprinted with permission from Yin et al. (35).

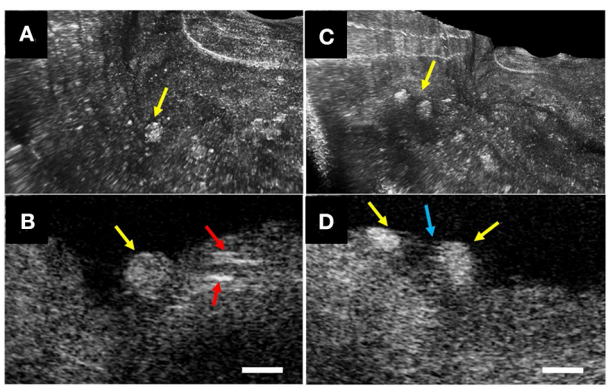

FIGURE 7 | Intravascular μOCT for inflammatory cells in human cadaver coronaries *ex vivo*. **(A)** Individual macrophages (yellow arrows) residing on the surface of a fibroatheromatous plaque that **(B)** appeared to be transmigrating through the endothelium toward a deposit of intimal cholesterol crystals (red arrows). **(C)** 3D-μOCT image showing a pair of macrophages tethered to the surface, **(D)** polarized toward one another with extended pseudopodia (blue arrow). Scale bars, 50 μm. Figure and capture reprinted with permission from Yin et al. (35).

CATHETER-BASED INTRAVASCULAR-μOCT

Recently, the optical imaging elements required to conduct intravascular μOCT were demonstrated (33, 34) and integrated into a catheter that had a size that was suitable for human coronary imaging (35). The imaging capability of the intravascular μOCT catheter was shown in human cadaver coronary arteries *ex vivo* and atherosclerotic rabbit aortae *in vivo* (35). μOCT circumferential views displayed cellular and subcellular coronary structures that were not readily identified by the standard OCT. For instance, small or large cholesterol crystal sheets were consistently noted in human lipid-rich plaques *ex vivo* (**Figure 6**) that were sometimes difficult to interpret in corresponding convention IVOCT images. As with the *ex vivo* bench top studies, smooth muscle cells could be clearly visualized as low-intensity, slit-like structures within the intima. Likewise, cross-sectional μOCT showed macrophage diapedesis in human coronaries *ex vivo*. 3D-rendering of μOCT images exhibited that individual macrophages residing on the surface of fibroatheromatous plaques that appeared to be transmigrating through the endothelium toward a deposit of intimal cholesterol crystals (**Figures 7A,B**) or with their pseudopods opposing each other (**Figures 7C,D**). Thrombus could be noted with cells that were consistent with leucocytes embedded in the intraluminal mass. The findings of this study (35) indicate that we are on the threshold of conducting intracoronary μOCT *in vivo* and await the development of clinical versions of these devices for the first-in-human studies.

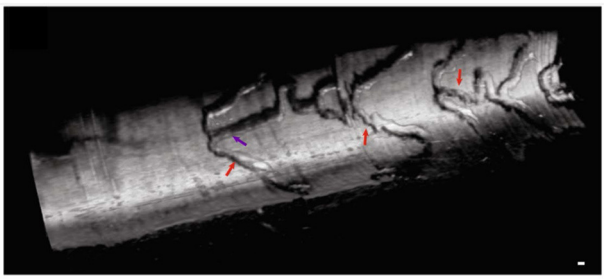

FIGURE 8 | Intravascular 3D-μOCT of a drug-eluting stent implanted in the atherosclerotic rabbit iliac artery *in vivo*. The artery was imaged immediately after the stent implantation. Stent struts are denoted by the purple and red arrows. Scale bar, 100 μm. Figure and capture reprinted with permission from Yin et al. (35).

LIMITATIONS OF μOCT AND TECHNOLOGICAL BARRIERS FOR CLINICAL APPLICATIONS

To achieve clinical intracoronary μOCT in the cardiac catheterization lab, several limitations and barriers still need to be resolved. First, to attain such high resolution images, μOCT is currently conducted at a shorter light wavelength (centered at 800 nm) that is lower than that of standard OCT (1,300 nm). The use of this shorter wavelength decreases the penetration depth of light in tissue, potentially further compromising its ability to assess intimal thickness and thus plaque remodeling. Second, imaging with μOCT collects ∼3 orders of magnitude more data than imaging with standard OCT, and so the image sizes of a μOCT pullback will be 1,000 times greater than those of a standard OCT pullback. This 1,000-fold increase in data puts a great strain on data acquisition sensitivity and electronics, so currently the frame rate of acquiring μOCT images is significantly slower than that of standard OCT. With today's technology, imaging the entire length of a coronary artery with isotropic 1–2 μm resolution would require many pullbacks, each needing a radiocontrast flush for blood clearance. Interpreting the immense amount of information provided by μOCT may be difficult for interventional cardiologist; it is likely that artificial intelligence will be needed to aid image analysis. 3D visualization of μOCT will also likely facilitate image understanding in real time. The development of machine learning algorithms and rapid 3D rendering are ongoing topics of investigation in the μOCT field. Future technological developments will be focused on addressing these limitations to enable practical application of μOCT in the cath lab.

POTENTIAL SCIENTIFIC AND CLINICAL IMPLICATIONS OF μOCT

Clinical applications of μOCT for coronary imaging has the potential to be extensive. In the very beginning of coronary plaque development, altered shear-stress affects the endothelial cell alignment and effectuates endothelial dysfunction (42). Although such a relationship between shear-stress and endothelial cell orientation has been known for a long while, the finding has not been demonstrated in living patients *in vivo*. Furthermore, visualization of ongoing inflammatory cell adhesion, plaque disruption and blood coagulation remain elusive in humans *in vivo*. For interventional cardiology, μOCT will provide precise information for acute thrombotic formation around stent struts (23) at a microscopic level. A longitudinal view of stent architecture by 3D-μOCT has been demonstrated in rabbit aorta *in vivo* (**Figure 8**) (35). The detailed information regarding stent malapposition (59) or stent fracture (60) could help in the early detection of a precursor of procedure-related stent thrombosis. Visualization of DES polymer cracking (61) and the tissue response to anti-proliferative agents delivered by drug-coated balloons (62) could help clinicians to predict the arterial healing process.

CONCLUSION

μOCT is a next-generation form of OCT that provides an order of magnitude increase in axial and lateral resolution. Our group has demonstrated that μOCT enables the visualization of structures relevant to coronary atherosclerosis pathogenesis and stent healing at cellular/subcellular levels. The recently developed μOCT coronary catheter brings this technology close to clinial use. Clinical studies will be conducted with intracoronary μOCT in the near future. Results will potentially change the landscape of coronary imaging and our understanding of coronary disease and its treatment.

AUTHOR CONTRIBUTIONS

All authors listed have made a substantial, direct and intellectual contribution to the work, and approved it for publication.

FUNDING

This work was supported by the US National Institutes of Health (contracts R01HL076398, R01HL122388, and R01HL137913), John and Dottie Remondi Family Foundation, the Mike and Sue Hazard Family Foundation, and the MGH Research Scholars program, the Cystic Fibrosis Foundation (contract TEARNE07XX0).

ACKNOWLEDGMENTS

We wish to acknowledge all laboratory members and collaborators worked for the μOCT project at the Wellman Center for Photomedicine, the Massachusetts General Hospital, Harvard Medical School. KN would like to thank for the supports by a Research Fellowship Programs from the MSD Life Science Foundation, and the Uehara Memorial Foundation (Japan). We also gratefully acknowledge the Hazard Family Foundation and John and Dottie Remondi Foundation for their generous support of μOCT work.

REFERENCES

1. Tearney GJ, Brezinski ME, Bouma BE, Boppart SA, Pitris C, Southern JF, et al. *In vivo* endoscopic optical biopsy with optical coherence tomography. *Science.* (1997) 276:2037–9. doi: 10.1126/science.276.5321.2037
2. Huang D, Swanson EA, Lin CP, Schuman JS, Stinson WG, Chang W, et al. Optical coherence tomography. *Science.* (1991) 254:1178–81. doi: 10.1126/science.1957169
3. Yun SH, Tearney GJ, Vakoc BJ, Shishkov M, Oh WY, Desjardins AE, et al. Comprehensive volumetric optical microscopy *in vivo*. *Nat Med.* (2006) 12:1429–33. doi: 10.1038/nm1450
4. Tearney GJ, Regar E, Akasaka T, Adriaenssens T, Barlis P, Bezerra HG, et al. Consensus standards for acquisition, measurement, and reporting of intravascular optical coherence tomography studies: a report from the International Working Group for Intravascular Optical Coherence Tomography Standardization and Validation. *J Am Coll Cardiol.* (2012) 59:1058–72. doi: 10.1016/j.jacc.2011.09.079
5. Yabushita H, Bouma BE, Houser SL, Aretz HT, Jang IK, Schlendorf KH, et al. Characterization of human atherosclerosis by optical coherence tomography. *Circulation.* (2002) 106:1640–5. doi: 10.1161/01.CIR.0000029927.92825.F6
6. Jang IK, Bouma BE, Kang DH, Park SJ, Park SW, Seung KB, et al. Visualization of coronary atherosclerotic plaques in patients using optical coherence tomography comparison with intravascular ultrasound. *J Am Coll Cardiol.* (2002) 39:604–9. doi: 10.1016/S0735-1097(01)01799-5
7. Tearney GJ, Yabushita H, Houser SL, Aretz HT, Jang IK, Schlendorf KH, et al. Quantification of macrophage content in atherosclerotic plaques by optical coherence tomography. *Circulation.* (2003) 107:113–9. doi: 10.1161/01.CIR.0000044384.41037.43
8. Bouma BE, Tearney GJ, Yabushita H, Shishkov M, Kauffman CR, DeJoseph Gauthier D, et al. Evaluation of intracoronary stenting by intravascular optical coherence tomography. *Heart.* (2003) 89:317–20. doi: 10.1136/heart.89.3.317
9. Jang IK, Tearney GJ, MacNeill B, Takano M, Moselewski F, Iftima N, et al. *In vivo* characterization of coronary atherosclerotic plaque by use of optical coherence tomography. *Circulation.* (2005) 111:1551–5. doi: 10.1161/01.CIR.0000159354.43778.69
10. Kawasaki M, Bouma BE, Bressner J, Houser SL, Nadkarni SK, MacNeill BD, et al. Diagnostic accuracy of optical coherence tomography and integrated backscatter intravascular ultrasound images for tissue characterization of human coronary plaques. *J Am Coll Cardiol.* (2006) 48:81–8. doi: 10.1016/j.jacc.2006.02.062
11. Gerbaud E, Weisz G, Tanaka A, Kashiwagi M, Shimizu T, Wang L, et al. Multi-laboratory inter-institute reproducibility study of IVOCT and IVUS assessments using published consensus document definitions. *Eur Heart J Cardiovasc Imaging.* (2016) 17:756–64. doi: 10.1093/ehjci/jev229
12. Kume T, Akasaka T, Kawamoto T, Watanabe N, Toyota E, Neishi Y, et al. Assessment of coronary intima-media thickness by optical coherence tomography: comparison with intravascular ultrasound. *Circ J.* (2005) 69:903–7. doi: 10.1253/circj.69.903
13. Kume T, Akasaka T, Kawamoto T, Okura H, Watanabe N, Toyota E, et al. Measurement of the thickness of the fibrous cap by optical coherence tomography. *Am Heart J.* (2006) 152:755.e1-4. doi: 10.1016/j.ahj.2006.06.030
14. Ali ZA, Maehara A, Généreux P, Shlofmitz RA, Fabbiocchi F, Nazif TM, et al. Optical coherence tomography compared with intravascular ultrasound and with angiography to guide coronary stent implantation (ILUMIEN III: OPTIMIZEPCI): a randomized controlled trial. *Lancet.* (2016) 388:2618–28. doi: 10.1016/S0140-6736(16)31922-5
15. Meneveau N, Souteyrand G, Motreff P, Caussin C, Amabile N, Ohlmann P, et al. Optical coherence tomography to optimize results of percutaneous coronary intervention in patients with non-ST-elevation acute coronary syndrome: results of the multicenter, randomized DOCTORS study (does optical coherence tomography optimize results of stenting). *Circulation.* (2016) 134:906–17. doi: 10.1161/CIRCULATIONAHA.116.024393
16. Prati F, Guagliumi G, Mintz GS, Costa M, Regar E, Akasaka T, et al. Expert review document part 2: methodology, terminology and clinical applications of optical coherence tomography for the assessment of interventional procedures. *Eur Heart J.* (2012) 33:2513–20. doi: 10.1093/eurheartj/ehs095
17. Maehara A, Matsumura M, Ali ZA, Mintz GS, Stone GW. IVUS-Guided versus OCT-guided coronary stent implantation: a critical appraisal. *J Am Coll Cardiol Img.* (2017) 10:1487–503. doi: 10.1016/j.jcmg.2017.09.008
18. Ali ZA, Karimi Galougahi K, Maehara A, Shlofmitz RA, Ben-Yehuda O, Mintz GS, et al. Intracoronary optical coherence tomography 2018: current status and future directions. *J Am Coll Cardiol Intv.* (2017) 10:2473–87. doi: 10.1016/j.jcin.2017.09.042
19. Kubo T, Shinke T, Okamura T, Hibi K, Nakazawa G, Morino Y, et al. Optical frequency domain imaging vs. intravascular ultrasound in percutaneous coronary intervention (OPINION trial): one-year angiographic and clinical results. *Eur Heart J.* (2017) 38:3139–47. doi: 10.1093/eurheartj/ehx351
20. De Bruyne B, Pijls NH, Kalesan B, Barbato E, Tonino PA, Piroth Z, et al. Fractional flow reserve-guided PCI versus medical therapy in stable coronary disease. *N Engl J Med.* (2012) 367:991–1001. doi: 10.1056/NEJMoa1205361
21. Maron DJ, Hochman JS, Reynolds HR, Bangalore S, O'Brien SM, Boden WE, et al. Initial invasive or conservative strategy for stable coronary disease. *N Engl J Med.* (2020) 382:1395–407. doi: 10.1056/NEJMoa1915922
22. Pasternak RC, Baughman KL, Fallon JT, Block PC. Scanning electron microscopy after coronary transluminal angioplasty of normal canine coronary arteries. *Am J Cardiol.* (1980) 45:591–8. doi: 10.1016/S0002-9149(80)80009-9
23. Otsuka F, Finn AV, Yazdani SK, Nakano M, Kolodgie FD, Virmani R. The importance of the endothelium in atherothrombosis and coronary stenting. *Nat Rev Cardiol.* (2012) 9:439–53. doi: 10.1038/nrcardio.2012.64
24. Janoudi A, Shamoun FE, Kalavakunta JK, Abela GS. Cholesterol crystal induced arterial inflammation and destabilization of atherosclerotic plaque. *Eur Heart J.* (2016) 37:1959–67. doi: 10.1093/eurheartj/ehv653
25. Kolodgie FD, Burke AP, Nakazawa G, Virmani R. Is pathologic intimal thickening the key to understanding early plaque progression in human atherosclerotic disease? *Arterioscler Thromb Vasc Biol.* (2007) 27:986–9. doi: 10.1161/ATVBAHA.0000258865.44774.41
26. De Maria GL, Scarsini R, Banning AP. Management of calcific coronary artery lesions: is it time to change our interventional therapeutic approach? *J Am Coll Cardiol Intv.* (2019) 12:1465–78. doi: 10.1016/j.jcin.2019.03.038
27. Otsuka F, Joner M, Prati F, Virmani R, Narula J. Clinical classification of plaque morphology in coronary disease. *Nat Rev Cardiol.* (2014) 11:379–89. doi: 10.1038/nrcardio.2014.62
28. Liu L, Gardecki JA, Nadkarni SK, Toussaint JD, Yagi Y, Bouma BE, et al. Imaging the subcellular structure of human coronary atherosclerosis using micro-optical coherence tomography. *Nat Med.* (2011) 17:1010–4. doi: 10.1038/nm.2409
29. Iyer JS, Batts SA, Chu KK, Sahin MI, Leung HM, Tearney GJ, et al. Micro-optical coherence tomography of the mammalian cochlea. *Sci Rep.* (2016) 6:33288. doi: 10.1038/srep33288
30. Chu KK, Kusek ME, Liu L, Som A, Yonker LM, Leung H, et al. Illuminating dynamic neutrophil trans-epithelial migration with micro-optical coherence tomography. *Sci Rep.* (2017) 8:45789. doi: 10.1038/srep45789
31. Gardecki JA, Singh K, Wu CL, Tearney GJ. Imaging the human prostate gland using 1-μm-resolution optical coherence tomography. *Arch Pathol Lab Med.* (2019) 143:314–8. doi: 10.5858/arpa.2018-0135-OA
32. Leung HM, Birket SE, Hyun C, Ford TN, Cui D, Solomon GM, et al. Intranasal micro-optical coherence tomography imaging for cystic fibrosis studies. *Sci Transl Med.* (2019) 11:eaav3505. doi: 10.1126/scitranslmed.aav3505
33. Yin B, Chu KK, Liang CP, Singh K, Reddy R, Tearney GJ. μOCT imaging using depth of focus extension by self-imaging wavefront division in a common-path fiber optic probe. *Opt Express.* (2016) 24:5555–64. doi: 10.1364/OE.24.005555
34. Yin B, Hyun C, Gardecki JA, Tearney GJ. Extended depth of focus for coherence-based cellular imaging. *Optica.* (2017) 4:959–65. doi: 10.1364/OPTICA.4.000959
35. Yin B, Piao Z, Nishimiya K, Hyun C, Gardecki JA, Mauskapf A, et al. 3D cellular-resolution imaging in arteries using few-mode interferometry. *Light Sci Appl.* (2019) 8:104. doi: 10.1038/s41377-019-0211-5
36. Aird WC. Phenotypic heterogeneity of the endothelium: I. Structure, function, and mechanisms. *Circ Res.* (2007) 100:158–73. doi: 10.1161/01.RES.0000255691.76142.4a

37. Vanhoutte PM, Shimokawa H, Feletou M, Tang EH. Endothelial dysfunction and vascular disease - a 30th anniversary update. *Acta Physiol.* (2017) 219:22–9. doi: 10.1111/apha.12646
38. Vergallo R, Crea F. Atherosclerotic plaque healing. *N Engl J Med.* (2020) 383:846–39. doi: 10.1056/NEJMra2000317
39. Farb A, Burke AP, Tang AL, Liang TY, Mannan P, Smialek J, et al. Coronary plaque erosion without rupture into a lipid core. A frequent cause of coronary thrombosis in sudden coronary death. *Circulation.* (1996) 93:1354–63. doi: 10.1161/01.CIR.93.7.1354
40. Nishimiya K, Yin B, Piao Z, Ryu J, Osman H, Leung HM, et al. Micro-optical coherence tomography for endothelial cell visualization in the coronary arteries. *J Am Coll Cardiol Img.* (2019) 12:1878–80. doi: 10.1016/j.jcmg.2019.01.021
41. Jelev L, Surchev L. A novel simple technique for en face endothelial observations using water-soluble media -'thinned-wall' preparations. *J Anat.* (2008) 212:192–7. doi: 10.1111/j.1469-7580.2007.00844.x
42. Malek AM, Alper SL, Izumo S. Hemodynamic shear stress and its role in atherosclerosis. *JAMA.* (1999) 282:2035–42. doi: 10.1001/jama.282.21.2035
43. Herrmann J, Higano ST, Lenon RJ, Rihal CS, Lerman A. Myocardial bridging is associated with alteration in coronary vasoreactivity. *Eur Heart J.* (2004) 25:2134 42. doi: 10.1016/j.ehj.2004.08.015
44. Jia H, Abtahian F, Aguirre AD, Lee S, Chia S, Lowe H, et al. *In vivo* diagnosis of plaque erosion and calcified nodule in patients with acute coronary syndrome by intravascular optical coherence tomography. *J Am Coll Cardiol.* (2013) 62:1748–58. doi: 10.1016/j.jacc.2013.05.071
45. Prati F, Regar E, Mintz GS, Arbustini E, Di Mario C, Jang IK, et al. Expert review document on methodology, terminology, and clinical applications of optical coherence tomography: physical principles, methodology of image acquisition, and clinical application for assessment of coronary arteries and atherosclerosis. *Eur Heart J.* (2010) 31:401–15. doi: 10.1093/eurheartj/ehp433
46. Tabas I. Macrophage death and defective inflammation resolution in atherosclerosis. *Nat Rev Immunol.* (2010) 10:36–46. doi: 10.1038/nri2675
47. Partida RA, Libby P, Crea F, Jang IK. Plaque erosion: a new *in vivo* diagnosis and a potential major shift in the management of patients with acute coronary syndromes. *Eur Heart J.* (2018) 39:2070–6. doi: 10.1093/eurheartj/ehx786
48. Yahagi K, Kolodgie FD, Otsuka F, Finn AV, Davis HR, Joner M, et al. Pathophysiology of native coronary, vein graft, and in stent atherosclerosis. *Nat Rev Cardiol.* (2016) 13:79–98. doi: 10.1038/nrcardio.2015.164
49. Nishimiya K, Matsumoto Y, Uzuka H, Ogata T, Hirano M, Shindo T, et al. Beneficial effects of a novel bioabsorbable polymer coating on enhanced coronary vasoconstricting responses after drug-eluting stent implantation in pigs *in vivo*. *J Am Coll Cardiol Intv.* (2016) 9:281–91. doi: 10.1016/j.jcin.2015.09.041
50. Ali ZA, Serruys PW, Kimura T, Gao R, Ellis SG, Kereiakes DJ, et al. 2-year outcomes with the absorb bioresorbable scaffold for treatment of coronary artery disease: a systematic review and meta-analysis of seven randomised trials with an individual patient data substudy. *Lancet.* (2017) 390:760–72. doi: 10.1016/S0140-6736(17)31470-8
51. Chinetti-Gbaguidi G, Colin S, Staels B. Macrophage subsets in atherosclerosis. *Nat Rev Cardiol.* (2015) 12:10–7. doi: 10.1038/nrcardio.2014.173
52. Kashiwagi M, Liu L, Chu KK, Sun CH, Tanaka A, Gardecki JA, et al. Feasibility of the assessment of cholesterol crystals in human macrophages using micro optical coherence tomography. *PLoS One.* (2014) 9:e102669. doi: 10.1371/journal.pone.0102669
53. Quillard T, Araújo HA, Franck G, Shvartz E, Sukhova G, Libby P. TLR2 and neutrophils potentiateendothelial stress, apoptosis and detachment: implications for superficial erosion. *Eur Heart J.* (2015) 36:1394–404. doi: 10.1093/eurheartj/ehv044
54. Katayama Y, Tanaka A, Taruya A, Kashiwagi M, Nishiguchi T, Ozaki Y, et al. Feasibility and clinical significance of *in vivo* cholesterol crystal detection using optical coherence tomography. *Arterioscler Thromb Vasc Biol.* (2020) 40:220–9. doi: 10.1161/ATVBAHA.119.312934
55. Ridker PM, Everett BM, Thuren T, MacFadyen JG, Chang WH, Ballantyne C, et al. Antiinflammatory therapy with canakinumab for atherosclerotic disease. *N Engl J Med.* (2017) 377:1119–31. doi: 10.1056/NEJMoa1707914
56. Tardif JC, Kouz S, Waters DD, Bertrand OF, Diaz R, Maggioni AP, et al. Efficacy and safety of low-dose colchicine after myocardial infarction. *N Engl J Med.* (2019) 381:2497–505. doi: 10.1056/NEJMoa1912388
57. Terkeltaub R. Update on gout: new therapeutic strategies and options. *Nat Rev Rheumatol.* (2010) 6:30–8. doi: 10.1038/nrrheum.2009.236
58. Duewell P, Kono H, Rayner KJ, Sirois CM, Vladimer G, Bauernfeind FG, et al. NLRP3 inflammasomes are required for atherogenesis and activated by cholesterol crystals. *Nature.* (2010) 464:1357–61. doi: 10.1038/nature08938
59. Lee SY, Im E, Hong SJ, Ahn CM, Kim JS, Kim BK, et al. Severe acute stent malapposition after drug-eluting stent implantation: effects on long-term clinical outcomes. *J Am Heart Assoc.* (2019) 8:e012800. doi: 10.1161/JAHA.119.012800
60. Chowdhury PS, Ramos RG. Images in clinical medicine. Coronary-stent fracture. *N Engl J Med.* (2002) 347:581. doi: 10.1056/NEJMicm020259
61. Rizas KD, Mehilli J. Stent polymers: Do they make a difference? *Circ Cardiovasc Interv.* (2016) 9:e002943. doi: 10.1161/CIRCINTERVENTIONS.115.002943
62. Chowdhury MM, Singh K, Albaghdadi MS, Khraishah H, Mauskapf A, Kessinger CW, et al. Paclitaxel drug-coated balloon angioplasty suppresses progression and inflammation of experimental atherosclerosis in rabbits. *J Am Coll Cardiol Basic Trans Science.* (2020) 5:685–95. doi: 10.1016/j.jacbts.2020.04.007

Conflict of Interest: GT receives catheter materials from Terumo Corporation. Massachusetts General Hospital has a licensing arrangement with Terumo Corporation. He has the rights to receive royalties from this licensing arrangement and he receives sponsored research funding pertaining to coronary OCT from Vivolight, Canon Inc., and CN USA Biotech Holdings and AstraZeneca sponsor intracoronary μOCT research in GT's lab. GT has a financial/fiduciary interest in SpectraWave, a company developing an OCT-NIRS intracoronary imaging system and catheter. His financial/fiduciary interest was reviewed and is managed by the Massachusetts General Hospital and Partners HealthCare in accordance with their conflict of interest policies. He also has a consulting arrangement with SpectraWave.

The remaining author declares that the research was conducted in the absence of any commercial or financial relationships that could be construed as a potential conflict of interest.

frontiers in Cardiovascular Medicine

ORIGINAL RESEARCH
published: 14 July 2021
doi: 10.3389/fcvm.2021.628610

The Role of Four-Dimensional Automatic Right Ventricular Quantification Technology to Determine RV Function and Hemodynamics in Patients With Pulmonary Hypertension Compared With Right Heart Catheterization

Weichun Wu[1†], Bingyang Liu[2†], Min Huang[3†], David H. Hsi[4], LiLi Niu[1], Yue Tian[1], Jingru Lin[1], Jiangtao Wang[5], Shuai Yang[1,6], Hongquan Lu[1], Changming Xiong[2], Zhenhui Zhu[1*] and Hao Wang[1*]*

[1] State Key Laboratory of Cardiovascular Disease, Department of Echocardiography, National Center for Cardiovascular Diseases, Fuwai Hospital, Chinese Academy of Medical Sciences and Peking Union Medical College, Beijing, China, [2] State Key Laboratory of Cardiovascular Disease, Department of Cardiology, Pulmonary Vascular Disease Center, National Center for Cardiovascular Diseases, Fuwai Hospital, Chinese Academy of Medical Sciences and Peking Union Medical College, Beijing, China, [3] Department of Ultrasound, Meishan People's Hospital, Meishan, China, [4] Heart and Vascular Institute, Stamford Hospital, Stamford, CT, United States, [5] General Electric Healthcare, Beijing, China, [6] Department of Cardiology, Capital Institute of Pediatrics, Beijing, China

Background: Four-dimensional automatic right ventricular quantification technology (4D auto-RVQ) is a new method that can simultaneously measure right ventricular (RV) structure and strain. The role of 4D auto-RVQ in determining RV function and hemodynamics is not clear. The role of 4D auto-RVQ in determining RV function and hemodynamics is not clear. We assessed the 4D auto-RVQ to measure right heart structure, function, and hemodynamics in patients with pulmonary hypertension (PHTN) correlated with right heart catheterization (RHC).

Methods: We enrolled a prospective cohort of 103 patients with PHTN and 25 healthy controls between September 2017 and December 2018. All patients with PHTN underwent echocardiography and RHC. Patients were included if they underwent two-dimensional (2D) and 4D auto-RVQ echocardiographic sequences on the same day as RHC. We analyzed RV functional indices using 2D and 4D auto-RVQ analyses. We divided patients with PHTN into three groups according to echocardiographic image quality as follows: high (n = 24), average (n = 48), and poor (n = 4). Hemodynamic parameters were measured using RHC, including mean right atrial pressure, mean pulmonary arterial pressure, RV cardiac index (RV-CI), and pulmonary vascular resistance.

Results: There were significant differences in most 2D and 4D auto-RVQ parameters between patients with PHTN and healthy controls. Interobserver variability showed

OPEN ACCESS

Edited by:
Patrick W. Serruys, Imperial College London, United Kingdom

Reviewed by:
Aphrodite Tzifa, Mitera Hospital, Greece
Runqing Huang, Mayo Clinic, United States

***Correspondence:**
Hao Wang
amystamford@163.com
Zhenhui Zhu
dr.zhu@139.com
Changming Xiong
xiongcmfw@163.com

† These authors have contributed equally to this work and share first authorship

Specialty section:
This article was submitted to Cardiovascular Imaging, a section of the journal Frontiers in Cardiovascular Medicine

Received: *12 November 2020*
Accepted: *10 June 2021*
Published: *14 July 2021*

Citation:
Wu W, Liu B, Huang M, Hsi DH, Niu L, Tian Y, Lin J, Wang J, Yang S, Lu H, Xiong C, Zhu Z and Wang H (2021) The Role of Four-Dimensional Automatic Right Ventricular Quantification Technology to Determine RV Function and Hemodynamics in Patients With Pulmonary Hypertension Compared With Right Heart Catheterization. Front. Cardiovasc. Med. 8:628610. doi: 10.3389/fcvm.2021.628610

significant agreement with 4D auto-RVQ for most measurements except for 4D end-diastolic volume. Indices measured by auto 4D-RVQ in the high-quality image group had a good correlation with RHC but not in the average- and poor-quality image group. Mid-RV diameter showed the best predictive power for the right RV-CI [area under the curve (AUC) 0.935; 95% confidence interval (CI), 0.714–0.997; $p < 0.001$]. RV end-systolic volume >121.50 mL had a 71.43% sensitivity and a 100% specificity to predict right RV-CI (AUC, 0.890; 95% CI, 0.654–0.986; $p < 0.001$).

Conclusions: 4D auto-RVQ may be used to estimate RV function and some hemodynamic changes compared with RHC in PHTN patients with high image quality. Furthermore, a large sample of the study is needed to evaluate RV function by 4D auto-RVQ in PHTN patients with average image quality.

Keywords: pulmonary hypertension, 4D-echocardiography, strain, right heart catheterization, right heart function

INTRODUCTION

Echocardiography is the most commonly used imaging technique for the study of right ventricular (RV) morphology, volume, function, and tissue characterization (1, 2). The accuracy of 2DE is inferior to cardiac magnetic resonance imaging (3). Because of the complex RV geometry, 2DE cannot capture RV inflow and outflow in the same image acquisition. Real-time three-dimensional echocardiography (3DE), also named four-dimensional echocardiography (4DE), is a more accurate and quicker method to assess RV volume and function than 2DE, but in some cases, this approach still poses some technical difficulties (4).

The right ventricle has a unique crescent shape and complex muscle moment, which influences the accurate evaluation of RV function. In patients with pulmonary hypertension (PHTN), the right heart chambers are significantly enlarged, and the scanning width of the echocardiography is insufficient to cover the entire right ventricle. The walls of the right ventricle can be difficult to identify. RV strain has been extensively used to evaluate the myocardial function and has predictive potential in patients with PHTN. RV strain is also recommended in European guidelines as part of the echocardiographic assessment of the right heart in adults (5, 6).

Right heart catheterization (RHC) is recommended to confirm the diagnosis of pulmonary arterial hypertension (PAH) and to support treatment decisions (7). RV hemodynamic deterioration, which can be measured by RHC, such as changes in mean pulmonary arterial pressure (PAP), pulmonary vascular resistance (PVR), and decrease in RV cardiac index (CI), is associated with poor clinical outcomes in patients with PHTN (8). PHTN is a progressive and life-threatening disease leading to RV pressure overload, dysfunction, and ultimately death. RHC can reliably measure indices of right heart function, such as cardiac output (CO) and RV-CI.

Recently, 4D automatic RV quantification (4D auto-RVQ) has emerged as a new technology for comprehensive RV assessment. This technique can simultaneously measure RV volume, tricuspid annular plane systolic exertion (TAPSE), RV diameter, 4D ejection fraction (4D-EF), and longitudinal strain of the RV free wall and septum (9). In our study, we attempted to use this technology to estimate right heart function and important hemodynamic indices, as well as to obtain other indirect information on right heart structure and function in patients with PHTN.

MATERIALS AND METHODS

Study Population

Our study was a prospective cross-sectional project by design. Adult inpatients with PHTN and healthy volunteers were enrolled from September 2017 to December 2018. All patients with PHTN underwent echocardiography and RHC. Patients with PHTN were included if they had a diagnosis of idiopathic PAH, chronic thromboembolic PAH, connective tissue disease PAH, or residual PAH after surgery for congenital heart disease by RHC with a mean PAP of >25 mm Hg (7). Patients were included if they underwent 2D and 4D auto-RVQ on the same day. Patients were excluded if they were <18 years of age, if echocardiographic images were inadequate for tracing. The exclusion criteria included congenital heart disease before the operation, serious valvular heart disease, significant coronary heart disease, atrial fibrillation, acute heart failure, renal or hepatic failure, and chronic obstructive pulmonary disease. Healthy adult volunteers served as healthy controls. These volunteers had no cardiac defects or family history of cardiac disease.

Our primary endpoint is the role of 4D auto-RVQ to determine RV function and hemodynamics in PHTN patients compared with RHC data. The secondary endpoint is the accuracy and characteristic of 4D auto-RVQ indices in PHTN patients compared to normal people.

Written informed consent was obtained from all participants or their legal representatives. The present study was approved by the ethics committee of Fuwai Hospital (no. 2018-1063). All procedures were performed in accordance with the 1964 Helsinki Declaration and its later amendments.

2DE Acquisition and Analysis

All patients underwent standard transthoracic echocardiography using a GE Vivid E9 (GE Healthcare, Milwaukee, WI, USA) with a 3.5-MHz phased-array transducer. Consecutive

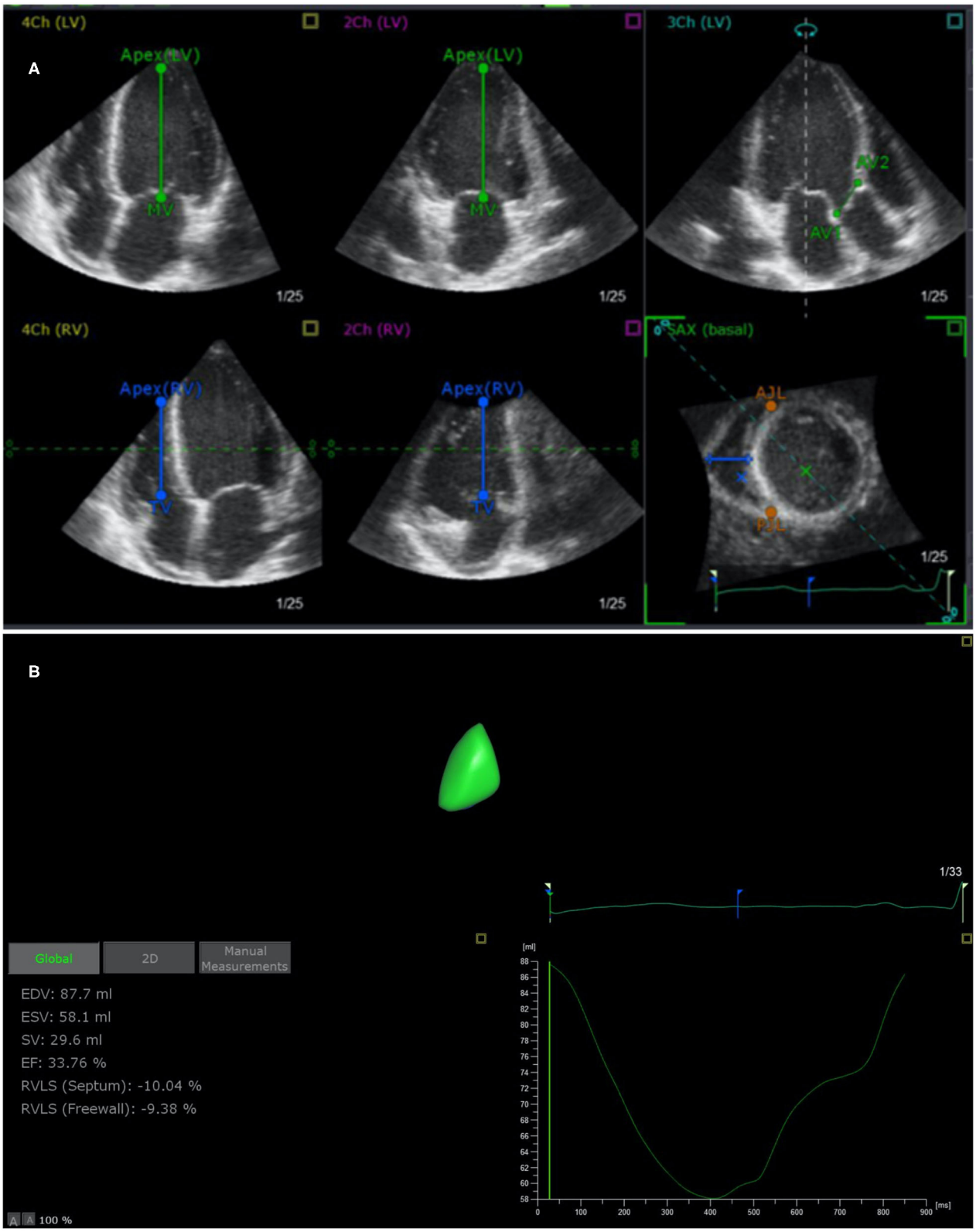

FIGURE 1 | End-systolic verification and editing of endocardial RV borders using TomTec 4D RV Function 2.0 **(A)** and 4D auto-RVQ measurement **(B)**. RV, right ventricular; EDV, end-diastolic volume; ESV, end-systolic volume; EF, ejection fraction; RVLS (septum), right ventricular longitudinal strain of the septum; RVLS (free wall), right ventricular longitudinal strain of the free wall; TAPSE, tricuspid annular plane systolic excursion.

cardiac cycles were recorded during breath-holding with stable electrocardiography tracing. All patients underwent standard 2DE and Doppler echocardiography examinations with detailed evaluation of right heart function. A comprehensive evaluation of the right ventricle by 2DE obtained six standardized views, including the parasternal long-axis, RV inflow, parasternal short-axis, apical four-chamber, and subcostal views.

Offline analysis was then performed on digitally stored images. Indices of 2DE included TAPSE and RV fractional area change. Right heart size was quantified as RV end-diastolic area at the end of the electrocardiogram (ECG) T-wave. RV chamber size was assessed at the apex of the ECG R-wave in the apical four-chamber view with a focus on the right ventricle. We measured pulmonary systolic pressure by Doppler tricuspid regurgitation peak velocity plus estimated right atrial pressure.

4D Auto-RVQ Acquisition and Analysis

Digital data were analyzed offline (EchoPAC 7 Workstation version 201, GE Healthcare; TomTec 4D RV Function 2.0). Measurements using 4D auto-RVQ were acquired using the 4-V matrix-array transducer on the cardiac ultrasound GE system. Images were acquired using single beats with frame rates of ≥12 FPS. Apical RV-focused four-chamber views were acquired with patients in the lateral decubitus position. The transducer position was modified for optimal simultaneous visualization of the tricuspid valve, cardiac apex, and RV outflow tract. We visualized left ventricular apex, mid–mitral valve, aortic annulus, RV apex, mid–tricuspid valve, and RV diameter in the short-axis view (**Figure 1**) and performed an automatic calculation to determine 4D end-diastolic volume (4D-EDV), 4D end-systolic volume (4D-ESV), 4D stroke volume (4D-SV), and 4D-EF. The longitudinal strain of RV septum and free wall and TAPSE, RV diameter (middle/basal/longitudinal RV diameter). All the measurements were performed by trained technicians blinded to clinical data, according to the guidelines of the American Society of Echocardiography (10).

Right Heart Catheterization

Hemodynamic parameters, including mean right atrial pressure, mean PAP, and mixed venous oxygen saturation, were recorded by RHC. CO was measured using the thermodilution method. RV-CI was calculated as CO ÷ body surface area. PVR was calculated as (mean PAP – PAWP) ÷ CO [PAWP (pulmonary artery wedge pressure)]. CI <2.5 L/min/m^2 was defined as reduced right heart function (7). The interval between echocardiography and RHC was <24 h in 76 of 103 participants. For the other 27 patients, RHC was performed >24 h after echocardiography; therefore, their hemodynamic indices were not included in the analysis.

Statistical Analysis

Analyses were performed using SPSS version 20.0 (SPSS, Inc., Chicago, IL, USA) and MedCalc 19.0.5. Continuous data are presented as mean ± standard deviation. Categorical data are presented as absolute numbers or percentages. Differences between groups were analyzed using the χ^2 test. Pearson correlation analysis was performed to evaluate the relationship

TABLE 1 | Clinical, 2DE, and 4D auto-RVQ characteristics of 76 patients with pulmonary arterial hypertension.

Variables	PHTN (*n* = 76)	Healthy control (*n* = 25)	*p*-value
Age (years)	37.13 ± 13.46	36.28 ± 12.56	>0.05
Gender (male)	24 (31.6%)	9 (21.4%)	>0.05
BSA (m^2)	1.57 ± 0.26		
NT-proBNP (pg/mL)	932.85 (322.2, 2,155.5)		
Hemodynamics (*n* = 76)			
RAP (mm Hg)	4.56 ± 4.01		
mPAP (mm Hg)	53.22 ± 14.58		
RV-CI (L/min/m^2)	2.95 (2.38, 3.50)		
PVR (dyn·s·cm^{-5})	940.29 (771.29, 1,236.50)		
SvO_2 (%)	69.39 ± 5.75		
6 MWD (m)	404.82 ± 98.74		
Clinical classification			
IPAH	40 (52.6%)		
CTEPHTN	15 (19.7%)		
CTD-PAH	10 (13.2.0%)		
PAH after operation of CHD	5 (6.6%)		
2DE RV characteristics			
RVD (mm)	30.0 (25.0, 36.0)	22.0 (19.3, 24.0)	<0.001
RAD (mm)	42.0 (36.0, 53.0)	33.0 (29.0, 37.5)	<0.001
RV-FAC	31.88 ± 1.22	48.74 ± 9.83	0.001
TAPSE (mm)	16.0 (15.0, 20.0)	22.0 (19.8, 24.0)	<0.001
TR (m/s)	4.3 (3.6, 4.7)	1.86 (0.75, 2.28)	<0.001
TV E/A	1.2 (0.7, 1.5)	1.29 (1.12, 1.41)	0.081
LVEF (%)	69.14 ± 7.33	68.56 ± 6.38	0.769
4D auto-RVQ characteristics			
RV-ESV (mL)	109.57 ± 47.51	54.70 ± 20.73	<0.001
RV-SV (mL)	34.62 ± 14.00	41.77 ± 13.37	0.047
RV-EF (%)	24.99 ± 7.86	43.69 ± 7.23	<0.001
RVLS (s, %)	−7.36 ± 5.10	−12.36 ± 3.83	0.0001
RVLS (fw, %)	−11.27 ± 5.66	−20.51 ± 6.45	<0.001
RVD (basal, mm)	39.08 ± 6.20	27.77 ± 4.09	<0.001
RVD (mid, mm)	47.70 ± 10.22	35.15 ± 15.58	<0.001
RVD (long, mm)	71.10 ± 12.10	64.57 ± 11.12	0.035
TAPSE (mm)	10.60 ± 3.93	17.75 ± 1.94	<0.001
RV-FAC (%)	19.42 ± 6.23	37.82 ± 9.35	<0.001

Continuous variables are described as mean ± standard deviation if they are normally distributed, whereas those with a skewed distribution are described as median (interquartile range). Categorical data are described as counts (proportions). PAH, pulmonary arterial hypertension; BSA, body surface area; WHOFC, World Health Organization functional class; NT-proBNP, N-terminal pro-brain natriuretic peptide; RAP, right atrial pressure; mPAP, mean pulmonary arterial pressure; RV-CI, right ventricular cardiac index; PVR, pulmonary vascular resistance; SvO_2, mixed venous oxygen saturation; 6MWD, 6-min walking distance; IPAH, idiopathic PAH; CTEPHTN, chronic thromboembolic pulmonary hypertension; CTD-PAH, connective tissue disease-induced PAH; CHD, congenital heart disease; 2DE, two-dimensional echocardiography; RV, right ventricular; RA, right atrial; D, diameter; RVAW, right ventricular anterior wall; TAPSE tricuspid annular plane systolic excursion; TR, tricuspid regurgitation velocity; TV E/A, tricuspid valve blood early and atrium flow; LVEF, left ventricle ejection fraction; RVLS (s, %), right ventricular septum longitudinal strain; RVLS (fw, %), right ventricular free wall longitudinal strain; TAPSE, tricuspid annular plane systolic excursion; ESV, end-systolic volume; FAC, fractional area change; RVD (basal/mid/long), right ventricular diameter (basal, middle, longitudinal).

between 4D auto-RVQ and strain, as well as those parameters measured using the reference method. Interobserver agreement for qualitative analysis score using 4D auto-RVQ manual and software assessments was calculated using the intraclass correlation coefficient. Receiver operating characteristic (ROC) curves were used to investigate and compare the predictive ability of 4D auto-RVQ parameters to evaluate right heart function. A p-value of <0.05 was considered statistically significant.

RESULTS

There were 103 adult patients with PHTN and 25 healthy controls from September 2017 to December 2018. We excluded 27 patients on whom RHC was not performed on the same day as echocardiography. Finally, 76 patients diagnosed with PHTN by RHC were recruited. We divided patients with PHTN ($n = 76$) into three groups according to echocardiographic image quality as follows: high image quality ($n = 24$), average image quality ($n = 48$), and poor image quality ($n = 4$). Clinical and conventional echocardiographic and 4D auto-RVQ characteristics of adult patients with PHTN are described in **Table 1**.

There were no significant differences in age and sex between the PHTN and control groups. Patients with PHTN were predominantly in World Health Organization functional class II or III, with a markedly decreased 6-min walking distance, increased mean PAP, decreased CO, and increased PVR.

The intraclass correlation coefficient is listed in **Table 2**. Interobserver variability showed significant agreement with a 4D auto-RVQ method for most of the measurements except 4D-EDV.

We performed a correlation analysis of the 4D auto-RVQ indices and RHC indices in all PHTN cases ($n = 76$). **Table 3** shows that there was no significant correlation between the RHC and most of the 4D indices in all PHTN patients.

In 24 patients with high image quality, 4D auto-RVQ indices had a very good correlation with RV-CI, and 4D-ESV had a good correlation with all important RHC indices (**Table 4**).

When all PHTN patients with high, average, and poor image quality data combined, the 4D auto-RVQ indices were not clinically meaningful based on the ROC curve analysis (**Table 5**).

ROC curves (**Figure 2**, **Table 6**) illustrated that all six 4D auto-RVQ parameters could predict right heart function in the subgroup of high-quality images, especially mid-RV diameter [area under the curve (AUC) 0.935; 95% confidence interval (CI), 0.714–0.997; $p < 0.001$]. A mid-RV diameter of >50.8 mm had an 85.7% sensitivity and a 90.9% specificity. A RV-ESV of >121.5 mL had a 71.4% sensitivity and a 100% specificity, as well as a Youden index of 0.714 to predict RV-CI (AUC, 0.890; 95% CI, 0.654–0.986; $p < 0.001$).

TABLE 2 | Interobserver variability with 4D auto-RVQ in PHTN and Healthy controls.

	Intraclass correlation	95% CI (lower)	95% CI (upper)	p-value
RV-EDV (mL)	0.012	−0.167	0.190	0.447
RV-ESV (mL)	0.840	0.778	0.886	< 0.001
RV-SV (mL)	0.480	0.330	0.607	< 0.001
RV-EF (%)	0.749	0.659	0.819	< 0.001
RVLS (s, %)	0.261	0.087	0.420	0.002
RVLS (fw, %)	0.317	0.147	0.469	< 0.001
RVD (basal, mm)	0.508	0.271	0.668	0.002
RVD (mid, mm)	0.653	0.537	0.745	< 0.001
RVD (long, mm)	0.541	0.400	0.656	< 0.001
TAPSE (mm)	0.182	0.003	0.350	0.023
RV-FAC (%)	0.631	0.508	0.728	< 0.001

RV, right ventricular; EDV, end-diastolic volume; ESV, end-systolic volume; EF, ejection fraction; RVLS (s, %), right ventricular septum longitudinal strain; RVLS (fw, %), right ventricular free wall longitudinal strain; TAPSE, tricuspid annular plane systolic excursion; FAC, fractional area change; RVD (basal/mid/long), right ventricular diameter (basal, middle, longitudinal).

TABLE 3 | Correlation between RHC and 4D auto-RVQ indices in all PHTN cases ($n = 76$).

	RV-CI (L/min/m^2)		mRAP (mm Hg)		mPAP (mm Hg)		PVR (dyn·s·cm^{-5})	
4D indices	**R**	**P**	**R**	**P**	**R**	**P**	**R**	**P**
RV-EDV (mL)	−0.131	0.268	0.221	0.061	0.223	0.056	0.080	0.496
RV-ESV (mL)	−0.153	0.196	0.225	0.055	0.269	0.020	0.124	0.294
RV-SV (mL)	−0.030	0.801	0.162	0.170	0.051	0.664	−0.045	0.700
RV-EF (%)	0.162	0.171	−0.135	0.257	−0.24	0.035	−0.195	0.096
RVLS (s, %)	0.037	0.758	−0.250	0.033	0.143	0.223	0.101	0.392
RVLS (fw, %)	−0.095	0.425	−0.126	0.289	0.140	0.235	0.168	0.152
RVD (basal, mm)	−0.266	0.031	0.275	0.025	0.081	0.513	0.063	0.612
RVD (mid, mm)	−0.073	0.541	0.103	0.388	−0.01	-0.078	0.030	0.802
RVD (long, mm)	0.029	0.806	0.182	0.126	0.008	0.948	−0.164	0.166
TAPSE (mm)	0.226	0.056	0.072	0.546	−0.078	0.511	−0.268	0.022
RV-FAC (%)	0.152	0.203	−0.099	0.406	−0.165	0.162	−0.203	0.085

RV, right ventricular; EDV, end-diastolic volume; ESV, end-systolic volume; EF, ejection fraction; RVLS (s, %), right ventricular septum longitudinal strain; RVLS (fw, %), right ventricular free wall longitudinal strain; TAPSE, tricuspid annular plane systolic excursion; FAC, fractional area change; RVD (basal/mid/long), right ventricular diameter (basal, middle, longitudinal); RV-CI, right ventricular cardiac index; mRAP, mean right atrial pressure; mPAP, mean pulmonary arterial pressure; PVR, pulmonary vascular resistance.

TABLE 4 | Correlation between RHC and 4D auto-RVQ indices in the high-quality image PHTN group ($n = 24$).

	RV-CI (L/min/m^2)		mRAP (mm Hg)		mPAP (mm Hg)		PVR (dyn·s·cm^{-5})	
4D indices	**R**	**P**	**R**	**P**	**R**	**P**	**R**	**P**
RV-EDV (mL)	−0.579	0.007	0.548	0.012	0.503	0.024	0.444	0.050
RV-ESV (mL)	−0.642	0.002	0.529	0.016	0.501	0.024	0.476	0.034
RV-SV (mL)	−0.126	0.596	0.358	0.122	0.281	0.230	0.145	0.541
RV-EF (%)	0.529	0.016	−0.211	0.371	−0.169	0.477	−0.293	0.211
RVLS (s, %)	−0.172	0.469	−0.225	0.340	0.351	0.129	0.565	0.009
RVLS (fw, %)	−0.519	0.019	−0.032	0.893	0.120	0.615	0.506	0.023
RVD (basal, mm)	−0.691	0.001	0.435	0.063	0.621	0.005	0.606	0.006
RVD (mid, mm)	−0.501	0.025	0.312	0.180	0.290	0.229	0.641	0.002
RVD (long, mm)	−0.204	0.402	0.678	0.001	0.720	0.0001	−0.056	0.819
TAPSE (mm)	0.070	0.775	0.357	0.133	−0.038	0.879	−0.324	0.176
RV-FAC (%)	0.510	0.026	−0.109	0.657	−0.163	0.504	−0.372	0.117

RV, right ventricular; EDV, end-diastolic volume; ESV, end-systolic volume; EF, ejection fraction; RVLS (s, %), right ventricular septum longitudinal strain; RVLS (fw, %), right ventricular free wall longitudinal strain; TAPSE, tricuspid annular plane systolic excursion; FAC, fractional area change; RVD (basal/mid/long), right ventricular diameter (basal, middle, longitudinal); RV-CI, right ventricular cardiac index; mRAP, mean right atrial pressure; mPAP, mean pulmonary arterial pressure; PVR, pulmonary vascular resistance.

TABLE 5 | All PHTN cases ($n = 76$) of 4D auto-RVQ areas of receiver operating characteristic (ROC) curves of various right ventricular function parameters.

	ROC curve area	95% CI	*p*-value	Cutoff	Sensitivity (%)	Specificity (%)	Youden index
RV-EDV (mL)	0.651	0.522–0.766	0.070	> 153.30	66.67	76.74	0.434
RV-ESV (mL)	0.664	0.535–0.777	0.040	> 117.50	66.67	79.07	0.457
RV-SV (mL)	0.561	0.431–0.685	0.485	> 40.20	42.86	81.40	0.242
RV-EF (%)	0.580	0.450–0.703	0.270	≤25.63	76.19	51.16	0.273
RVLS (s, %)	0.525	0.396–0.651	0.770	> −9.39	71.43	11.63	0.169
RVLS (fw, %)	0.646	0.516–0.761	0.070	> −9.78	61.90	72.09	0.340
RVD (basal, mm)	0.643	0.505–0.766	0.080	> 39.4	70.59	57.50	0.281
RVD (mid, mm)	0.585	0.455–0.707	0.320	> 55.20	42.86	86.05	0.289
RVD (long, mm)	0.566	0.435–0.690	0.440	> 76.4	42.86	85.71	0.286
TAPSE (mm)	0.618	0.487–0.738	0.140	≤6.5	33.33	90.48	0.238
RV-FAC (%)	0.658	0.527–0.773	0.029	≤19.17	71.43	64.29	0.357

RV, right ventricular; EDV, end-diastolic volume; ESV, end-systolic volume; EF, ejection fraction; RVLS (s, %), right ventricular septum longitudinal strain; RVLS (fw, %), right ventricular free wall longitudinal strain; TAPSE, tricuspid annular plane systolic excursion; FAC, fractional area change; RVD (basal/mid/long), right ventricular diameter (basal, middle, longitudinal).

DISCUSSION

Despite its clinical importance, the study of RV function is technically challenging, in patients with PHTN. It is usually very difficult to evaluate RV morphology and function using 2DE. Recently, 3DE and 4DE have been introduced and are reportedly feasible and clinically applicable for RV volumetric quantification in patients with acquired RV pressure or volume overload (11). At present, the advantages of 4DE could better reflect RV size and function. As a new technology, 4D auto-RVQ can combine the 3D echocardiographic morphological, functional, and strain characteristics for comprehensive RV evaluation. It has the potential to reflect changes in RV function and pulmonary artery hemodynamics (9, 12).

Our results showed that 4D auto-RVQ, like 3D echocardiography, can accurately detect RV volume measurements in both PHTN patients and healthy control with good interobserver reproducibility (13, 14). However, the intraclass correlation coefficient of 4D-EDV was suboptimal. This may be due to the large RV volume in patients with PHTN so the right ventricle could not be completely included in some cases. Furthermore, 4D auto-RVQ can possibly detect differences in RV diameter, volume, and function. RV volume and basal and middle diameters were significantly enlarged in PHTN, but the longitudinal diameter was not significantly changed. This may be due to lateral expansion of the RV in patients with PHTN. In terms of the strain indices measured by 4D auto-RVQ, the longitudinal strains of the septum and free wall were significantly lower in patients with PHTN compared with the control group (15, 16). Similar to our findings, some reports found that the longitudinal strain of the septum and free wall had the potential to independently predict intermediate- to high-risk features in PAH patients (17). Smith also showed that RV longitudinal strain of the free wall (hazard ratio, 7.63; 95% CI, 1.76–10.27; $p < 0.001$) was a significant determinant of all-cause mortality (18).

When analyzing the data from RHC and 4D auto-RVQ indices, we observed a good correlation between 4D

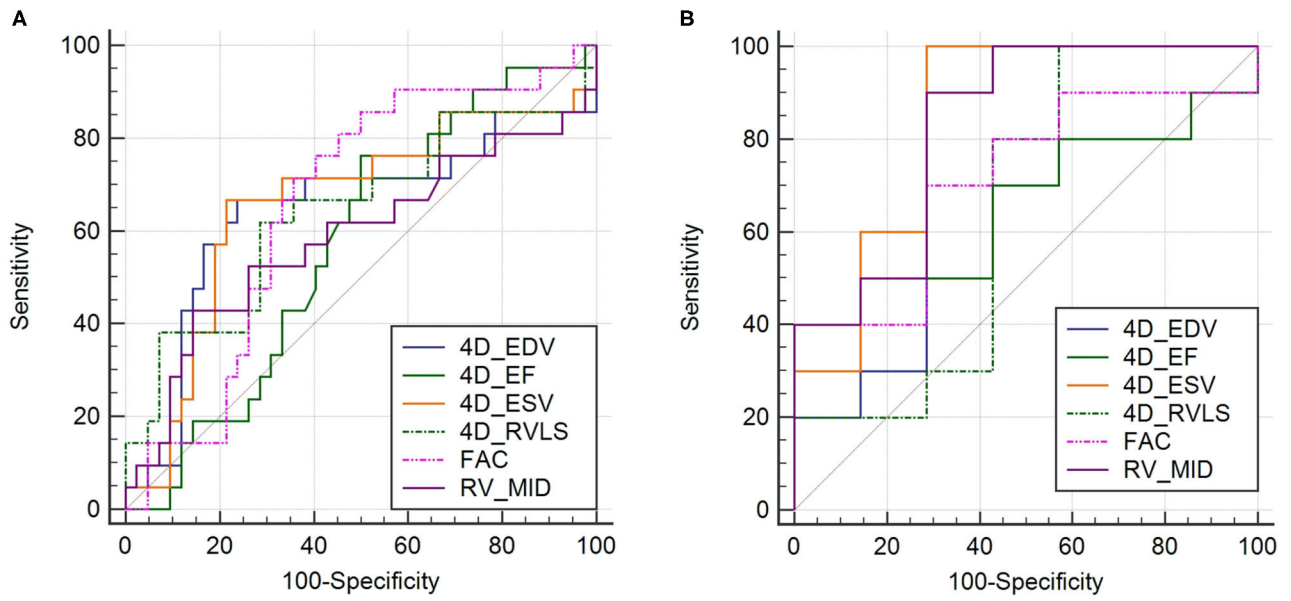

FIGURE 2 | Receiver operating characteristic curves in all patient groups of PHTN ($n = 76$) of 4D auto-RVQ areas of **(A)** and in the high-quality image group of PHTN ($n = 24$) **(B)**. 4D_EDV, four-dimensional end-diastolic volume; 4D_ESV, four-dimensional end-systolic volume; 4D_EF, four-dimensional ejection fraction; 4D-RVLS, right ventricular longitudinal strain of the free wall; FAC, fractional area change; RV_MID, mid–right ventricular diameter.

TABLE 6 | High-quality image group of PHTNs ($n = 24$) of 4D auto-RVQ areas of receiver operating characteristic (ROC) curves of various right ventricular function parameters.

	ROC curve area	95% CI	*p*-value	Cutoff	Sensitivity (%)	Specificity (%)	Youden index
RV-EDV (mL)	0.831	0.583–0.963	0.007	> 153.94	71.43	100	0.714
RV-ESV (mL)	0.890	0.654–0.986	0.001	> 121.50	71.43	100	0.714
RV-SV (mL)	0.636	0.381–0.845	0.421	> 41.45	57.14	90.91	0.481
RV-EF (%)	0.779	0.525–0.937	0.002	≤26.21	100	54.55	0.545
RVLS (s, %)	0.506	0.266–0.745	0.960	> −5.73	42.86	81.82	0.245
RVLS (fw, %)	0.773	0.518–0.993	0.019	> −9.95	71.43	81.82	0.532
RVD (basal, mm)	0.831	0.583–0.963	0.001	> 34.15	85.71	81.82	0.675
RVD (mid, mm)	0.935	0.714–0.997	0.000	> 50.8	85.71	90.91	0.766
RVD (long, mm)	0.600	0.340–0.824	0.540	> 78.6	42.86	100	0.428
TAPSE (mm)	0.557	0.302–0.792	0.714	≤11.3	71.43	60	0.314
RV-FAC (%)	0.800	0.539–0.951	0.011	≤14.66	71.43	90	0.614

RV, right ventricular; EDV, end-diastolic volume; ESV, end-systolic volume; EF, ejection fraction; RVLS (s, %), right ventricular septum longitudinal strain; RVLS (fw, %), right ventricular free wall longitudinal strain; TAPSE, tricuspid annular plane systolic excursion; FAC, fractional area change; RVD (basal/mid/long), right ventricular diameter (basal, middle, longitudinal).

quantification and RHC in patients with high-quality images, but not in the other two groups with suboptimal imaging quality. RV-ESV by 4D auto-RVQ tracked well with RV-CI, mean right atrial pressure, mean PAP, and PVR measurements with RHC. We propose that RV-ESV may be an effective indicator of right heart function and hemodynamic changes in patients with PHTN. RV function analysis needs to take into consideration of its afterload including PVR. Measurement of 4D-ESV, 4D-RV strain, and RV basal and middle diameters had a good correlation with PVR. In the high-quality image group, all six 4DE parameters predicted right heart function. The indices with the best predictive power were RV middle diameter and 4D-ESV. We did notice that some authors previously used RV-EF as an index compared with cardiac magnetic resonance imaging (19, 20).

In summary, 4D auto-RVQ is a possibly useful quantitative tool to measure RV function with validation by RHC and provide meaningful data reflecting RV function. It is important to obtain high-quality RV images and to include the entire RV within the scanning sector. Previous studies have shown that in patients with chronic PHTN, 3D and 3D speckle-tracking echocardiography parameters for global and regional RV dysfunction were better than conventional echocardiographic indices (21, 22). The software for 4D

auto-RVQ generates functional parameters from 4D datasets, making it an easy tool to implement in clinical practice and reducing the amount of time spent using multiple software parameters to simultaneously analyze 4D datasets and speckle-tracking echocardiography.

RHC remains the gold standard for RV hemodynamic evaluation, but 4D auto-RVQ has the potential to be included in routine clinical applications because it provides a relatively quantitative evaluation method for RV function in PHTN patients if high-quality echocardiographic images were acquired.

LIMITATIONS

There are several limitations to our data and results. As a single-center study in a cardiac referral center, we might have had selection bias. Among 103 patients, 27 patients did not simultaneously undergo ultrasonography and RHC and were excluded from the final analysis. World Health Organization functional class IV patients were not enrolled in the study. Our data are mainly applicable to patients with high-quality echocardiographic images. Our sample size was relatively small for an ROC analysis. Finally, we collected only the RHC data of PHTN without the results of cardiac magnetic resonance imaging. Thus, it is difficult to evaluate changes in cardiac volume in real time.

CONCLUSION

In conclusion, 4D auto-RVQ is a new method to estimate RV function and hemodynamic changes compared with gold-standard RHC in patients with PHTN only if high-quality echocardiographic images were acquired.

DATA AVAILABILITY STATEMENT

The raw data supporting the conclusions of this article will be made available by the authors, without undue reservation.

ETHICS STATEMENT

The studies involving human participants were reviewed and approved by the Ethics Committee of Fuwai Hospital (No. 2018-1063). Written informed consent to participate in this study was provided by the participants' legal guardian/next of kin.

AUTHOR CONTRIBUTIONS

WW, BL, and MH drafted the manuscript. LN, YT, JL, JW, SY, and HL contributed to data collection and statistical analysis. HW, DH, CX, and ZZ provided supervision and revised the manuscript. CX contributed to the conception, design, and supervision of the study. All authors contributed to the article and approved the submitted version.

FUNDING

The present study was supported by a grant from Capital Health Development and Scientific Research Projects (Grant No. 2016-2-4036). Fund from Construction of Key Laboratory (Cultivation) of Chinese Academy of Medical Sciences (2019PT310025).

ACKNOWLEDGMENTS

We thank Emily Woodhouse, Ph.D., from Liwen Bianji, Edanz Editing China (www.liwenbianji.cn/ac), for editing the English text of a draft of this manuscript.

REFERENCES

1. Dandel M, Hetzer R. Evaluation of the right ventricle by echocardiography: particularities and major challenges. *Expert Rev Cardiovasc Ther.* (2018) 16:259–75. doi: 10.1080/14779072.2018.1449646
2. Venkatachalam S, Wu G, Ahmad M. Echocardiographic assessment of the right ventricle in the current era: application in clinical practice. *Echocardiography.* (2017) 34:1930–47. doi: 10.1111/echo.13651
3. Gürdogan M, Ustabaşioglu FE, Kula O, Korkmaz S. Cardiac magnetic resonance imaging and transthoracic echocardiography: investigation of concordance between the two methods for measurement of the cardiac chamber. *Medicina.* (2019) 55:260. doi: 10.3390/medicina55060260
4. Kjaergaard J, Petersen CL, Kjaer A, Schaadt BK, Oh JK, Hassager C. Evaluation of right ventricular volume and function by 2D and 3D echocardiography compared to MRI. *Eur J Echocardiogr.* (2006) 7:430–8. doi: 10.1016/j.euje.2005.10.009
5. Lang RM, Badano LP, Mor-Avi V, Afilalo J, Armstrong A, Ernande L, et al. Recommendations for cardiac chamber quantification by echocardiography in adults: an update from the American Society of Echocardiography and the European Association of Cardiovascular Imaging. *Eur Heart J Cardiovasc Imaging.* (2015) 16:233–70. doi: 10.1093/ehjci/jev014
6. Zaidi A, Knight DS, Augustine DX, Harkness A, Oxborough D, Pearce K, et al. Echocardiographic assessment of the right heart in adults: a practical guideline from the British Society of Echocardiography. *Echo Res Pract.* (2020) 7:G19–41. doi: 10.1530/ERP-19-0051
7. Galiè N, Humbert M, Vachiery J-L, Gibbs S, Lang I, Torbicki A, et al. 2015 ESC/ERS Guidelines for the diagnosis and treatment of pulmonary hypertension: The Joint Task Force for the Diagnosis and Treatment of Pulmonary Hypertension of the European Society of Cardiology (ESC) and the European Respiratory Society (ERS): Endorsed by: Association for European Paediatric and Congenital Cardiology (AEPC), International Society for Heart and Lung Transplantation (ISHLT). *Eur Respir J.* (2015) 46:903–75. doi: 10.1183/13993003.01032-2015
8. Miller WL, Grill DE, Borlaug BA. Clinical features, hemodynamics, and outcomes of pulmonary hypertension due to chronic heart failure with reduced ejection fraction: pulmonary hypertension and heart failure. *JACC Heart Fail.* (2013) 1:290–9. doi: 10.1016/j.jchf.2013.05.001
9. Aubert R, Venner C, Huttin O, Haine D, Filippetti L, Guillaumot A, et al. Three-dimensional echocardiography for the assessment of right ventriculo-arterial coupling. *J Am Soc Echocardiogr.* (2018) 31:905–15. doi: 10.1016/j.echo.2018.04.013
10. Rudski LG, Lai WW, Afilalo J, Hua L, Handschumacher MD, Chandrasekaran K, et al. Guidelines for the echocardiographic assessment of the right heart in adults: a report from the American Society of Echocardiography endorsed by the European Association of Echocardiography, a registered branch of the European Society of Cardiology, and the Canadian

Society of Echocardiography. *J Am Soc Echocardiogr.* (2010) 23:685–713. doi: 10.1016/j.echo.2010.05.010
11. Knight DS, Grasso AE, Quail MA, Muthurangu V, Taylor AM, Toumpanakis C, et al. Accuracy and reproducibility of right ventricular quantification in patients with pressure and volume overload using single-beat three-dimensional echocardiography. *J Am Soc Echocardiogr.* (2015) 28:363–74. doi: 10.1016/j.echo.2014.10.012
12. Zhang XM, Zhuang Q, Yang MH, Wang W, Zheng Y, Qiao ZQ, et al. [Value of four-dimensional echocardiography combined with speckle tracking technique on the assessment of right heart function and prognosis in patients with pulmonary arterial hypertension]. *Zhonghua Xin Xue Guan Bing Za Zhi.* (2018) 46:965–71. doi: 10.3760/cma.j.issn.0253-3758.2018.12.007
13. Nagata Y, Wu VC-C, Kado Y, Otani K, Lin F-C, Otsuji Y, et al. Prognostic value of right ventricular ejection fraction assessed by transthoracic 3D echocardiography. *Circ Cardiovasc Imaging.* (2017) 10:e005384. doi: 10.1161/CIRCIMAGING.116.005384
14. Moceri P, Duchateau N, Baudouy D, Schouver E-D, Leroy S, Squara F, et al. Three-dimensional right-ventricular regional deformation and survival in pulmonary hypertension. *Eur Heart J Cardiovasc Imaging.* (2018) 19:450–8. doi: 10.1093/ehjci/jex163
15. Jone P-N, Schäfer M, Pan Z, Bremen C, Ivy DD. 3D echocardiographic evaluation of right ventricular function and strain: a prognostic study in paediatric pulmonary hypertension. *Eur Heart J Cardiovasc Imaging.* (2018) 19:1026–33. doi: 10.1093/ehjci/jex205
16. Leong DP, Grover S, Molaee P, Chakrabarty A, Shirazi M, Cheng YH, et al. Nonvolumetric echocardiographic indices of right ventricular systolic function: validation with cardiovascular magnetic resonance and relationship with functional capacity. *Echocardiography.* (2012) 29:455–63. doi: 10.1111/j.1540-8175.2011.01594.x
17. Liu B-Y, Wu W-C, Zeng Q-X, Liu Z-H, Niu L-L, Tian Y, et al. The value of three-dimensional echocardiography in risk stratification in pulmonary arterial hypertension: a cross-sectional study. *Int J Cardiovasc Imaging.* (2020) 36:577–84. doi: 10.1007/s10554-019-01743-1
18. Smith BCF, Dobson G, Dawson D, Charalampopoulos A, Grapsa J, Nihoyannopoulos P. Three-dimensional speckle tracking of the right ventricle: toward optimal quantification of right ventricular dysfunction in pulmonary hypertension. *J Am Coll Cardiol.* (2014) 64:41–51. doi: 10.1016/j.jacc.2014.01.084
19. Kidawa M, Chizyński K, Zielińska M, Kasprzak JD, Krzeminska-Pakula M. Real-time 3D echocardiography and tissue Doppler echocardiography in the assessment of right ventricle systolic function in patients with right ventricular myocardial infarction. *Eur Heart J Cardiovasc Imaging.* (2013) 14:1002–9. doi: 10.1093/ehjci/jes321
20. Gopal AS, Chukwu EO, Iwuchukwu CJ, Katz AS, Toole RS, Schapiro W, et al. Normal values of right ventricular size and function by real-time 3-dimensional echocardiography: comparison with cardiac magnetic resonance imaging. *J Am Soc Echocardiogr.* (2007) 20:445–55. doi: 10.1016/j.echo.2006.10.027
21. Vitarelli A, Mangieri E, Terzano C, Gaudio C, Salsano F, Rosato E, et al. Three-dimensional echocardiography and 2D-3D speckle-tracking imaging in chronic pulmonary hypertension: diagnostic accuracy in detecting hemodynamic signs of right ventricular (RV) failure. *J Am Heart Assoc.* (2015) 4:e001584. doi: 10.1161/JAHA.114.001584
22. Lu KJ, Chen JXC, Profitis K, Kearney LG, DeSilva D, Smith G, et al. Right ventricular global longitudinal strain is an independent predictor of right ventricular function: a multimodality study of cardiac magnetic resonance imaging, real time three-dimensional echocardiography and speckle tracking echocardiography. *Echocardiography.* (2015) 32:966–74. doi: 10.1111/echo.12783

Conflict of Interest: The authors declare that the research was conducted in the absence of any commercial or financial relationships that could be construed as a potential conflict of interest.

Advantages of publishing in Frontiers

OPEN ACCESS
Articles are free to read for greatest visibility and readership

FAST PUBLICATION
Around 90 days from submission to decision

HIGH QUALITY PEER-REVIEW
Rigorous, collaborative, and constructive peer-review

TRANSPARENT PEER-REVIEW
Editors and reviewers acknowledged by name on published articles

Frontiers
Avenue du Tribunal-Fédéral 34
1005 Lausanne | Switzerland

Visit us: www.frontiersin.org
Contact us: frontiersin.org/about/contact

REPRODUCIBILITY OF RESEARCH
Support open data and methods to enhance research reproducibility

DIGITAL PUBLISHING
Articles designed for optimal readership across devices

FOLLOW US
@frontiersin

IMPACT METRICS
Advanced article metrics track visibility across digital media

EXTENSIVE PROMOTION
Marketing and promotion of impactful research

LOOP RESEARCH NETWORK
Our network increases your article's readership